ABSTRACT

Title of Dissertation: QUANTUM COHERENT DYNAMICS IN A DC SQUID PHASE QUBIT USING AN LC FILTER.

Hyeokshin Kwon, Doctor of Philosophy, 2011

Dissertation Directed By: Professor Frederick C. Wellstood
Department of Physics

A dc SQUID phase qubit consists of two Josephson junctions in a loop. One junction acts as a qubit with two lowest energy levels forming the $\left|0\right\rangle$ and $\left|1\right\rangle$ status. The second junction and the loop inductance act to isolate the qubit junction from noise. In this thesis, I report on the improvement of the relaxation time and the coherence time in a dc SQUID phase qubit that used an LC filter. I also report the measurement of anomalous switching curves.

In order to improve the relaxation and coherence times, I used two isolation networks, an LC isolation network and an inductive isolation network, to decouple the device from the current bias lines. This produced a very large total effective resistance of the input leads that increases the relaxation time of the qubit. In addition, I connected a low-loss SiN_x shunting capacitor across the qubit junction to reduce dielectric losses.

I measured two dc SQUID phase qubits. Device DS6 had a 4 $(\mu m)^2$ $Al/AlO_x/Al$ qubit junction with a critical current of 0.5 μA and a 1 pF shunting capacitor. It used an

LC filter made from a 10 nH inductor and a 145 pF capacitor. The capacitors contained N-H rich SiN_x which produced a loss tangent of about 7×10^{-4}. Device DS8 had a 2 $(\mu m)^2$ $Al/AlO_x/Al$ qubit junction with a critical current of 77 nA and an LC filter similar to the first one. The shunting capacitor contained Si-H rich SiN_x.

Using a pulse readout technique, I measured the characteristics of the qubits, including the transition spectrum, Rabi oscillations, relaxation, Ramsey fringes and state tomography. The best relaxation time T_1 for device DS6 was 32 ns and 280 ns for device DS8. The best Rabi decay time T' for DS6 was 42 ns while for device DS8 it was 120 ns. From these and other data I obtained estimates for the best coherence time T_2 in device DS6 of 61 ns and 76 ns in device DS8.

In DS8, I observed anomalous switching curves; *i.e.* switching curves which were qualitatively different from conventional switching curves. In the conventional case, the switching curve for the superposition state is the weighted sum of the $|0\rangle$ and $|1\rangle$ curves, but it was not in device DS8. Instead, the switching curve shifted along the current axis as the exited state probability increased. I present a model for understanding the behavior and use this model to extract the probability to be in the excited state.

QUANTUM COHERENT DYNAMICS IN A DC SQUID PHASE QUBIT USING AN LC FILTER

by

Hyeokshin Kwon

Dissertation submitted to the Faculty of the Graduate School of the
University of Maryland, College Park, in partial fulfillment
of the requirements for the degree of
Doctor of Philosophy
2011

Advisory Committee:
Professor Frederick C. Wellstood, Advisor/Chair
Professor Christopher J. Lobb
Professor J. Robert Anderson
Professor Richard L. Greene
Professor Ichiro Takeuchi

Dedicated to my dear family.

Acknowledgements

I thank my advisors Prof. Bob Anderson, Prof. Chris Lobb and Prof. Fred Wellstood for their support and help during my graduate study. First of all, I was not able to finish my graduate study without Prof. Fred Wellstood. He was an excellent teacher who taught me everything I needed for my research, a great collaborator with whom I could discuss physics, an expert who gave me the solutions for any problem I faced during my research, and my role model as a great physicist who works hard and has smart thoughts. Prof. Chris Lobb and Prof. Bob Anderson were excellent researchers and physicists who always showed passion and intuition about my research. They were nice thoughtful caring advisers who gave me great help whenever I needed it.

I would like to thank my committee members, Prof. Richard Greene and Prof. Ichiro Takeuchi for their helpful advice and comments on my thesis. I also thank Prof. Alex Dragt who gave very helpful comments about my research from a theoretical point of view. I thank Prof. Steve Anlage who helped me figure out problems with the microwave measurement and I also thank Prof. Michael Fuhrer and Prof. Richard Greene who created the opportunity for students to give practice talks at the CNAM seminar.

Dr. Rupert Lewis was a great role model as a postdoc. He was a great researcher and an expert on cryogenics. He helped students including myself whenever they needed help. He showed me everything I needed to learn and gave me good advice about whatever problems I was having.

Dr. Sudeep Dutta was a great teacher who answered any trivial questions I asked about research. He also showed how students should work in the lab. I thank him for teaching me much of the fundamental physics of my research.

I thank Dr. Tauno Palomaki who taught me how to run the dilution refrigerator and measure qubits. He was a role model as a graduate student who worked hard.

I thank Dr. Hanhee Paik who was a good friend, a great caregiver and a helpful advisor who could discuss research and life. She taught me how to make devices at the beginning. She also helped deposit SiN_x layers many times when she was working as a postdoc at LPS.

I thank Tony Przybysz. He and I were a good team. We ran the dilution refrigerator and measured the devices together. During my graduate study, I enjoyed discussing and chatting with him about my research. I also must thank Ben Cooper who is an expert on the physics of our research. Whenever I had trouble with theoretical problems, he did not hesitate to share ideas.

I am grateful to other former and current group members: Dr. John Matthews, Dr. Gus Vlahacos, Saurabh Paul and Rangga Budoyo. They helped me whenever I needed help and gave me helpful suggestions about my research.

I am also grateful for me theoretical help of Dr. Kaushik Mitra, Dr. Fred Strauch and Dr. Eite Tiesinga. They gave me ideas and insight about theoretical aspects of my research. My research could not have been completed without them.

I owe a tremendous amount to QC group members at LPS. Dr. Ben Palmer helped me test devices and deposit SiN_x for my first device. Dr. Kevin Osborn gave me much information on SiN_x which was important for my research. Vitaly Zaretskey helped me dice my wafers many times. Dr. Zaeill Kim was always there to discuss our research at group meetings and conferences.

I am grateful to many students and staff at CNAM. Chaun Jang and Dr. Dan Lenski helped me use the SEM. If Paul Bach and Dr. Zianhao Zhang did not lend me liquid helium, my research would have stopped many times. Brian Straughn and Doug Bensen were always there to solve mechanical problems.

Everyone associated with the Physics department and the CNAM offices was nice. I thank Belta Pollard, Cleopatra White, Grace Sewlall, Cheryl Ekstrom, Yuri Kubota, Jane Hessing, Linda O'Hara, Jesse Anderson and Al Godinez for their kind help.

I also thank my many Korean friends at NIST and at UMD for their personal support and for many useful discussions about my research: Dr. Hongki Min, Dr. Sooyong Jung and Dr. Youngjae Song at NIST and Dr. Kihwan Kim, Dr. Jonghee Lee, Dr. Youngsoo Yoon, Sungjae Cho, Chaun Jang, Hongsuk Kang, Doojin Kim, Jaekwang Jung, Seung-Yong Lee, Jinwoo Kim, Dr. Yousin Kim, Kwan Lee, Dohun Kim, Prof. Kiyong Kim, Prof. Eun-Suk Seo, Prof. Ho Jung Paik and Prof. Young S. Kim at the University of Maryland, College Park. I thank Chaun Jang, Dr. Hongki Min and Sungjae Cho, who kept me updated about graphene and Dr. Kihwan Kim, who let me know what was going on in ion-trap quantum computing research.

It was always a pleasure to discuss general science and physics with my friends who attended Seoul National University with me and are/were graduate students at various universities in the U.S. I was welcomed by them and had fun with them: Ouk-Jae Lee at Cornell University, Seonggeun Cho at the University of Rochester, Joonho Jang, Hyungjin Ma and Young-Ill Joe at UIUC, Wonseok Shin at Stanford University, Joonhyuk Choi at Harvard University, Jiwon (Benjamin) Choi at Columbia University and Hyun-Jung Lee at Georgia Tech.

Finally, I deeply thank my parents, Jaeyoon Kwon and Byungran Seo, and my brother Hyukihn Kwon for their endless support and love. My parents gave me their total support when I decided to study physics in Korea. They have always emphasized that I must do whatever I really want to do. Their teachings have led me to continue studying physics without losing my passion. I also deeply thank Ahryang Lee for everything and I cannot imagine my Ph. D. without her.

Table of Contents

List of Tables x

List of Figures xi

Chapter 1 Introduction 1
- 1.1 Quantum Computation 1
  - 1.1.1 General Concept 1
  - 1.1.2 DiVincenzo Criteria 3
  - 1.1.3 Qubits 5
- 1.2 Phase Qubits 7
- 1.3 Overview of the Thesis 9

Chapter 2 The dc SQUID Phase Qubit 11
- 2.1 Josephson Junctions 11
- 2.2 RCSJ Model of a Josephson Junction 16
- 2.3 The Junction Hamiltonian 18
- 2.4 The dc SQUID Phase Qubit 23
  - 2.4.1 SQUID Hamiltonian 24
  - 2.4.2 Current-Flux Characteristics 29
  - 2.4.3 f_{01} vs. I_b 32
  - 2.4.4 Tunneling 35

Chapter 3 Sources of Decoherence and Protection from Decoherence in the dc SQUID Phase Qubit 37
- 3.1 Dynamics of a Two-Level System 37
  - 3.1.1. Bloch Sphere 38
  - 3.1.2 Energy Relaxation 42
  - 3.1.3 Dephasing 44
  - 3.1.4 Decoherence 46
  - 3.1.5 Inhomogeneous Broadening 48
- 3.2 Current Noise 49
- 3.3 Critical Current Noise 57
- 3.4 Charge Noise 57
- 3.5 Flux Noise 58
- 3.6 Dielectric Loss and Charged TLS's 59
- 3.7 Dielectric Loss in the Substrate and Other Dielectric Layers 61
- 3.8 Summary 62

Chapter 4 Layout and Fabrication of dc SQUID Phase Qubit 63
- 4.1 Design of Devices DS6 and DS8 63
- 4.2 Fabrication Procedure 69
- 4.3 Optical Lithography 69
- 4.4 SiN_x Film 75

4.4.1 Deposition of SiN_x in HDCVD 76
4.4.2 Multi Layer Process and Etching 78
4.5 Al/AlO_x/Al Junctions 81
4.5.1 Double-Angle Evaporation 81
4.5.2 Oxidation and Critical Current 84
4.5.3 Liftoff 85
4.5.4 Wire Bonding 86
4.5.5 Wafer Dicing 87
4.6 Parameters for Devices DS6 and DS8 88
4.7 Summary 89

Chapter 5 Experimental Setup 90
5.1 Introduction 90
5.1.1 Operating Procedure for the Refrigerator 91
5.1.2 Shielding, Wiring and Filters 97
5.2 Measurement Instruments 103
5.2.1 Low Noise Amplifier 103
5.2.2 Arbitrary Waveform Generator and Pulse Generator 106
5.2.3 Microwave Source and Mixers 107
5.2.4 Filters, Attenuators and Power Dividers 110
5.3 Measurement Setup 111
5.3.1 I-Φ Measurement 111
5.3.2 Γ vs. I_p Measurement 113
5.3.3 Measuring the Frequency Spectrum 114
5.3.4 Switching Curves Measurement 116
5.3.5 Measurement of Rabi Oscillations 116
5.3.6 Relaxation Measurement 117
5.3.7 Spin Echo Measurement 118
5.3.8 State Tomography Measurement 118
5.4 Summary 120

Chapter 6 Results of Qubit Characterization 122
6.1 Device DS6 123
6.1.1 Current-Flux (I-Φ) Characteristics 123
6.1.2 Escape Rate and Switching Curves 123
6.1.3 Transition Frequency Spectrum 126
6.1.4 Splitting Characterization 131
6.1.5 Relaxation Rate 133
6.1.6 Rabi Oscillations, Ramsey Fringe and Decoherence 136
6.2 Device DS8 139
6.2.1 Current-Flux (I-Φ) Characteristics 139
6.2.2 Switching Curves 141
6.2.3 Transition Frequency Spectrum 143
6.2.4 Splitting Characterization 146
6.2.5 Relaxation Rate 148
6.2.6 Rabi Oscillations, Ramsey Fringe and Decoherence 150

6.2.7 State Tomography 150
6.3 Comparison of DS6, DS8 and DS3 157
6.4 Summary 159

Chapter 7 Understanding the Anomalous Switching Curves 160
7.1 Introduction 160
7.2 Strong Coupling and the Born-Oppenheimer Approximation 165
7.2.1 Coupling Regime 165
7.2.2 Hamiltonian of the dc SQUID Phase Qubit 167
7.2.3 Device Parameters outside the Weak Coupling Regime 169
7.2.4 Working through the Born-Oppenheimer Approximation 173
7.2.5 Dependence of the Barrier Height on the Qubit State 176
7.2.6 Superposition State 178
7.3 Analysis of Switching Curves 182
7.3.1 Analysis Procedure 182
7.3.2 Comparing the Model to Measured Switching Curves 186
7.4 Switching Curves during a Rabi Oscillation 188
7.5 Switching Curves during a Relaxation 191
7.6 Unusual Implications for State Measurement 195
7.7 Summary 199

Chapter 8 Conclusions 200
8.1 Design and Characterization of a dc SQUID Phase Qubit 200
8.2 Anomalous Switching Curves 202
8.3 Future Work 203

Bibliography 205

List of Tables

3.1 Expected T_1 from the design parameters for DS8 61

4.1 Parameters for dc SQUID phase qubit DS6 87

4.2 Parameters for dc SQUID phase qubit DS8 88

5.1 Commercial electronics used in the experiments 103

6.1 Parameters obtained for devices DS3, DS6 and DS8 157

List of Figures

1.1 Schematic diagrams for various superconducting qubits 8

2.1 Current-voltage (I-V) characteristic curve and RCSJ model 14

2.2 Tilted washboard potential 17

2.3 Schematic of a dc SQUID phase qubit 25

2.4 Potential surface $U(\gamma_1, \gamma_2)$ for a dc SQUID phase qubit with $I_b = 0\ \mu A$ 27

2.5 Potential surface $U(\gamma_1, \gamma_2)$ for a dc SQUID phase qubit with $I_b = 0.7\ \mu A$ 28

2.6 Simulation of I-Φ curve 31

2.7 Simulation of transition frequencies 34

3.1 Representation of a qubit state as a point on the Bloch sphere 39

3.2 Representation of a qubit state rotation on the Bloch sphere 45

3.3 Various possible sources of decoherence in a dc SQUID phase qubit 47

3.4 Schematic diagram for devices DS6 and DS8 51

3.5 Calculated relaxation time T_1 vs. frequency f of the LC and LJ circuit 53

3.6 Calculated relaxation time T_1 vs. frequency f including radiation 56

4.1 Diagram and photograph of device DS6 64

4.2 Photograph of the LC filter area of devices DS6 and DS8 66

4.3 Photograph of the SQUID loop area of devices DS6 and DS8 68

4.4 Equipment for fabrication and measurement at CNAM 70

4.5 Equipment for fabrication and measurement in the Kim Bldg. 71

4.6 Photograph of the qubit junction area of devices DS6 and DS8 77

4.7 Schematic diagram for double angle evaporation process 82

5.1 Photograph of Model 200 TLE Dilution Refrigerator 92

5.2 Photographs of shielding 98

5.3 Schematic of refrigerator wiring 100

5.4 Photograph of the switch box area and timer 101

5.5 Overview of experimental set-up for a typical measurement 105

5.6 Measured voltage pulse 108

5.7 Photographs of Marki microwave mixers 109

5.8 Experimental set-up for microwave measurements 112

5.9 Biasing scheme for the Rabi and relaxation measurements 115

5.10 Biasing scheme for the spin-echo and state tomography 119

5.11 Measured microwave pulses for state tomography 121

6.1 I-Φ curve for device DS6 and bias trajectories 124

6.2 Escape rate measurement in device DS6 125

6.3 P_s vs. I_p for device DS6 127

6.4 False color plot of frequency transition spectrum of device DS6 129

6.5 0-to-1 transition spectrum for device DS6 130

6.6 FWHM at different current bias points in device DS6 132

6.7 Spectroscopic width of 0-to-1 transition in device DS6 134

6.8 Plot of switching probability P_s vs. time t 135

6.9 Ramsey fringe measurement in device DS6 138

6.10 I-Φ curve for device DS8 and bias trajectories 140

6.11 P_s vs. I_p for device DS8 142

6.12 0-to-1 transition spectrum for device DS8 144

6.13 T_2^* vs. f_{01} for device DS8 145

6.14 Resonance peaks near an avoided level crossing in DS8 147

6.15 Best and typical relaxation curves for DS8 149

6.16 Best and typical Rabi oscillation curves for DS8 151

6.17 Ramsey fringe curves for DS8 152

6.18 Radial state tomography of device DS8 for the $\left|0\right\rangle$ state 154

6.19 Radial state tomography of device DS8 for the $\left(\left|0\right\rangle+\left|1\right\rangle\right)/\sqrt{2}$ state 155

6.20 Radial state tomography of device DS8 for the $\left|1\right\rangle$ state 156

7.1 Simulation of conventional switching probability s-curves 162

7.2 Measured switching curves 164

7.3 Schematic picture of U of the qubit and isolation junction 171

7.4 Extracted $\hat{I}_{11}$, $\hat{I}_{01}$, $\hat{I}_{00}$ curves 183

7.5 Selected s-curves measured during a Rabi oscillation in device DS8 187

7.6 Full measured s-curves during a Rabi oscillation in device DS8 189

7.7 Full measured s-curves during a relaxation in device DS8 190

7.8 Extracted Rabi oscillation and relaxation curves in device DS8 192

7.9 Measured s-curves at $f = 3.420$ GHz in device DS8 193

7.10 Measured s-curves during a Rabi oscillation at different biases 194

7.11 False color plot of dP_s/dI_p vs. time t 198

Chapter 1

Introduction

1.1 Quantum Computation

1.1.1 General Concept

Computers have developed to the point where they are routinely used for calculating complicated problems that a human could never solve by hand. However, even if the performance of modern computers is outstanding, there are some problems that would take far too long for any classical computer to solve. One problem of this type is simulation of quantum systems with many degrees of freedom. As a possible solution, in the early 1980's Feynman proposal using a quantum computer to simulate the behavior of quantum systems [1], He was able to show that such a computer would be more efficient than a conventional "classical" computer at performing such simulations.

Another key problem for classical computers is cryptography. In order to block private information from being revealed during communication, information is routinely encrypted. The standard method is RSA encryption [2]. The security of RSA is based on the difficulty of the factoring of large numbers. Essentially, if two large prime factors are multiplied to produce a public key, then it is typically very hard to find the original numbers from just knowledge of the public key; these prime factors are necessary to decode the information encoded by the public key. Peter Shor showed, in principle, that numbers could be factored much faster using a quantum computer [3]. More than any other result, the possibility of breaking RSA led to wide interest in research towards developing a quantum computer.

The fundamental component of a quantum computer is a quantum bit or qubit. A qubit is just a two-level quantum system. The two states are typically labeled the ground state |0> and the excited state |1> [4]. Unlike a classical bit, which can only take on values of 0 or 1, a qubit can be in a quantum superposition of the $\left|0\right\rangle$ and $\left|1\right\rangle$ state. In theory, one qubit can contain an unlimited amount of information by spanning a 2-dimensional Hilbert space and allowing coefficients of the superposition state to have arbitrary precession. However, there is an essential binary (0 or 1) limitation to find the coefficients of a superposition state when a state is measured. In addition to superposition states, multiple qubits can be entangled with each other [5]. Ultimately it is because of superposition and entanglement that a quantum computer would be able to solve some types of problems that are intractable to conventional computers.

Since Feynman first described the concept of quantum computing, a few key algorithms have been developed. In 1985, Deutsch suggested an algorithm that showed that a quantum computer could perform a certain calculation much faster than a classical computer [6]. Using the Deutsch-Jozsa algorithm [7], one can use a quantum computer to find whether a function f(x) is constant. Only one evaluation of the function f(x) is needed to solve whether the f(x) is constant in a quantum computer. In contrast, $2^{n-1}+1$ evaluations are needed in a classical computer, where n is the number of possible values of x. This was the first proof that a quantum computer could work more efficiently than a classical computer. After Deutsch's work, Peter Shor showed that finding the prime factors of an integer and a discrete logarithm problem could be solved efficiently using a quantum computer [3]. Both algorithms were based on the quantum Fourier transform which is a variation on the well-known classical Fourier transform.

A different type of algorithm was discovered by Lov Grover. Grover's quantum algorithm involves the search of a database, and Grover showed this search was more efficient than could be accomplished with a classical computer [8]. If there is a data space with N elements, then a classical computer takes on average N/2 attempts to find a property which matches a given criterion. However, Grover showed that a quantum computer can find it in only $\sqrt{N}$ steps using his algorithm.

While only a few distinct quantum algorithms have been discovered, those algorithms showed in principle that a quantum computer can in certain cases outperform a classical computer. This naturally raises the question of whether such a computer can be built in practice.

1.1.2 DiVincenzo Criteria

In order for a quantum computer to be used in the real world, the qubits in a quantum computer must satisfy a few specific criteria. In 1996, David DiVincenzo suggested five criteria for qubits, what are now called the DiVincenzo criteria [9, 10]. The criteria are as follows.

(1) Well defined qubit and scalability. A qubit used in a quantum computer must be a well defined quantum two-level system. A multi-level system could be used, but a two-level system is simplest. One also expects to be able to control two energy levels more easily than multiple levels. Another important issue is the ability to make multiple qubits. A practical quantum computer will need to have at least thousands of qubits, so the ability to scale to a large number of qubits is critical.

(2) State initialization. If a quantum system is not set in a well-defined initial state, we cannot perform a meaningful calculation. In principle, it can be easy to initialize a quantum state by simply cooling the system to a very low temperature and minimizing external noise.

(3) Long coherence times. The main difficulty in realizing a quantum computer from superconducting qubits is decoherence. A quantum superposition state contains amplitude and phase information that needs to be preserved during quantum operations. Environmental noise and dissipation lead to dephasing and relaxation, limiting the time over which the phase of a superposition state is preserved. For example, in Shor's algorithm, about 300 gate operations were needed to simulate the factoring of 15 into 5 and 3 [11]. If we assume a gate operation time of 10 ns, then 3 μs would be necessary for the entire computation.

(4) Universal gates. The ability to perform any possible state manipulation is important for constructing a universal computer. It is sufficient to have arbitrary single qubit gate operations and a two-qubit CNOT gate for constructing arbitrary gate operations in a quantum computer [4].

(5) Measurement capability. At the end of a quantum computation, the result of the calculation must be read out. The measurement process is dependent on the physical system. A projective measurement onto the 0 and 1 qubit state is needed to measure the state. In this case, when a qubit is in a superposition state $|\Psi\rangle = \alpha|0\rangle + \beta|1\rangle$, the outcomes of the measurement are $|0\rangle$ with a probability of $|\alpha|^2$ and $|1\rangle$ with a probability of $|\beta|^2$.

1.1.3 Qubits

Significant advances have been made in quantum computation during the last decade. About a decade ago, Chuang and co-workers first claimed to have done some single quantum computations using nuclear magnetic resonance (NMR) techniques. It is now recognized that the states accessible in such bulk NMR experiments are separable, and required exponential number of steps to prepare [12]. These computations are better thought of as simulations of quantum computation. Indeed, it was later pointed out that these experiments do not show exponential speed-up as would be expected from a true quantum computation [13, 14]. Since then, many types of qubits have been developed and many demonstrations have been reported of true quantum gates in two-qubit systems [10]. Many systems have satisfied some of the DiVincenzo criteria, however there is no perfect system yet for quantum computation.

NMR. In the NMR approach, a nucleus with spin ½ is the qubit. Nuclear magnetic resonance techniques are used to control the nuclear spins. Although we cannot call NMR a very early quantum computer, because of critical problems with scaling and the measurement processes, the NMR approach has provided valuable insight into how to do quantum computations.

Quantum dots. There are two main types of quantum dots that are being studied as qubits [15]. Semiconductor charge quantum dots are qubits in which an electron is confined to two adjacent quantum dots. In a spin quantum dot, the qubit is a spin state of one or more electrons trapped in an artificial potential well [15]. Most quantum dots are made using e-beam lithography on a silicon wafer and so this is a scalable technique. The state of the quantum dot can be initialized by electron injection and gate operations have been demonstrated [16-18]. So far the coherence times in charge quantum dots have been relatively short and it is still difficult to address individual qubits in a spin quantum dot. However, great progress has been made on both types and they remain viable as potential qubits.

Trapped ions and neutral atoms. Laser cooling and trapping techniques can be used to create neutral atom or ion qubits [19, 20]. The vibrational normal modes of a 1-D trapped ion system allow for controlled coupling between the ions. Trapped ions satisfy most of the DiVincenzo criteria. About 10 ions have already been trapped [21] and it is expected that more than 100 ions will be trapped in the near future. Focused laser light can control the state of each qubit and the system is initialized by optical pumping. Neutral atom systems have some similarities to the ion trap systems. Neutral atoms are trapped using an optical lattice and some key challenges involve producing two-qubit gates [19].

Superconducting qubits. All superconducting qubits contain one or more Josephson junctions. About two decades after macroscopic quantum tunneling was observed in Josephson junctions [22], macroscopic quantum coherent oscillations were reported in a charge qubit [23]. This was the first demonstration that devices based on a Josephson junction might be useful as a qubit. A Josephson junction can be thought of as an anharmonic oscillator. The anharmonicity of the junction produces unequal energy level spacings and this allows the state of the qubit to be controlled. Superconducting qubits can be fabricated using standard photolithographic techniques and so the approach is scalable. By cooling the device to low temperatures, ground state initialization can be achieved. Single qubit gates and double qubit states have already been demonstrated [24], and the measurement fidelity can be reasonably good [25].

Superconducting qubits can be broadly divided into three kinds: charge, flux and phase qubits (see Fig. 1.1). In a charge qubit, the number of Cooper pairs on a small island is a relatively sharply defined quantum variable. This is achieved by making the Josephson energy $E_J=\hbar I_0/2e$ where I_0 is the critical current of the Josephson junction about the same as the charging energy $E_C= e^2/2C$ where C is the island capacitance. [23]. Variations on the charge qubit include quantronium [26] and the transmon [27]. In a flux qubit, the flux in a small superconducting loop is a good quantum variable and the ratio E_J/E_C is typically larger than 1. In a phase qubit [28, 29], the phase difference across a Josephson junction is the sharply defined quantum variable and the ratio E_J/E_C is much larger than 1.

1.2 Phase Qubits

The phase qubit has been investigated by the Maryland group since Ramos *et. al.* first suggested that a current-biased Josephson junction could be used as a qubit [28]. This suggestion was motivated by much earlier work on macroscopic quantum tunneling phenomenon [22, 30-32]. Within a year of this proposal, Martinis's group at NIST, Boulder, demonstrated Rabi oscillations in a dc SQUID phase qubit [29]. The Maryland

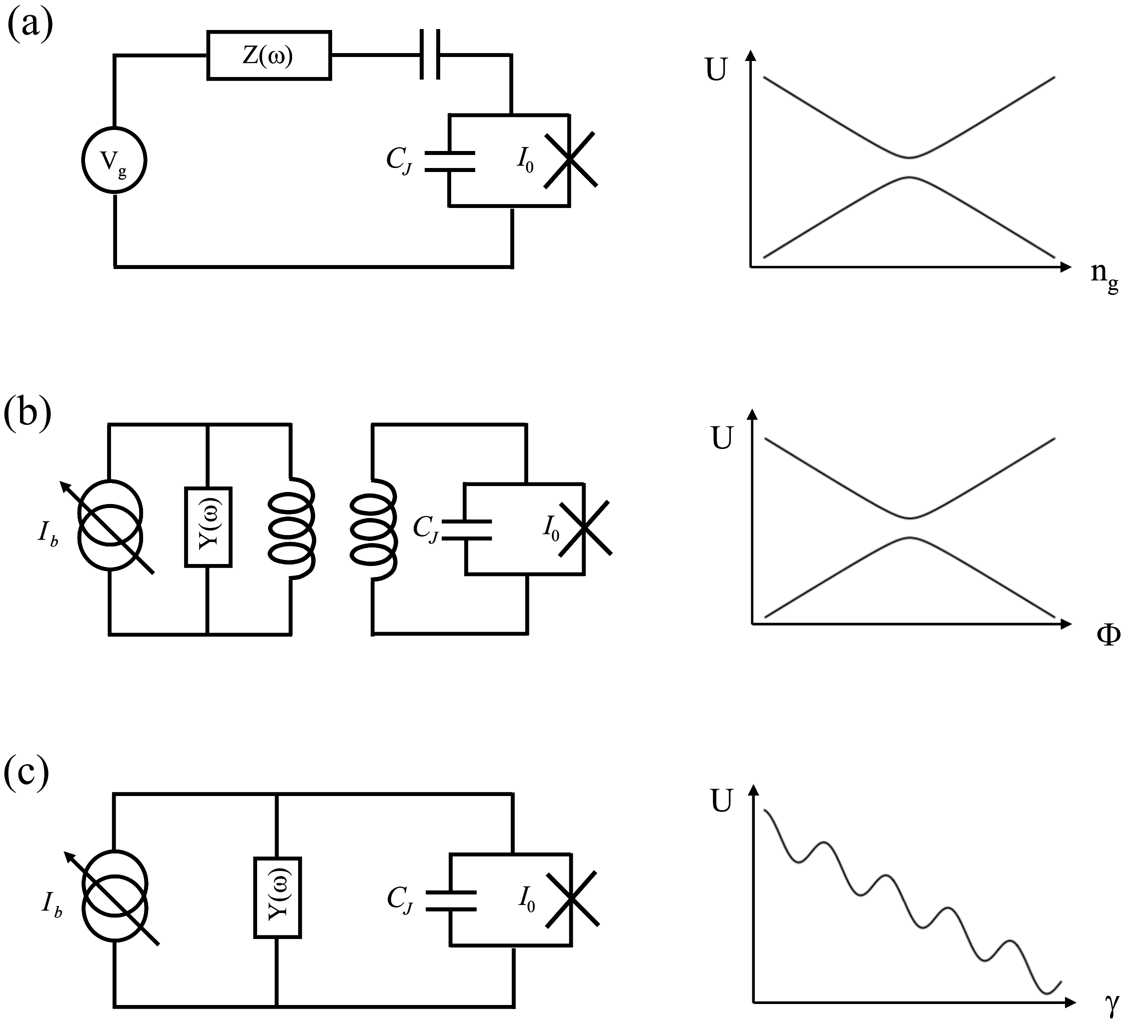

Figure 1.1: Schematic diagram and the potential energy U for various superconducting qubits: (a) charge qubit, (b) flux qubit, and (c) phase qubit. U is the potential energy, n_g is the reduced gate voltage, Φ is the flux, γ is the phase difference across the junction, I_b is the bias current, C_J is the junction capacitance and I_0 is the critical current of the junction.

group switched to dc SQUID phase qubits several years later and this is the type of phase qubit I worked on.

The dc SQUID phase qubit consists of two junctions in a loop [33-35]. After Martinis moved to UCSB, his group continued working on phase qubits and they soon developed a new scheme using an rf-SQUID as a qubit combined with a dc SQUID which they used to read out the state [36, 37]. The UCSB group achieved notable success, including demonstration of a Bell's inequality experiment [38].

Prior to my work, the group at Maryland used the dc SQUID phase qubit scheme (LJ isolation) to reduce current noise from the bias lines and inductor-capacitor (LC) isolation to reduce high frequency noise from the leads. Both isolation techniques were intended to improve the relaxation time T_1 [33, 35, 39-41]. Rabi oscillations were observed, but the coherence times T_2 were a few tens of ns. T. A. Palomaki found that by reducing the size of the qubit junction, the coherence times became somewhat longer [42]. My work involved making yet smaller junctions [~$(\mu m)^2$] and attaching a shunting capacitor made with low-loss SiN_x [43] to reduce dielectric loss and two-level systems (TLS). As I discuss in this thesis, this led to marked improvements in the relaxation time T_1 and the coherence time T_2.

1.3 Overview of the Thesis

In this thesis, I discuss the design and fabrication of dc SQUID phase qubits and then discuss my measurements on devices. My goal was to improve the coherence time of the dc SQUID phase qubit and in fact, my devices achieved much longer times than previous devices built in our group. I also observed a remarkable, puzzling and unexpected phenomenon which we called “anomalous s-curves.”

In Chapter 2, I review the basic theory of Josephson junctions and phase qubits. In Chapter 3, I give a brief explanation of the dynamics of two level systems and decoherence and I discuss how the dc SQUID phase qubit is designed to reduce decoherence. In Chapters 4 and 5, I describe how I made and measured devices. In Chapter 6, I show my experimental results on a dc SQUID phase qubit. In Chapter 7, I discuss my observation of anomalous switching curves in a dc SQUID phase qubit. I also discuss possible causes of the anomalous behavior and the implications the behavior has for interpreting measurements on these devices. Finally, I conclude with a summary of my key results in Chapter 8.

Chapter 2

The dc SQUID Phase Qubit

In this chapter, I discuss some of the main theoretical aspects of the dc SQUID phase qubit. I first present the RCSJ (resistively and capacitively shunted junction) model and use it to explain how junctions behave classically. I then apply the model to an asymmetric dc SQUID and find the SQUID Hamiltonian. Finally, I discuss the quantum behavior of the dc SQUID phase qubit, including tunneling, decoherence, and how the transition frequency depends on current and flux.

2.1 Josephson Junctions

While still a graduate student, Brian Josephson predicted theoretically that current could flow from a superconducting electrode, through a thin insulating layer, and into a second superconducting electrode without any voltage drop. This lossless flow of current is now called the dc Josephson effect [44] and the superconducting-insulator-superconductor structure is called an SIS Josephson junction. This and other remarkable predictions of Josephson were soon verified experimentally and eventually became the basis for many superconducting devices, including all superconducting qubits.

The equation governing the dc Josephson effect can be written as

$$I_J = I_0 \sin \gamma \tag{2.1}$$

where I_J is the supercurrent (lossless) through the junction, I_0 is the critical current of the junction, and γ is the difference in the phase of the order parameter between the two superconducting electrodes [45]. Josephson also showed that the time derivative of the phase difference γ is related to the voltage across the junction by

$$V_J = \frac{\Phi_0}{2\pi} \frac{d\gamma}{dt} \tag{2.2}$$

where $\Phi_0 = h/2e = 2.07 \times 10^{-15}$ T·m^2 is the flux quantum. By taking a time derivative of Eq. 2.1, solving for $d\gamma/dt$ and substituting this into Eq. 2.2, one can show that the voltage across the junction can also be written as

$$V_J = L_J \frac{dI_J}{dt} \tag{2.3}$$

where we have defined the Josephson inductance by

$$L_J = \frac{\Phi_0}{2\pi} \frac{1}{\sqrt{I_0^{\,2} - I_J^{\,2}}} \tag{2.4}$$

and $\sqrt{I_0^{\,2} - I_J^{\,2}} = I_0 \cos \gamma$. If L_J is constant, then Eq. 2.3 would be just what one would expect for the voltage across an inductor. Since L_J depends on the current, we see that Eq. 2.3 implies that a Josephson junction acts as a non-linear inductor. L_J is known as the Josephson inductance. The nonlinearity of the inductance of the junction is the key property of the junction that allows it to work as a phase qubit.

Figure 2.1(a) shows a current vs. voltage (I-V) characteristics measured for device DS8. This device is actually a dc SQUID phase qubit, which has two junctions in parallel, rather than one junction. Nevertheless, the I-V characteristics are very similar to what one would measure with a single junction, with the difference being visible only if a magnetic flux is applied to the device. The plot shows that current can flow with no voltage drop (this is the supercurrent) provided that the current does not exceed about 1 μA. Current can flow above this level, but it produces a voltage across the junction. For a junction, the maximum value of the supercurrent is just the critical current I_0.

As Fig. 2.1(a) shows that if a current greater than the critical current is applied a voltage develops across the junction. In section 2.2, I discuss why this happens. For now, we can see that according to Eq. 2.2 a dc voltage V_J will appear across the junction when the phase advances steadily with time, and thus the phase is constant only at points on the (zero-voltage) supercurrent branch while it advances steadily at other points (non zer-voltage) on the I-V characteristic. Notice also in Fig 2.1(a) that a sudden increase in the current through the junction occurs at around 360 μV. This rapid rise in the current happens when there is enough energy available to break a Cooper pair and produce two quasiparticles. It takes energy 2Δ to break a Cooper pair, and energy eV is available via tunneling, so the rise in current happens when $eV_J = 2\Delta$, where $\Delta \approx 180$ μeV is the superconducting energy gap in aluminum.

Due to the Josephson inductance, a junction can store an effective inductive energy and this will depend on the current flowing through it. The overall scale for this inductive energy is set by the Josephson energy [45], which is defined as

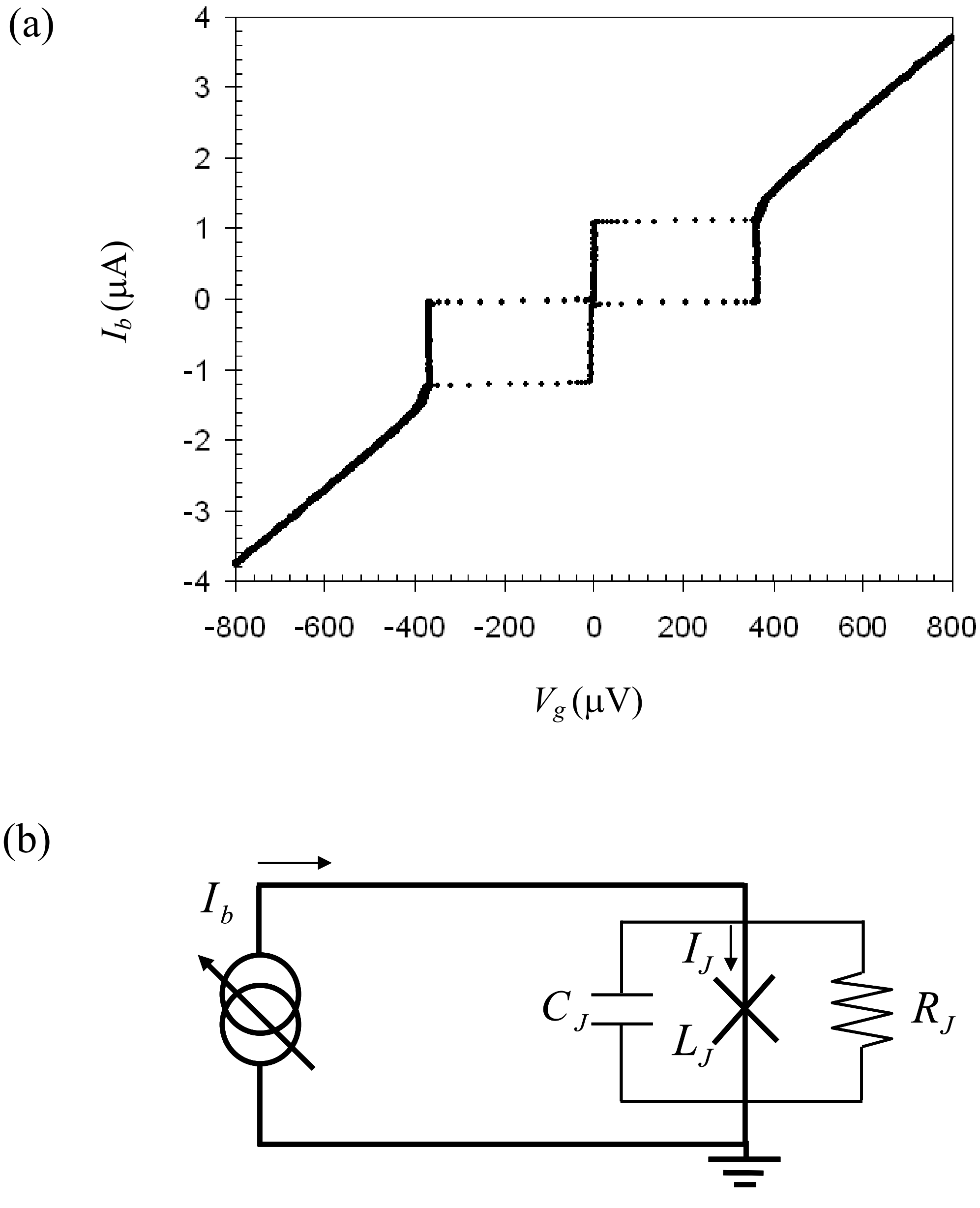

Figure 2.1 (a) Current-voltage characteristic curve (I-V) for Al/AlO$_x$/Al dc SQUID phase qubit DS8. The critical current of the device is a bit larger than 1 μA. (b) RCSJ model of a current biased Josephson junction.

$$E_J = \frac{\Phi_0}{2\pi} I_0 . \tag{2.5}$$

To see that this is the correct energy scale, notice that if a current I_0 flows through a fixed Josephson inductance $L_J = \Phi_0/2\pi I_0$, then the energy stored in the inductor would be just

$$\frac{1}{2} L I^2 = \frac{1}{2} \frac{\Phi_0}{2\pi I_0} (I_0)^2 = E_J / 2 \tag{2.6}$$

Of course in a Josephson junction, the Josephson inductance depends on the current, so Eq. 2.6 is not correct except in an overall scale. The full current-dependent expression defines the potential energy U of the junction and I discuss this in the following section. A junction can also store electrostatic energy since two superconducting electrodes and a thin insulating layer form a capacitor. The overall energy scale for the electrostatic energy is set by a single electron charging energy [45]

$$E_C = \frac{e^2}{2} \frac{1}{C_J} \quad . \tag{2.7}$$

This is just the electrostatic energy due to one electron on a capacitor C_J.

In superconducting qubits, the ratio E_J/E_C determines which quantum variable is relatively well-defined or sharp [45]. For E_J/E_C much less than 1, the flow of current is small, charging effects such as the Coulomb blockade are dominant and the number of pairs N typically becomes a sharply-defined quantum variable. If $E_J/E_C >> 1$, then Coulomb blockade effects are negligible and the current flowing through the junction becomes important [45]. In this regime, γ is a relatively sharply defined quantum variable. This is the limit that phase qubits operate in, including the dc SQUID phase qubit.

2.2 RCSJ Model of a Josephson Junction

A real Josephson junction will generally have some loss (a parallel resistive path across the junction) and some shunting capacitance and it can be modeled as a simple circuit consisting of three parallel elements: a resistor R_J, a capacitor C_J and an ideal tunnel junction (*i.e.* no capacitance and no dissipation). This defines the resistively and capacitively shunted junction (RCSJ) model [see Fig 2.1 (b)]. This simple circuit model is very useful for understanding the dynamics of circuits that include Josephson junctions.

Examining Fig. 2.1 (b) and using conservation of current, the total current I_b through the three parts of a junction in the RCSJ model can be written as

$$I_b = C_J \frac{dV_J}{dt} + \frac{V_J}{R_J} + I_0 \sin\gamma \,. \tag{2.8}$$

The first term is the displacement current through the shunting capacitor, the second term is the current through the shunting resistance, and the last term is the current though the ideal junction. Using Eq. 2.2, the ac Josephson effect, Eq. 2.8 can be written in the form

$$m_J \frac{d^2\gamma}{dt^2} = -\frac{dU(\gamma)}{d\gamma} - \eta \frac{d\gamma}{dt} \tag{2.9}$$

where $m_J = C_J\left(\Phi_0/2\pi\right)^2$, $\eta = \Phi_0{}^2/4\pi^2 R_J$ and

$$U(\gamma) = -\frac{\Phi_0}{2\pi} I_0 \cos\gamma - \frac{\Phi_0}{2\pi} I_b\gamma = -E_j \cos\gamma - \frac{\Phi_0}{2\pi} I_b\gamma \,. \tag{2.10}$$

The potential $U(\gamma)$ defined by Eq. 2.10 is called the tilted washboard potential (See Fig. 2.2). The tilt of the potential is set by the bias current I_b through the term $-\left(\Phi_0 I_b/2\pi\right)\gamma$.

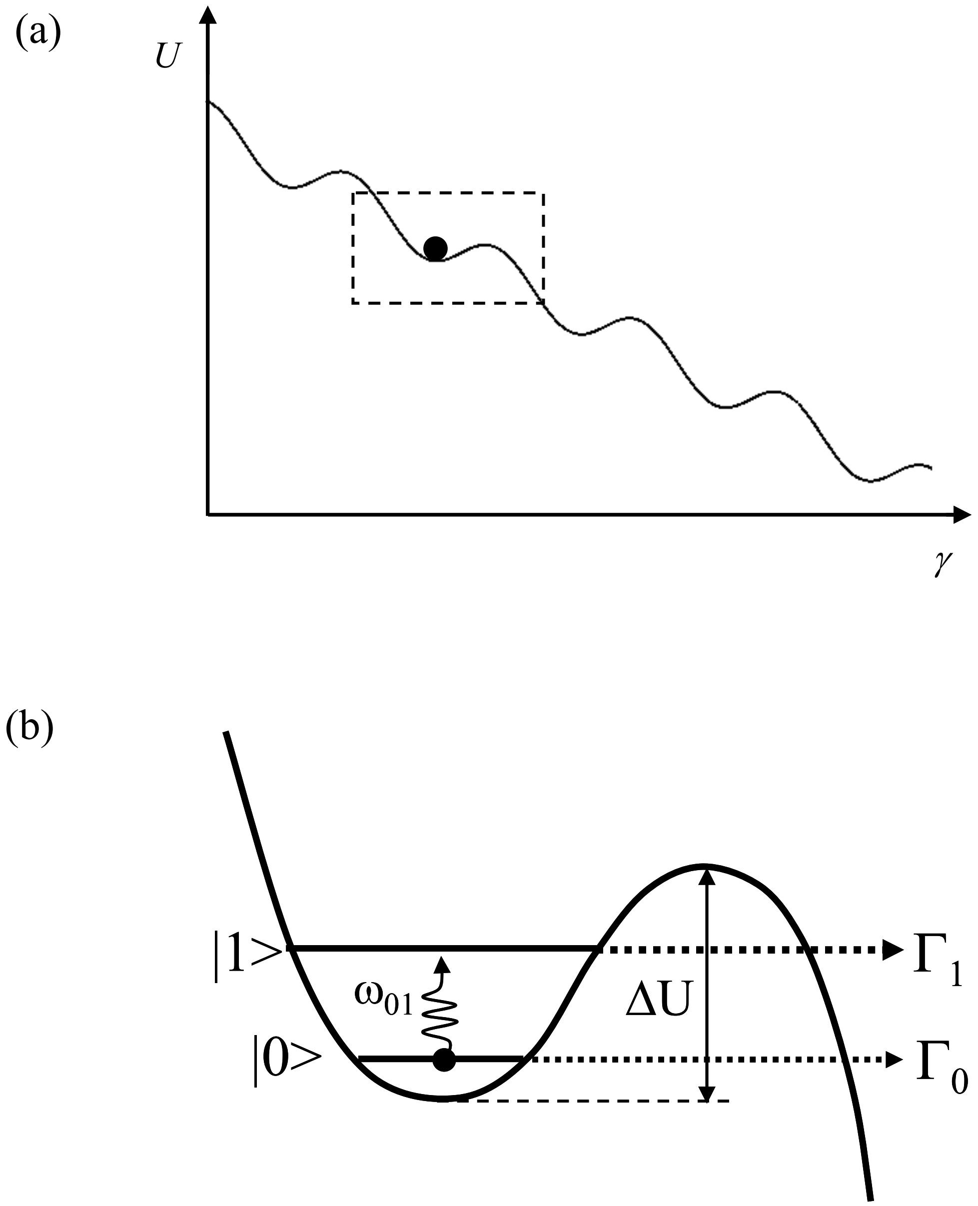

Figure 2.2 (a) Tilted washboard potential for a junction biased with $I_b = 0.5\ I_0$. The phase particle is trapped inside one of the potential wells so $d\gamma/dt$ is zero and the voltage across the junction is zero. (b) Detailed view of a dotted region in (a). If the phase particle is in a higher energy level $\left|1\right\rangle$, it can tunnel out from the well more rapidly than in a lower level $\left|0\right\rangle$ because the effective barrier is smaller.

The size of the ripples in the washboard is set by E_J.

We can think of γ as being analogous to a spatial coordinate x. Note that Eq. 2.9 is then just the classical equation of motion for a particle of mass m_J moving on a tilted washboard potential while also experiencing a damping force $-\eta v$, where $v = d\gamma/dt$ is the velocity of the particle.

2.3 The Junction Hamiltonian

From the classical equation of motion (Eq. 2.9), one can find the Hamiltonian of the phase particle [46]

$$H = T + U = \frac{p_\gamma^{\;2}}{2m_J} - \frac{\Phi_0}{2\pi}(I_0 \cos\gamma + I_b \gamma) \tag{2.11a}$$

where

$$p_\gamma = m_J \frac{d\gamma}{dt} = \frac{\hbar}{2e} C_J V_J \tag{2.11b}$$

is the canonical momentum of the phase particle. We can also write the Hamiltonian as

$$H = \frac{1}{2}\left[\frac{1}{C_J}\left(\frac{2\pi}{\Phi_0}\right)^2\right](\hbar N)^2 - \frac{\Phi_0 I_0}{2\pi}(\cos\gamma + \frac{I_b}{I_0}\gamma) \tag{2.12a}$$

or

$$H = 4E_C N^2 - E_J(\cos\gamma + I_b\gamma/I_0)\,. \tag{2.12b}$$

Here I have introduced $N = Q/2e = C_J V_J/2e$ as the excess number of pairs on the positive plate of the junction capacitor and thus $p_\gamma = m_J \frac{d\gamma}{dt} = \frac{\hbar}{2e} C_J V_J = \hbar N$. From these last two forms of H, we see that the kinetic energy term ($p_\gamma^2/2m$) is just the familiar electrostatic potential energy stored in the junction capacitance. The next term is just the Josephson energy, and the last term can be thought of as minus the work done by the source that supplies the bias current.

In quantum mechanics, the phase difference γ and the number of Cooper pairs N are complementary operators. That is, they obey the commutation relation $[N, \gamma] = I$ [45]. This relation also means that N and γ satisfy an uncertainty relation

$$\left\langle (\Delta N)^2 \right\rangle \left\langle (\Delta \gamma)^2 \right\rangle \geq \frac{1}{4}. \tag{2.13}$$

where ΔN is the uncertainty in the number of excess pairs on the junction capacitor and $\Delta\gamma$ is the uncertainty in the phase difference across the junction. For phase qubits, $E_J/E_C >> 1$. It can be shown that in this limit the ground state has $\left\langle (\Delta \gamma)^2 \right\rangle << 1$, and thus the number of pairs is not well defined in a phase qubit. Thus, the Josephson junction of the phase qubit has a small dispersion in the phase difference but the number of Cooper pairs cannot be precisely defined.

In order to understand the quantum mechanics of the current-biased Josephson junction, the Hamiltonian of the junction needs to be examined in some detail. It turns out that it is difficult to solve Schrödinger's equation with the full cosine term and tilt term in the potential $U(\gamma)$ [46]. Instead, one can expand $U(\gamma)$ near the potential minimum $\gamma_{\min} = \arcsin(I_b / I_0)$. Since γ is relatively well-defined for a phase qubit, this should be reasonable approximation. One finds

$$U(\gamma') \approx \frac{\Phi_0}{2\pi} \left\{ \frac{1}{2} \sqrt{I_0^{\;2} - I_b^{\;2}}\, \gamma'^2 - \frac{1}{6} I_b \gamma'^3 \right\} + U_0 \tag{2.14}$$

where $\gamma' = \gamma - \gamma_{\min}$ and U_0 is constant [47].

If I keep only the square term in the approximate potential $U(\gamma')$ (see Eq. 2.14), then the Hamiltonian of the junction becomes

$$H(\gamma') \approx \frac{p_{\gamma'}{}^2}{2m_J} + \frac{\Phi_0}{2\pi}\frac{1}{2}\sqrt{I_0{}^2 - I_b{}^2}\,\gamma'^2 \quad . \tag{2.15}$$

where $p_{\gamma'} = p_\gamma$. This is of the form $H(x) = \frac{p(x)^2}{2m} + \frac{1}{2}m\omega_p{}^2 x^2$ where ω_p is the plasma frequency of the junction, or resonance frequency of the harmonic oscillator. Thus a junction acts like a simple harmonic oscillator to this level of approximation and many properties of the junction can be understood on this basis.

If the phase particle is trapped in a potential well, Eq. 2.12 should be a good approximation, and there will be sharply defined energy levels [see Fig. 2.2(b)]. The number of energy levels in the well is approximately

$$N_{level} = \frac{\Delta U}{\hbar\omega_p} \tag{2.16}$$

where ΔU is the barrier height and it depends on the bias current I_b (see Eq. 2.18).

Using the simple harmonic oscillator approximation, one can obtain some important quantum properties of the junction. From Eq. 2.15 we can identify an effective spring constant $k_J = E_J\sqrt{1-\left(I_b/I_0\right)^2}$. Formally, this can be obtained by taking the second derivative of potential U with respect to γ at the potential minimum. The plasma frequency can then be written as

$$\omega_P = \sqrt{\frac{k_J}{m_J}} = \sqrt{\frac{2\pi I_0}{\Phi_0 C_J}}\left(1-\left(\frac{I_b}{I_0}\right)^2\right)^{1/4} = \frac{\sqrt{8E_C E_J}}{\hbar}\left(1-\left(\frac{I_b}{I_0}\right)^2\right)^{1/4} = \frac{1}{\sqrt{L_J C_J}} \tag{2.17}$$

Note that the junction area is a common factor in I_0 and C_J. Since L_J is proportional to $1/I_0$, this means that $\omega_P = 1/\sqrt{L_J C_J}$ is independent of the junction area but proportional to the critical current density. This assumes C_J is due to just the junction tunnel barrier (there is no added capacitor across the junction) and that the critical density is independent of area.

The barrier height ΔU is just the difference in the potential from the local minimum to the local maximum. One can show that [48]

$$\Delta U \approx \frac{4\sqrt{2}}{3} E_J \left(1 - \frac{I_b}{I_0}\right)^{\frac{3}{2}}. \tag{2.18}$$

If the phase particle is undergoing driven oscillations in a potential well, it can escape from the well if the energy of the particle becomes larger than the barrier ΔU [49].

If the potential U is written as a Taylor series expansion and terms kept up to γ'^3, the potential can be written as [31]

$$U \approx \frac{27}{4} \Delta U \left(\frac{\gamma'}{\gamma_0}\right)^2 \left(1 - \frac{\gamma'}{\gamma_0}\right) + U_0. \tag{2.19}$$

where $\gamma' \equiv \gamma - \gamma_0$ and $\gamma_0 = \frac{1}{2\omega_p}\sqrt{\frac{54\Delta U}{m}}$. Unlike the simple harmonic oscillator, this cubic potential yields energy levels with unequal spacings. This means that transitions can be driven selectively between specific levels by a proper choice of the driving frequency. For this potential, the transition frequency ω_{01} between the ground state and the first excited state is given by [46]

$$\omega_{01} \approx \omega_p \left(1 - \frac{5}{36}\alpha\right) \tag{2.20}$$

and the transition frequency between the first excited state and the second excited state is given by

$$\omega_{12} \approx \omega_p \left(1 - \frac{5}{18}\alpha\right) \tag{2.21}$$

where $\alpha = 1/N_{level} = \hbar\omega_p/\Delta U$ is approximately the number of levels in the potential well.

Examination of Eqs. 2.20 and 2.21 reveals that ω_{01} is larger than ω_{12} because the second term in Eq. 2.20 is larger than the second term in Eq. 2.18. From Eqs. 2.20 and 2.21, we see that the difference between ω_{01} and ω_{12} depends on the potential barrier height, which is also dependent on the bias current. The difference ω_{01} - ω_{12} is important because it is a measure of the anharmonicity of the system; the anharmonicity should not be too small, or it will be difficult to selectively manipulate the quantum state of the qubit.

Another important quantity is the rate at which the system can tunnel from a given energy level into the non-zero voltage state or "running state". This can be calculated using the WKB approximation. For the two lowest energy levels E_0 and E_1, one finds [46]

$$\Gamma_0 \approx 12.7\left(\frac{7.2\,\Delta U}{\hbar\omega_p}\right)^{\frac{1}{2}} \frac{\omega_p}{2\pi} \exp\left(-\frac{7.2\,\Delta U}{\hbar\omega_p}\right) \tag{2.22}$$

$$\Gamma_1 \approx 393.2\left(\frac{7.2\,\Delta U}{\hbar\omega_p}\right)^{\frac{3}{2}} \frac{\omega_p}{2\pi} \exp\left(-\frac{7.2\,\Delta U}{\hbar\omega_p}\right) \tag{2.23}$$

Note that for typical bias conditions $\alpha = \hbar\omega_p/\Delta U \approx$ 1/4. From these expressions, we can then see that the escape rate for the first excited state is about a factor of 500 higher than the ground state. Experimentally, this means the state of the qubit can be distinguished by monitoring the escape rate: If the junction is in the excited state, its escape rate will be much larger than if the junction is in the ground state.

2.4 The dc SQUID Phase Qubit

A single Josephson junction has no protection from current noise or dissipation from the bias leads because the junction is directly connected to the leads. In some of the group's first phase qubits [39], an LC filter was connected across the output of the junction to prevent low frequency noise from reaching the device. Such a filter can be effective at high frequencies (above the LC resonance frequency of the filter) but it has no effect at low frequencies, *i.e*. it is a low-pass filter.

To provide broad-band isolation (from dc to above the transition frequency of the qubit) Martinis *et. al.* first proposed adding an inductance and a second junction across the qubit junction [29] (see Fig. 2.3). The current bias leads are then connected across the resulting loop. This structure is just the familiar dc SQUID in which the added "isolation junction" and loop inductance act as an inductive network to block noise from reaching the qubit junction. The noise filtering is particularly effective if the isolation junction has a relatively large critical current, producing a Josephson inductance that is small compared to the loop inductance. With this design, Martinis *et. al.* were able to demonstrate the first Rabi oscillations in a phase qubit, and our group later adopted this design and began making modifications to try to improve the coherence times [42, 50-52].

2.4.1 SQUID Hamiltonian

Figure 2.3 shows a schematic diagram of a dc SQUID phase qubit. For a dc SQUID phase qubit, the two junctions typically have different critical currents ($I_{01} \neq I_{02}$), the two arms of the SQUID loop have different inductances ($L_1 >> L_2$) and the junction capacitance C_1 and C_2 will also be different. The current bias line is connected to the isolation junction *J2* in series with a small inductance L_2. The qubit junction *J1* is in series with L_1. The bias current I_b splits between two arms of the SQUID loop and one can write

$$I_b = I_1 + I_2 \tag{2.24a}$$

where

$$I_1 = C_{J1} \frac{d}{dt}\left(\frac{\Phi_0}{2\pi}\frac{d\gamma_1}{dt}\right) + I_{01}\sin\gamma_1 + \frac{V_{J1}}{R_{J1}} \tag{2.24b}$$

and

$$I_2 = C_{J2} \frac{d}{dt}\left(\frac{\Phi_0}{2\pi}\frac{d\gamma_2}{dt}\right) + I_{02}\sin\gamma_2 + \frac{V_{J2}}{R_{J2}}. \tag{2.24c}$$

Here I_{01} and I_{02} are the critical currents of the junctions *J1* and *J2*, respectively, γ_1 and γ_2 are the phase differences across *J1* and *J2* respectively and I_1 and I_2 are the current, in the qubit arm and isolation arm of the SQUID, respectively. I will now drop the V_{J1}/R_{J1} and V_{J2}/R_{J2} terms because the dissipative terms cannot be incorporated into a simple Hamiltonian.

Another constraint is the flux-phase relationship around the SQUID loop. Considering the phase differences across the junctions *J1* and *J2* and neglecting any flux from the current bias line, the one can write [45, 53]

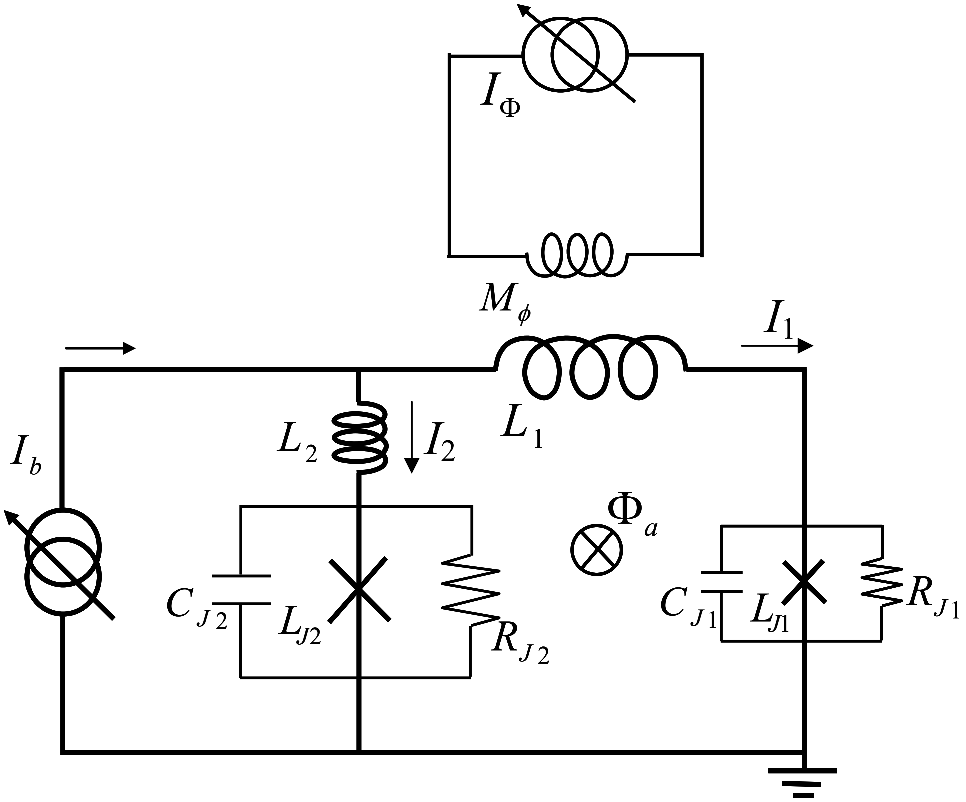

Figure 2.3: Schematic for a dc SQUID phase qubit. Junction 1 (J1) is the qubit junction and junction 2 (J2) is the isolation junction (also called the detection junction). Bias current I_b is applied to the SQUID and divides between the two arms of the SQUID loop depending on L_{J1}, L_{J2}, L_1 and L_2. External flux Φ_a is applied to the loop through mutual inductance M_ϕ.

$$\gamma_1 - \gamma_2 = 2\pi\left(n + \frac{\Phi_t}{\Phi_0}\right) = 2\pi n + 2\pi\frac{\Phi_a - L_1 I_1 + L_2 I_2}{\Phi_0} \tag{2.25}$$

where Φ_t is the total flux inside the SQUID loop and Φ_a is the applied flux. The constant integer n can be ignored. From Eq. 2.24 and Eq. 2.25 and the ac Josephson relation, one can find the effective potential U for the SQUID [53],

$$\begin{aligned} U(\gamma_1, \gamma_2, I_b, \Phi_a) = &-\frac{\Phi_0}{2\pi}\left(I_{01}\cos\gamma_1 + I_{02}\cos\gamma_2\right) - \frac{\Phi_0}{2\pi} I_b\left(\frac{L_1}{L}\gamma_1 + \frac{L_1}{L}\gamma_2\right) \\ &+\left(\frac{\Phi_0}{2\pi}\right)^2 \frac{1}{2L}\left(\gamma_1 - \gamma_2 - 2\pi\frac{\Phi_a}{\Phi_0}\right)^2 \end{aligned} \tag{2.26}$$

where $L = L_1 + L_2$ is the total inductance of the loop. The dc SQUID phase qubit equations are that of a particle moving in a 2-D tilted washboard potential [53]. Using Eq. 2.26, the SQUID Hamiltonian can be written as

$$\begin{aligned} H = T + U = &\frac{p_{\gamma_1}^{\;2}}{2m_{J1}} + \frac{p_{\gamma_2}^{\;2}}{2m_{J2}} - \frac{\Phi_0}{2\pi}\left(I_{01}\cos\gamma_1 + I_{02}\cos\gamma_2\right) \\ &-\frac{\Phi_0}{2\pi} I_b\left(\frac{L_1}{L}\gamma_1 + \frac{L_1}{L}\gamma_2\right) + \left(\frac{\Phi_0}{2\pi}\right)^2 \frac{1}{2L}\left(\gamma_1 - \gamma_2 - 2\pi\frac{\Phi_a}{\Phi_0}\right)^2 \end{aligned} \tag{2.27}$$

where $m_{J1}=(\Phi_o/2\pi)^2 C_{J1}$ and $m_{J2}=(\Phi_o/2\pi)^2 C_{J2}$. Figures 2.4 and 2.5 show plots of the dc SQUID potential for device DS8 which has $I_{01} << I_{02}$ and $L_1 << L_2$. Figure 2.4 shows the potential with $I_b = 0$ and $\Phi_a = 0.37\Phi_o$, while Fig. 2.5 shows $I_b = 0.7$ μA and $\Phi_a = 0.37\Phi_o$. Notice that along the γ_1 direction (the phase difference across the qubit), the potential curves upward steadily from the minimum [see Figs. 2.4(c) and 2.5(c)]. Thus the device cannot escape by tunneling in the γ_1 direction. On the other hand, there is a finite potential barrier in the $+\gamma_2$ direction [see Figs 2.4(b) and 2.5(b)], so the device can tunnel to the running state in this direction. Thus with this choice of parameters, the device can only switch to the voltage state if the isolation junction switches.

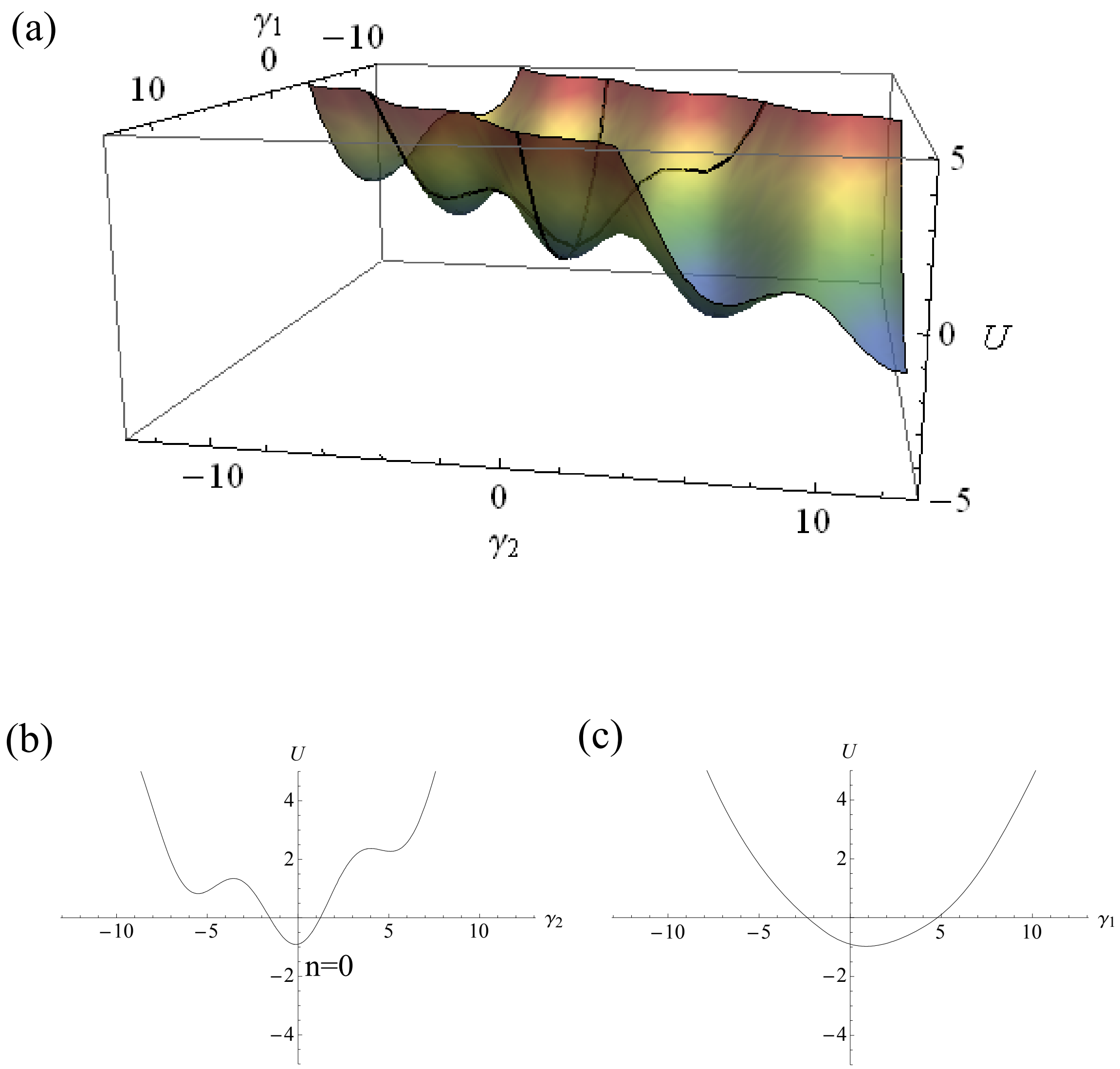

Figure 2.4: (a) Potential surface $U(\gamma_1, \gamma_2)$ for a dc SQUID phase qubit with $I_b = 0$, $\Phi_a = 0.37\ \Phi_o$, $I_{01} = 0.08\ \mu\text{A}$ and $I_{02} = 1.37\ \mu\text{A}$. The black curves are cross sections through the 3-D potential at $\gamma_1 = 0$ and $\gamma_2 = 0$. Tunneling only happens along the $+\gamma_2$ direction since the potential continues to curve upward in the $-\gamma_2$ direction and along the +/- γ_1 direction. (b) Plots of the potential along the cross sections at $\gamma_1 = 0$ and (c) at $\gamma_2 = 0$.

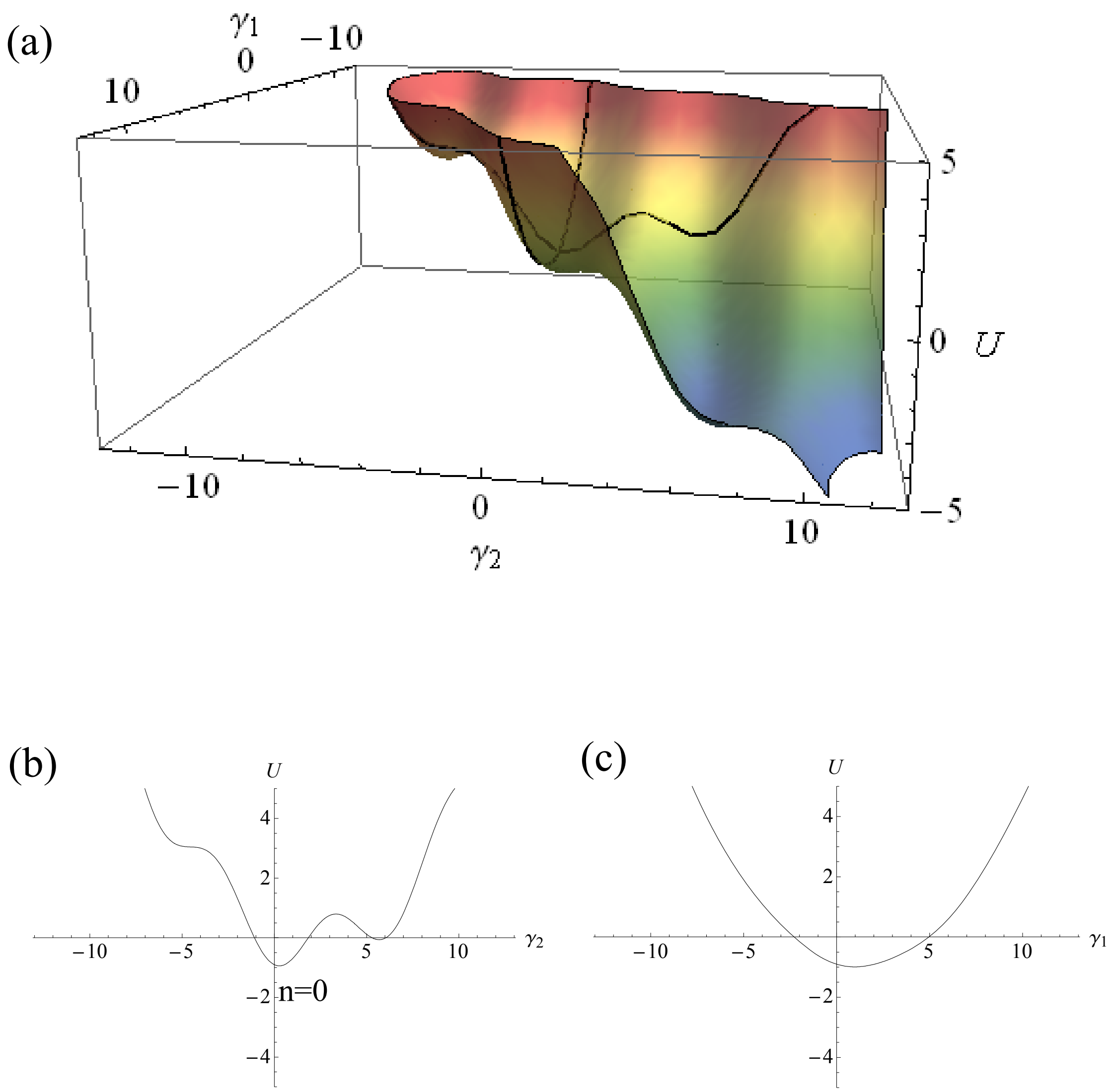

Figure 2.5: (a) Potential surface $U(\gamma_1, \gamma_2)$ for a dc SQUID phase qubit with $I_b = 0.7$ μA, $\Phi_a = 0.37\ \Phi_o$, $I_{01} = 0.08$ μA and $I_{02} = 1.37$ μA. The black curves are cross sections through the 3-D potential at $\gamma_1 = 0$ and $\gamma_2 = 0$. Tunneling only happens along the $+\gamma_2$ direction since the potential continues to curve upward in the $-\gamma_2$ direction and along the +/- γ_1 direction. (b) Plots of the potential along the cross sections at $\gamma_1 = 0$ and (c) at $\gamma_2 = 0$.

I note that the parameters for my devices DS6 and DS8 were quite different from our previous group's SQUID phase qubits. In particular, the critical current of the qubit junction was much smaller than that of the isolation junction and much smaller than Φ_o/L. The behavior of DS6 and DS8 was affected by this choice, as will be discussed in detail in Chapters 6 and 7.

2.4.2 Current-Flux (I-Φ) Characteristics

The critical current of a SQUID is determined by the critical currents of the junctions and the flux applied to the SQUID loop. The applied flux is important because it produces circulating current in the loop. The total current through each junction will be the sum of the circulating current and the bias current. The resulting I-Φ characteristic can be found using Eq. 2.24 and Eq. 2.25 by finding the maximum values of I_b for which $d\gamma_1/dt = d\gamma_2/dt = 0$ is still a solution.

The critical current can be found using the method of Lagrange multipliers [54]. One can define

$$\begin{aligned} I' = {} & I_{01}\sin\gamma_1 + I_{02}\sin\gamma_2 \\ & + \lambda\left(\gamma_2 - \gamma_1 + 2\pi\frac{\Phi_a}{\Phi_0} + 2\pi\frac{L_2 I_{02}}{\Phi_0}\sin\gamma_2 - 2\pi\frac{L_1 I_{01}}{\Phi_0}\sin\gamma_1 - 2\pi n\right) \end{aligned} \tag{2.28}$$

where I' is a critical point of the current in the loop and λ is the Lagrange multiplier. Setting $\partial I'/\partial\lambda = 0$, $\partial I'/\partial\gamma_1 = 0$ and $\partial I'/\partial\gamma_2 = 0$ [54], the parameter λ can be eliminated. From the first and the second equations, one obtains

$$2\pi\frac{\Phi_a}{\Phi_0} = -\left(\gamma_2 - \gamma_1 + 2\pi\frac{L_2 I_{02}}{\Phi_0}\sin\gamma_2 - 2\pi\frac{L_1 I_{01}}{\Phi_0}\sin\gamma_1\right) \tag{2.29}$$

$$\cos\gamma_1 = -\left(\frac{I_1}{I_2\cos\gamma_2} + \frac{2\pi}{\Phi_0}(L_1+L_2)I_{01}\right)^{-1} . \tag{2.30}$$

Notice that for $\gamma_1 = \gamma_2 = \pm\pi/2$, Eq. 2.30 is well satisfied and one finds a maximum value of $I' = I_{01} + I_{02}$ and a minimum value of $\pm(I_{01} - I_{02})$. Finding other solutions requires numerical analysis.

Figure 2.6 shows a calculated I-Φ curve using the parameters of device DS8. The parameters were I_{01} = 0.077 μA, I_{02} = 1.365 μA, M_ϕ = 1.53 pH, L_1 = 1.5 nH and L_2 = 60 pH. The I-Φ curve matches the data (see Fig. 6.10).

Some general remarks can be made about the form of the SQUID Hamiltonian. The coupling strength between the two junctions is related inversely to $\beta = L(I_{01} + I_{02})/\Phi_0$ [55]. If $\beta \leq 1$, the two junctions are strongly coupled and the device can be treated as a single junction. For $\beta >> 1$, the two junctions are weakly coupled. In the weak coupling limit, the two junctions act independently and the critical current of the smaller junction will be the main factor in limiting the maximum possible circulating current in the loop. In the large β limit with $I_{01} << I_{02}$, the number of metastable flux states in the loop is approximately [56]

$$N_\Phi \approx 1 + \frac{2LI_{01}}{\Phi_0} . \tag{2.31}$$

For I_{01} = 0.1 μA, I_{02} = 1 μA and L = 1.5 nH, I obtain $\beta \approx 0.825$ and $N_\Phi \approx 1.15$ and thus the two junctions are strongly coupled and only one flux state will be present as expected given the small value of $I_{01}L$. Note that in Fig. 2.5, there are an infinite number of potential minima, but any two minima are equivalent if γ_1 and γ_2 differ by a multiple of 2π.

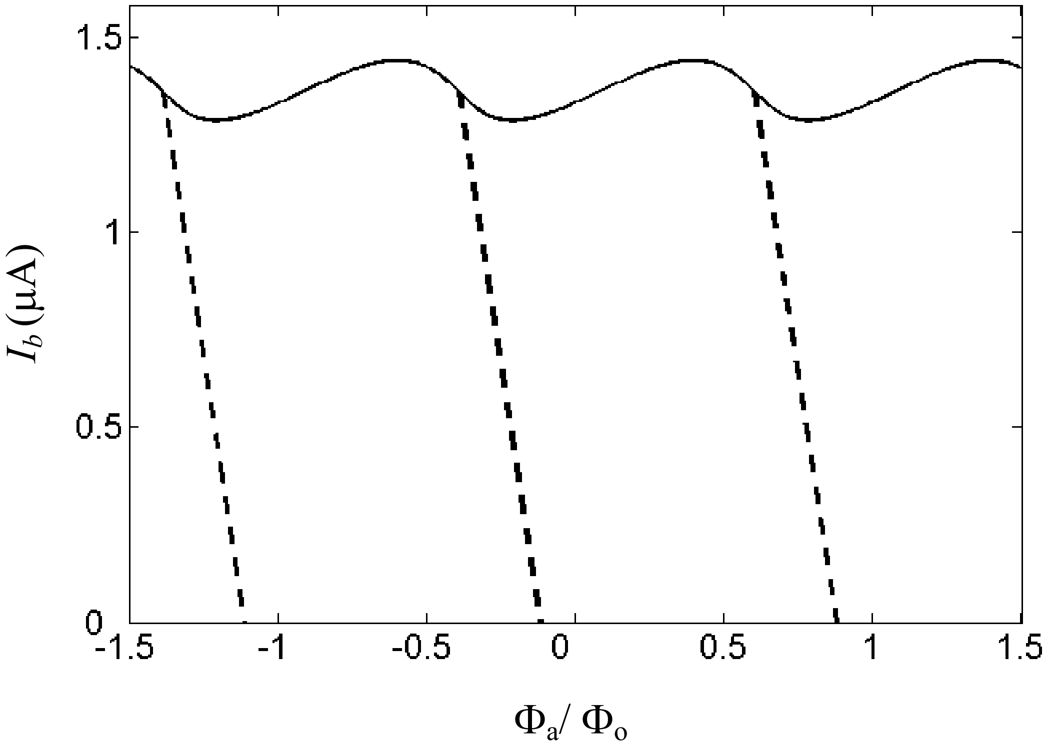

Figure 2.6: Simulation of I-Φ curve. The solid curves mean switching of the junctions. Parameters were those of device DS8, I_{01} = 0.077 μA, I_{02} = 1.365 μA, M_a = 1.53 pH, L_1 = 1.5 nH and L_2 = 60 pH. Dashed lines show separation between different flux states.

2.4.3 f_{01} vs. I_b

The 0-to-1 transition frequency of a single junction in the cubic approximation is given by Eq. 2.20. If the potential barrier height ΔU is written out explicitly, the 0-to-1 and 1-to-2 transition frequencies can be written as

$$\omega_{01} \approx \frac{\sqrt{8E_C E_J}}{\hbar}\left[1-\left(\frac{I_b}{I_0}\right)^2\right]^{\frac{1}{4}} - \frac{5}{6\sqrt{2}}\frac{E_C}{\hbar}\left(1+\frac{I_b}{I_0}\right)^{\frac{1}{2}}\left(1-\frac{I_b}{I_0}\right)^{-1} \tag{2.32}$$

$$\omega_{12} \approx \frac{\sqrt{8E_C E_J}}{\hbar}\left[1-\left(\frac{I_b}{I_0}\right)^2\right]^{\frac{1}{4}} - \frac{5}{3\sqrt{2}}\frac{E_C}{\hbar}\left(1+\frac{I_b}{I_0}\right)^{\frac{1}{2}}\left(1-\frac{I_b}{I_0}\right)^{-1}. \tag{2.33}$$

The first term in each equation is just ω_p and the second term comes from the cubic approximation of the potential $U(\gamma')$. Of course, these expressions are only valid for an isolated junction. In fact, they will be a poor approximation for my SQUIDs because the two junctions are strongly coupled.

Resonance frequency from normal modes in a dc SQUID

In my devices, the full Hamiltonian for the dc SQUID has to be considered, rather than the Hamiltonian of a single junction.

In order to get the approximate resonance frequencies of a dc SQUID, I treated the two junctions as LC resonators. When they coupled together by the loop inductance, they produce normal modes with two different frequencies. Using B. K. Cooper's calculation [57] of the normal modes, I obtain the transition frequencies $f_{01}(I_b)$ and $f_{02}(I_b)$ as a function of the bias current I_b and the flux. Using Eq. 2.27, the cubic expansion of the dc SQUID potential around the local minimum at (γ_{1m}, γ_{2m}) yields an approximate Hamiltonian [57]:

$$H = \frac{p_{\gamma_1}{}^2}{2m_{J1}} + \frac{p_{\gamma_2}{}^2}{2m_{J2}} - \left(\frac{\Phi_0}{2\pi}\right)^2 \left(\frac{1}{2L_{J1}} + \frac{1}{2L}\right)\phi_1{}^2 + \left(\frac{\Phi_0}{2\pi}\right)^2 \left(\frac{1}{2L_{J2}} + \frac{1}{2L}\right)\phi_2{}^2$$
$$- \left(\frac{\Phi_0}{2\pi}\right)^2 \frac{1}{L}\phi_1\phi_2 - \frac{1}{6}\frac{\Phi_0}{2\pi}\left(I_{01}(\sin\gamma_{1m})\phi_1{}^3 - I_{02}(\sin\gamma_{2m})\phi_2{}^3\right) \tag{2.34}$$

where $m_{J1} = C_{J1,}\, m_{J2} = C_{J2,}\ \gamma_i = \gamma_{im} + \phi_I$ (γ_{im} denotes the value at the local minimum of the potential) and $\cos\gamma_i = \cos\gamma_{im}\left(1 - \frac{\phi_i{}^2}{2}\right) - \sin\gamma_{im}\left(\phi_i - \frac{\phi_i{}^3}{6}\right)$. Ignoring cubic terms, the equations of motion are

$$-m_{J1}\phi_1'' = \frac{1}{L_1'}\phi_1 - \frac{1}{L}\phi_1 \tag{2.35}$$

$$-m_{J2}\phi_2'' = \frac{1}{L_2'}\phi_2 - \frac{1}{L}\phi_2 \tag{2.36}$$

where $\frac{1}{L_1'} = \frac{1}{L_1} + \frac{1}{L}$ and $\frac{1}{L_2'} = \frac{1}{L_2} + \frac{1}{L}$. By substituting the solutions $\phi_1 = \alpha_1 e^{i\omega t}$ and $\phi_2 = \alpha_2 e^{i\omega t}$ into Eqs. 2.35 and 2.36, I obtain [57]

$$\omega^4 - \left(\frac{1}{L_1'}\frac{1}{C_1} + \frac{1}{L_2'}\frac{1}{C_2}\right)\omega^2 + \frac{1}{L_1'}\frac{1}{C_1} \times \frac{1}{L_2'}\frac{1}{C_2} - \frac{1}{L}\frac{1}{C_1} \times \frac{1}{L}\frac{1}{C_2} = 0. \tag{2.37}$$

From Eq. 2.37, the two solutions are obtained as

$$\omega_+ = \sqrt{-\frac{1}{2}\left(\frac{1}{L_1'}\frac{1}{C_1} + \frac{1}{L_2'}\frac{1}{C_2}\right) + \frac{1}{2}\sqrt{\left(\frac{1}{L_1'}\frac{1}{C_1} + \frac{1}{L_2'}\frac{1}{C_2}\right)^2 - 4\frac{1}{L_1'L_2'C_1C_2} - \frac{1}{L^2C_1C_2}}} \tag{2.38}$$

$$\omega_- = \sqrt{-\frac{1}{2}\left(\frac{1}{L_1'}\frac{1}{C_1} + \frac{1}{L_2'}\frac{1}{C_2}\right) - \frac{1}{2}\sqrt{\left(\frac{1}{L_1'}\frac{1}{C_1} + \frac{1}{L_2'}\frac{1}{C_2}\right)^2 - 4\frac{1}{L_1'L_2'C_1C_2} - \frac{1}{L^2C_1C_2}}}\ . \tag{2.39}$$

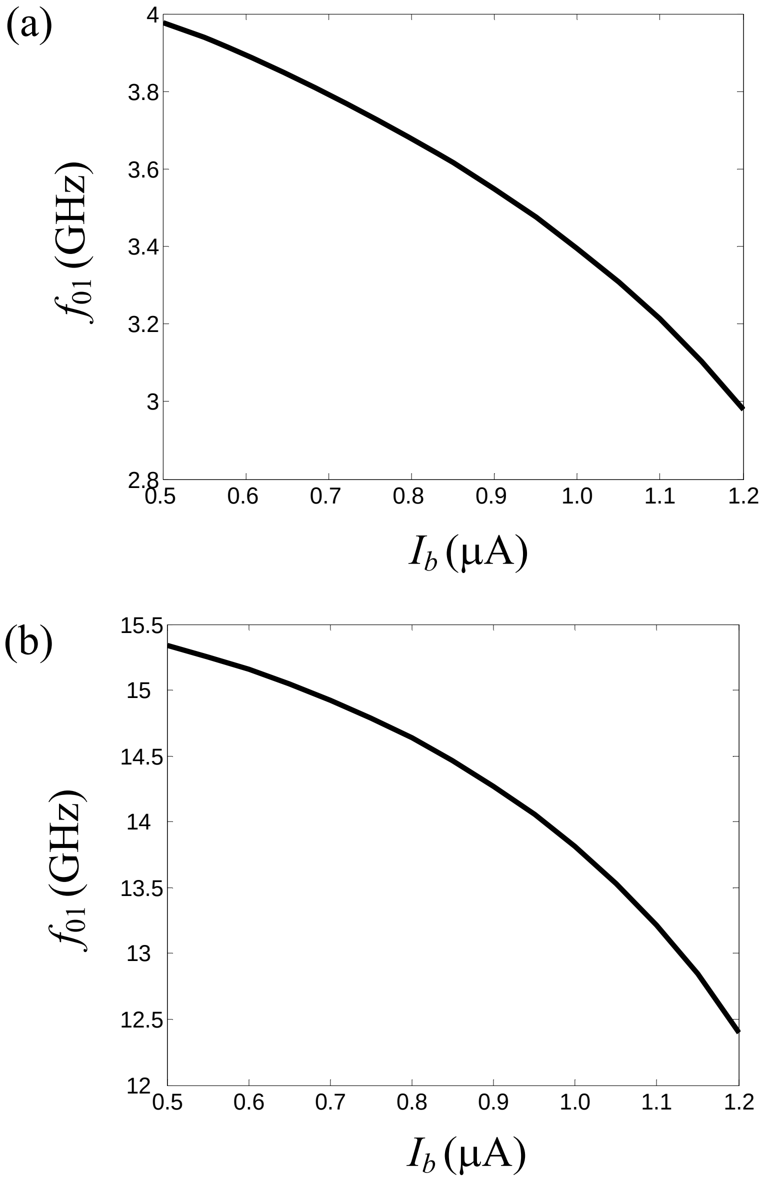

Figure 2.7: Simulation of transition frequencies for (a) the qubit junction (ω_- vs. I_b) and (b) the isolation junction (ω_+ vs. I_b) obtained from a harmonic approximation to the normal mode calculation. Parameters were those of device DS8, I_{01} = 0.077 μA, I_{02} = 1.365 μA, $\Phi_a = 0$, L_1 = 1.5 nH, L_2 = 60 pH, C_1 = 0.88 pF and C_2 = 0.5 pF.

ω_- can be considered as the resonance frequency for the qubit junction and ω_+ can be considered as the resonance frequency of the isolation junction. In Fig. 2.7(a), ω_- vs. I_b is plotted and in Fig. 2.7(b), ω_+ vs. I_b is plotted. As I will discuss in Chapter 6, Fig. 2.7(a) matches the energy spectrum data for device DS8 (see Fig. 6.12). Using parameters of $I_{01} = 0.077$ μA, $I_{02} = 1.365$ μA, $\Phi_a = 0$, $L_1 = 1.5$ nH, $L_2 = 60$ pH and $C_2 = 0.5$ pF, I was also able to extract $C_1 = 0.88$ pF by fitting.

2.4.4 Tunneling

As discussed above, the switching rate of a Josephson tunnel junction can be understood as quantum tunneling through a potential barrier ΔU. Using the WKB method, the tunneling rate from the *n-th* level is [46]

$$\Gamma_n \approx \frac{\sqrt{2\pi}}{n!}\left(\frac{432\,\Delta U}{\hbar\omega_p}\right)^{\frac{n+1}{2}}\frac{\omega_p}{2\pi}\exp\left(-\frac{7.2\,\Delta U}{\hbar\omega_p}\right). \tag{2.40}$$

where $\Delta U \approx 2\hbar E_J(1-I/I_0)^{3/2}$ and $\omega_p = \sqrt{2\pi I_0/\Phi_0 C}(1-(I/I_0)^2)^{1/4}$. This result is found by making the cubic approximation for an isolated junction [46]. In a single-junction circuit, the average tunneling rate $\langle\Gamma\rangle$ of the qubit junction is the combination of the tunneling rates at each energy level depending on the probability distribution of the qubit. The average tunneling rate is written as

$$\langle\Gamma\rangle = \sum_{n=0}^{N}\Gamma_n p_n \tag{2.41}$$

where p_n is the probability of the qubit being in the *n-th* energy level.

However, in devices DS6 and DS8, the escape rate of the device does not depend directly on the energy level of the qubit because as I noted above, only the isolation junction coordinate γ_2 can tunnel. In Chapter 7, I discuss how this leads to anomalous switching curves.

Chapter 3

Sources of Decoherence and Protection from Decoherence in the dc SQUID Phase Qubit

In this chapter, I discuss decoherence in the dc SQUID phase qubit. In order to understand the decoherence mechanisms, I adopt a simple two-level model for the qubit. Generally, noise coming from the environment can couple to the qubit and cause excitation, relaxation or dephasing. There are many possible sources of noise in superconducting qubits including current noise, critical current noise, charge noise and flux noise. In the following section, I briefly discuss the dynamics of the qubit. I then discuss the main noise sources that produce decoherence and what efforts I made to reduce decoherence in my devices. Finally, I discuss some additional decoherence sources, such as discrete two-level-systems in dielectrics.

3.1 Dynamics of a Two-Level System

Ideally, a qubit is a quantum system with just two eigenstates, *i.e.* a two-level system. I assume that the two eigenstates are the ground state $\left|0\right\rangle$ and the excited state

$|1\rangle$. Since the excited state $|1\rangle$ has a higher energy than $|0\rangle$, in order to raise the system from $|0\rangle$ to $|1\rangle$, energy needs to be supplied. In general, any pure state of the system can be written as

$$|\Psi\rangle = \alpha|0\rangle + \beta e^{i\phi}|1\rangle, \tag{3.1}$$

where α, β, and ϕ are real and α and β satisfy

$$\sqrt{|\alpha|^2 + |\beta|^2} = 1 \tag{3.2}$$

to preserve normalization of the wavefunction. The factor ϕ is the phase of the superposition state.

3.1.1 Bloch Sphere

A useful way to visualize a pure state of a two-level system is as a point on the Bloch sphere (see Fig. 3.1) [58]. The idea is that since α and β obey Eq. 3.2 and can be taken as real, then we can define an angle θ such that $\alpha = \cos(\theta/2)$ and $\beta = \sin(\theta/2)$. The state Ψ then becomes

$$|\Psi(\phi,\theta)\rangle = \cos\left(\frac{\theta}{2}\right)|0\rangle + e^{i\phi}\sin\left(\frac{\theta}{2}\right)|1\rangle \tag{3.3}$$

where $0 \le \theta \le \pi$ and $0 \le \phi \le 2\pi$. Given the angles θ and ϕ, the quantum state is completely determined.

If a projective measurement is performed for the qubit state, the probabilities $|\alpha|^2$ and $|\beta|^2$ are obtained from the projection of the qubit state to the ground state $|0\rangle$ or the

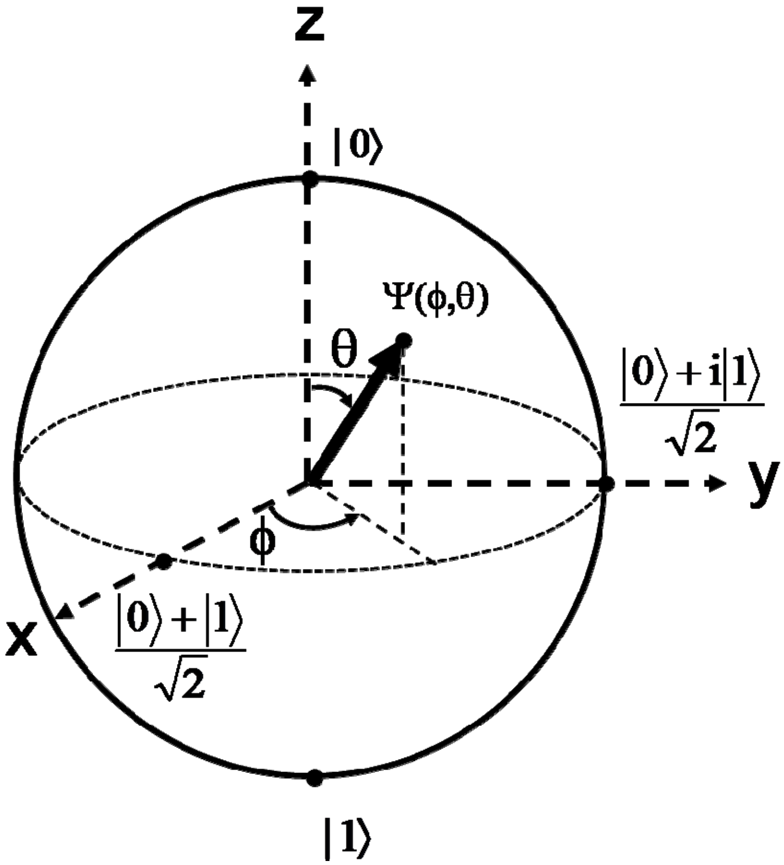

Figure 3.1: Representation of a qubit state as a point on the Bloch sphere. The vector corresponds to the quantum state $\Psi(\phi,\theta)$, having probabilities of $\alpha^2 = [\cos(\theta/2)]^2$ to be in the state $|0\rangle$ and $\beta^2 = [\sin(\theta/2)]^2$ to be in the state $|1\rangle$. For example, when the vector points along the x-axis, the state is $(|0> + |1>)/\sqrt{2}$.

excited state $\left|1\right\rangle$. For example, the point (1, 0, 0) on the Bloch sphere (*i.e.* on the x-axis) corresponds to θ = π/2 and ϕ = 0 and the quantum state $\left|\Psi\right\rangle = \cos(\pi/4)\left|0\right\rangle + \sin(\pi/4)\left|1\right\rangle = (\left|0\right\rangle + \left|1\right\rangle)/\sqrt{2}$. Similarly, the ground state $\left|0\right\rangle$ is on the +z-axis at (0, 0, 1) and $\left|1\right\rangle$ is on the –z-axis at (0, 0, -1).

To understand the dynamics of the phase qubit it is useful to reduce the system to an equivalent two-level system. I will assume that the bias current *I*(*t*) contains a dc current I_{dc}, as well as low frequency noise $I_{lf}(t)$ and microwave current $I_{\mu\omega}$,

$$\begin{aligned} I(t) &= I_{dc} + \Delta I(t) \\ &= I_{dc} + I_{lf}(t) + I_{\mu\omega x}(t)\cos(\omega t) + I_{\mu\omega y}(t)\sin(\omega t) \end{aligned} \tag{3.4}$$

Here I have written the microwave current as an in-phase part $I_{\mu\omega x}(t)\cos(\omega t)$ and an out-of-phase part $I_{\mu\omega y}(t)\sin(\omega t)$. In the Hamiltonian *H*, the time dependent terms can be treated as a perturbation, and the Hamiltonian becomes

$$H = \frac{p_\gamma^{\;2}}{2m_J} - \frac{\Phi_0}{2\pi}\left(I_0\cos\gamma + I_{dc}\gamma\right) + \frac{\Phi_0}{2\pi}\Delta I(t)\gamma = H_0 + H' \tag{3.5}$$

where $H_0 = \frac{p_\gamma^{\;2}}{2m_J} - \frac{\Phi_0}{2\pi}\left(I_0\cos\gamma + I_{dc}\gamma\right)$ is the unperturbed Hamiltonian of the junction and $H' = -\frac{\Phi_0}{2\pi}\Delta I(t)\gamma$ is the time-dependent perturbation.

To proceed, I now make a two-level approximation by reducing the Hilbert space to that spanned by the two lowest states in a well. The reduced Hamiltonian *H* can then be written as

$$H = \begin{pmatrix} E_0 & 0 \\ 0 & E_1 \end{pmatrix} - \frac{\Phi_0}{2\pi}\begin{pmatrix} \gamma_{00}\Delta I(t) & \gamma_{01}\Delta I(t) \\ \gamma_{10}\Delta I(t) & \gamma_{11}\Delta I(t) \end{pmatrix} \tag{3.6}$$

where the basis states of the unperturbed Hamiltonian H_0 are $|0\rangle$ and $|1\rangle$, the corresponding eigenenergies are E_0 and E_1, and the matrix elements γ_{ij} are defined by $\gamma_{ij} = < i \,|\, \gamma \,|\, j >$.

Given the Hamiltonian Eq. 3.4, I can write the time-dependent Schrödinger equation

$$i\hbar \frac{\partial \Psi}{\partial t} = H\Psi = H_0 \Psi + H' \Psi \; . \tag{3.7}$$

In general, we can always write

$$\Psi(t) = a(t)\, e^{-iE_0 t/\hbar} |0\rangle + b(t)\, e^{-iE_1 t/\hbar} |1\rangle \tag{3.8}$$

Then, the Schrödinger equation becomes

$$i\hbar \begin{pmatrix} \dfrac{\partial a}{\partial t} e^{-iE_0 t/\hbar} - a(t) \dfrac{iE_0}{\hbar} e^{-iE_0 t/\hbar} \\ \dfrac{\partial b}{\partial t} e^{-iE_1 t/\hbar} - b(t) \dfrac{iE_1}{\hbar} e^{-iE_1 t/\hbar} \end{pmatrix} = \begin{pmatrix} E_0 a(t) e^{-iE_0 t/\hbar} \\ E_1 b(t) e^{-iE_1 t/\hbar} \end{pmatrix} - \frac{\Phi_0}{2\pi} \begin{pmatrix} \gamma_{00} \Delta I(t) & \gamma_{01} \Delta I(t) \\ \gamma_{10} \Delta I(t) & \gamma_{11} \Delta I(t) \end{pmatrix} \begin{pmatrix} a(t) e^{-iE_0 t/\hbar} \\ b(t) e^{-iE_1 t/\hbar} \end{pmatrix}. \tag{3.9}$$

Rearranging and canceling common factors, one finds

$$i\hbar \begin{pmatrix} \dfrac{\partial a}{\partial t} \\ \dfrac{\partial b}{\partial t} \end{pmatrix} = -\frac{\Phi_0}{2\pi} \begin{pmatrix} \gamma_{00} \Delta I(t) & \gamma_{01} \Delta I(t) e^{i\omega_{01} t/\hbar} \\ \gamma_{10} \Delta I(t) e^{-i\omega_{01} t/\hbar} & \gamma_{11} \Delta I(t) \end{pmatrix} \begin{pmatrix} a(t) \\ b(t) \end{pmatrix}. \tag{3.10}$$

I now make the assumption that the microwave drive frequency ω is the same as the 0-to-1 transition frequency ω_{01}. I can then make the rotating wave approximation by assuming that only term with frequency near 0 or ω_{01} will contribute, while time-dependent terms such as $e^{\pm 2i\omega_{01} t/\hbar}$ can be neglected. Further analysis [59] shows that Eq. 3.10 reduces to

$$i\hbar \frac{\partial \Psi_{rot}}{\partial t} = H'_{rot}\, \Psi_{rot} \tag{3.11}$$

where $\Psi_{rot} = \begin{pmatrix} a(t) \\ b(t) \end{pmatrix}$ and

$$H'_{rot} = \frac{\Phi_0}{2\pi} I_{\mu\omega x}(t)\ \sigma_x + \frac{\Phi_0}{2\pi} I_{\mu\omega y}(t)\ \sigma_y + \frac{1}{2}\frac{\partial E_{10}}{\partial I_{dc}} \Delta I_{lf}(t)\sigma_z\,. \tag{3.12}$$

where σ_x, σ_y and σ_z are Pauli operators. With this form for H', we see that in-phase microwaves produce rotations about the x-axis of the Bloch sphere, out-of-phase microwaves produce rotations about the y-axis and low frequency bias current changes produce rotations about the z-axis.

3.1.2 Energy Relaxation

A qubit that is in the excited state $|1\rangle$ does not stay there forever, but instead relaxes to $|0\rangle$ because of energy dissipation. Of course, the qubit can only lose energy if it is coupled to one or more other quantum systems. If the qubit loses energy to another quantum system, the state information will be lost. The average time for the qubit to decay from the excited state $|1\rangle$ to the ground state $|0\rangle$ is called the relaxation time T_1. There are several possible causes of relaxation including dissipation in the leads (associated with Johnson-Nyquist noise) [60, 61], dielectric loss, and coupling to discrete two-level systems. Dissipation from the current bias leads needs to be carefully dealt with because these lines are directly connected to the SQUID phase qubit.

The energy level spacing in a phase qubit is controlled by the bias current and the applied flux. Noise on these bias leads will affect the system in two ways. High frequency noise that is close to the qubit resonance frequency ω_{01} will cause transitions between $|0\rangle$ and $|1\rangle$. On the other hand, low frequency noise in $I_{lf}(t)$ does not cause transitions, but instead leads to dephasing, *i.e.* rotations in the phase ϕ on the Bloch sphere. This can be seen from Eq. 3.12.

Now suppose the qubit is initialized to $|1\rangle$. Noise $I_{\mu\omega x}$ and $I_{\mu\omega y}$ at ω_{01} will lead to transitions. Since these currents enter into the Hamiltonian H'_{rot} as σ_x and σ_y terms, we can understand their effect as producing random rotations θ_x and θ_y about the x and y axis on the Bloch sphere (see Fig. 3.2). For small noise, we will assume θ_x and θ_y follow a Gaussian distribution. Martinis *et al*. found that the probability of the system staying in $|1\rangle$ can be written in terms of the power spectral density of the current noise $S_I(\omega_{01}/2\pi)$ at the transition frequency [59] as

$$P_1(t) = \frac{1}{2} + \frac{1}{2}\exp\left[-\frac{E_c}{E_{01}}\left(\frac{\Phi_o}{2\pi}\right)S_I(\omega_{01}/2\pi)\,t\right] \tag{3.13}$$

The relaxation T_1 can then be expressed as [59]

$$T_1 = \frac{2\hbar\omega_{10}C_J}{S_I(\omega_{01}/2\pi)} \tag{3.14}$$

where $S_I(\omega_{01}/2\pi)$ is the quantum current noise power spectral density at frequency ω_{01} [62]. Equation 3.14 includes absorption and emission events [thermal and zero-point noise are included in $S_I(\omega_{01}/2\pi)$]. I will examine this result in detail in section 3.2.

3.1.3 Dephasing

In addition to rotations around the x and y axes on the Bloch sphere, there can also be rotations about the z-axis. Such rotations change the phase ϕ of the qubit state (see Fig. 3.2). From Eq. 3.12, we see that such rotations will be caused by the $\Delta I_{lf}(t)$ term since it is associated with σ_z. Considering this current noise term, the change in the phase $\Delta\phi(t)$ at time t due to current noise can be written as

$$\Delta\phi(t) = \frac{\partial\omega_{01}}{\partial I_{dc}} \int_0^t dt' I_n(t') \tag{3.15}$$

where $I_n(t)$ is the current noise. The mean square deviation $\left\langle \Delta\phi^2(t) \right\rangle$ can then be written as [59]

$$\left\langle \Delta\phi^2(t) \right\rangle = \left(\frac{\partial\omega_{01}}{\partial I_{dc}} \right)^2 \int_0^{\omega_{01}} S_I(\omega/2\pi) W(\omega) \frac{d\omega}{2\pi} \tag{3.16}$$

where $W(\omega) = \dfrac{\sin^2(\omega t/2)}{(\omega t/2)^2}$ is a spectral weight function. The integral was cutoff for frequencies higher than ω_{01} because such high-frequency noise causes relaxation and this has already been accounted for in T_1.

The dephasing time T_ϕ can be obtained from Eq. 3.16 if we have an expression for the noise spectral density $S_I(\omega/2\pi)$. I note that the spectral weight $W(\omega)$ is constant at low frequencies and becomes very small at frequencies $\omega >> 2/t$. Thus, the phase noise $\left\langle \phi^2(t) \right\rangle$ will mainly have contributions from low frequency noise. For a white noise power spectrum $S_I(\omega/2\pi) = S_0$, the integral is easily calculated from Eq. 3.16 and finds [59]

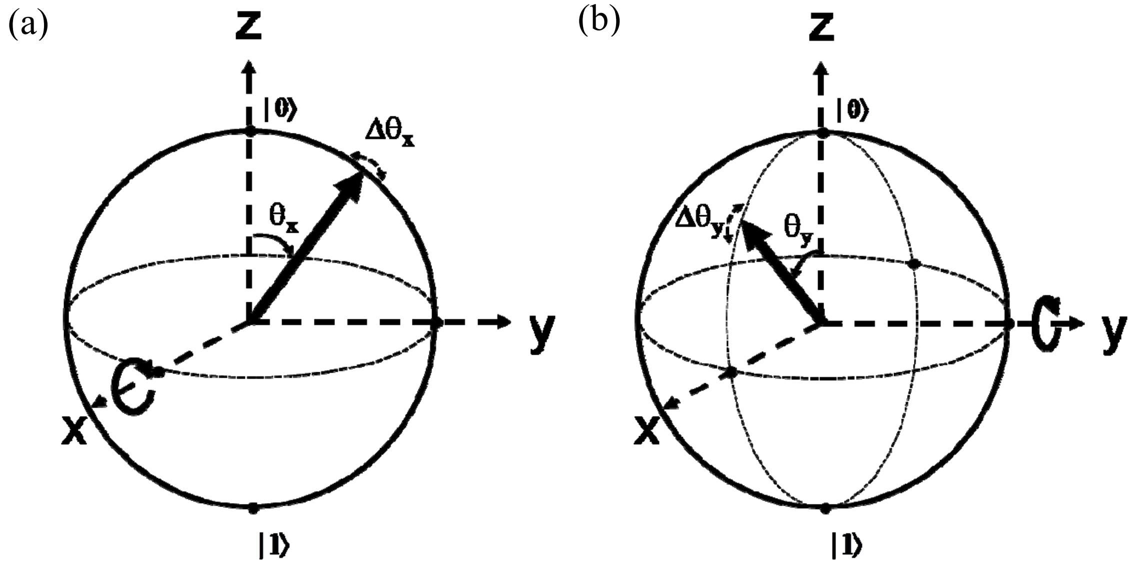

Figure 3.2: Representation of a qubit state rotation in the Bloch sphere. Random rotations (a) $\Delta\theta_x$ about the x axis and (b) $\Delta\theta_y$ about the y axis are shown in the Bloch sphere. Small current noise at frequency ω_{01} produces θ_x and θ_y rotations and this causes relaxation on excitation of the qubit state.

$$\left\langle \Delta\phi^2(t) \right\rangle = \left(\frac{\partial \omega_{01}}{\partial I} \right)^2 S_0 \frac{t}{2}. \tag{3.17}$$

This result implies the mean squared phase uncertainty increases linearly in time and the low frequency noise power determines the dephasing. From Eq. 3.17, we can define the dephasing rate $1/T_\phi$ [59]

$$\frac{1}{T_\phi} = \frac{1}{2} \left(\frac{\partial \omega_{01}}{\partial I} \right)^2 S_0. \tag{3.18}$$

3.1.4 Decoherence

Because a real qubit can never be completely isolated from external noise (see Fig. 3.3), the dynamics of the qubit will deviate from that of an ideal isolated two-level system. Both relaxation and dephasing will generally be present. The associated characteristic time constant T_2 for the system to lose amplitude or phase information is called the coherence time. The decoherence rate $1/T_2$ is related to T_ϕ and T_1 by [50]

$$\frac{1}{T_2} = \frac{1}{T_\phi} + \frac{1}{2T_1}. \tag{3.19}$$

I note that T_2 can be directly measured in a spin-echo experiment [112]. If there is no dephasing, then T_ϕ is infinite, and Eq. 3.19 reduces to $T_2 = 2T_1$. Thus, one can conclude that the coherence time T_2 is limited by the relaxation time T_1 and generally satisfies $T_2 \le 2T_1$. Thus if one finds $T_2 \approx 2T_1$, then dephasing is relatively unimportant and T_1 will need to be increased to achieve improvements in T_2. Indeed this appeared to be the case in many of our group's earlier qubits and that is why I focused on improving T_1 in my research.

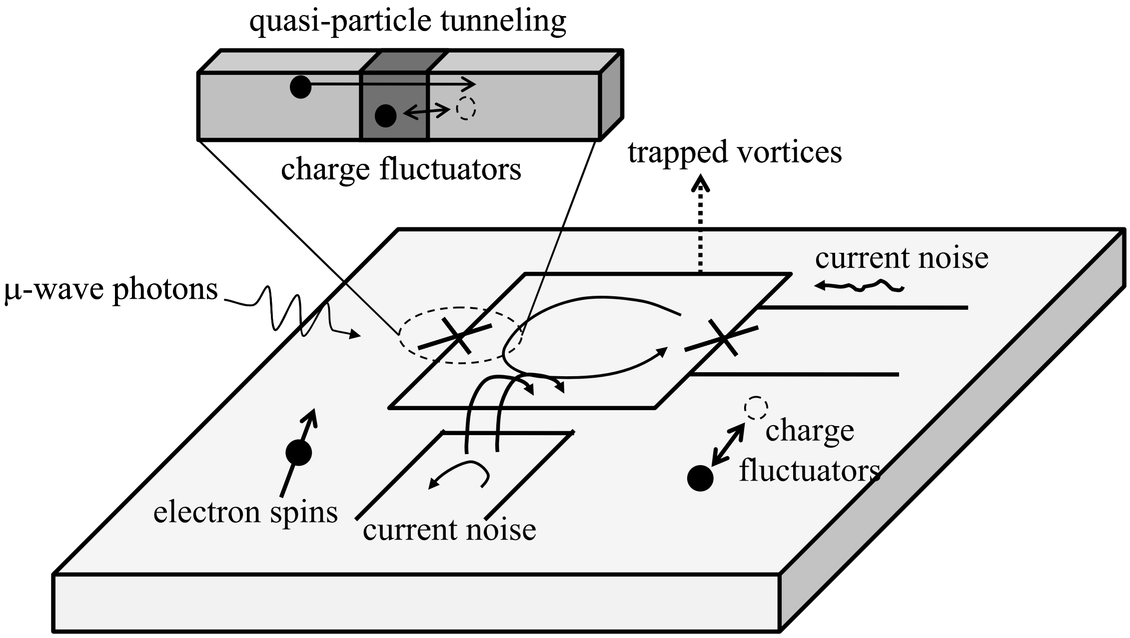

Figure 3.3: Various possible sources of decoherence in a dc SQUID phase qubit including current noise in the bias leads, charge fluctuators (TLS's) in the tunnel junction, fluctuating electron spins and charge fluctuators in the substrate or other dielectric layers.

3.1.5 Inhomogeneous Broadening

In atomic physics, the absorption lines in a spectrum show a Lorentzian shape because of the finite radiative lifetime. However, if the atoms are in a gas, then the center frequency of the absorption line changes depending on the atom's velocity in the gaseous state. The velocities follow a Maxwell-Boltzmann distribution and this causes a Gaussian broadening of the absorption [63].

For phase qubits, a similar situation happens. Low frequency current noise ($f << f_{01}$) causes the resonance frequency of the qubit to shift from one measurement to the next, producing inhomogeneous broadening in the resonance spectrum. The relation between the spectroscopic coherence time T_2^* and the line width of the resonance peak measured in microwave spectroscopy [63, 64] is

$$T_2^* = \frac{1}{2\pi\Delta f_{HWHM}} = \frac{1}{\pi\Delta f_{FWHM}} \tag{3.20}$$

where Δf_{HWHM} is the half-width at half-maximum and Δf_{FWHM} is the full width at half maximum of the absorption line. The spectroscopic coherence time T_2^* is generally shorter than the coherence time T_2 because of inhomogeneous broadening (low-fequency noise or shot-to-shot variations), and we can write

$$\frac{1}{T_2^*} = \frac{1}{T_2} + \frac{1}{T^\dagger} \tag{3.21}$$

where $T^\dagger$ is the inhomogeneous lifetime [64].

3.2 Current Noise

Our dc SQUID phase qubits have a direct connection to the current bias line. Because of this, one must be very careful to ensure that current noise in the leads is prevented from reaching the qubit.

To understand the effects of current noise, consider a single parallel LC resonator with small damping. The current fluctuations in the current bias line can be calculated using the current-current correlation function. One can write [59]

$$\langle I(t)I(0)\rangle = \frac{\hbar\omega_0}{2L}\left\{\left[\coth\left(+\frac{\hbar\omega_0}{2kT}\right)+1\right]e^{+i\omega_0 t} - \left[\coth\left(-\frac{\hbar\omega_0}{2kT}\right)+1\right]e^{-i\omega_0 t}\right\} \tag{3.22}$$

where L is the inductance of the LC circuit, ω_0 is the resonance frequency and T is the temperature.

To find the noise due to an arbitrary admittance $Y(\omega)$, one needs to sum Eq. 3.22 over a distribution of resonance frequencies. The spectral density of the current noise can be written as [59, 62]

$$S_I(\omega/2\pi) = \frac{2\hbar\omega}{1-\exp(-\hbar\omega/k_B T)}\mathrm{Re}[Y(\omega)]. \tag{3.23}$$

For $\hbar\omega >> kT$, one finds the zero-point noise contribution

$$S_I(\omega/2\pi, T=0) = 2\hbar\omega\,\mathrm{Re}[Y(\omega)] \tag{3.24}$$

where $Y(\omega) = 1/Z(\omega)$ is the admittance of the circuit with impedance $Z(\omega)$. From Eq. 3.24, and Eq. 3.14, I find

$$\frac{1}{T_1} \approx \frac{\mathrm{Re}[Y(\omega)]}{C_1}. \tag{3.25}$$

Eq. 3.25 also be written as

$$T_1 \approx R_{eff} C_1 \tag{3.26}$$

where $R_{eff} = 1/\mathrm{Re}[Y(\omega)]$ is the effective shunting resistance of the circuit (as seen by the qubit) and C_I is the capacitance of the qubit, which includes a junction capacitance C_J and any shunting capacitance C_x. Achieving a large T_1 thus requires achieving a large R_{eff} and a large C_I.

LJ and LC isolation to reduce current noise

Figure 3.4(a) shows a schematic diagram of a phase qubit with an arbitrary isolation network between the qubit and a current source. In Fig. 3.4(b), I show a circuit for an LC-isolated dc SQUID phase qubit connected to a current source with 50 Ω shunting (line) impedance. An inductor L_f and capacitor C_f form an LC filter network, while inductors L_1 and L_2 and the isolation junction *J2* form a broad-band inductive isolation network [29]. The two networks act together as a combined isolation network that steps up the characteristic impedance, $Z_o \approx 50$ Ω, of the bias leads to a much larger effective shunting resistance R_{eff} across the junction.

We can find R_{eff} by considering the impedance of both networks. Suppose the circuit is cut at points p and q in Fig. 3.4. The impedance of the LC filter network and lead impedance Z_0 from point p to ground is then

$$\mathrm{Z_f}(\omega) = \mathrm{i}\omega L_f + \frac{Z_0}{i\omega Z_0 C_f + 1} \tag{3.27}$$

where L_f is the inductance and C_f is the capacitance of the LC filter. The impedance to ground at point q for the isolation junction part of the LJ isolation network is then

$$\mathrm{Z_{J2}}(\omega) = \mathrm{i}\omega L_2 + \frac{i\omega L_{J2}}{1-\omega^2 L_{J2} C_{J2}} \tag{3.28}$$

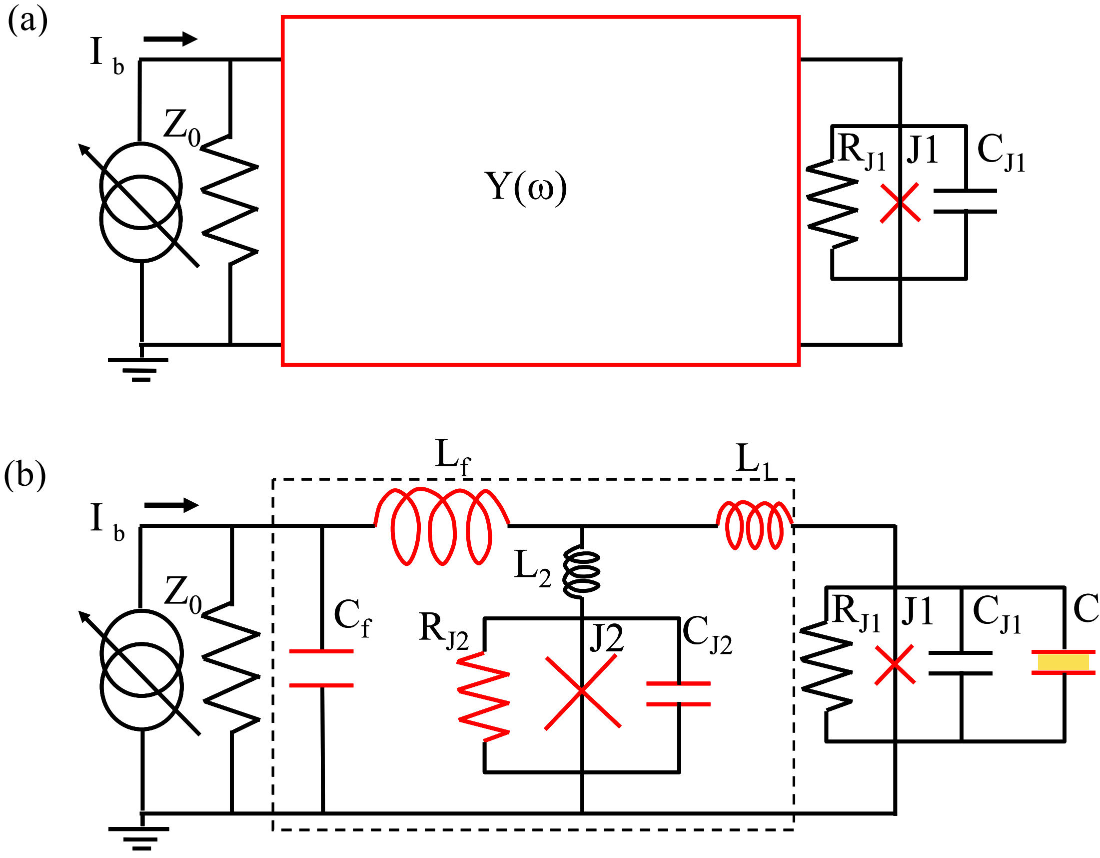

Figure 3.4: (a) Schematic diagram of a phase qubit connected to a current source by an arbitrary isolation circuit admittance $Y(\omega)$. (b) Schematic diagram for devices DS6 and DS8 which have LC isolation, LJ isolation and a shunting capacitor directly connected across the qubit junction *J1*. The dotted line in (b) indicates components producing the admittance $Y(\omega)$ in (a), which includes the bias line admittance Z_0.

where L_2 is the inductance of the arm of the SQUID loop that contains the isolation junction *J2*, L_{J2} is the Josephson inductance of the junction *J2* and C_{J2} is the capacitance of the isolation junction. Notice that Z_{J2} and Z_f are in parallel with each other and are series with L_1. One can then obtain the total impedance for the two networks as seen by the junction *J1*:

$$Z_{\text{total}}(\omega) = \text{i}\omega L_1 + \frac{Z_2(\omega)Z_f(\omega)}{Z_2(\omega)+Z_f(\omega)} \quad . \tag{3.29}$$

Finally, the effective shunting resistance R_{eff} is obtained from

$$1/\text{R}_{\text{eff}}(\omega) = \text{Re}[1/Z_{total}(\omega)]. \tag{3.30}$$

Figure 3.5 shows plots of the relaxation time T_1 versus frequency that I calculated from total impedance Z_{total} of the circuit using Eqs. 3.26 and 3.30 assuming that the only source of relaxation is the leads. For Fig. 3.5(a), I used L_1 = 1.2 nH, L_2 = 30 pH, and L_{J2} = 0.137 nH. These are the parameters for device DS6. For Fig. 3.5(b), I used L_1 = 1.5 nH, L_2 = 60 pH and L_{J2} = 0.427 pH. These are the parameters for device DS8. Because of different circuit parameters, the plot for device DS8 [see Fig. 3.5(b)] shows smaller relaxation time (smaller R_{eff}) than that for device DS6 [see Fig. 3.5(a)]. Both plots show strong frequency dependence, with higher frequencies giving a longer relaxation time T_1. For an operating frequency of 6-7 GHz in device DS6, T_1 reaches 2 to 3 ms, while at operating frequencies of 3-4 GHz in device DS8, T_1 is 50 to 100 μs. Of course these times are only for dissipation due to the current bias leads, and other sources of dissipation will be present and lead to shorter T_1 values.

An approximate equation for R_{eff} can be written by considering each isolation term separately and assuming $\omega \gg \omega_f$. One finds

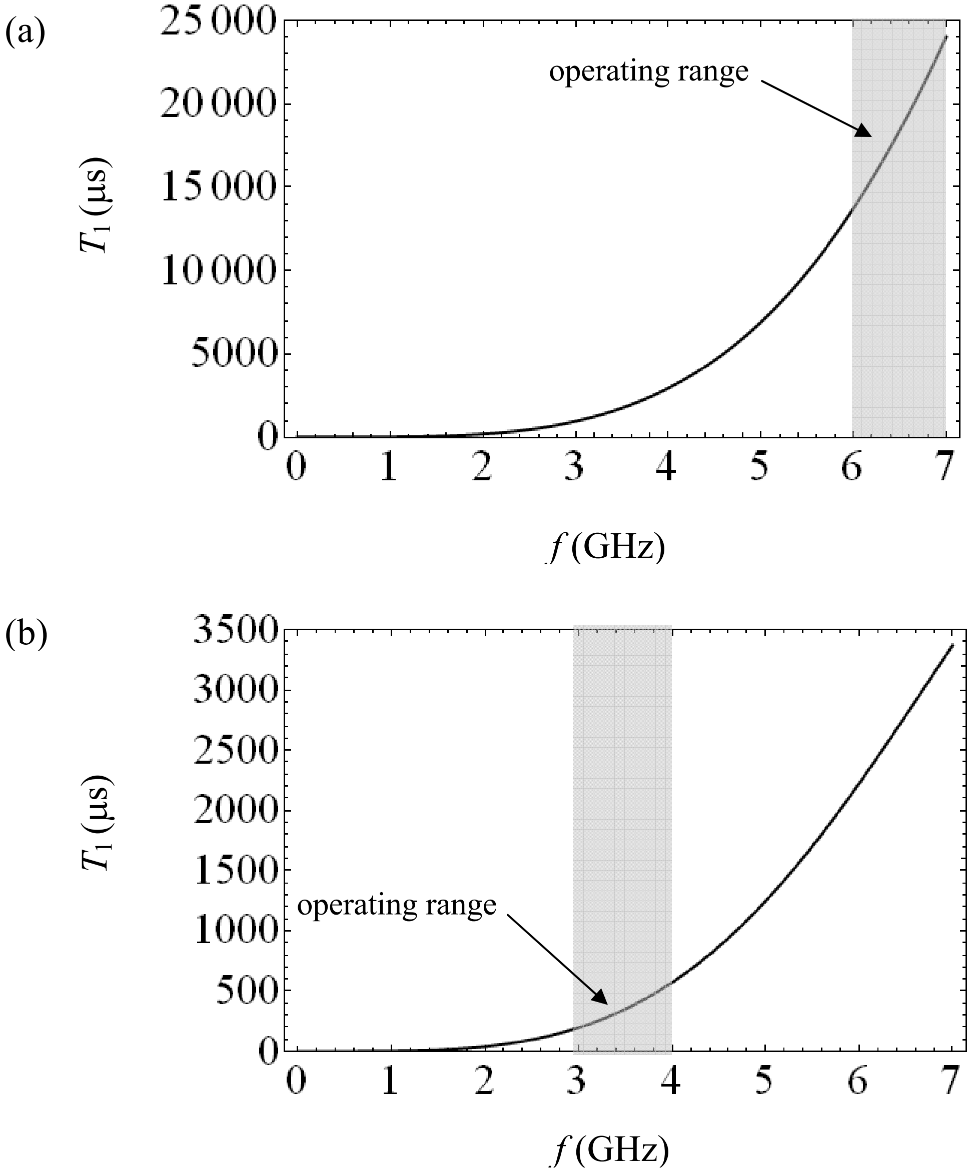

Figure 3.5: Predicted relaxation time T_1 versus frequency f due to the bias current leads. Values found using parameters (a) for device DS6 and (b) for device DS8. T_1 depends strongly on frequency and both curves have a similar dependence.

$$R_{eff} \approx \left(\frac{\omega}{\omega_f}\right)^4 \left(\frac{L_1 + L_2 + L_{J2}}{L_2 + L_{J2}}\right)^2 Z_0 \cong r_I Z_0 \qquad (3.31)$$

where Z_0 is the line impedance of 50 Ω and $\omega_f/2\pi = 1/2\pi\sqrt{L_f C_f}$ is the resonance frequency of the filter and I introduce the isolation factor $r_I \approx \left(\frac{\omega}{\omega_f}\right)^4 \left(\frac{L_1 + L_2 + L_{J2}}{L_2 + L_{J2}}\right)^2$.

In Eq. 3.31, the factor $\left(\frac{\omega}{\omega_f}\right)^4$ is due to the LC-filter network can be found from Eq. 3.27 in the limit $\omega >> \omega_f$; The LC network acts as a low-pass filter causing isolation to increase rapidly as the frequency increases.

For device DS6 parameters, $\omega_f \approx 2\pi\times130$ MHz and the qubit operating frequency was $\omega \approx 2\pi\times6.5$ GHz. One obtains $\left(\omega/\omega_f\right)^4 \approx 6\times10^6$. Parasitic capacitance between the coils of the filter's inductor, and stray inductance in the leads to the filter capacitor, will cause self-resonances and reduce the isolation above the self-resonance frequency. The wavelength at 6 GHz is comparable to the overall size of the filter and so we expect that a lumped circuit model for the filter elements will fail. A detailed electromagnetic simulation would be needed to simulate the filter behavior. Also the device DS6 has $L_1 \approx 1.2$ nH, $L_2 \approx 20$ pH and $L_{J2} \approx 120$ pH (corresponding to the isolation junction critical current of $I_{02} \approx 2.5$ μA). In this case, the second isolation factor will be about 90. Combining the two factors, one obtains an overall isolation factor of about 5.7×10^8 at 6.5 GHz in device DS6. For a bias line impedance of $Z_0 \approx 50$ Ω, an effective resistance $R_{eff} \approx 28$ GΩ is obtained from Eq. 3.31. The more accurate result from Eq. 3.27 is $R_{\mathrm{eff}} \approx 17$ GΩ.

Radiation resistance

T. A. Palomaki suggested [42] that radiation resistance is a possible source of decoherence in our dc SQUID phase qubits. The idea is that the SQUID loop can act like an antenna and radiate electromagnetic energy. He suggested that the qubit junction would drive current through the loop, producing an oscillating magnetic dipole. The resulting radiation produces an equivalent series impedance in the loop (the radiation resistance) given by [65, 66]

$$Z_{\mathrm{rad}}(\omega) \cong 320\pi^4 \left(A_{loop} \left(\frac{\omega}{2\pi v_c} \right)^2 \right)^2 \tag{3.32}$$

where A_{loop} is the loop area and v_{c} is the velocity of the waves in the substrate. Adding Eq. 3.32 to Eq. 3.29, one finds a total impedance for the circuit, as seen by the qubit junction, given by

$$Z'_{\mathrm{total}}(\omega) = \mathrm{i}\omega L_1 + \frac{Z_2(\omega) Z_f(\omega)}{Z_2(\omega) + Z_f(\omega)} + Z_{rad}(\omega). \tag{3.33}$$

From my device design, $A_{\mathrm{loop}} \approx (400\ \mu\mathrm{m})^2$ and $v_c \approx 10^8$. In Fig. 3.6, I show plots of the relaxation time T_1 versus frequency obtained from Eq. 3.33. The T_1's are suppressed by factors of 100 to 1000 compared to Fig. 3.5. However, before taking this number too seriously, note that Eq. 3.32 is based on radiation into free space. This is completely inappropriate for my devices because they were enclosed in a metal box that did not have modes at the operating frequency. Figure 3.6 shows the importance of this box!

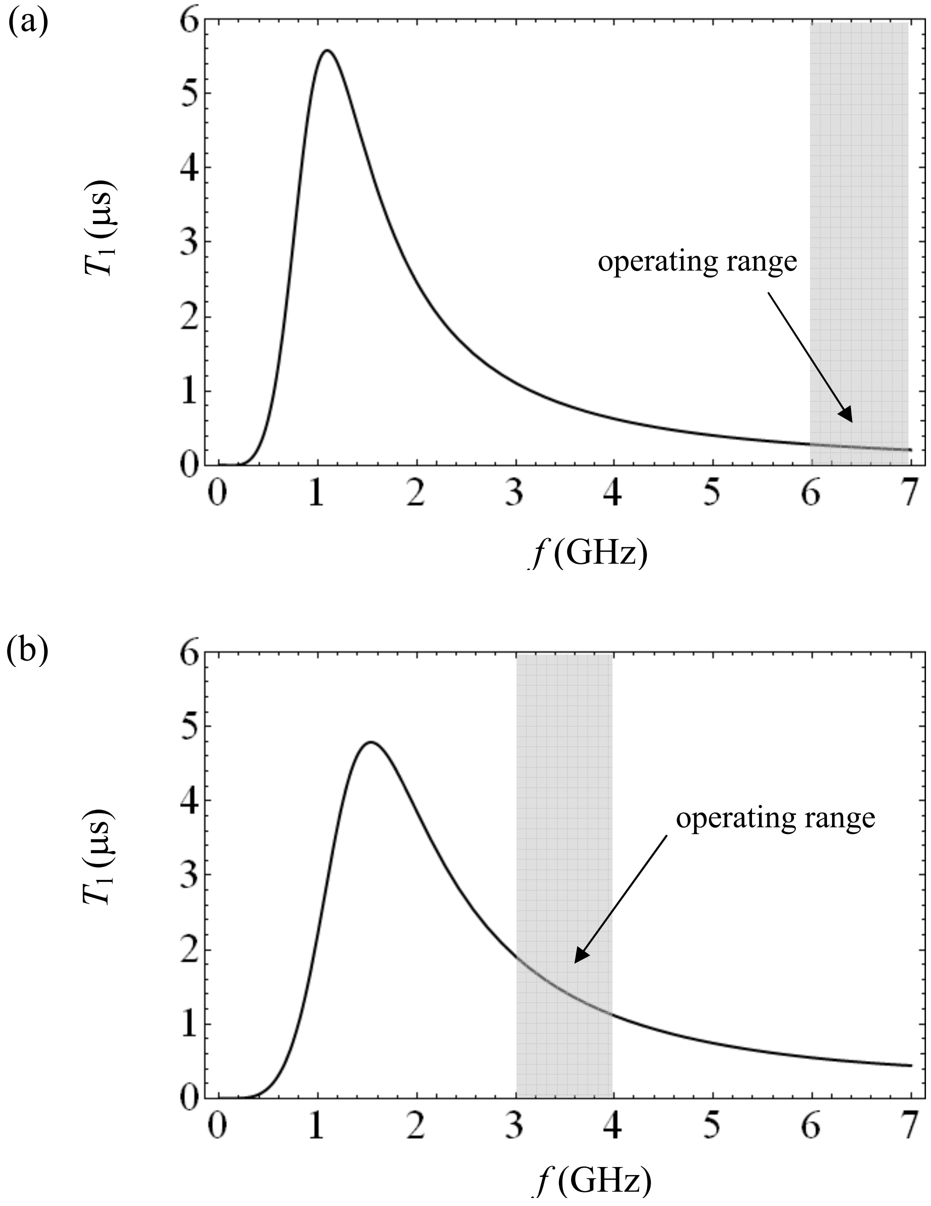

Figure 3.6: Calculated relaxation time T_1 versus resonance frequency f obtained from the noise spectral density of the LC and LJ isolation circuit including an approximate radiation resistance term that neglects the fact that the device is enclosed in a small sample box. Plots are (a) for device DS6 and (b) for device DS8. These T_1's are much shorter than in Fig. 3.5.

3.3 Critical Current Noise

Another potential source of decoherence is critical current noise. Charge trapping at defect sites in a junction barrier can block Cooper-pair tunneling through the junction because of Coulomb repulsion. If charges trap and untrap randomly, the critical current of the junction will fluctuate [67, 68]. Consider a junction with many traps in which each trap has its own characteristic lifetime and undergoes statistically independent switching. The noise spectrum of each trap will be a Lorentzian and under plausible assumptions, a collection of TLS's will produce an overall $1/f$ spectrum [69, 70]. The main assumptions one needs to make are that the untrapping process is activated and that there is a uniform distribution of trapping barrier heights. In this case, the critical current noise power spectrum will obey

$$S_{I_0}(f) = A_{I_0} / f \tag{3.34}$$

where A_{I_0} is a temperature-dependent constant.

From experiments [71], the noise power spectral density is about $S_{I_0}(1Hz) \approx 10^{-26} A^2 / Hz$ normalized to a 1 μm^2 junction area with a critical current of 1 μA at 100 mK. This number is very small and leads to a dephasing time T_ϕ that would be longer than μs in typical phase qubits. Thus, the critical current noise is not expected to be a concern in phase qubits.

3.4 Charge Noise

Charge noise produces large effects in sub-micrometer junctions [72]. Low-frequency charge noise has been measured and one finds a noise spectral density having

1/*f* form, $S_q(f) = A_q / f$. From single electron transistor (SET) measurement of charge noise, one typically finds $A_q \approx (10^{-3}\ e)^2$ [73]. The rms charge noise σ_q is [74]

$$\sigma_q{}^2 \approx \int_{f_{\min}}^{f_{\max}} d\omega\, S_q(f) \approx A_q \ln(f_{\max} / f_{\min}) \approx 30\, A_q \approx 3 \times 10^{-5} e^2 \ . \tag{3.35}$$

where f_{max} is the maximum frequency of the measurement and f_{min} is the minimum.

In a phase qubit, the relaxation rate produced by charge noise becomes very small. Further analysis [74] reveals that the dephasing time should scale as $\frac{1}{T_\phi} \approx \omega_{01} \sigma_q{}^2 \left(\frac{4E_C}{E_J} \right)^2$. Since $E_J >> E_C$ for a phase qubit, this results in a very small dephasing from charge noise (this idea is the basis for the transmon [27]). Thus, charge noise has not been a big concern in the phase qubits.

3.5 Flux Noise

SQUIDs cooled below 1 K have been found to exhibit a peculiar excess low-frequency flux noise [69, 70, 75, 76, 113]. In a wide range of SQUIDs, it has been found that $S_\Phi \approx 10^{-10} \Phi_0{}^2 / f$ to $10^{-12} \Phi_0{}^2 / f$ [69]. This noise is now understood to be produced by randomly fluctuating electron spins on the surface of the SQUID [76]. This noise level is small enough that we do not expect it to contribute significantly to decoherence in our SQUID phase qubits.

Another type of flux noise arises from the flux bias line. In this case, current noise on the flux bias line leads to a flux noise in the SQUID given by

$$S_\Phi(f) = M_\phi{}^2 S_I(f) = \frac{M_\phi{}^2 4\pi\hbar f}{Z_0} \quad (for\ hf >> kT) \tag{3.36}$$

where M_ϕ is the mutual inductance between the SQUID loop and the flux bias line. The spectral density of this flux noise has the same general form as current noise except for the M^2 term. Because M_ϕ is very small (~ 1 pH in my devices), the flux noise coming from the flux bias line will produce a relatively large effective impedance. Further consideration reveals that this would produce a relaxation rate of $\frac{1}{T_1} = \frac{1}{R_{eff} C_1} = \frac{{M_\phi}^2}{Z_0 L^2 C_1}$.

For device DS6, $M_\phi \approx 1$ pH, $L \approx 1$ nH, $C_1 \approx 1$ pF, so $T_1 \approx 50$ μs.

3.6 Dielectric Loss and Charged TLS's

Phase qubits can couple to charged parasitic two-level systems (TLS's) that reside in the dielectric layer of the junction or other dielectric layers [76, 77]. If the frequency spacing between the qubit |0> and |1> is equal to the resonance frequency of a TLS, an avoided level crossing or energy splitting occurs in the transition spectrum of the qubit. In this case, the relaxation of the qubit is dependent on the coupling to the TLS's. The relaxation rate can be written as [42]

$$\frac{1}{T_1} = \pi^2 \int \left. \frac{d^2 N}{df \, d\Delta_f} \right|_{f_{01}} \left| \Delta_f \right|^2 d\Delta_f \tag{3.37}$$

where Δ_f is the size of the frequency splitting and $Nd\Delta fdf$ is the number of defects with a splitting size between Δ_f and $\Delta_f + d\Delta f$ and transition frequencies between f and $f + df$. From Eq. 3.37, we see that T_1 will be longer if the number of TLS's is reduced and the coupling is reduced (which reduces the splitting Δ_f).

In the limit of a continuous distribution of TLS's in the junction, the effective resistance is just $R_{eff} = 1/\omega_{01} C_1 \tan(\delta)$ where tan(δ) is the loss tangent. In this case, one finds

$$\frac{1}{T_1} = \omega_{01} \tan(\delta) . \tag{3.38}$$

For AlO_x in the junction capacitor, it is believed that tan(δ) ≈ 1.6×10^{-3} [78]. At $\omega_{01} = 2\pi\times3.5$ GHz, one finds $T_1 \approx 72$ ns which is short.

Adding a shunting capacitor to reduce the effect of dielectric loss

The above discussion on dielectric relaxation highlights a serious problem in phase qubits. Compared to the effect of current noise discussed at the beginning of this chapter [35], dielectric loss is much more important. To reduce the effect of dielectric loss in the junction, Martinis *et. al*. pointed out that one could add a larger, lower-loss capacitor across the junction. In this case, the total capacitance would be $C_1 = C_J+C_x$ where C_1 is the total effective capacitance of the qubit junction C_J is the geometrical capacitance of the qubit junction and C_x is the capacitance of any additional capacitors connected directly across the qubit junction. The effective shunting resistance would be $R_{tot} \approx \frac{R_{eff} R_x}{\left(R_x + R_{eff}\right)}$ and the resulting relaxation time is

$$T_1 = R_{tot} C_1 = \frac{R_{eff} R_x}{\left(R_x + R_{eff}\right)} \left(C_{J1} + C_x\right) \tag{3.27}$$

where R_x is the dielectric loss in C_x and R_{eff} is due to all other losses. If $R_x << R_{eff}$, then $\frac{R_{eff} R_x}{\left(R_x + R_{eff}\right)} \approx R_x$. Also $C_1 \approx C_x$ if I choose to have $C_x >> C_{J1}$, and thus $T_1 \approx R_x C_x$.

Thus, if the dielectric loss from the shunting capacitor is included, the relaxation time T_1 becomes $T_1 \approx R_x C_1 \approx 1/\omega_{01}\tan(\delta_x)$ instead of $1/\omega_{01}\tan(\delta_J)$. The key to observing much longer T_1 is to use a better dielectric for the shunting capacitor *i.e.* make sure $\tan(\delta_x) << \tan(\delta_J)$. For example, using $\tan(\delta_x) \approx 3\times10^{-5}$ for SiN_x at $\omega_{01} = 2\pi\times3.5$ GHz, I can expect to have a value of $T_1 \approx 1.5$ μs in device DS8. This assumes I can completely neglect loss in the junction, but unfortunately this was not a good approximation for my device. In general, one must use the full result given by Eq. 3.27. Including loss in the junction with $C_x \approx 0.83$ pF, $C_J \approx 0.05$ pF, $R_x \approx 1.8\times10^6\ \Omega$, $\tan(\delta_x) \approx 3\times10^{-5}$, $R_J \approx 5.7\times10^5\ \Omega$ and $\tan(\delta_J) \approx 1.6\times10^{-3}$, one finds $T_1 \approx 300$ ns.

3.7 Dielectric Loss in the Substrate and Other Dielectric layers

Silicon substrates have been widely used as qubit substrates because they are cheap, easily obtained, and well-suited for doing photolithography or e-beam lithography. However, silicon substrates contain significant impurities and have a native oxide (SiO_2) which has significant dielectric loss. The substrate itself can cause dissipation and has been suspected to be a source of decoherence [78].

Because of concerns about loss in silicon substrates, most superconducting qubit groups now build devices on single-crystal sapphire (Al_2O_3). Single-crystal sapphire has a loss tangent of order 10^{-6} to 10^{-7} [79]. From Eq. 3.25, $\tan(\delta)$ of 10^{-6} at a resonance frequency of 3.5 GHz yields $T_1 \approx 45$ μs, which is quite long.

3.8 Summary

In this chapter, I presented an overview of decoherence sources in the phase qubit. I then discussed techniques for protecting the qubit from the main decoherence sources. Fundamentally, a phase qubit is insensitive to charge noise because $E_J/E_C >> 1$. Critical current noise and flux noise are present but should produce relatively little impact with proper choice of the device parameters. Most of the low-frequency noise is expected to come from the current bias leads because the leads are directly connected to the qubit. To minimize the impact of current noise and relaxation from dissipation in the leads, I attached two isolation networks (LC and LJ) between the leads and the qubit junction. Dielectric loss in the insulating layer of the junction also causes relaxation. The effect of dielectric loss in the junctions can be minimized by attaching a low loss SiN_x shunting capacitor across the junction.

Table 3.1: Expected T_1 from the design parameters for DS8 (see Table 4.2).

Design	R_{eff} (Ω)	T_1
LC & LJ isolation	0.4×10^9	400 μs
radiation*	1.6×10^6	1.4 μs
dielectric loss (SiN_x)	1.8×10^6	1.6 μs
dielectric loss (AlO_x)	5.7×10^5	500 ns
Total loss from all of the above	3.4×10^5	300 ns

* This result assumes the device was in free space. Since the device was actually in a sample box of size $L << \lambda_{01}$ (where $\lambda_{01} \approx 6$ cm is the wavelength of 5 GHz), this radiation will be nearly completely suppressed.

Chapter 4

Layout and Fabrication of dc SQUID Phase Qubit

In this chapter, I discuss the design parameters for my devices and how I made them using optical lithography.

4.1 Design Parameters of Devices DS6 and DS8

As I discussed in Chapter 3, noise from the environment can lead to short coherence times in superconducting qubits. In order to increase the coherence times, I needed to isolate the qubit from the bias lines. The basic scheme we used was to add isolation elements to form a filter network between the bias leads and the qubit junction. In addition, two level systems (TLS's) in the qubit tunnel junctions were believed to be contributing significant dissipation. In order to increase the relaxation time of our phase qubits, I add a low-loss shunting capacitor across the qubit junction. The basic layout of my devices is shown in Fig. 4.1 (a).

As discussed in Chapter 3, a major concern was that at high frequencies the current bias leads and flux line could introduce significant dissipation. To reduce the

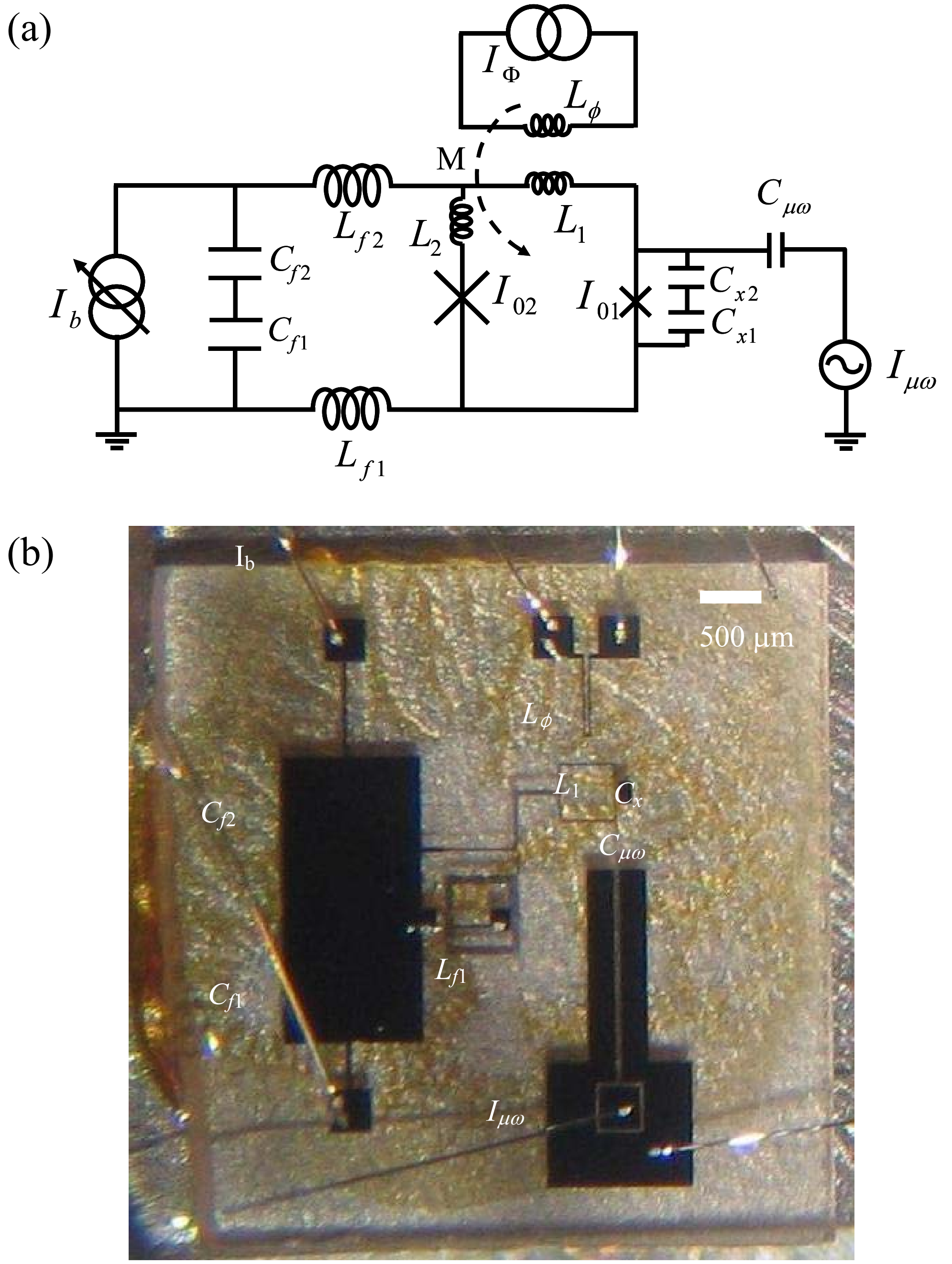

Figure 4.1 (a) Schematic of dc SQUID phase qubit. The qubit junction is isolated from bias current noise by the isolation junction (LJ) and an inductor-capacitor (LC) network. (b) Photograph of device DS6. The device is bonded with Al wire to gold contact pins in the Al sample box.

effect of dissipation from the leads, I added an on-chip LC filter between the SQUID and the current bias leads to produce large impedance [80]. For good isolation, the inductance and capacitance of the filter must be chosen so that the resonance frequency of the LC filter is well below the plasma frequency of the qubit junction. In devices DS6, I chose the resonance of the isolation circuit to be about 130 MHz [50] by using a total inductance of 10 nH and a total capacitance of 145 pF [see Fig. 4.2(a)]. In device DS8, I used a total inductance of 10 nH and total capacitance of 148 pF [see Fig. 4.2(b)]. Thus the filter resonances were much lower than the plasma frequencies of the qubit junctions in both devices; f_{01} was designed to be in the range of 5-8 GHz, while the actual range was 3-4 GHz.

To simplify fabrication of the 148 pF filter capacitance, it was built from two capacitors connected in parallel [see C_{f1} and C_{f2} in Fig. 4.1(a)]. There were some differences in the layout of the filter in the two devices (see Fig. 4.2). In DS6, I used a single filter inductor (L_{f1}); *i.e.* $L_{f2} = 0$. In DS8, I used two counter-wound inductors (L_{f1} and L_{f2}) in series and the capacitors arranged symmetrically to minimize the possible pick up of magnetic noise by the large spiral inductors.

For the inductors in the LC filters, I used a square spiral inductor of about 10 nH. By using a multi-turn coil, I could achieve a relatively large inductance in a relatively small size. For a spiral inductor with an inner diameter d_{in}, an outer diameter d_{out} and n turns, the inductance can be found using a modified Wheeler formula [81]:

$$L_f \approx 2.34\mu_o \frac{n^2 d_{avg}}{1+2.75\rho} \tag{4.1}$$

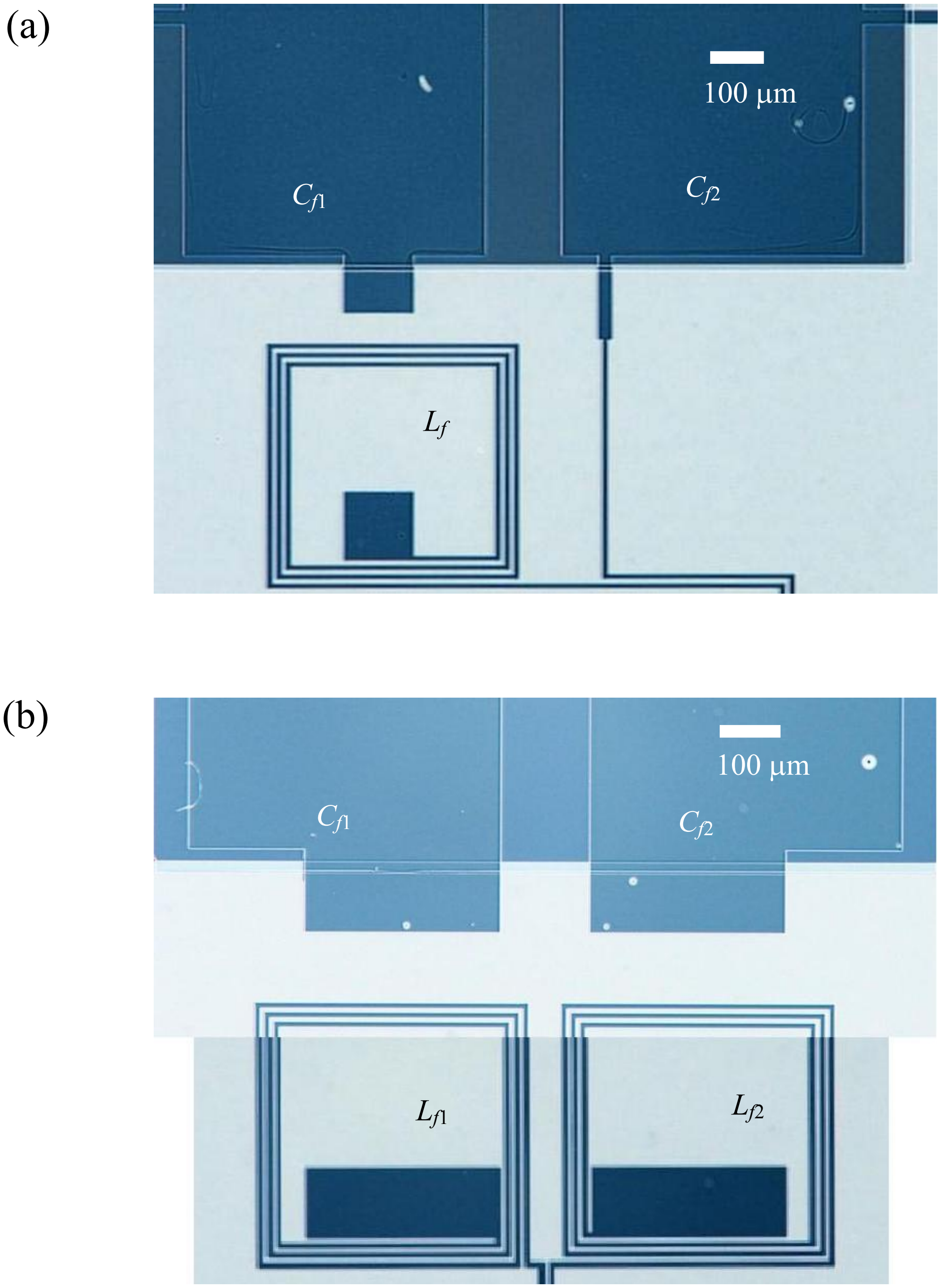

Figure 4.2 (a) Photograph of the LC filter area of device DS6. The side which does not have a square spiral inductor is connected to ground. (b) Photograph of the LC filter area of device DS8. The two inductors L_{f1} and L_{f2} are wound as a field gradiometer to limit pickup of uniform magnetic field noise.

where $d_{avg} = (d_{in}+d_{out})/2$ and $\rho = (d_{out}-d_{in})/(d_{out}+d_{in})$. Using an Al film with $d_{in} = 470$ μm and $d_{out} = 500$ μm, one finds $L_f \approx 10$ nH. Note that the total length of one coil (about 6 mm) is not much shorter than $\lambda/4 \approx 12$ mm at 3 GHz. This suggests that the coil could have a self-resonance frequency at a frequency of about 6 GHz; as the frequency approaches the self resonance the filter would not function as effectively as intended.

The standard approach for reducing low-frequency noise in dc SQUID phase qubits is to add an isolation junction and loop inductance. This forms an inductive divider that protects the qubit junction from bias current noise [29]. I chose the arm of the SQUID with the qubit in it to have inductance $L_1 \approx 1.6$ nH, estimated using the rough design rule for the inductance of a thin wire of 1 nH/mm. The other side of the SQUID loop (with the isolation junction in it) had a small inductance $L_2 \approx 30$ pH (the L_2 lines are very short as seen in Fig. 4.3). These values were similar to those used previously in the group.

There were some other differences between device DS6 and DS8. In device DS8, I deliberately made the area of the qubit junction two times smaller than that of device DS6, while the isolation junction of device DS8 was two times larger than that of DS6. Because of these differences in the parameters, device DS8 should have been better isolated from the leads than device DS6.

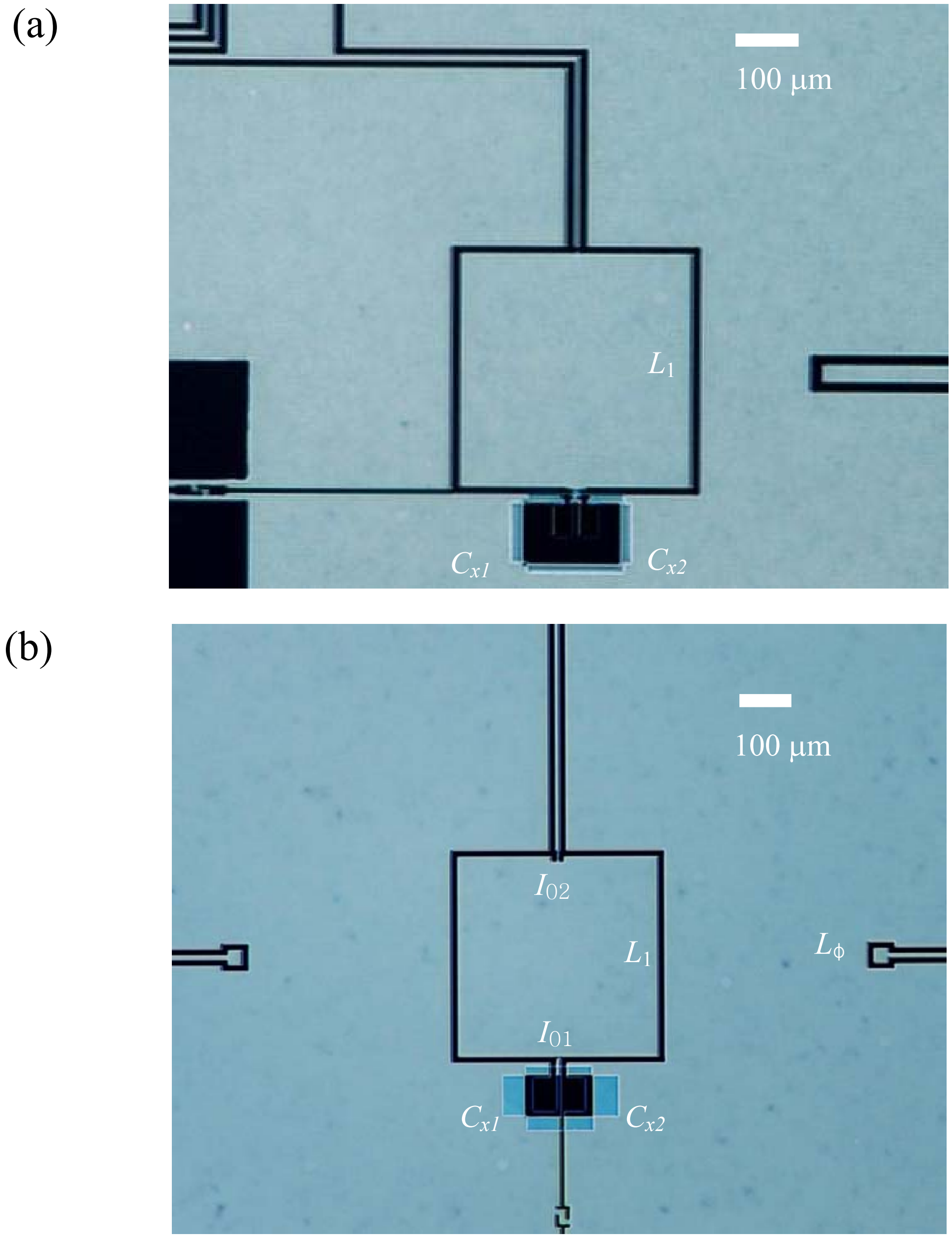

Figure 4.3 (a) Photograph of SQUID loop area of device DS6. The color has been reversed to show the device more clearly. The shunting capacitor is connected to the qubit junction, which is located near the bottom of the picture. (b) Picture of SQUID loop area of DS8. The light blue color is SiN_x. One of the flux bias lines is a dummy line to keep the design symmetric.

4.2 Fabrication Procedure

I built devices DS6 and DS8 using optical lithography in the Fablab at the University of Maryland. To achieve the lowest dissipation at microwave frequencies, I built the devices on a sapphire wafer. The patterns for devices DS6 and DS8 were created using ICED, which is software for 2-D CAD [82]. I sent the CAD files to the Microlab at the University of California, Berkeley, where the photomasks were made [83]. My fabrication method was based on H. Paik's recipe [52], although I changed some parameters and added some steps that were important for my devices. In particular, I needed more steps to build the LC filters.

4.3 Optical Lithography

In optical lithography, patterns are made using chemical resists that change when they are exposed to ultraviolet (UV) light. When a positive photoresist is exposed to UV light, its chemical bonds are broken and the exposed area becomes sensitive to the developer when the resist is in the developer. To make patterns, I used a chromium photomask which is basically a glass plate coated with chromium that has been patterned. The smallest features on the masks I used were 2 μm.

I used a Karl-Suss MJB3 contact mask aligner [84] in the Kim building Fablab [see Fig. 4.5(a)]. This system requires accurately placing the mask on the substrate, but some misalignment is inevitable. Better contact between the substrate and the mask gave better patterns.

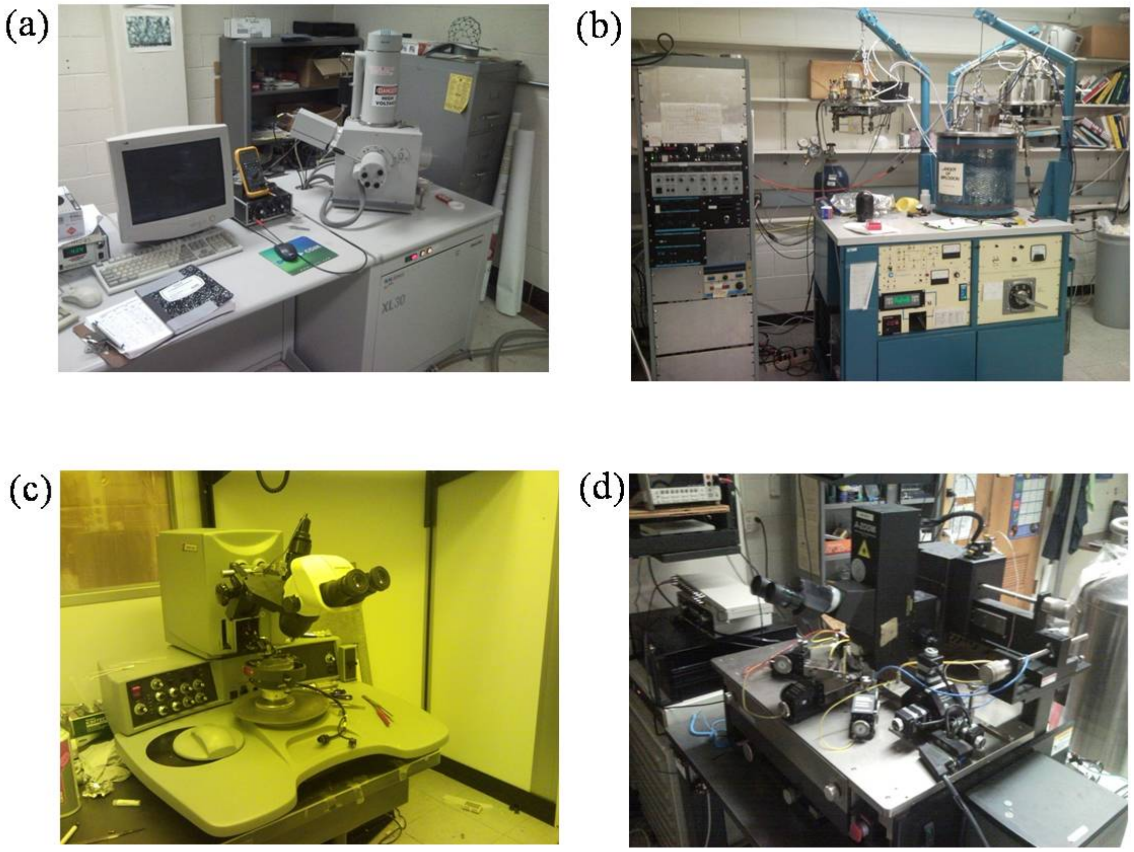

Figure 4.4: Equipment for fabrication at CNAM. (a) Philips XL30 SEM , (b) thin film evaporator, (c) K&S Model 4523 wire bonder and (d) probe station.

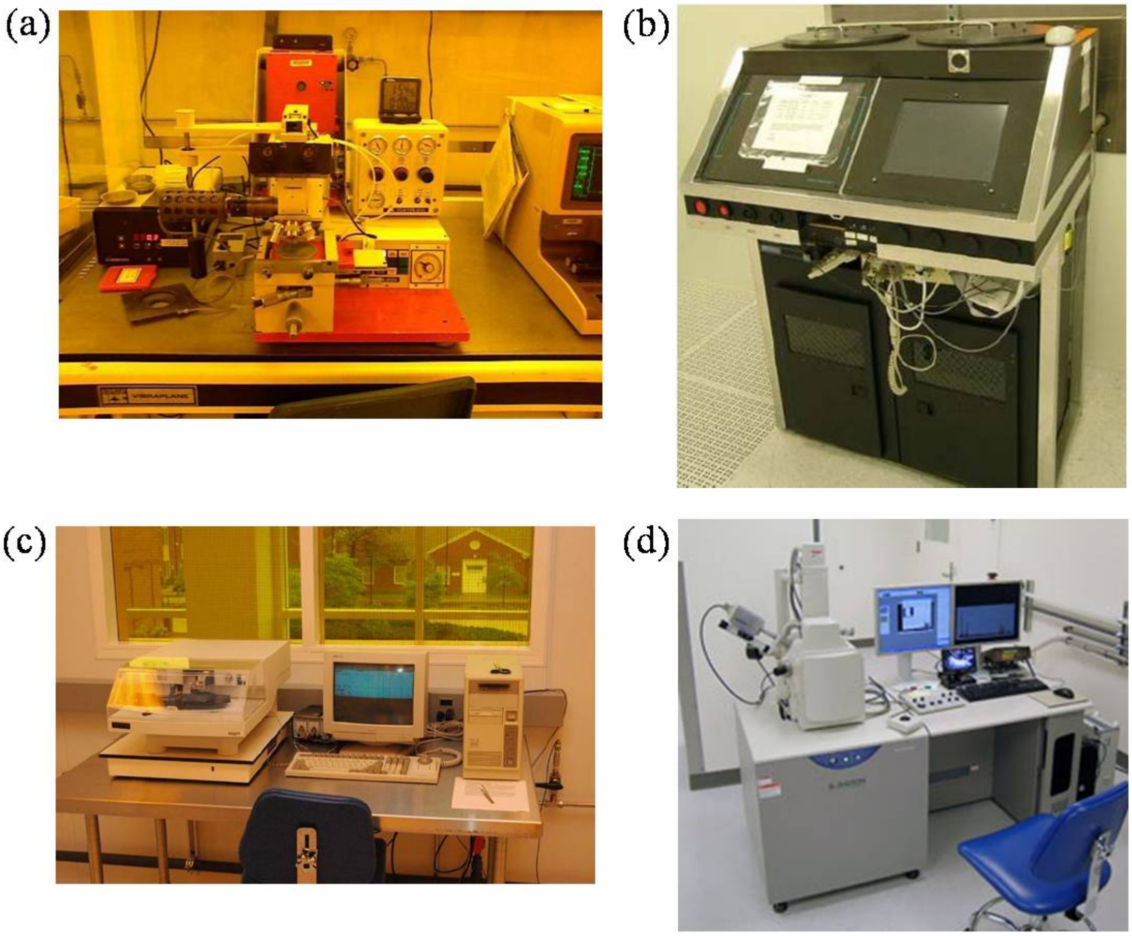

Figure 4.5: Equipment for optical lithography and measurements in the Kim Building. (a) Trion Reactive Ion Etcher (RIE), (b) Karl Suss MJB-3 Mask Aligner, (c) AlphaStep 500 and (d) Hitachi S-3400 Variable Pressure SEM.

The junctions in my device were made using double-angle evaporation and this required making a suspended photoresist bridge [85]. This is a relatively easy process, but I still had to pattern the resist many times to get good suspended bridges. Even if I used the same baking time and UV exposure time and power, the pattern did not always develop correctly because the thickness of the undercut layer of the resist LOR30B varied a bit or the contact between the mask and the wafer varied. Also, there were differences in the speed at which small patterns and large patterns developed. If I tried to develop a large pattern completely, the small qubit junction bridge was usually gone. So, I needed to stop developing in the middle, look at the patterns through the microscope, and check whether they were developed enough. If they were not fully developed, the surface showed rainbow interference colors. Despite these difficulties, I was able to fabricate several good devices.

The following gives the recipe I used for making devices.

Fabrication Steps for the Bottom Layer

1. Prepare a mask and a new 3″ sapphire (Al_2O_3) wafer.
2. Use an O_2 plasma etch in the Trion RIE [see Fig. 4.5(b)] at 400 mTorr and 200 W for 30 s to clean the wafer.
3. Spray acetone, methanol and isopropanol on the mask to clean it, and blow dry with N_2 gas immediately.
3. Prepare about 2 mL of photoresist S1813 and place wafer on spinner.
4. Drop S1813 liquid on top of the wafer. It should be dropped carefully or bubbles will for and produce an irregular surface.

5. Set the spinning time to 45 s. Start spinning the wafer and raise the speed to 4500 rpm to achieve a thickness of 12.5 μm.
6. Bake the wafer at 110 ^{o}C for 1 min on a hot plate.
7. Spray acetone, methanol and isopropanol (in order), and blow dry with N_2 gas immediately.
8. Place the mask and set the wafer into position on the Karl Suss mask aligner and then expose UV light for about 10 s with strength of 8 mW/cm^2.
9. Develop the resist for 30-40 s in photoresist developer MF-319 with agitation. Rinse with water immediately after developing.
10. Dry the wafer with N_2 gas.

Fabrication Steps for the SiN_x Layer

1. Prepare negative photo resist NR-9 1500 and set the wafer on the spinner.
2. Set the spinning time to 40 sec. Start spinning the wafer and raise the speed up to 4000 rpm to make a thickness of 1.3 μm. Sometimes I used a lower spin speed to make a thicker layer.
3. Bake the wafer at 150 °C for 1 min on a hot plate.
4. Expose the resist in the Karl Suss mask aligner to 365 nm wavelength UV light. I exposed the wafer a couple of times at slightly different positions to prevent any contact between the top electrode and bottom electrode at the edges of the filter capacitors.
5. Bake the wafer at 100 °C for 1 min on a hot plate.

6. Develop the pattern by immersing in RD6 developer. Development time for a 1.5 um thick film is 12 sec.
7. Rinse the wafer with de-ionized water and dry using N_2.

Fabrication Steps for the Top Layer

1. Prepare the mask for the top layer.
2. Use an O_2 plasma etch at 400 mTorr with a power of 200W for 30 sec to clean the wafer.
3. Spray the mask with acetone, methanol and isopropanol, and blow dry with N_2 gas immediately.
4. Prepare photoresist LOR30B in a 10 mL beaker. About 4 mL of LOR30B is enough to cover a 3″ wafer.
5. Start spinning the wafer with a slow speed of 10-20 rpm and pour LOR30B resist on the spinning wafer while it is rotating.
6. Immediately increase the speed from 10-20 rpm to 3300 rpm and spin for about 45 s. The resist should then be about a 2.6 μm thick.
7. Bake the wafer at 150 °C for 10 min on a hot plate.
8. Prepare S1813 photoresist and put the wafer back on the spinner.
9. Drop S1813 resist on top of the LOR30B layer without making any bubbles.
10. Set the speed to 4500 rpm and spin for 45 s. This makes a resist layer of thickness 12.5 μm on top of the LOR30B.
11. Bake the wafer at 110 ˚C for 1 min on a hot plate.

12. Spray acetone, methanol and isopropanol on the mask to clean the surface, and blow dry with N_2 gas immediately.
13. Place the mask and set the sample position in the Karl Suss mask aligner. Expose UV light for about 10 seconds with strength of 8 mW/cm^2. I had to be careful to align the bottom plate through the top mask's transparent patterns and find the right contact place for the top layer. It is also important to make sure the wafer does not touch the mask doing this alignment. I take the wafer a little bit away from the mask and only make them contact each other again when I am done with positioning.
14. Prepare photoresist developer MF-319 (or CD-26).
15. Develop the resist for 30-40 s in MF-319 developer with agitation and rinse with DI water immediately. The developing time depends on the photoresist and exposure conditions. I had to check the developed patterns through the microscope, and if the patterns were not developed, soak the wafer for a few more seconds and check again.
16. Dry the wafer with N_2 gas.

4.4 SiN_x Film

In order to reduce the effects of charged two-level systems, a good dielectric film was needed to make the shunting capacitor that was connected across the qubit junction. In DS6, I used low-stress amorphous silicon nitride (SiN_x) to make a shunting capacitor. This turned out to be relatively lossy material. In DS8, I used low-loss (high-stress) SiN_x film to make the added capacitor. Depositing and patterning the SiN_x required several additional steps in the process.

4.4.1 Deposition of SiN_x in HDCVD

Figure 4.6 shows the region near the qubit junctions in devices DS6 and DS8. The $Al/AlO_x/Al$ layers were deposited on top of the SiN_x layer and over its patterned edge. In order to obtain good coverage of the Al on the edge of the 100 nm thick SiN_x layer, the $Al/AlO_x/Al$ layers had a total thickness of 120 nm. The thickness of the SiN_x layer was measured by Alpha Step 500 [see Fig. 4.5(c)].

In device DS6, I used a low-stress SiN_x film to make the capacitors. The film was deposited by B. S. Palmer at LPS using CVD. The film showed $\tan(\delta) \approx 7\times10^{-4}$ which was somewhat less than $\tan(\delta) \approx 1.6\times10^{-3}$ [78] of the AlO_x in the junction. The process B. S. Palmer used was developed by H. Paik and K. D. Osborn, who investigated the properties of SiN_x films produced using various CVD parameters [43]. They used an inductively coupled plasma (ICP) chemical vapor deposition system (Oxford Instruments PlasmaLab System 100) to deposit the films and this same machine was used for my films. This machine is also called a high density CVD (HDCVD). They found that high-stress films contained a smaller amount of N-H impurities and exhibited lower loss than other SiN_x films [43]. The films were deposited at T = 300 °C at a pressure of 5 mTorr. The precursor gas flow rate of SiH_2 was set to 10 sccm and the rate of N_2 was a bit higher than 12 sccm in this case.

Low-loss high-stress SiN_x was used in device DS8. The high stress produced several problems during the fabrication process. The first problem was that small pores appeared in the films. In particular, when H. Paik deposited a low-loss SiN_x film on top of an Al layer, sub-micrometer sized holes appeared in the aluminum. H. Paik and I

(a)

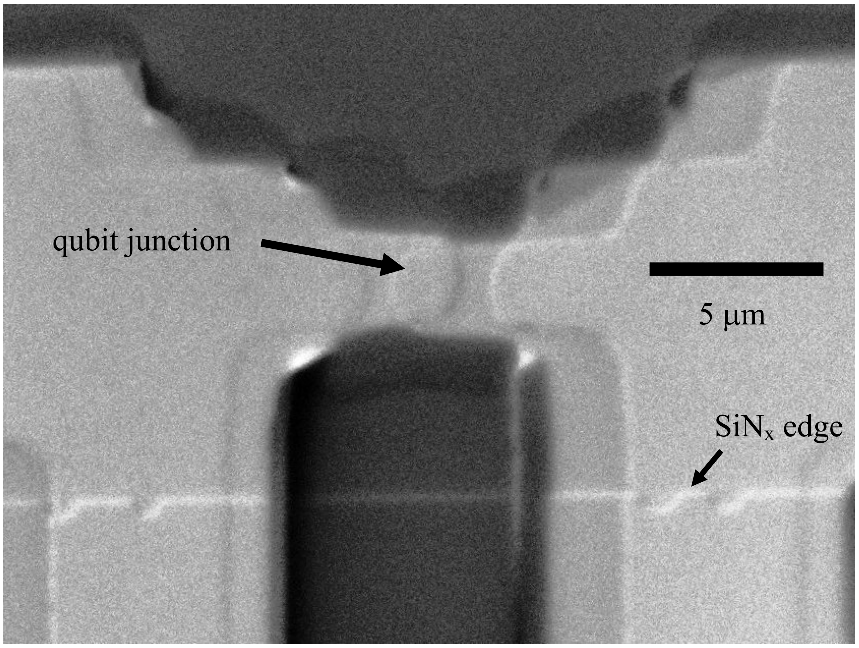

(b)

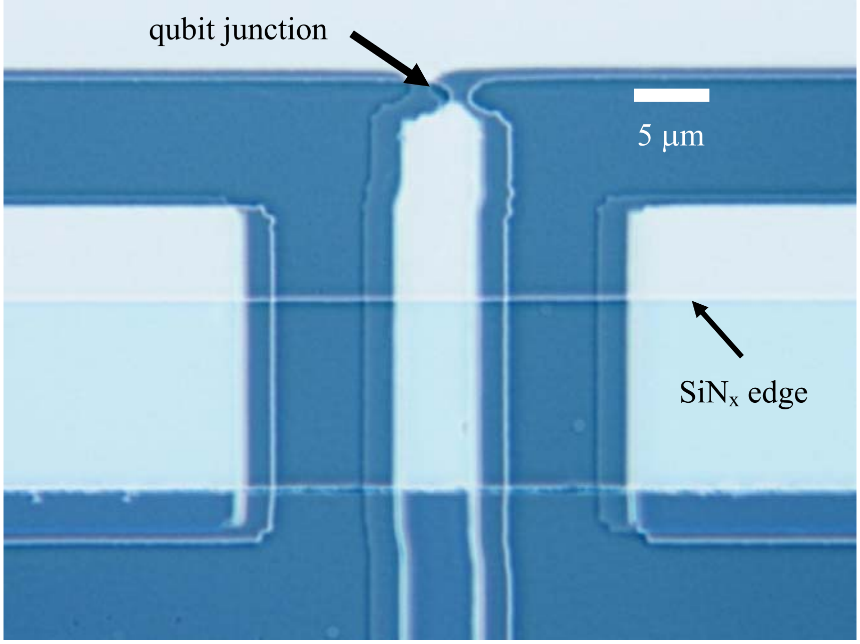

Figure 4.6 (a) SEM picture of the qubit junction area of device DS6 taken by Hitachi S-3400 [see Fig. 4.5(d)]. The oval overlap area in the center is the qubit junction. The multiple edges are from the Al/AlO$_x$/Al double angle evaporation and the SiN$_x$ layer. The junction area is about 4 μm^2. (b) Photograph of the qubit junction area of device DS8. The area of the qubit junction is about 2 μm^2.

suspected some residue from the resist during the lift-off process or some dirt introduced during the SiN_x deposition process in the CVD chamber. We did not find a complete solution to this problem, but after several trials cleaning the substrate, and varying the CVD parameters, she obtained a good SiN_x film which did not seem to have pores in it. Another problem was the fragility of the film. When I tried contacting a mask to the wafer using the mask aligner, the high-stress (Si-H rich) SiN_x films sometimes peeled off; the high-stress films seemed to be much more fragile than the low-stress (N-H rich) films, which is to be expected [43]. I got the patterning to work by not contacting too close during lithography.

The protective photo resist layer must be removed before starting deposition of SiN_x. As I noted above, the SiN_x for device DS6 was deposited by B. S Palmer. For DS8, H. Paik prepared the bottom Al layer using HD-PECVD and then deposited a low-stress SiN_x layer. [43]. The films were deposited at T = 300 °C at a pressure of 5 mTorr. The precursor gas flow rate of SiH_2 was set to 10 sccm and the rate of N_2 was similar to 10 sccm in this case.

4.4.2 Multi Layer Process and Etching

The nitride layer was patterned by dry etching using a Trion RIE in the Kim Building Fablab after the pattern was defined using optical lithography.

For this step, I used a negative resist (NR9-1500) to protect the SiN_x film and the bottom Al plates. I used the same photomask as the one for the bottom Al plates. Doing several UV exposures, a pattern (see Fig. 4.6) with a bit larger area than the capacitor was exposed to protect the layers below it. After developing the negative resist using RD6, I etched the exposed SiN_x in the RIE chamber [see Fig. 4.4(b)]. The etching rate for SiN_x using SF_6 gas was about 100 nm/min at a pressure of 150 mTorr and a power of 100 mW. I used SF_6 gas for etching because the gas made a smooth edge at the SiN_x layer, so the Al film could better cover the edge. For complete removal of the SiN_x film, about 1.5 minute of etching was sufficient. I later used a probe station [see Fig. 4.4(d)] to check the connectivity of the top aluminum layer over the SiN_x layer and I used the device only if the connectivity was okay.

Fabrication Steps for the Bottom Al Layer

1. Vent the chamber of the cryo-pumped evaporator in room 0219 using compressed nitrogen. I used the simple evaporation top because I only needed to deposit Al in one direction for the bottom layer of the capacitors.
2. Add Al shot to the Al basket and place the sample on the sample stage. Sometimes I put more Al shot in additional electrodes in case a basket failed.
3. Check if the sample shutter is closed, close the chamber top plate, and start rough pumping.
4. Wait until the pressure goes below 500 mTorr, close the roughing valve, open the main gate valve to the cryopump (high vacuum), and turn off the roughing pump.
5. About 1-2 hours later, check the pressure. If the pressure is at $< 2\text{x}10^{-6}$ Torr, prepare Al evaporation. If the pressure $> 2\text{x}10^{-6}$ Torr, then I evaporated some Al to help getter water.
6. Open the valves for the cooling water for the electrodes and crystal monitor.
7. Check if the display for the crystal monitor shows the correct program (#8) for Al, turn

on the electrode power and turn the voltage knob to the threshold voltage 2.3 V.

8. Every 30 sec, increase the electrode voltage by 0.05 V until the pressure or the current through the electrode goes up suddenly. It typically increases suddenly around 2.7 V (current: 20-25 A).
9. Increase the voltage slowly until the crystal monitor shows that Al is evaporating at more than 1.0 nm/s.
10. Open the shutter and simultaneously push the zero button of the display to check the thickness. Continue depositing Al and then close the shutter when the thickness of the Al layer reaches the desired thickness (40 nm).
11. Turn off the power to the electrodes and wait about 10 min for the electrodes to cool down.
12. Vent the chamber and take out the sample.
13. Close the chamber and turn on the roughing pump until the pressure reaches 500 mTorr.
14. Close the valves to the cooling water for the electrodes and the crystal monitor.

Fabrication Steps for Plasma Etch of the SiN_x Layer

1. Take the wafer to the Trion Plasma Etcher in the Kim Building cleanroom.
2. Set up the parameters for a SiN_x etch.
3. I etched using SF_6 gas for about 1.5 minutes.

4.5 Al/AlOx/Al Junctions

My dc SQUID phase qubits have two Josephson junctions, which I fabricated by depositing Al/AlO$_x$/Al tri-layers. In the past, Nb/AlO$_x$/Nb junctions were also used in our group, but we stopped using Nb junctions in qubits because they had consistently low coherence times [33, 39, 41]. There are several different fabrication processes that can be used to make Al/AlO$_x$/Al junctions. The preferred method is to deposit three layers in turn in an evaporator using a double-angle evaporation technique [85]. Another approach involves deposit an AlO$_x$ layer and a top Al layer after ion-milling the surface of a bottom Al layer. In order to avoid possible defects from the ion-milling process, I chose double-angle evaporation to make Al/AlO$_x$/Al junctions.

4.5.1 Double-Angle Evaporation

The key step in building a junction using double-angle evaporation is making the suspended resist bridge (see Fig. 4.7). To make a bridge, two kinds of resists are required. I used S1813 resist for the top layer and LOR30B resist for the bottom layer. LOR30B develops faster with a lower UV dosage than S1813 and this produces an undercut. This undercut allows all the LOR30B to be removed underneath a thin (≈ 2 μm) resist line of S1813. After the LOR30B layer under the S1813 bridge area is totally removed by the developer, the line “floats” above the substrate. Once the bridge pattern was obtained, Al films were deposited using double-angle evaporation to form Al/AlO$_x$/Al tri-layer junctions, as detailed in the following set of steps.

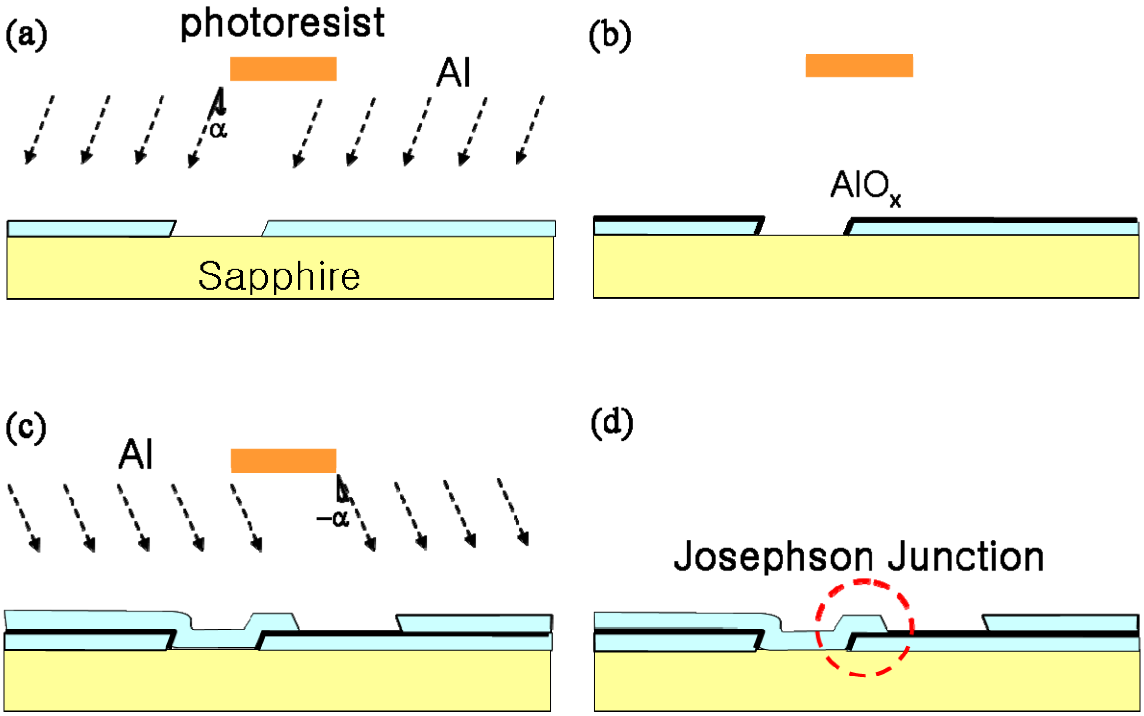

Figure 4.7: Schematic diagram of the double-angle evaporation process. (a) The first aluminum layer is deposited at a fixed angle α. The shadowed area is not deposited on the substrate due to the photoresist bridge. (b) By injecting oxygen gas, an AlO_x layer is formed on top of the aluminum layer. (c) The second aluminum layer is deposited at angle –α. (d) After liftoff, the process leaves a Josephson junction made of tri-layer $Al/AlO_x/Al$.

Fabrication Steps for the Al/AlO$_x$/Al Tri-Layer

1. Vent the chamber of the evaporator [see Fig. 4.4(b)] and prepare the ion-mill top.
2. Put Al shot in the Al wire baskets on electrodes #1 and #3 and mount the wafer on the sample stage. Also place additional Al shot in electrodes #2 and #4 in case one of the wire boats breaks.
3. Mark two angles on the sample stage with respect to the vertical. The angles vary from 25 to 40° depending on the junction size. I used 36° for DS8. Double-check the direction of the stage rotation. Set the stage to the first angle and align the deposition top with the front of the chamber.
4. Check if the shutter is closed and place the top on the chamber and start the rough pump.
5. Open the O_2 gas cylinder and the O_2 gas input valve of the chamber.
6. Turn on the O_2 valve for about 1 min to purge the O_2 lines.
7. Wait until the pressure drops to below 500 mTorr, and turn on the cryopump for high vacuum.
8. About 1-2 hours later, check the pressure and if the pressure is $< 2\times10^{-6}$ Torr, then start the deposition.
9. Open the cooling water valves for the electrodes and crystal monitor.
10. Check if the display shows the correct program (#8) for Al. Check that the #1 electrode is connected. Turn on the electrode power and turn the voltage knob to the threshold voltage of 2.3 V.
11. Every 30 sec, turn the knob up by 0.05 V until the pressure or the current to the electrode goes up suddenly.

12. Increase the voltage slowly until the crystal thickness monitor shows Al is evaporating at 1 nm/s or higher.
13. Open the shutter, simultaneously push the zero button of the crystal thickness monitor, deposit Al, and close the shutter when the thickness of the Al layer reaches 40 nm.
14. Let the wafer cool for 10 min.
15. Bleed in O_2 until the pressure goes up to about 5 Torr, close it and wait for for 10 min for DS8. I used 9 Torr for 8.5 min for DS6.
16. Turn on the high vacuum pump until the pressure is below $2x10^{-6}$ Torr.
17. Change the angle of the sample stage to the second angle (36° for DS8).
18. Deposit Al from electrode #3 following steps to 13 above.
19. Turn off the power and the ion gauge. Wait for about 10 min until the electrodes cool down.
20. Vent the chamber and take out the sample.
21. Close the chamber and turn on the rough pump. Wait until the pressure goes below 500 mTorr and then close the roughing valve and switch off the roughing pump.
22. Close all cooling water valves.

4.5.2 Oxidation and Critical Current

The double-angle evaporation includes an oxidation process to make an AlO_x layer for the tunnel barrier (see Fig. 4.7). After the bottom Al layer was deposited, oxygen gas was injected into the chamber at $P \approx 9$ Torr. The bridge size was typically about 2 μm × 2 μm and the thickness of the photoresist LOR30B making an undercut was about 2.6 μm. For device DS6, a 4 μm^2 qubit junction was deposited by using two deposition angles of ±45° and for device DS8, a 2 μm^2 qubit junction was deposited by using lower deposition angles of ±36°. The critical current density of the junction depends on the pressure and the time interval that the Al is exposed to oxygen gas. The critical current density varies inversely with the exposure (pressure×time) [86]. Following a recipe of H. Paik and T. A. Palomaki, I expected to have about 0.3 $\mu A/\mu m^2$ by using 18 Torr for 10 min. In device DS6, I obtained a critical current density of about 0.1 $\mu A/\mu m^2$ when I used 9 Torr for 8 min. In device DS8, I had a critical current density of about 0.04 $\mu A/\mu m^2$ with oxidation at 5 Torr for 9 min. These low current densities were probably due to a problem in the cryo-pump, but I was not able to sort out exactly what produced these low current densities.

4.5.3 Liftoff

The last step is to liftoff the Al films deposited during formation of the Al/AlO_x/Al tri-layer. The liftoff process is particularly important because it ends the lithographic process and if it fails, the patterns are ruined. PG remover is one of the chemicals I use for liftoff of the resist [87]. A relatively large amount of PG remover was needed because I used a thick LOR30B layer. It usually took about 1 hour to finish liftoff but sometimes it took longer than that. After the liftoff process, I cleaned the wafer using acetone, methanol and isopropanol to remove any residue.

Fabrication Steps for Liftoff of a Positive Photoresist

1. Prepare PG remover in a clean beaker that is large enough to hold the wafer.

2. Soak the wafer in the PG remover and heat it to 60 °C on a hot plate.
3. About 1 hour later, replace the remover with a fresh solution and resume for another 1 hour.
4. Dry the sample with N_2 gas.
5. Seal the sample with a layer of photoresist to protect the devices (the sample oxidizes “immediately” on exposure to air and water vapor).

Fabrication Steps for Liftoff of a Negative Photoresist

1. Remove the resist using a resist remover RR4 at 110 °C, PG remover at 80 °C, or acetone at room temperature.
2. Clean the wafer using solvents and water, and bake the wafer to evaporate water at above 100 °C.
3. Dry the sample using N_2 gas.

4.5.4 Wire Bonding

Instead of making bridges to connect the lines for the LC filter (see Fig. 4.2), I used aluminum wire bonds. This simplified the fabrication process. It was not always so easy to make wire bonds because the patterns are small and the bonding foot was relatively large ($\approx 50 \times 50\ \mu m^2$).

Steps for Wire Bonding

1. Remove the resist on top of the sample using acetone and blow dry with N_2 gas.

2. Place the chip on the sample stage of the K&S Model 4523 wire bonder [see Fig. 4.4(c)] in room 0205C and check Al wire is being used.
3. Raise the tool lever.
4. Select 2nd mode to handle the lever without bonding.
5. Change the control lever option from semi-auto to manual.
6. Increase the height of the chip until it is a little bit below the bonding height.
7. Pull down the tool lever.
8. Control the height of the chip and turn the sample stage while pushing down the control lever and looking at the chip through the microscope.
9. Set the height so that the tip is almost touching the surface of the chip.
10. Change to the 1st mode and select options with optimized parameters and check the loop dial number for the bonding height.
11. Start pushing the control lever to make a bond for the first foot. If the bond does not stick to the surface, change the height and parameters of the bonding force and time.
12. After the first bond, move the sample stage with the left hand mouse (in only the up and down direction) and set the new bonding place.
13. Push the lever and make a second bond. Check that the bonds are stuck well to the surface by touching the wires very gently.

4.5.5 Wafer Dicing

The wafers were diced into 5 mm×5 mm pieces at LPS using a dicing machine with a diamond saw. In order to protect the qubits, the wafer was covered by S1813 photoresist.

4.6 Parameters for Devices DS6 and DS8

Table 4.1 and 4.2 give the design values and measured values of key parameters of device DS6 and DS8 respectively. Some of the actual parameters were quite different from my design values due to fabrication problems I encountered.

For example, the qubit junction in device DS8 was designed for a critical current density of 0.3 μA/μm^2, but the actual device had 0.04 μA/μm^2. This was probably due to a problem with the cryogenic pump used during the oxidation process. Although there was a significant discrepancy between the values for these design parameters and the measured parameters, I obtained good results from these devices and they worked as qubits.

Table 4.1: Design and measured values of parameters for dc SQUID phase qubit DS6.

Element	Size (μm x μm)	Design Value	Measured Value
Bond Pad	300 × 300	-	-
I_{01}	2 × 2	1 μA	0.50 μA
I_{02}	2 × 10	5 μA	2.46 μA
L_1	400 × 400	1.5 nH	1.2 nH (L_1+L_{J1})
L_2	10 × 20	20 pH	30 pH (L_2+L_{J2})
C_1 (=C_J+C_x)	2 × 2 (C_J), 30 × 50 (C_x)	1 pF	1.08 pF
$C_{\mu w}$	-	1 fF	not measured
M_Φ	-	1 pF	2.5 pF

Table 4.2: Design and measured values of parameters for dc SQUID phase qubit DS8.

Element	Size (μm x μm)	Design Value	Measured Value
Bond Pad	300 × 300	-	-
I_{01}	2 × 1	1 μA	0.077 μA
I_{02}	2 × 10	10 μA	1.365 μA
L_1	400 × 400	1.5 nH	1.5 nH (L_1+L_{J1})
L_2	10 × 5	5 pH	60 pH (L_2+L_{J2})
C_1 (=C_J+C_x)	2 × 1 (C_J), 45 × 65 (C_x)	1 pF	0.88 pF
$C_{\mu w}$	-	1 fF	not measured
M_Φ	-	1 pF	1.53 pF

4.7 Summary

In this chapter, I discussed how I selected some of the parameters for the devices and explained how I fabricated my qubits. Two devices DS6 and DS8 were successfully fabricated in the cleanroom. Both devices were made using optical lithography to build Al/AlO$_x$/Al junctions on a sapphire substrate. Specific fabrication steps were presented. The parameters of both devices match the designed values reasonably well except that the actual critical currents which were two times smaller than the design in device DS6 and about 10 times smaller than designed in DS8.

Chapter 5

Experimental Setup

5.1 Introduction

In this chapter, I describe the experimental arrangements I used for making measurements on devices DS6 and DS8. I first describe the cryogenic parts of the apparatus, I then discuss the electrical wiring, and finally I describe the techniques I used for making measurements on the qubits.

For device DS6, the electrical setup was similar to what T. A. Palomaki [42] used previously for measuring his phase qubits. For device DS8, I modified the microwave setup to allow me to measure spin-echos, Ramsey fringes and state tomography; the group had not been able to do spin-echo or tomography measurements before because of the short coherence times in our previous devices.

One of the basic requirements for doing the experiments was to get the devices cold enough. Clearly, the operating temperature needed to be less than the critical temperature $T_c \approx 1.2$ K of the aluminum that I used to construct my qubits. While cooling the device to $T << T_c$ does reduce loss due to quasiparticles, the main reason I needed to cool to mK temperatures was to reduce thermal noise that causes excitation and relaxation of the qubit. In particular, the thermal energy k_BT should be much lower than the qubit energy level spacing hf_{01}; for a qubit 0-to-1 transition frequency of f_{01} = 3 GHz, one finds that T should be much less that 140 mK.

5.1.1 Operating Procedure for the Refrigerator

To test devices DS6 and DS8, I used an Oxford Instruments TLE 200 dilution refrigerator (see Fig.5.1). This refrigerator has been used for more than 15 years in our group; it was used previously by A. Berkley, H. Xu, H. Paik, S. K. Dutta and T. A. Palomaki for most of their phase qubit work [42, 47, 50-52]. The cooling power of this refrigerator is about 200 μW at 100 mK and it settles to a base temperature of less than 20 mK. In fact, for my experiments, thermometer R7 on the mixing chamber indicated slightly lower than 20 mK most of the time. To maintain the system, every four days I had to fill the outer dewar of the refrigerator with 100 L of liquid ^{4}He.

The specific procedure I used for operating this dilution refrigerator has been described by T. A. Palomaki [42] and can be summarized as follows:

Preparation for Cool-down

1. Clean the ^{3}He/^{4}He mixture by circulating it through the nitrogen trap.
2. Check the resistances of the sample electrical lines.
3. Ground the bias lines (and myself to protect the device) and mount the sample box on the cold stage of the refrigerator.
4. Verify electrical connection to the sample by measuring the resistances of the lines to the sample with the multimeter set on the 40 kΩ scale.

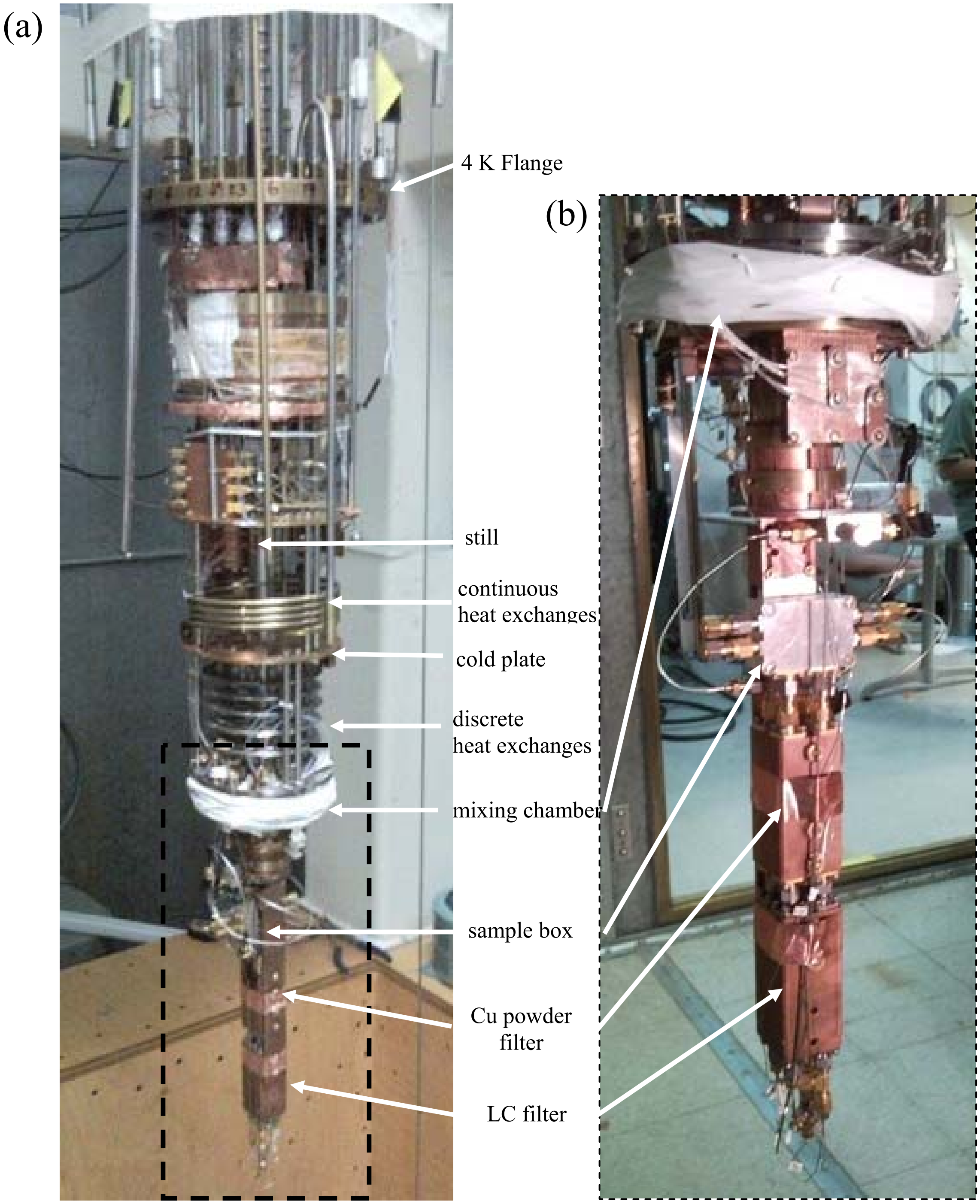

Figure 5.1: (a) Photograph of the beta refrigerator, a Model 200 TLE Dilution Refrigerator by Oxford Instruments with LC and copper powder filters. (b) Detailed view of the dashed area in (a) from opposite direction.

5. Attach the inner vacuum can.

6. Pump out the can to a pressure of 10^{-5} Torr.

7. Leak test the 1 K pot with a ^{4}He leak detector.

8. Check the ^{4}He needle valve for the 1 K pot.

9. Pump out any residual gas in the dilution unit (if the unit was properly warmed up, this will be just air or water vapor and it should not be sent back to the keg or it will just contaminate the mixture again).

10. Leak test the dilution unit.

11. Check impedance of the mixture flow in the dilution unit (condenser line pressure should increase by about 10 mbar in 5 minutes).

12. Leak test the can and the refrigerator top connectors.

13. Set up the magnet.

14. Check that the heaters and thermometers are functioning properly.

15. Attach the transfer siphon.

Cool to 77 K

1. Raise the dewar.

2. Leak-test the vacuum can by filling the bath space with ^{4}He gas.

3. Flush the 1 K pot and leave pressurized with ^{4}He at over 1 atm.

4. Start transfer of liquid N_2 with L-tube seated.

5. Stop pumping on the vacuum can with the leak detector.

6. Insert ^{4}He exchange gas into the vacuum can at a pressure of 1 mbar.

7. Continue transferring liquid N_2.

8. Stop transfer when thermometer resistor R2 reaches 83 Ω indicating that liquid N_2 fills the dewar.
9. Re-check the electrical conductivity of the device lines.
10. Wait about 12 hours for system to cool to 77 K.

Preparation for ^{4}He transfer

1. Pump out the helium exchange gas from the vacuum can.
2. Seat the L-tube and pressurize the bath with N_2 gas to pull out liquid until no liquid is coming out.
3. Leak-test the dilution unit.
4. Leak-test the bath filling by ^{4}He gas.

Cool to 4 K

1. Start slowly transferring liquid ^{4}He with the L-tube.
2. Keep liquid ^{4}He transfer going until thermometer resistor R1 reaches 19 Ω.
3. Pump out the exchange gas when resistor thermometer resistor R1 is near 20 Ω.
4. Stop the ^{4}He transfer when the level-meter shows the dewar is full.
5. Re-check the electrical conductivity of the device lines.

Condensation of ^{3}He/^{4}He mixture

1. Start water chiller for ^{3}He main circulation pump.
2. Leak-test the dilution unit.
3. Start running the 1 K pot.

4. Start condensing the ^{3}He/^{4}He mixture.

5. Turn off all electronics inside the screen room.

6. Finish condensing when R7 is above 5 kΩ.

7. Re-check the electrical conductivity of the device lines.

Calibrated resistance thermometers are mounted on each stage on the refrigerator. While the system is cooling down, I checked the thermometers regularly to verify that the temperature of each part of the refrigerator was changing as expected. If there is a leak or an unintended thermal short, the temperatures of the different stages will often provide the first indication of a problem.

The values of the thermometers are measured using a Picowatt AVS-47 resistance bridge. Thermometer R7 is generally the most important because it indicates the temperature of the mixing chamber. The R7 thermometer is made of RuO_2 and works down to about 20 mK. The Picowatt bridge measures the resistance of the thermometer using a 4-point technique and converts this value to a temperature using [51]

$$\ln(T) = -7.98 + \frac{53.2}{\ln(R)} + 354\frac{\ln(R)}{R} \tag{5.1}$$

where T is in kelvin and R is the resistance in ohms.

The refrigerator also has a superconducting NbTi magnet mounted on the outside of the vacuum can, although I did not use it in my experiments. This magnet can produce a vertical magnetic field of strength 11.13 mT/A at the location of the sample box.

The procedures for a normal operation and warm-up are summarized in the following:

Normal operation

1. Main circulation pump and Roots blower are running.
2. Pressure at still ≈ 0.6 mbar, still temperature ≈ 0.6 K, cold plate temperature ≈ 100 mK, mixing chamber temperature ≈ 20 mK and still power ≈ 15 mW.

Cleaning the cold traps

1. Stop circulation by turning off the Roots blower and closing the condenser valve.
2. Save the mixture in the gas panel by closing the valves except for the panel area.
3. Open the trap connection valve and collect the mixture in the nitrogen trap.
4. Isolate helium trap area and collect the mixture.
5. Take out the liquid nitrogen trap, warm up and pump it out.
6. Pull out the helium trap, warm it up and pump it out.

Pulling the mixture

1. Stop circulation by turning off the Roots blower and closing the condenser valve.
2. Heat the refrigerator by turning on MXC heater to 2 mW and Still heater to 50 mW slowly.
3. Pump out the can to protect any thermal shock during the warm-up.
4. Heat the mixing chamber a bit more (MXC heater at 20 mW) to remove mix.
5. Pump out the condenser line.

Warming up

1. Make sure mixture has been removed.

2. Stop the pot and pot heater.
3. Blow out the helium bath with helium gas.
4. Drop the μ-metal shield and then the dewar.
5. Let the fridge warm up and for about a day, add some exchange gas to speed up the process.
6. Remove the vacuum can when the fridge is above freezing.

5.1.2 Shielding, Wiring and Filters

The system has several layers of protection to minimize the impact of external vibration, magnetic field noise and radio-frequency interference. All of the leads going to the device are heavily filtered. The qubits are mounted in a superconducting aluminum box [see Fig. 5.2(c)] to shield out rf interference and magnetic field fluctuations. The refrigerator has copper heat shields at 4 K and 0.7 K [see Fig. 5.2(b)] and a stainless steel vacuum can that also contribute to the shielding of rf interference and magnetic field fluctuations down to a few Hz. The outer part of the dewar is aluminum and this also acts to shield the refrigerator from external rf noise and magnetic fields at audio and higher frequencies. To reduce the magnetic field at the mixing chamber, a μ-metal shield of thickness ≈ 1 mm, diameter ≈ 0.6 m and height ≈ 2 m surrounds the dewar. The refrigerator and some of the readout amplifiers are enclosed in a double-wall shielded room [see Fig. 5.2(a)] from Universal Shielding Corporation and to further reduce external rf interference, the entire experiment is located in a basement lab in the physics building.

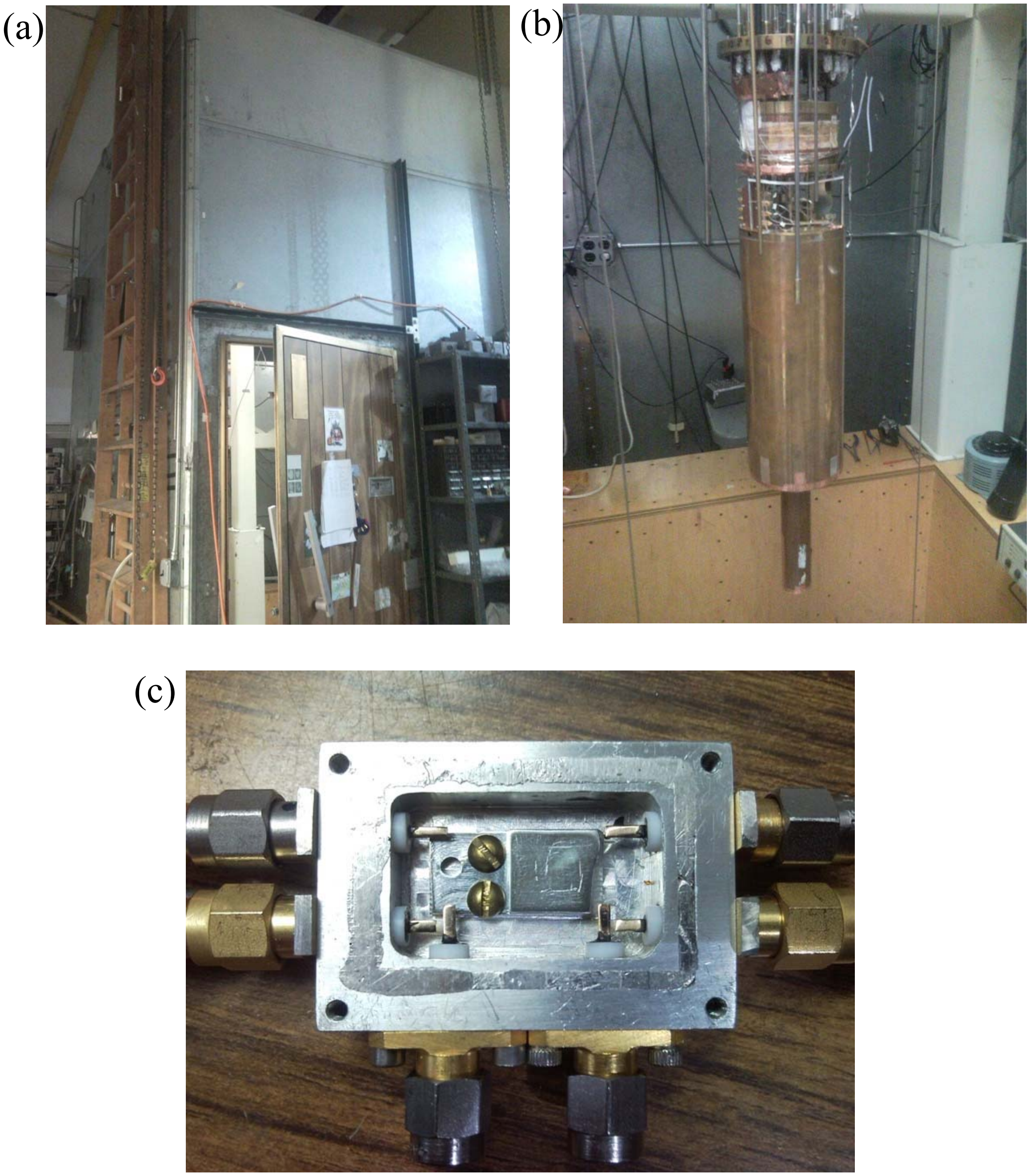

Figure 5.2: Photographs of (a) Double-wall shielded room from Universal Shielding Corporation, (b) copper heat shields and (b) superconducting aluminum sample box.

Figure 5.3 shows a schematic diagram of the wiring and filters in the refrigerator. In order to measure the devices, four main lines are used: the current bias line, the flux bias line, the voltage readout line, and the microwave line. For the microwave line, a single continuous section of UT-34-SS-SS coax is used to avoid impedance mismatch and frequency-dependent response from the line. It is made of stainless steel and it is connected from the top of the refrigerator to the mixing chamber with thermal grounds at stages in between (see Fig. 5.3).

The other lines have several stages, starting at a room temperature. Going through the wall of the shielded room, the cables pass through a π-filter with a cutoff frequency of 20 kHz. For the current- and flux-bias lines, the line is sent to an AMP03 differential amplifier. This buffer amplifier isolates the ground of the voltage source from the ground of the dilution refrigerator. Resistors are located between the buffers and a set of switch boxes [see Fig. 5.4(a)]. Small currents (about 1 to 10 μA) sent to the devices go through bias resistors on the current bias line (100 kΩ) and on the flux bias line (2 kΩ). The switch boxes allow the bias lines to be connected to the ground of the refrigerator when they are closed to protect the device from electrostatic discharge.

The second stage for the lines goes from the top plate of the refrigerator insert (at 300 K) to the 1 K pot (see Fig. 5.3). The top part of the current bias line is made of coated manganin wires that connect an SMA connector box on top of the refrigerator to a 4 K patch box just above the 1 K pot. The manganin wires are twisted pairs, but only one wire in each pair is used for the measurement. The top part of the flux line and the voltage line is made of LakeShore CC-SR-10 coax, from the 300 K SMA connector box to a 0.7 K patch box (see Fig. 5.3). To minimize heating in the flux line, LakeShore CC- SR-10

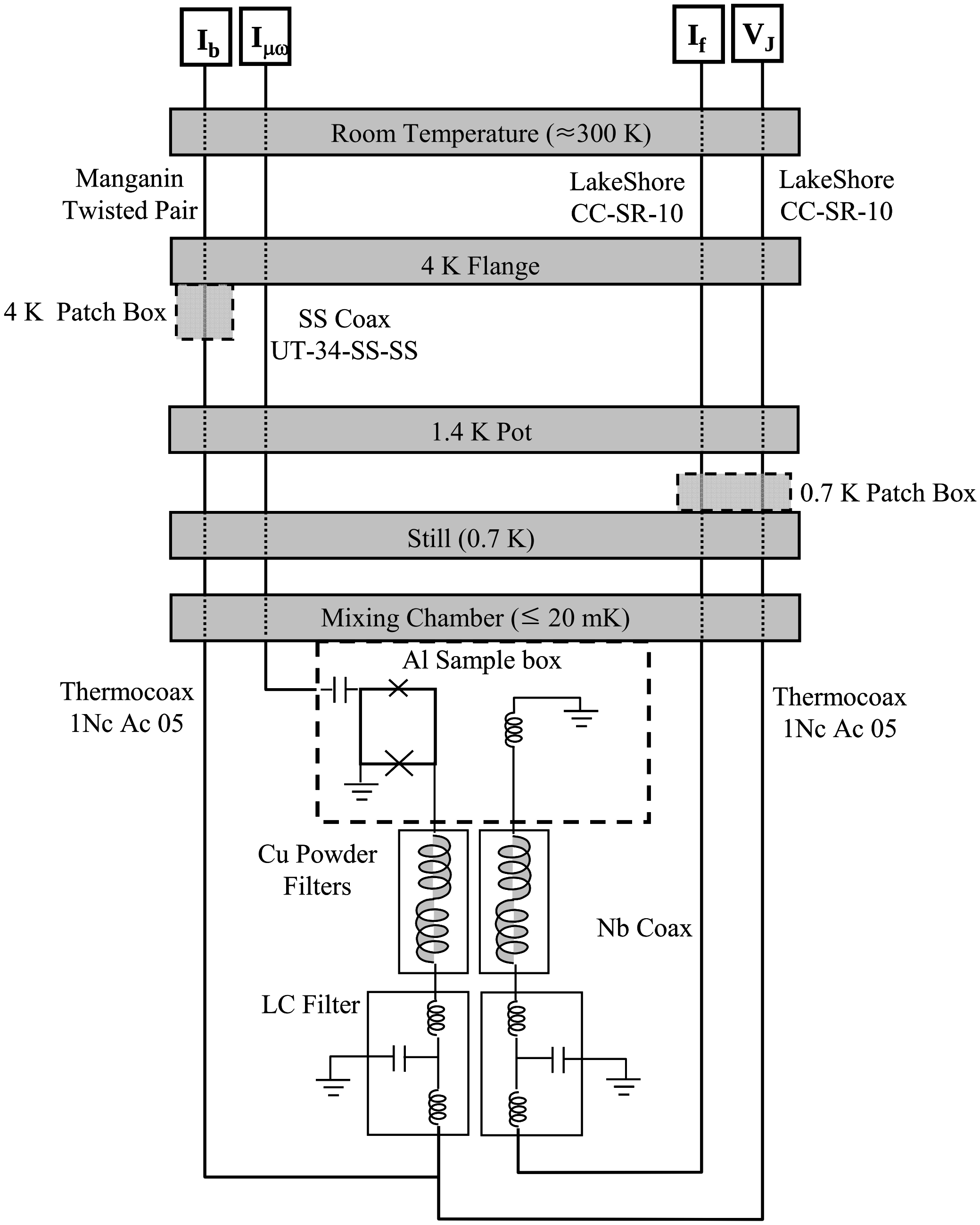

Figure 5.3: Schematic of refrigerator wiring. I_b is the current bias, $I_{\mu\omega}$ is the microwave current, I_ϕ is the flux bias and V_J is the junction voltage. In the patch boxes, the wires are thermally connected to a stage of the refrigerator. Some of the lines are commercial coaxial cable (*e.g,* thermocoax) while others were hand-made co-axial lines (*e.g.* Nb coax).

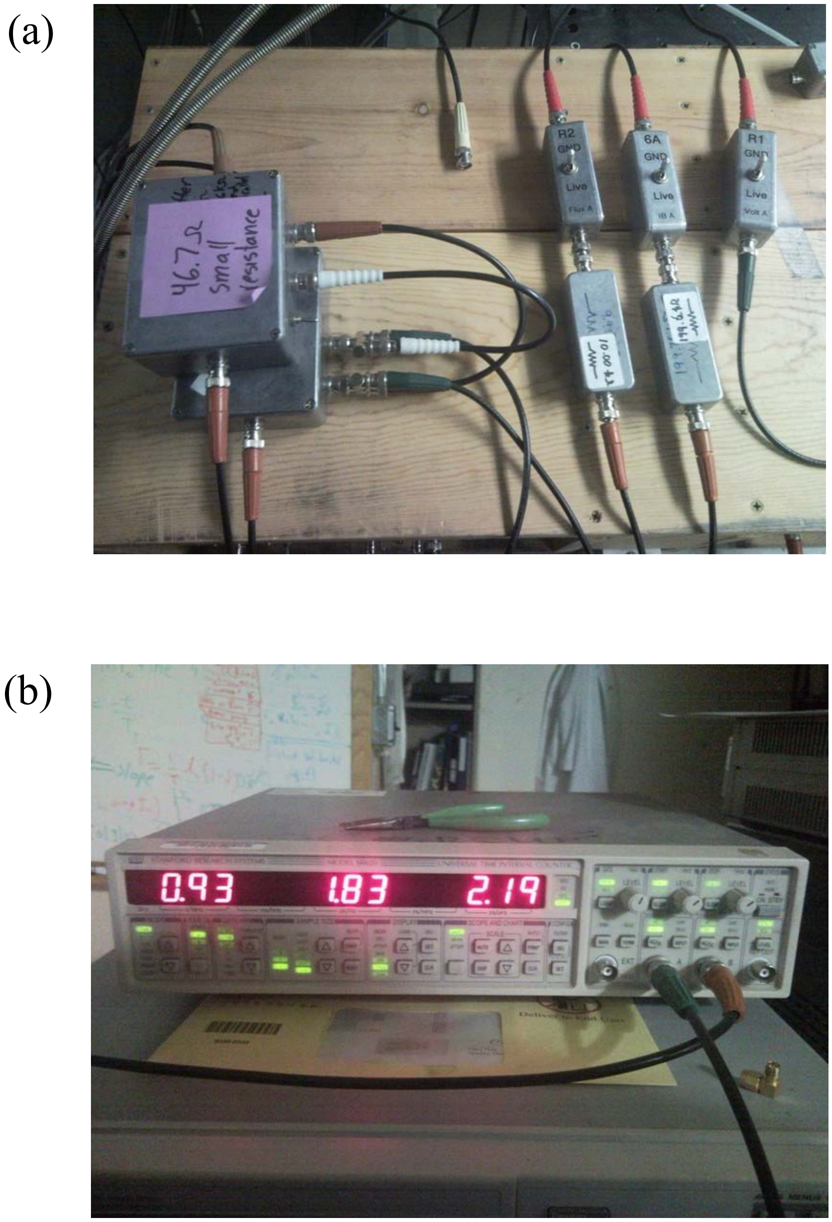

Figure 5.4: (a) Photograph of the bias resistors located between a home-made buffer and switch boxes. (b) Photograph of Stanford Research Systems SR620 Universal Time Interval Counter.

coax, which has a low resistance (8 Ω) with about 1 m length and a thermal conductivity of 0.0016 W/cm K at 4.2 K was chosen. At the patch box, the lines are thermally anchored to the still plate which has a relatively high cooling power.

A Thermocoax (1 Nc Ac 05) [88, 89] cable is used for both the current and voltage bias lines between the 1 K pot and the mixing chamber. This line has a stainless steel (304L) jacket with a thickness of 0.15 mm, the center wire is 80:20 NiCr alloy with a diameter of 0.17 mm and the dielectric is MgO. This type of Thermocoax is now commonly used at low temperature to provide high attenuation at microwave frequencies. The current line and voltage line are connected each other at the LC and powder filters, which are attached to the mixing chamber (see Fig. 5.3). Between 4 K and the LC filter (at the mixing chamber), the flux line is a homemade "niobium coax" (see Fig. 5.3). It is threaded through Teflon tubing inside a stainless steel tube. Because only slow signals are applied to this line, impedance mismatch is not an issue.

The LC and a copper powder filters are located beneath the sample box attached to the mixing chamber [see Fig. 5.1(b) and Fig. 5.3]. The LC filter is an L (3.3 mH) – C (100 pF) – L (3.3 mH) T-filter [50] with a 3dB cutoff of 10 MHz. Copper wire is used to ensure thermal contact. The copper powder filter [90] uses a 50:50 mix of Stycast and 200 mesh copper powder, molded into a copper tube. The 75 μm diameter niobium wire with a copper cladding was wound around the powder core. Because Nb becomes superconducting below 9 K, negligible heating is produced in the meter long wire wrapping the core.

5.2 Measurement Instruments

When I started doing measurements, I initially used a Dynatech Exact Model 628 as a master clock to generate a repetitive signal with a frequency of between 100-1000 Hz; I mostly used a frequency of 700 Hz. I used this timing signal to trigger a saw tooth ramp voltage signal with a frequency of 1 kHz produced from an Agilent 33120A Arbitrary Waveform Generator (AWG). The frequency of 1 kHz is fast enough for the measurement and low enough for passing through the π-filter on the screen-room wall. Also, compared to the ramp frequency of 1 kHz, a reference frequency of 700 Hz is slow enough to allow the qubit to re-initialize after a measurement. The output pulse from the master clock was usually sent to the Agilent 33120A AWG via an opto-isolator (to prevent ground loops) and also to an SR620 timer that is used to detect the junction switching signal (see Fig. 5.5). In addition to the clock, there are many other instruments used in the measurement (see Table 5.1 and Fig. 5.5). I briefly discuss several key instruments in this section.

5.2.1 Low-noise Amplifier

I used a low-noise amplifier to boost the switching voltage signal even though this signal is relatively large (350 μV for Al junctions). A very low noise and relatively large bandwidth are only necessary for doing a traditional escape rate measurement [22, 30], while this is much less important for the pulsed current measurements [33, 91]. Never the less, the voltage output from the qubit was amplified using a 16-JFET amplifier built by our group [50]. The voltage noise of a JFET is mainly caused by Johnson noise in the channel. The voltage noise from N parallel JFETs is $1/\sqrt{N}$ of a single JFET. Using 16

JFETs, the amplifier achieves a gain of 40 and a voltage noise of less than $0.3\,\mathrm{nV}/\sqrt{\mathrm{Hz}}$. The bandwidth of the JFET amplifier is about 3 MHz and its current noise is less than $1\,\mathrm{pV}/\sqrt{\mathrm{Hz}}$. The output of the JFET amplifier is fed to a second-stage amplifier that was also developed in our group [50]. This amplifier used an AD797 or AD829 op-amp, and has a gain of 50 and a bandwidth of 1 MHz. The input noise of the AD797 is about $4\,\mathrm{nV}/\sqrt{\mathrm{Hz}}$. The combined two-stage amplifiers yield a gain of 2000, an input voltage noise of $0.4\,\mathrm{nV}/\sqrt{\mathrm{Hz}}$ and a bandwidth of about 2 MHz.

Table 5.1 Commercial electronics used in my experiments.

Function	**Instrument**
I_b, I_ϕ	Agilent 33120A Arbitrary Waveform Generator (AWG), Opt. 001
Master Clock	Dynatech Nevada Exact 628 Function Generator
Timer	Stanford Research Systems SR620 Universal Time Interval Counter, Opt. 01 [see Fig. 5.4(b)]
Amplifiers	Stanford Research Systems SR560 Low-Noise Amplifier
Pulse Generator	Stanford Research Systems DG 535 Digital Delay Generator, Opt. 01
Microwave Generator	Hewlett-Packard 83731B Synthesized Signal Generator Hewlett-Packard 83732B, Opt. 1E1, 1E2, 1E5, 1E8, 1E9, 800
GPIB	National Instruments PCI-GPIB
DAC/ADC	National Instruments PCI-6110 Data Acquisition Card & BNC-2110 BNC Connector Block
Temperature	Picowatt AVS-47 resistance bridge
Oscilloscope	Tektronix TD7404B

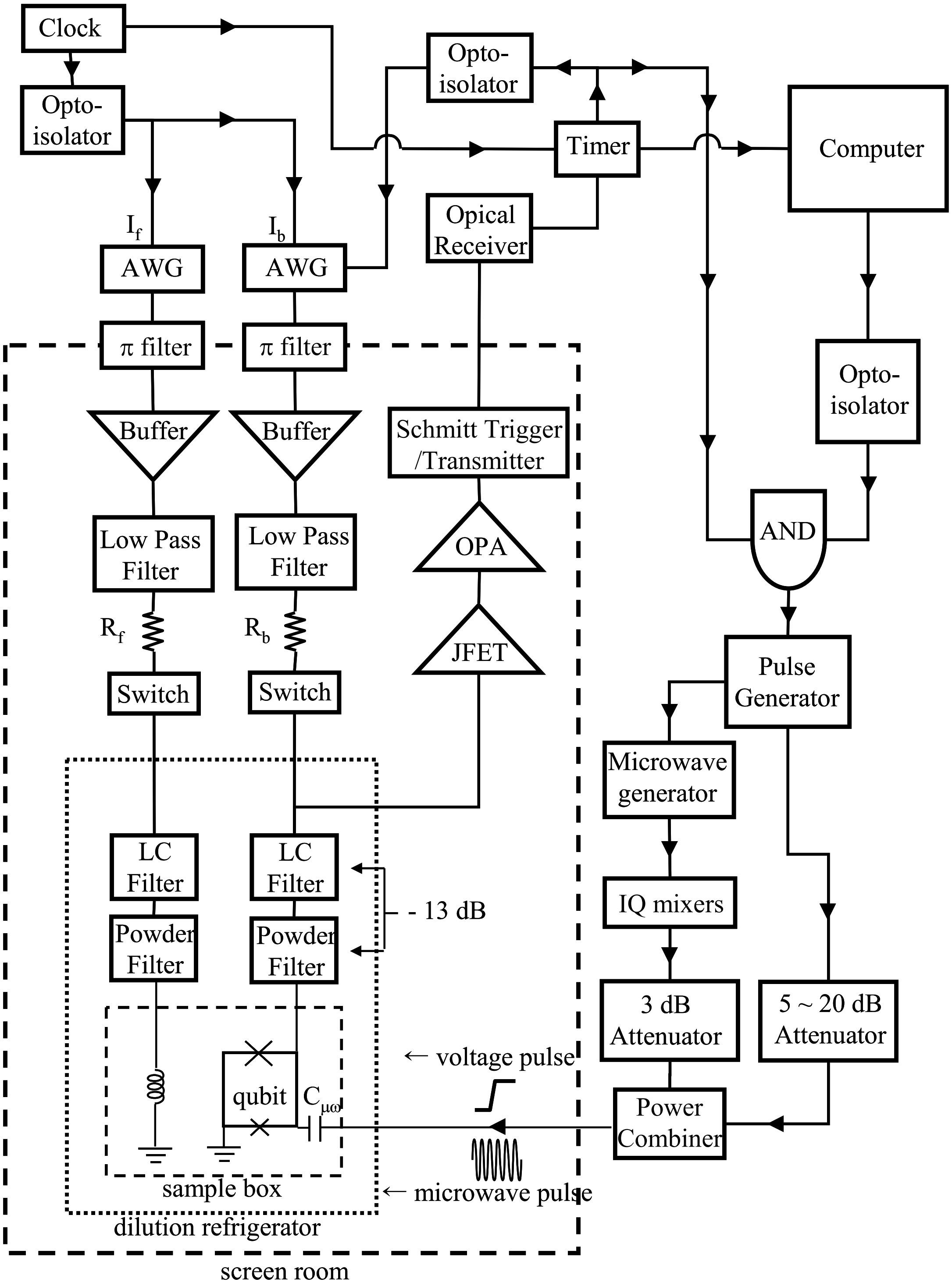

Figure 5.5: Overview of experimental set-up for a typical measurement.

5.2.2 Arbitrary Waveform Generator and Pulse Generator

To supply a current or voltage bias, I used an Agilent 33120A Arbitrary Waveform Generator (AWG). A reference pulse coming from the Dynatech master clock is sent to the SYNC input of the AWG. The SYNC front panel output of the AWG is connected via an opto-isolator to input A of the SR620 timer. I typically set the input trigger level to trigger at the maximum value of the slope. The signal of the AWG was set to burst mode, single trigger, and arbitrary waveform. Using a Labview program, the desired waveform was drawn and the waveform information sent to the AWG to make the desired voltage signals. Usually, the repetition frequency of the signal from the AWG was set to 1 kHz. At 1 kHz, the accuracy of the amplitude is ±0.1 % of the specified output and so, 1 to 2 Volts peak to peak produced an uncertainty of ±1 mV.

I used a Stanford Research Systems DG 535 Digital Delay Generator to generate a square pulse signal which was sent to the qubit via the microwave line for pulsed state measurements (see section 5.3.2). This pulse also set the timing of the microwave signal. To control the timing using the computer, an opto-isolated 5 V pulse from a DAC (connected to the computer) was combined with an input pulse from the timer through an AND gate (see Fig. 5.5). The output of the AND gate triggered the DG 535 pulse generator to initiate the pulse signal. To modulate the microwave signal, a TTL pulse with high Z-load was sent from the pulse generator. For a measurement pulse going directly to the device, a high Z-load is also set and a VAR pulse with a modifiable voltage output was used to control the amplitude of the signal. The rise time of the square signal pulse was 2 ns in my measurements because I used the lower voltage output range on the pulse generator. The jitter time of the signal was about 200 ps. With the short rise time, I could create a short current pulse in the qubit by sending a step-function signal to the small on-chip capacitor $C_{\mu\omega}$ that couples the microwave line to the device (see Fig. 5.6).

5.2.3 Microwave Source and Mixers

I used an HP83732b microwave source to generate current $I_{\mu\omega}$ in the 3.5 GHz range to excite the qubit. This source has a frequency resolution of 1 Hz and a fractional drift per day of 1.5×10^{-9}.

For state tomography measurements, I used Marki Microwave mixers M8-0412 and IQ-0318 [92] (see Fig. 5.7). The output of the Marki mixers is controlled by an I port. The output of the IQ mixers is controlled by two ports, I and Q, which modulate the in-phase and out-of-phase amplitude. An input microwave signal must also be sent to the LO port. I sent only dc signals to the I and Q ports to modulate the phase of the signal. The phase of the output signal is then determined by

$$\phi(t) = \tan^{-1}\left[\frac{I(t)}{Q(t)}\right]. \tag{5.2}$$

Two critical disadvantages of the mixers are leakage of the signal and the need to carefully calibrate the output versus frequency and amplitude. Ideally, if there is no signal from the I and Q ports, then the output should not have any signal, but some signal is transmitted through the mixers and this leakage signal needed to be corrected to properly control the state of the qubit.

In order to calibrate the phase of the microwave signal going out from the mixers, I checked the phase difference between the input signal and the output signal using a

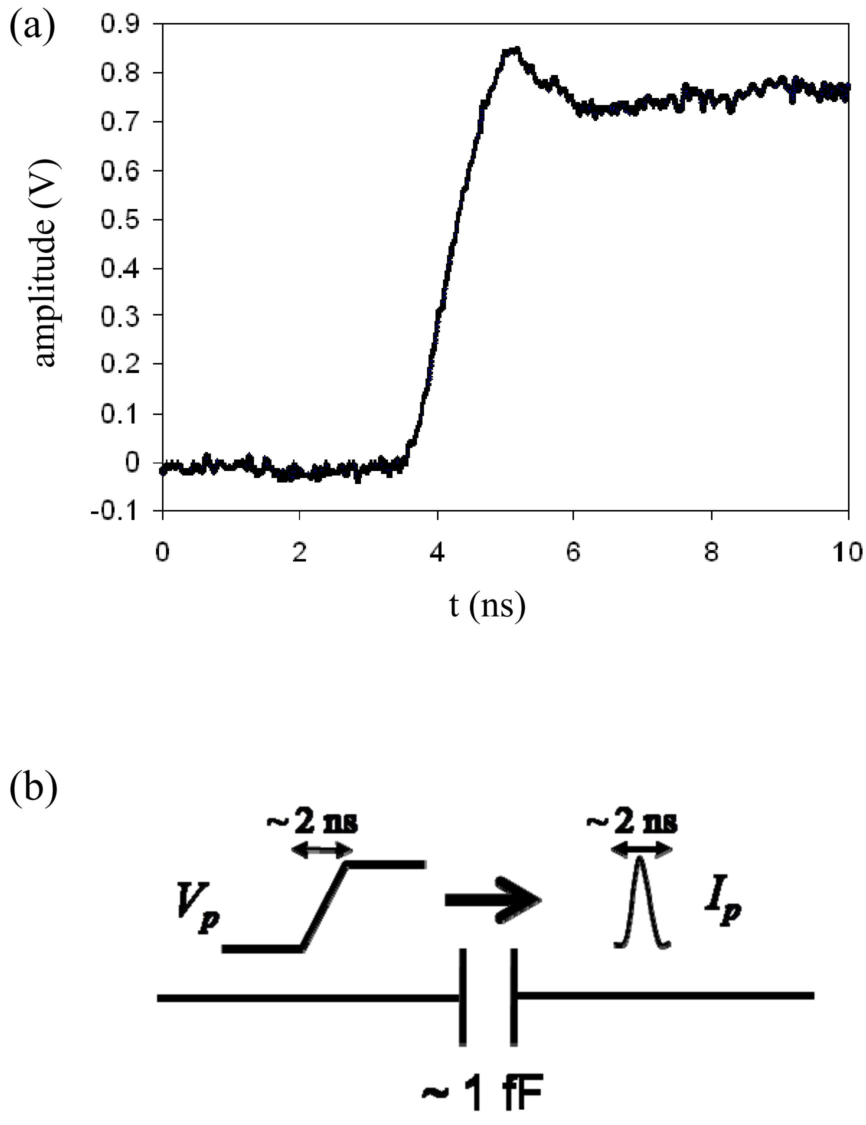

Figure 5.6: (a) Voltage pulse observed by an oscilloscope. The voltage amplitude was about 0.8 V in this case and the pulse has small ripples near the step. The ripples get worse at lower voltage amplitude, which were typically used for measurements. (b) The voltage pulse transforms to a current pulse after passing through the small capacitor $C_{\mu\omega}$ on the microwave line (see Fig. 5.5).

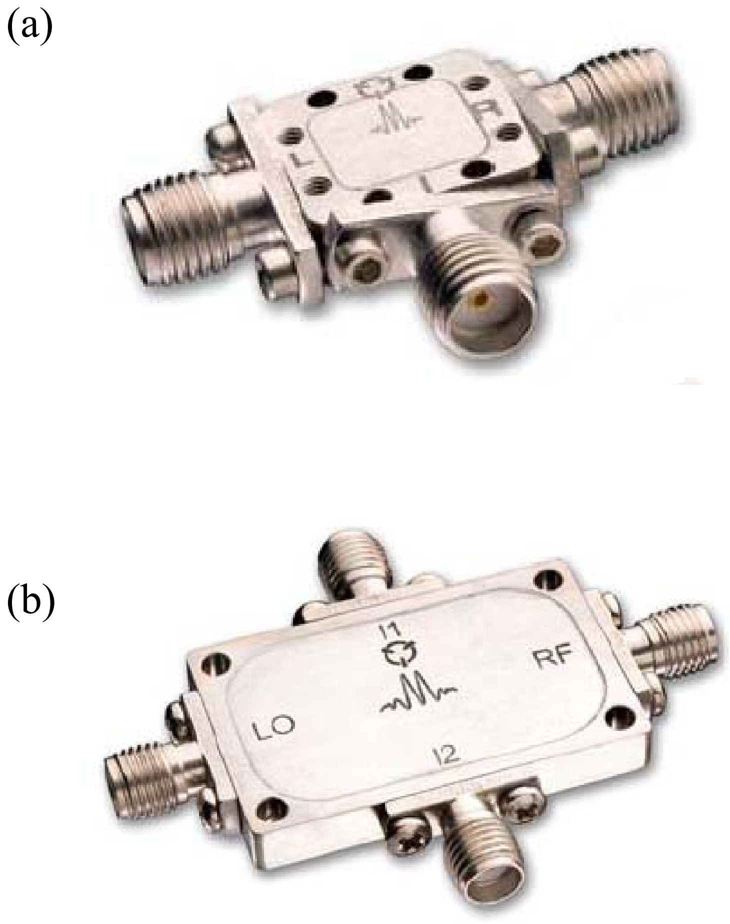

Figure 5.7: Photographs of Marki microwave mixers. The model numbers were (a) M8-0412 and (b) IQ-0318. M8-0412 was used to control the length of the microwave pulses and IQ-0318 was used to control the amplitude of the microwave pulses for state tomography.

Tektronix TDS7404B oscilloscope. Because its resolution was much better than 1 ns, I could observe the output phase directly. I adjusted the input level at the I and Q ports of the IQ mixer to achieve an accurate phase at the output. This was done by hand.

I controlled the duration of the microwave pulse by using a M8-0412 mixer first and controlled the phase between two signals by using an IQ-0318 mixer (see Fig. 5.8). Additionally, use of two mixers reduced leakage more than one mixer. In order to reduce noise and out-of-band components from the mixers, I used a VLF5000 (5 GHz) low-pass filter and a VHF1300 (1.3 GHz) high-pass filter after the mixers.

5.2.4 Filters, Attenuators and Power Dividers

There are no electrical elements on the microwave line inside the refrigerator, but I added filters and attenuators outside of the refrigerator. The square voltage signal from the DG535 pulse generator has a short (2-3 ns) rise time and there is a small voltage ripple right after the rising slope (see Fig. 5.6). I used a Mini-Circuits SBLP-200 low-pass filter to remove some high frequency components of the voltage signal. In addition, the amplitude of the voltage signal from the DG535 pulse generator was too large for me to use directly to generate qubit switching. So, I attached 5 to 20 dB attenuators to reduce the amplitude of the output signal from the pulse generator (see Fig. 5.5). I used a HP116678 power divider (used as a combiner) to combine the microwave signal and the square pulse signal and feed them to the microwave line.

5.3 Measurement Setup

My measurement setup is based on that developed by S. K. Dutta and T. A. Palomaki [42, 51]. They were not able to do some types of measurements (*e.g.* spin-echo) because of short coherence times. Also, I did not need to do a flux shaking to initialize the flux state of the SQUID because my SQUIDs only had one stable flux state. The basic set-up I used for the measurements is shown in Fig. 5.8.

5.3.1 I-Φ Measurement

One of the first measurements I would make was to find how the switching current depended on the applied flux. I used a Labview routine to set the maximum current in a linear ramp generated by the AWG. I next checked how much current I_Φ^{max} on the flux bias line was required to put one flux quantum in the SQUID loop. I chose the voltage step size for the current and the flux bias after considering the measurement time and the resolution I needed an I-Φ graph. If fine steps ($\Delta\Phi \approx 0.08\ \Phi_o$) are used, it took about a half day for a bias range of a couple of flux states.

Measuring the I-Φ curve at the beginning was useful for checking whether the device was okay. The I-Φ also provided basic information about when the device switched and I could use it to set the bias current I_b and flux bias I_ϕ. The maximum bias current when the device switches is very close to $I_{01}+I_{02}$ and the minimum bias current is very close to $I_{01}-I_{02}$ (see Fig. 6.1 and Fig. 6.10). The value of L_1 is given by one over the slope of the isolation branch and M_ϕ can be found from the periodicity of the branches. By varying I_b and I_ϕ, the transition frequency was tuned.

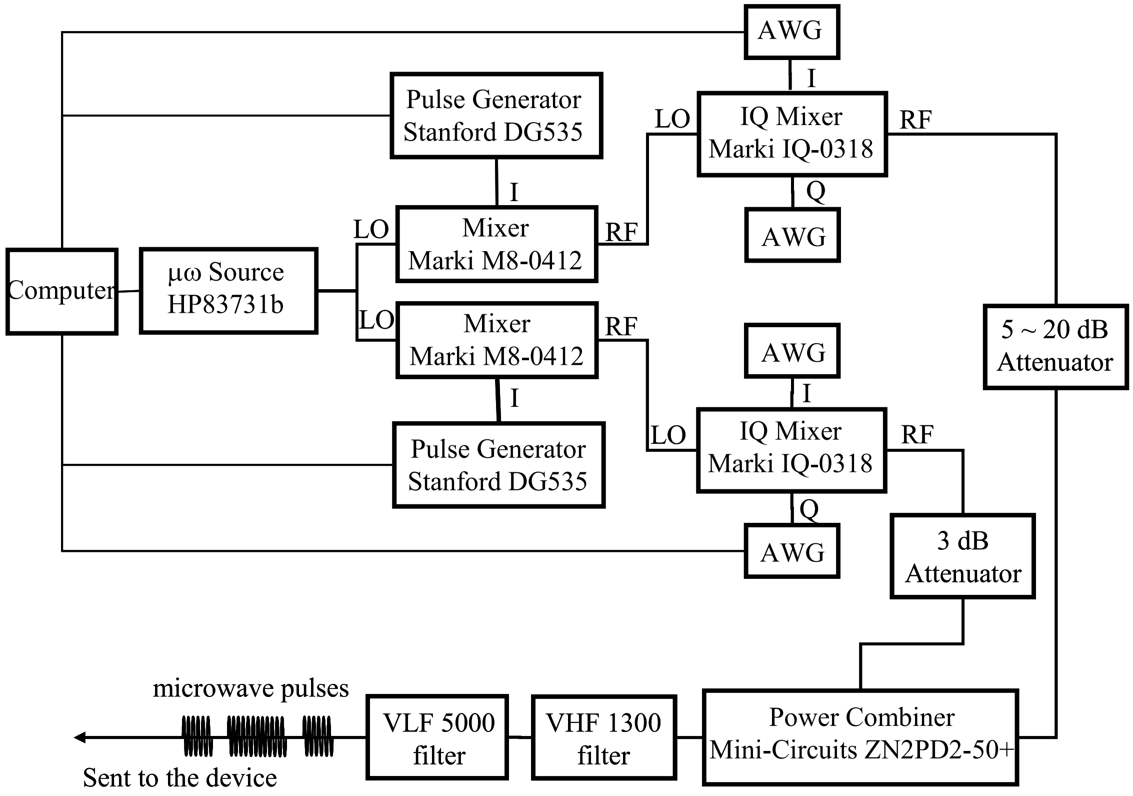

Figure 5.8: Experimental set-up for microwave measurements. The diagram includes only a part of the microwave-related measurements. The pulse generators are synchronized to each other and match a reference clock. A square voltage pulse from the pulse generator controls the timing of the microwave signal through mixers M8-0412.

5.3.2 Γ vs. I_p Measurement

To measure the escape rate of the qubit, the bias current I_b was increased linearly with time and the time when the switching occurred was recorded to a resolution of better than 1 ns using a homemade Schmitt trigger and SR620 timer [see Fig. 5.4 (b)]. A typical repetition frequency was 1 kHz for the current bias ramp. I used 10^3 to 10^6 repetitions and used the switching times to create a histogram of switching events versus time. Since the current increased linearly with time, I could convert this to a histogram of events versus current. Such histograms can be used to find the escape rate versus current. Usually, I ramped the bias current I_b at a rate of order 1 μA/ms. I can define the histogram such that $h(t)\ \Delta t$ is the number of switching events observed between time t and $t+\Delta t$. The escape rate versus time can then be obtained from [48, 50]

$$\Gamma(t) = -\frac{1}{\Delta t}\ln\left(\frac{N_T(t+\Delta t)}{N_T(t)}\right), \tag{5.3}$$

where $N_T(t) = \sum_t^{\infty} h(t)$ is the number of times that the junction did not switch before t (*i.e.* the number that survived at least to time t without switching). From the ramping rate of the bias current, the current can be calibrated versus time and the escape rate as a function of current $\Gamma(I)$ can be found. More details about this measurement can be found in refs. [42, 50-52].

The above technique is used for traditional escape rate measurements much as first used by Webb [93]. Instead, I mainly used a pulse measurement scheme. In this technique, a short current pulse is applied to the qubit [33, 36, 94] and one then checks whether the system switches. I used a step voltage signal from the DG535 pulse generator which was transformed to a short current pulse after passing through the small on-chip capacitor $C_{\mu\omega}$ in the microwave line. The rise time of the square voltage signal is about 2 ns which produces a current pulse with a narrow time width (see Fig. 5.9). The qubit preparation and pulse measurement can be repeated to find the average probability of switching P_s as a function of the pulse current I_p; the ratio of the number of the switching events to the total number of pulses applied. The number of switching events depends on the state of the qubit and the size of the current pulse.

5.3.3 Measuring the Frequency Spectrum

I measured the frequency spectrum in two different ways. Traditionally, a microwave signal at $f_{\mu\omega}$ was applied and the escape rate Γ measured versus the bias current I_b. The measurement was then repeated for different $f_{\mu\omega}$ [33–35]. It can be somewhat difficult to get a clear spectrum from this measurement because the contrast between the Γ with and without microwaves is low.

A better technique involves doing pulsed state measurement while applying microwaves. One then plots the switching probability P_s vs. I_p measurement. The idea is that the microwave signal is turned on and if the system is in resonance, the state of the qubit will be saturated (equally likely to be in 0 or 1). A short current pulse is then sent to read out the state. If the system is in the excited state, it will switch with a high probability, while if it is in the ground state, it will switch with a low probability. The timing of the microwave signal is controlled by a square voltage signal from the DG535 pulse generator through a trigger port of microwave source HP83731b. The timing of the current pulse is determined by the rising slope (see Fig. 5.9) of the square voltage signal

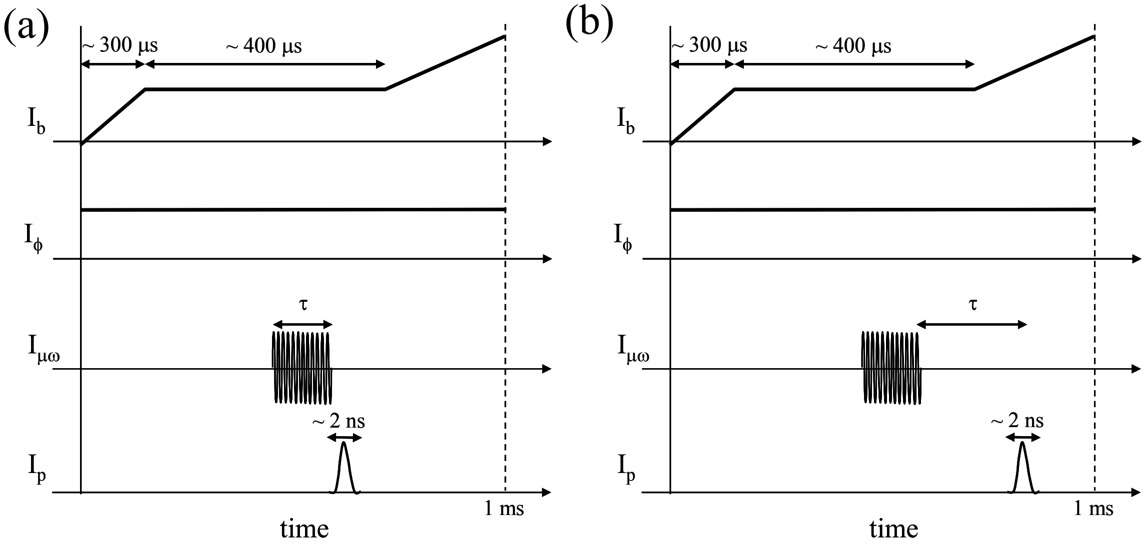

Figure 5.9: Biasing scheme for (a) a Rabi oscillation measurement and (b) a relaxation measurement using a pulsed readout technique. The current bias I_b starts from a small negative value to ensure retrapping while the flux bias current I_ϕ is held fixed. The time period of the microwave signal $I_{\mu\omega}$ and the width of the measurement current pulse I_p are exaggerated for clarity.

from the DG535 pulse generator. At a fixed microwave frequency, the pulse measurement was repeated for different flux bias current, and I then repeated this procedure for different applied microwave frequencies (see Fig. 6.4 and 6.10).

5.3.4 Switching Curve Measurement

Sending a small current to the device tends to make it switch to the voltage state if the sum of the pulse current and the bias current approaches the critical current of the SQUID. As discussed in Chapter 2, this switching is due to tunneling through a potential barrier. If the current is larger, then the potential well is more tilted and the tunneling increases. By changing the amplitude of the step voltage from the DG535 pulse generator, I control the amount of current sent to the device. I recorded switching probabilities for repeated measurement with different pulse current amplitude I_p. I typically sent down about 2000 pulses to find the average switching probability for a given current pulse size. If I increase the amplitude, the switching probability goes up and it forms a curve which has a lower slope at the beginning, a highest slope in the middle and a lower slope again at the end (see Fig. 7.2). Because of its shape, P_s vs. I_p is also called an s-curve. If the qubit is in the excited state, it tunnels out with a smaller amount of current. Thus, the s-curve of the excited state resembles the s-curve of the ground state, but shifted to lower currents (see Fig. 7.3).

5.3.5 Measurement of Rabi Oscillations

To measure a Rabi oscillation in the phase qubit, I set the current bias and the flux bias and then tuned the microwave frequency to be in resonance with the qubit 0-to-1 transition. The microwave pulse of length τ is then sent to the device, followed by a current pulse at a time τ after the start of the microwave pulse. The voltage output is then checked to see if the device has switched [see Fig. 2.1 (a)]. This process is repeated ~ 10^3 times to obtain P_s for the length τ of microwave pulse. The length of the microwave pulse is then increased by a few ns (usually 2 ns) and the whole process repeated. The time step should be much shorter than the period of the Rabi oscillations. Normally, the current pulse is sent right after the microwave signal is shut off. However, to avoid some measurement problems, I often sent a current pulse while the microwave was on. This might cause errors. However, when I compared Rabi oscillations from the two different measurements, there was not a significant difference (less than 10^{-2} difference in P_s).

5.3.6 Relaxation Measurement

To measure the relaxation time of the excited state of the qubit, I applied a relatively short microwave pulse at the resonance frequency to excite the system. A $\pi/2$ microwave pulse is ideal but all that is really needed is significant probability to be in $\left|1\right\rangle$. I used the HP83731b microwave source. I then wait a time τ and do a pulse measurement of the state. I repeat this many times for a range of τ to determine $P_s(\tau)$. I also do pulse measurements before the microwaves are turned on as a check.

T_1 is often obtained by fitting the $P_s(\tau)$ curve to an exponential decay with time constant T_1. In fact, I had to do a more complicated analysis because of anomalies in the switching behavior. This is discussed in Chapter 7.

5.3.7 Spin Echo Measurement

In device DS8, coherence times were long enough to do a spin echo measurement. For a spin echo measurement, it is necessary to control the timing of three microwave pulses. I applied a π/2 (90º rotation in the Bloch sphere) microwave pulse to drive the state of the qubit from the state $\left|0\right\rangle$ to the state $\left(\left|0\right\rangle + \left|1\right\rangle\right)/\sqrt{2}$. Next I waited a time τ, and then applied an in-phase π pulse. This was followed by another waiting period τ and by a second out-of-phase π/2 pulse [see Fig. 5.10(a)].

Because it was difficult to make three microwave pulses in our system, I used two short positive triggering voltage pulses sent to the microwave source for the first π/2 pulse and the π pulse, but I used one short negative triggering voltage pulse for the last π/2 pulse. A negative input voltage produced a 180º flipped phase for the microwave output.

5.3.8 State Tomography Measurement

It is essential to control the phase and the amplitude of the state of the qubit on the Bloch sphere. Experimentally this requires that we calibrate the IQ mixers, which control the phase shift and amplitude of the microwave signals [see Fig. 5.10(b)]. The measurement set-up shown in Fig. 5.11 shows how the mixers were used to produce microwave signals with different phases.

From the single microwave source, a microwave signal is sent to two Marki M8-0412 mixers. The output from the mixers is generated when the mixers receive a pulse at

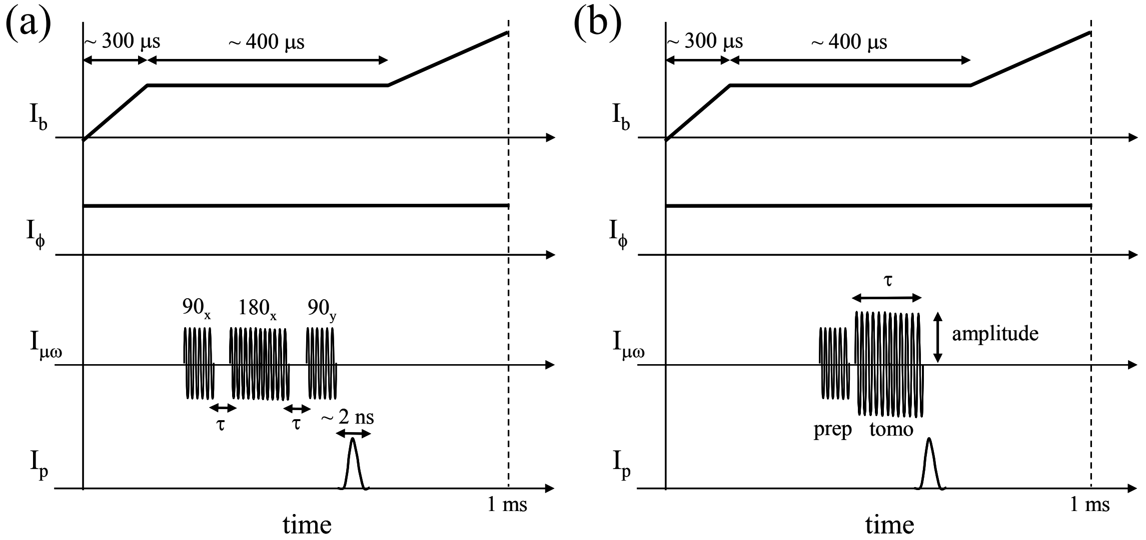

Figure 5.10: Biasing scheme for microwave measurements, (a) spin-echo measurement and (b) state tomography measurement using the IQ mixers. The current bias I_b starts from a small negative value to ensure retrapping while the flux bias current I_ϕ is held fixed. The time period of the microwave signal $I_{\mu\omega}$ and the width of the measurement current pulse I_p are exaggerated for clarity. The multiple microwave pulses were produced by IQ mixers.

their I-port from the DGD535 pulse generator. The signal coming out from the Marki mixers passes next to IQ mixers. The phase of the microwave signal was controlled by changing the voltage amplitude at the I and Q ports (using the AWG, constant voltages are sent to I and Q ports of the IQ mixers). The output microwave signals from the two IQ mixers (see Fig. 5.11) which have different phase information are combined using a power combiner and the resulting signal is sent to the device through the $I_{\mu\omega}$ wire. The phase and the amplitude are modulated by the voltage input signals to I and Q ports.

5.4 Summary

In this chapter, I described how I cooled and measured the devices. To achieve a low temperature, a dilution refrigerator was used and all bias lines were carefully filtered and thermally grounded. I described how I arranged the apparatus for the qubit measurements.

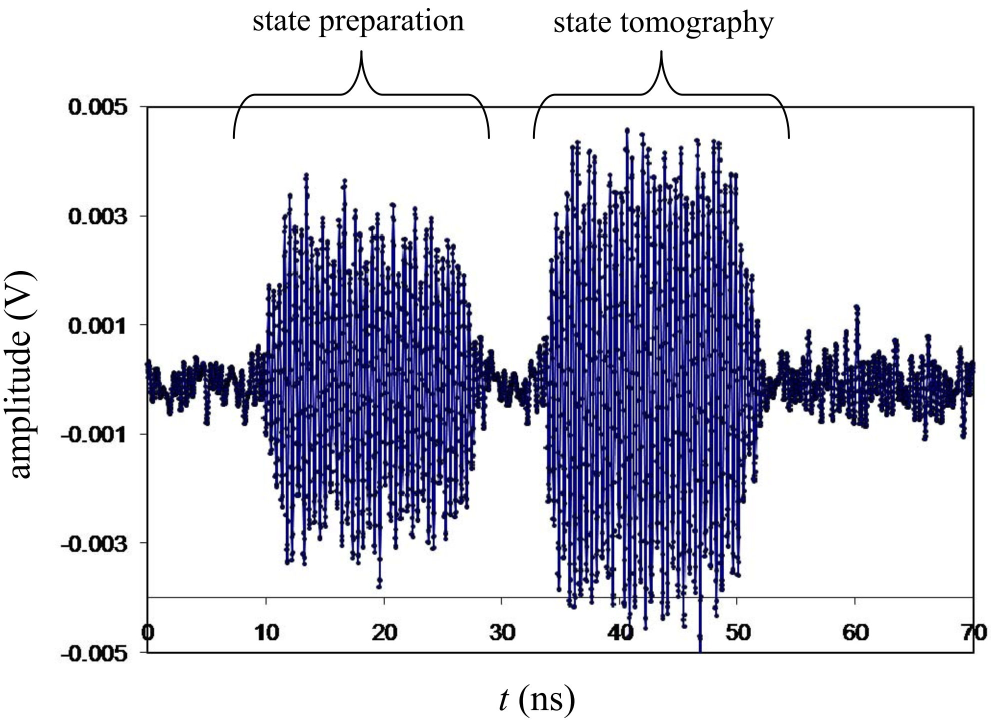

Figure 5.11: Microwave pulses for state preparation and the state tomography measured using an oscilloscope. The voltage amplitude was measured before the attenuator (see Fig. 5.8).

Chapter 6

Results of Qubit Characterization

The main goal of my research was to achieve a coherence time greater than 1 μs in a dc SQUID phase qubit. A second goal was to understand what limited the coherence time. In this chapter, I discuss my measurements of the energy spectrum, Rabi oscillation, Ramsey fringes and relaxation in two qubits (DS6 and DS8). From these measurements, I found the Rabi decay time T', the relaxation time T_1, and the spectroscopic coherence time T_2^* and used these to extract estimates for the coherence times T_2 and dephasing time T_ϕ. I also obtained state tomography data on device DS8 as a step towards demonstrating that I could manipulate the state on the Bloch sphere. Moreover, I observed a phenomenon that was quite unexpected: anomalous switching curves. I will discuss the behavior of the s-curves in Chapter 7.

6.1 Device DS6

6.1.1 Current-Flux (I-Φ) Characteristics

The switching current vs. flux (I-Φ) curves are useful to indentify flux states and provide some initial information about the device parameters. Figure 6.1 shows an I-Φ characteristic for device DS6. By fitting this data, I obtained I_{01}, I_{02}, L_1, L_2 and M_ϕ of DS6 (see Table 4.1). Switching histograms were taken by sweeping I_b at fixed values of I_ϕ.

In DS6, the overlap region between two neighbor flux states is not large and I could easily pick the trajectory that did not require flux shaking. The usual trajectory for the measurement followed the dashed line shown in Fig. 6.1. I ramped the bias flux first and then ramped the current to bias the system to make the current state close to the critical current. From this plot, one sees that $I_{01}+I_{02} \approx 2.96$ μA.

6.1.2 Escape Rate and Switching Curves

I measured device DS6 in two different ways, using an escape rate measurement and using a current pulse readout technique, as I discussed in Chapter 5. For escape rate measurements, the bias current and flux were ramped simultaneously with fixed slopes and I kept track of what current the device switched at. The ramp was typically repeated 5000 times for each bias condition (see Fig 6.1). The escape rate can be obtained from the switching histogram as I discussed in section 5.3.2.

When a continuous microwave pulse tuned to the qubit resonance frequency is sent to the device, an enhancement in the escape rate is observed. Figure 6.2 shows an example of four different $\Gamma(I)$ measurements. In these examples, I also applied a continuous microwave drive. Two peaks are visible and their locations depended on

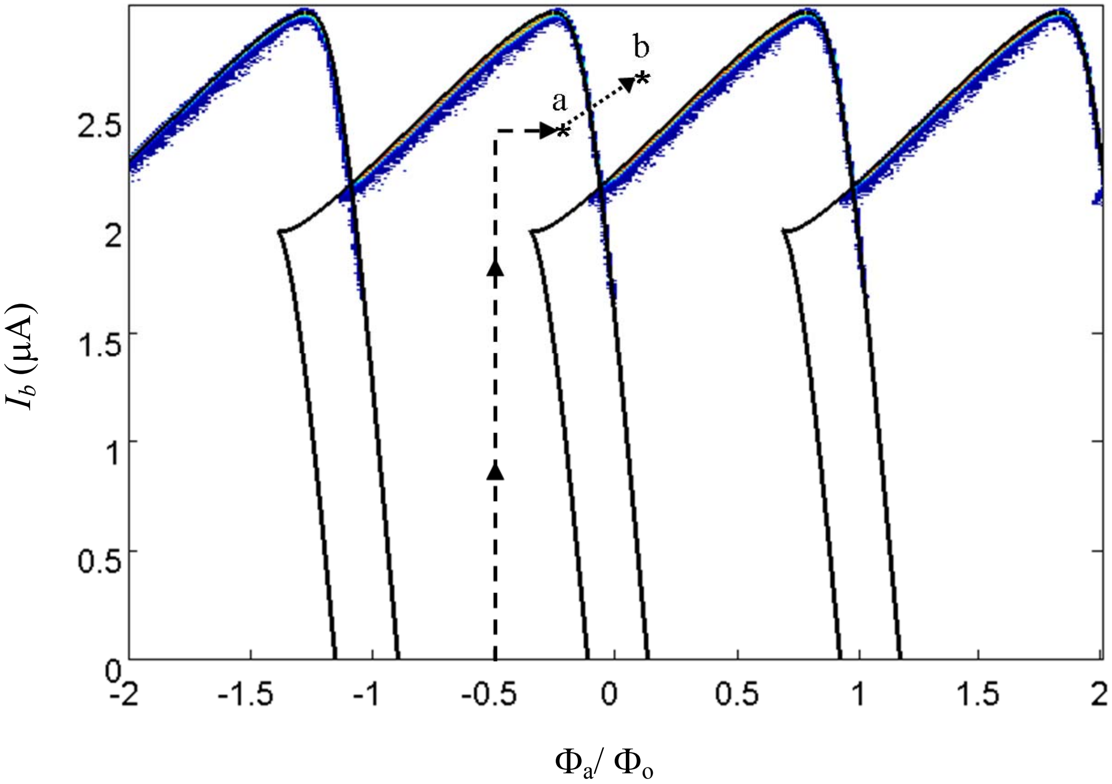

Figure 6.1: I-Φ curve for device DS6 and bias trajectories. If the trajectory goes over the blue curve and the junction will switch to the voltage state. Generally the device was biased below this curve (a dashed trajectory), at a point such as “a” and I used a pulse readout technique to measure the state of the qubit by pulsing the flux (towards “b”). For escape rate measurements, the bias current and flux were ramped simultaneously from “a” to “b” (a dotted trajectory). The color points are data and the solid lines are fit.

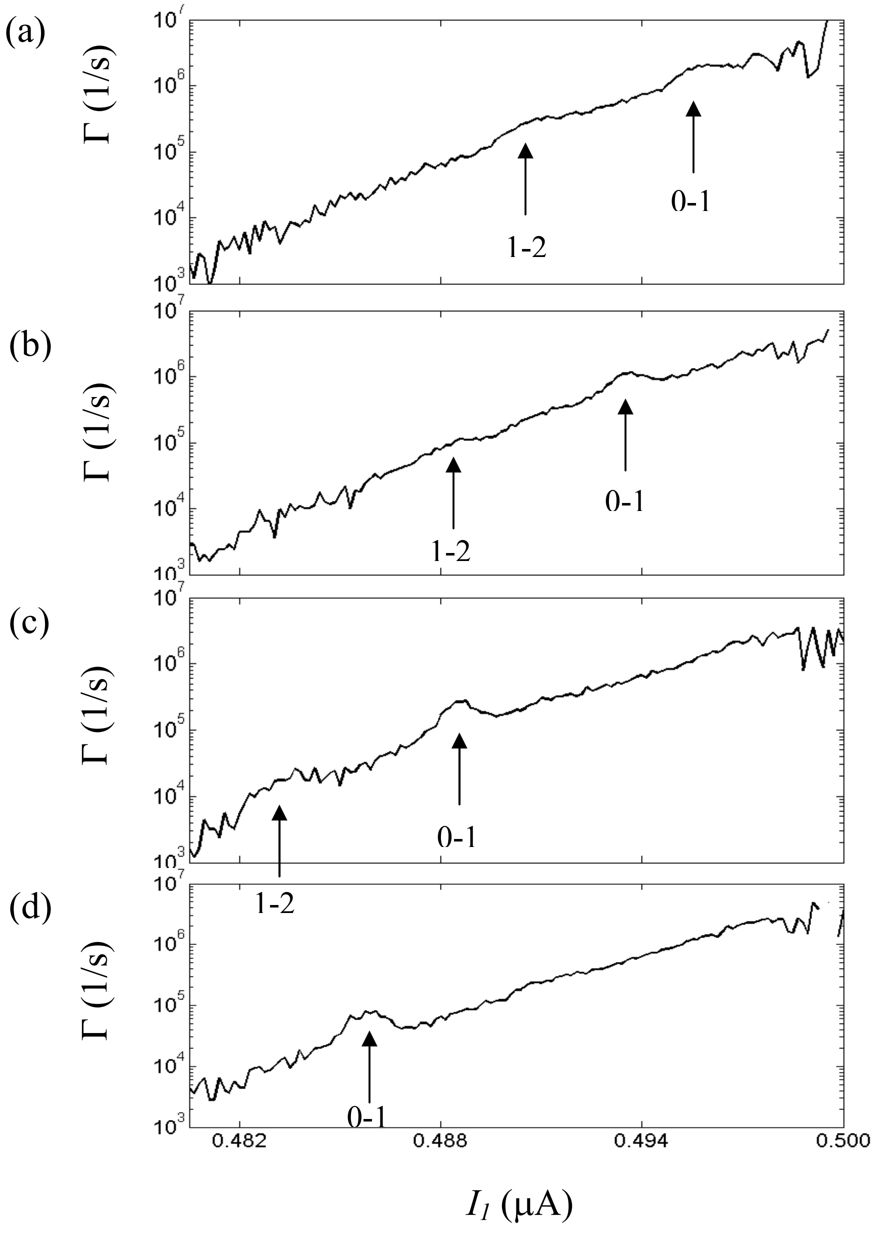

Figure 6.2: Escape rate measurement versus current measured in device DS6. The curves were measured while exciting the qubit using continuous microwaves with frequencies of (a) 4.3 GHz, (b) 4.4 GHz, (c) 4.6 GHz and (d) 4.7 GHz. The two small resonant peaks move to lower current when the frequency increases. The current bias was ramped from low to high current at 2.4 μA/ms. The bias current scale was calibrated using the I-Φ curves.

the applied frequency. By using the same procedure at different frequencies and biases, the energy spectrum is mapped out. I will discuss the spectrum in detail in section 6.1.7.

The other technique I used for measuring qubits was the current pulse readout technique [33, 36, 91]. The device is current and flux biased at the operating point and a short (2ns) current pulse is then applied. The device then switches or not, depending on the state of the qubit. Fig. 6.3 shows examples of switching curves obtained from device DS6. Here, the switching probability P_s is plotted versus the amplitude of the current pulse. The amplitude of the current pulse is estimated from the applied voltage and the capacitance $C_{\mu\omega}$ (see Fig. 5.6). In the single junction approximation, the switching curve at $P_s << 1$ should be a nearly straight line on a semi-log plot and this is not so clearly true in Fig. 6.3. For $P_s << 1$, the switching probability P_s is related to Γ and the current I by $P_s \approx \Gamma\tau$ and $\Gamma \approx \Gamma_0 \exp(\alpha I)$ where α is approximately constant. Also Fig. 6.3 shows that when I increased power of the microwave pulse, the switching curves shifted to lower current and widened. This behavior is actually anomalous because there is not a well-defined shoulder at about 50 %. This will be discussed in Chapter 8 [95].

6.1.3 Transition Frequency Spectrum

Figure 6.4 shows a section of the transition spectrum I measured for device DS6 [35]. Here I plotted the frequency along the x-axis and the current I_1 through the qubit junction (calibrated from the bias current I_b of the circuit using an inductive ratio) and the color represents the escape rate enhancement (see below). This data was taken by ramping the bias current and flux while applying microwaves and then recording the time (current) at which the device escaped to the voltage state. The microwave power at the

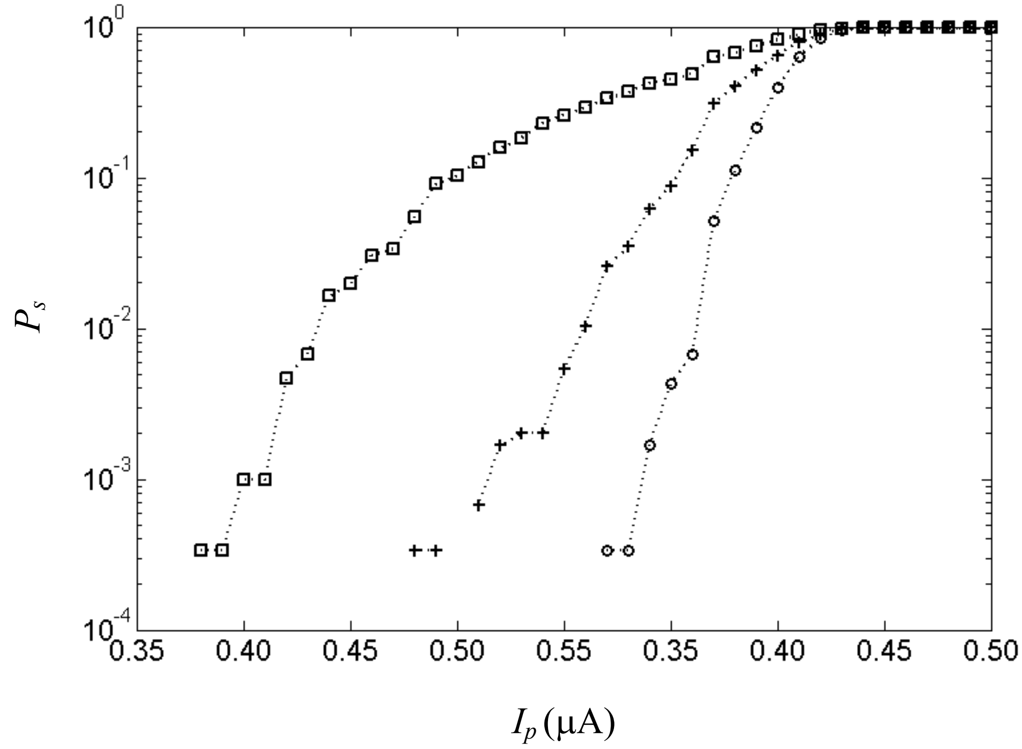

Figure 6.3: Switching probability P_s of device DS6 versus pulse amplitude at three different microwave powers after sending a long microwave pulse at an applied frequency of 6.930 GHz. The open circles were measured using a microwave pulse with an output power of -90 dBm, the crosses were measured with a power of -41 dBm and the open squares were measured with a power of -26 dBm. The switching curves should show a clear plateau that increase with increasing population in the excited state. The absence of a plateau is one feature of the anomalous switching curves.

source ranged between -58 to -70 dBm. I had to vary the power with the bias current. An enhancement in the escape rate was observed when the microwave frequency matched a transition frequency of the qubit. The bias ramp was repeated 5000 times at each microwave frequency with a 2 MHz step and the resulting histogram (counts vs. I_p) used to extract the escape rate Γ vs. I. In Fig. 6.4, the color is determined by the enhancement in the escape rate $\Delta\Gamma / \Gamma = (\Gamma_{\mu\omega} - \Gamma) / \Gamma$, where $\Gamma_{\mu\omega}$ is the escape rate which microwave power on and Γ is the escape rate when there is no power. For this measurement, the time when the junctions switched to the voltage state was recorded and this was converted to current by calibrating the ramp. The top curve shows the 0-to-1 transition and under that is a fainter 1-to-2 transition.

For comparison, Fig. 6.5 shows a transition spectrum of device DS6 at frequencies between 6 and 7 GHz that I obtained using the current pulse readout technique. In this case, I applied continuous low power microwaves ($P \approx$ -45 dBm) and the bias current and bias flux were kept constant for about 500 μs. I then applied a measurement pulse and recorded the probability of switching using 5000 pulses. I then stepped though a range of amplitudes of the bias current and flux. Because the current pulse was long (about 2 ns) compared to $1/\omega_{01}$, the pulse measurement was adiabatic and should not produce excitations of the qubit. I also tried a shorter (≈ 1 ns) current pulse, but it did not change the spectrum. Note that in Fig. 6.5, only the 0 to 1 transition is visible.

At any given bias current, the width of the peak in the spectrum can be converted into a spectroscopic coherence time T_2^* using [48]

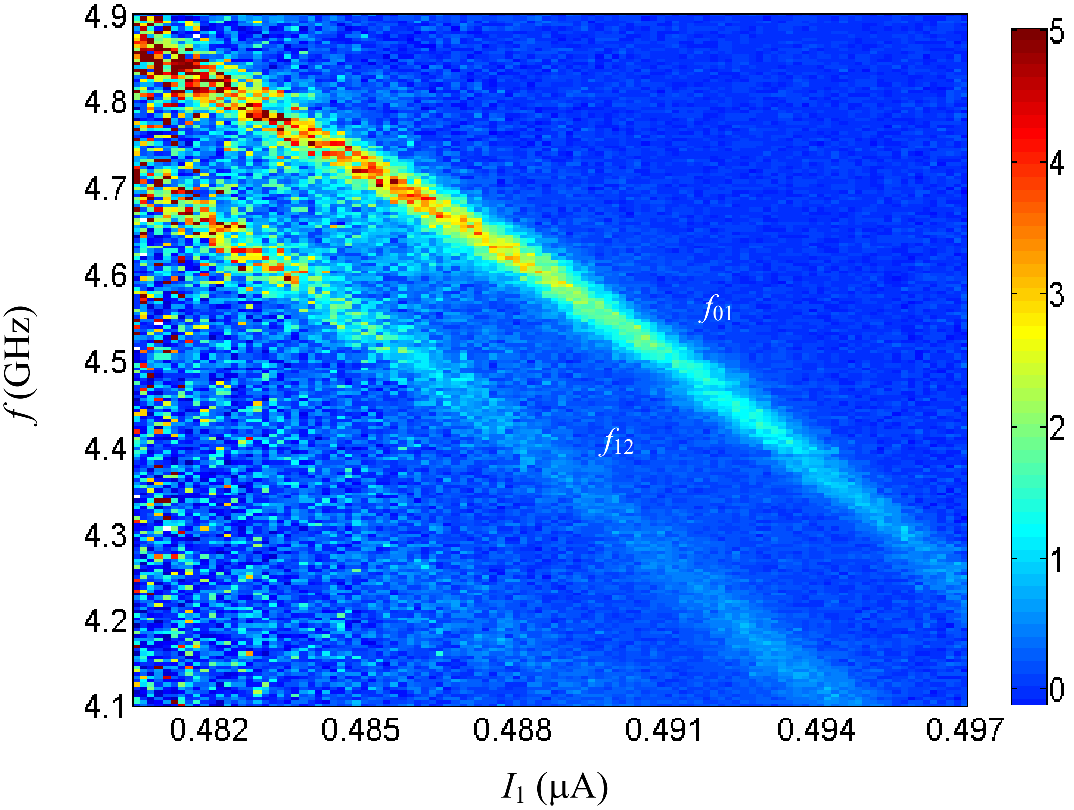

Figure 6.4: False color plot of frequency transition versus estimate current I_1 is the qubit junction of device DS6 measured using an escape rate measurement at $I_l \approx 0.49$ μA, $T \approx$ 20 mK and $P_{\mu\omega} \approx$ -48 to -70 dBm. The color scale represents the enhancement $(\Gamma_{\mu\omega}-\Gamma)/\Gamma = \Delta\Gamma/\Gamma$ in the escape rate, where $\Gamma_{\mu\omega}$ is the escape rate when a continuous microwave pulse was applied and Γ is the background escape rate. The upper curve corresponds to 0-to-1 transitions and the lower curve is for 1-to-2 transitions. The anharmonicity is about 200 MHz. The upper curve line has about a linewidth of 20 MHz which corresponds to $T_2^* \approx 16$ ns. The flux was $\Phi_a \approx 0.31\ \Phi_o$.

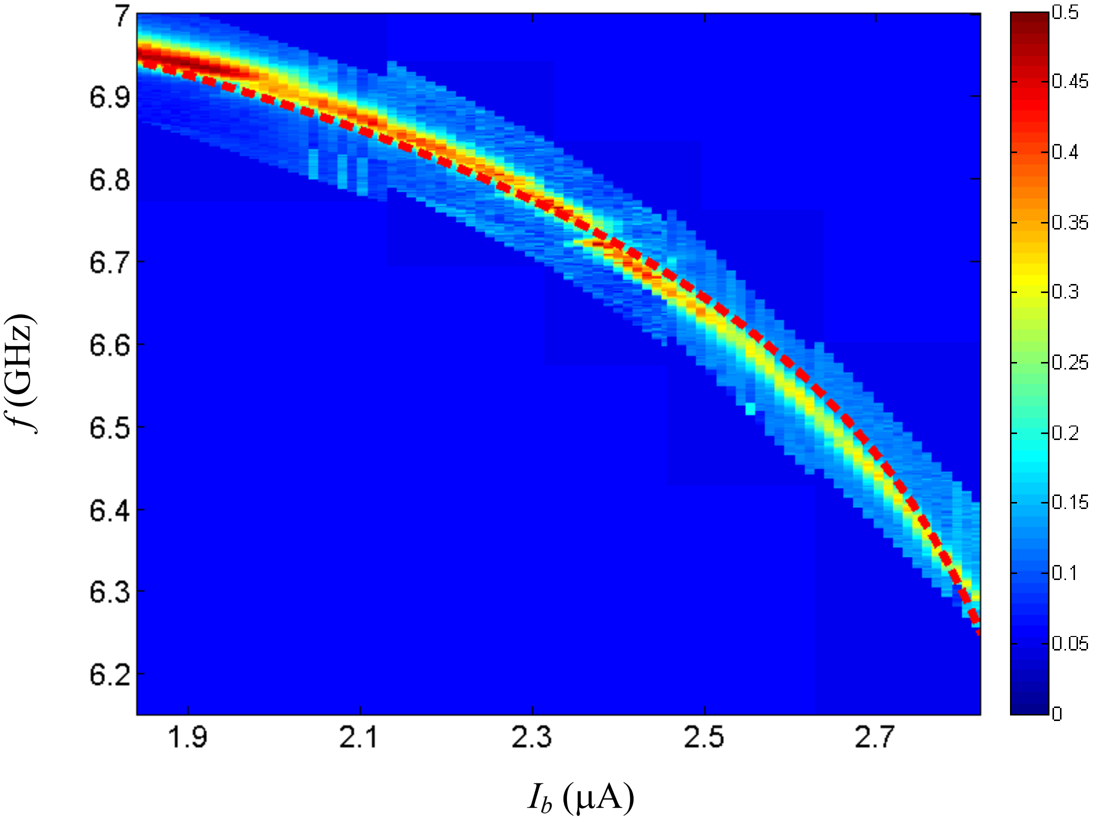

Figure 6.5: 0 to 1 transition spectrum of device DS6 measured using the current pulse readout technique [35]. The color scale represents the switching probability P_s that was obtained by repeating a single current pulse measurement. The blue background means no data taken, red means higher probability, and light blue means lower probability. A clearly visible splitting of about 30 MHz occurs around 6.7 GHz. A possible splitting occurs around 6.9 GHz. The flux was $\Phi_a \approx 0.06$ to $0.09\ \Phi_o$. A dashed red curve is fit using normal modes approximation as discussed in Chapter 2.

$$T_2^* = \frac{1}{\pi \Delta f_{FWHM}} \tag{6.1}$$

where Δf_{FWHM} is the FWHM (full width at half maximum) of the resonance peak. The FWHM changes depending on the current and flux bias. The longest T_2^* I obtained was 16 ns for a FWHM of 20 MHz at $I_b \approx 0.8$ μA (see Fig. 6.6). As Fig. 6.6 shows, there is some variation with I_b. The FWHM seems narrowest near 0.6 μA and 0.8 μA. The spectroscopic times were shorter than I expected and I hoped, but longer than or comparable to the best devices built previously in our group.

6.1.4 Splitting Characterization

In Fig. 6.5, there appears to be only one clear splitting (a 30 MHz splitting occurs around 6.7 GHz) and another likely splitting that we could not resolve well (around 6.8 GHz). The frequency range shown is about 0.7 GHz.

For comparison, I note that T. A. Palomaki found 8 splittings in a 1.2 GHz range for device DS3 [42]. This device was a dc SQUID phase qubit built on a sapphire substrate, but with a larger (15 μm^2) qubit junction and no shunting capacitor or LC filter. It is clear from Fig. 6.5 that far fewer splittings exist in device DS6, compared to device DS3, and this reduction in number is roughly consistent with device DS6 having a qubit junction area (4 μm^2) that was about four times smaller than that of device DS3.

Figure 6.7 shows linecuts (P_s vs. f) through the spectrum near the avoided level crossings in DS6: The minimum splitting size at this avoided crossing is 30 MHz. The FWHMs of the peaks changes; one of the peaks becomes narrower and smaller while the

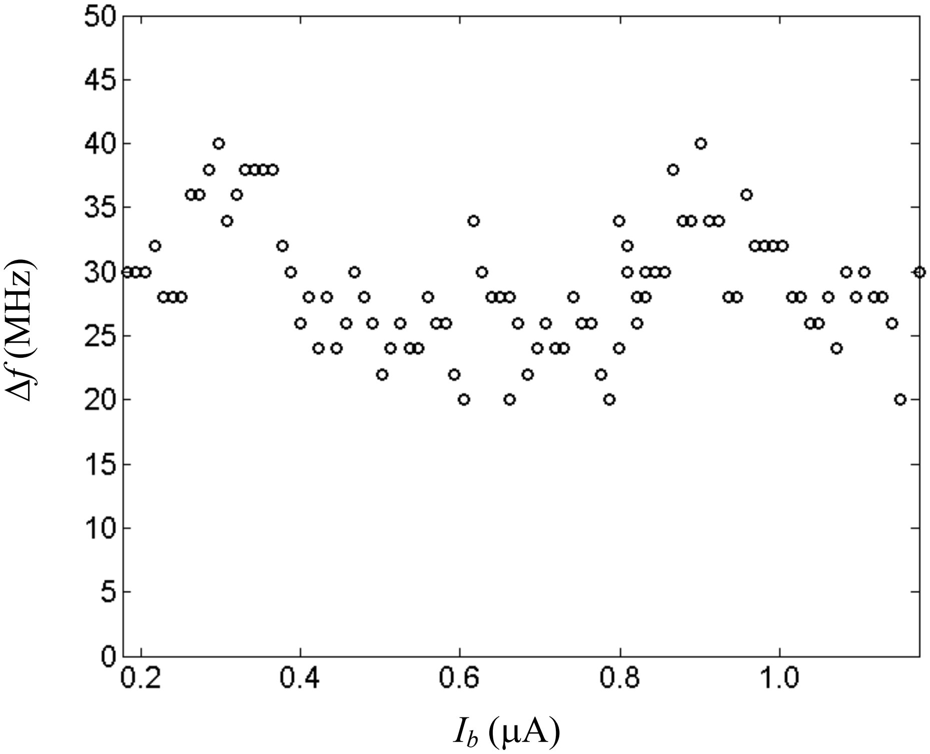

Figure 6.6: Full width at half maximum (FWHM) measured versus current bias for device DS6. The bias points near 0.6 μA and 0.8 μA seem to show the narrowest FWHM or longest spectroscopic coherence time T_2^*. The flux was $\Phi_a \approx 0.06$ to $0.09\ \Phi_o$.

other peak becomes wider and larger. This is consistent with coupling of the qubit to a single charged TLS [29].

6.1.5 Relaxation Rate

In device DS6, I generally took Rabi oscillation data and relaxation data in the same data set. Relaxation of the qubit was measured by turning off the microwave power after the Rabi oscillation measurement was done, so that relaxation occurred from the saturated state. Sometimes I saw a “kicking effect”; the probability suddenly increased a few ns after the microwave power was turned off. This effect was probably caused by a small change in the bias at the end of the microwave pulse. The relaxation time T_1 was extracted from fitting the whole relaxation curve, ignoring the kick.

The relaxation time T_1 varied a bit depending on the bias point. Fig. 6.8 (a) shows data when I applied resonant microwaves at 6.776 GHz. This data set had the longest T_1 I found in the device. Unfortunately, this was only $T_1 \approx 32$ ns and this was much shorter than I expected, even though it was actually a bit longer than any of our previous devices.

In order to check why T_1 was shorter than expected, recall that the relaxation time of the phase qubit can be written as

$$T_1 = \frac{\left(C_J + C_x\right)}{1/R_1 + 1/R_{eff} + 1/R_x} \quad , \tag{6.2}$$

where C_J is the capacitance of the qubit junction, C_x is the capacitance of the $\mathrm{SiN_x}$ capacitor connected across the qubit junction, and R_1 accounts for dissipation from dielectric loss in the tunnel junction dielectric and R_x accounts for loss in the dielectric

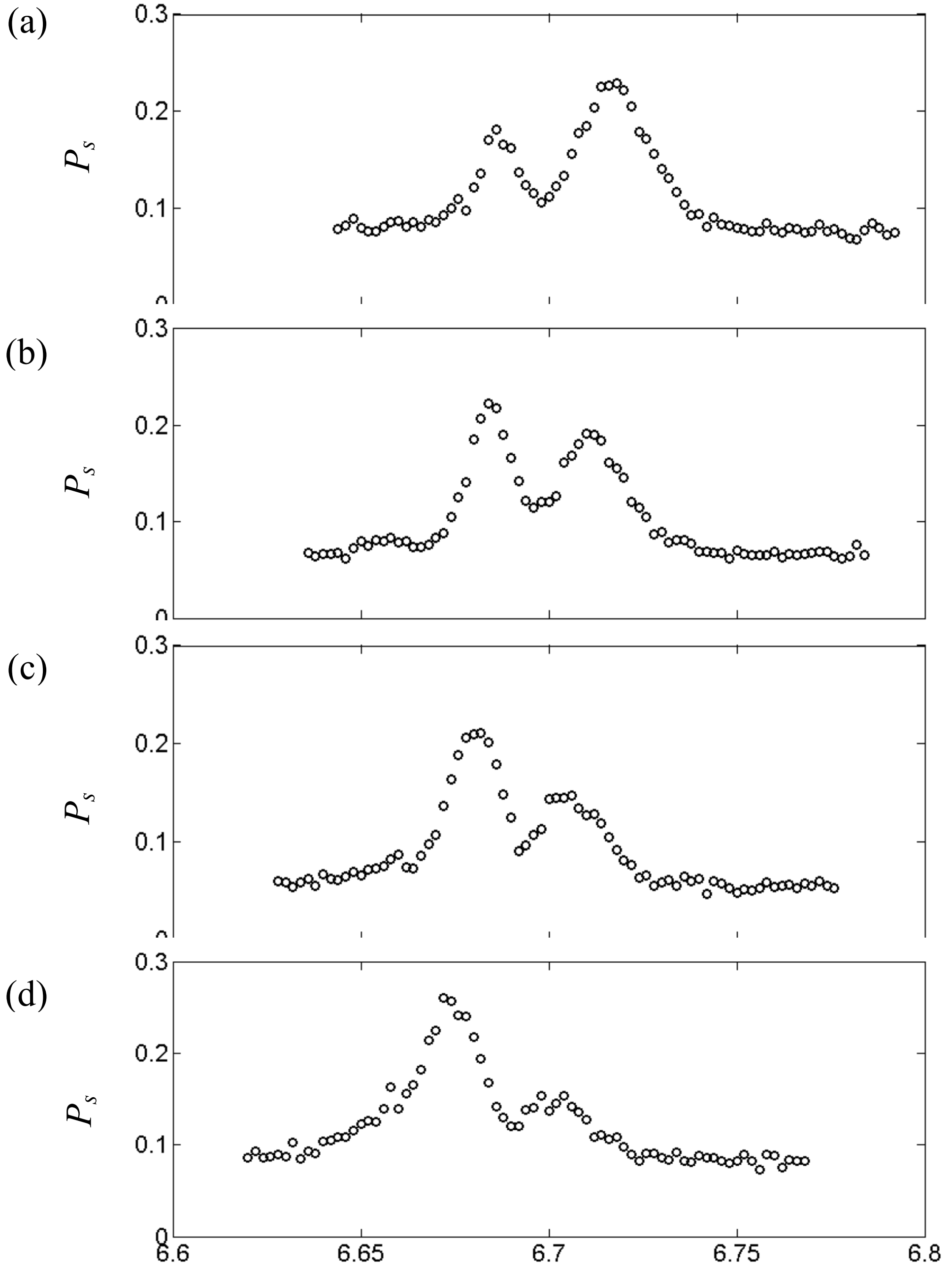

Figure 6.7: P_s of the 0-to-1 transition in device DS6 near an avoided level crossing around 6.7 GHz. The data was taken at (a) I_b = 0.69 μA, (b) I_b = 0.70 μA, (c) I_b = 0.71 μA and (d) I_b = 0.72 μA. The minimum splitting size is approximately 30 MHz.

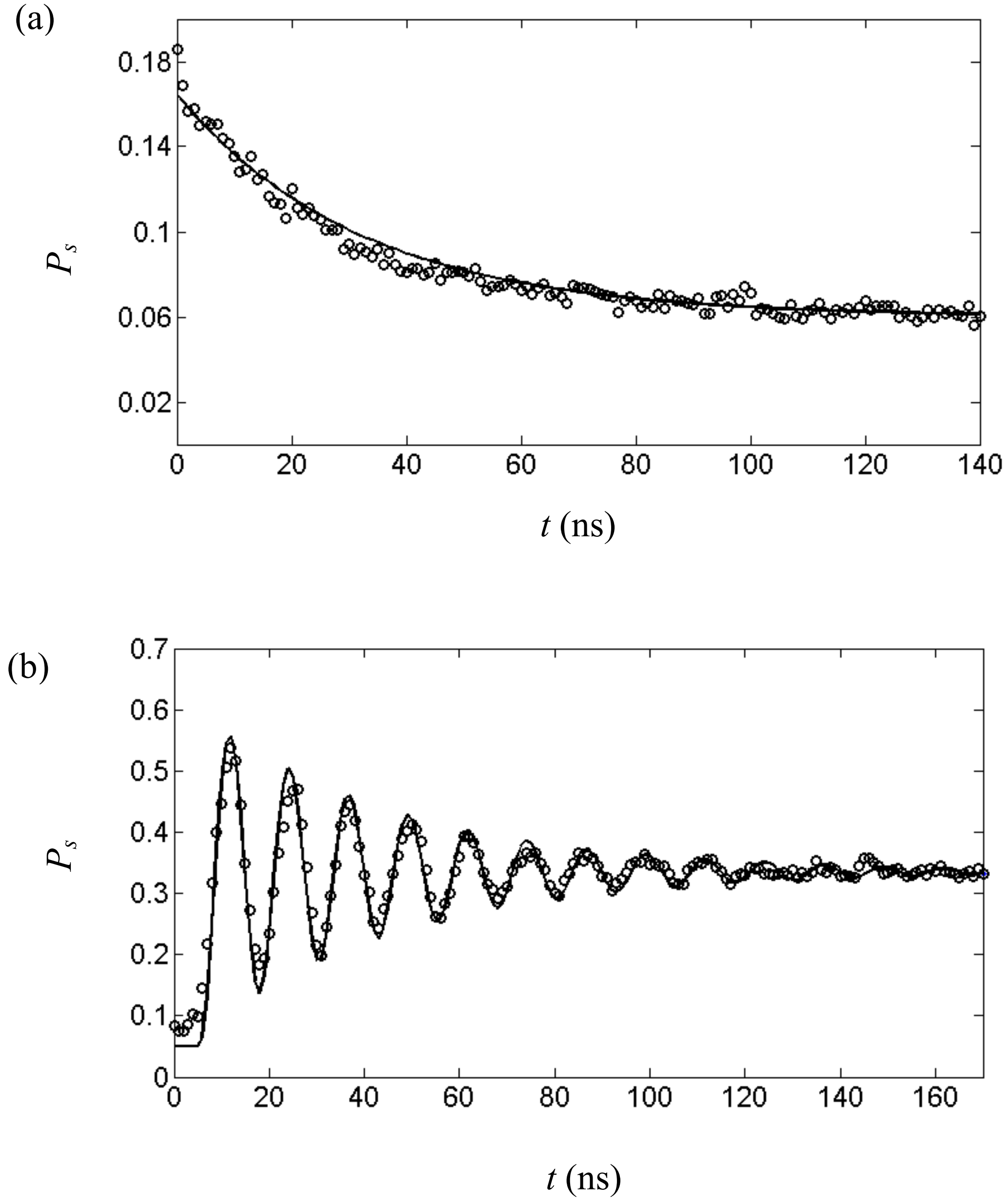

Figure 6.8: Plot of switching probability P_s versus time t following application of a resonant microwave pulse at 6.776 GHz. (a) Measured relaxation in device DS6. Solid curve is exponential fit with a relaxation time $T_1 \approx 32$ ns. (b) Points show Rabi oscillation data obtained from device DS6. The Rabi decay time of $T' \approx 42$ ns at 6.776 GHz was the longest I obtained in this device. Solid curve is fit to an exponentially decaying sine wave.

Used for C_x. In Eq. 6.2, R_{eff} is the effective resistance from the leads evaluated at the transition frequency of the qubit (see Chapter 3).

If I assume that $R_x << R_1 << R_{eff}$, then Eq. 6.2 gives $T_1 = R_x (C_J + C_x)$. If all of the loss is due to the SiN_x, then one can write $R_x = 1/ C_x\omega_{01}\tan(\delta_x)$ and thus $T_1 = (C_J + C_x) / C_x\omega_{01}\tan(\delta_x)$ where $\omega_{01}/2\pi$ is the resonant frequency of the qubit. For $T_1 \approx 32$ ns at a resonant frequency of 6.776 GHz and assuming $C_J + C_x \approx 1$ pF, one finds

$$\tan(\delta) \leq 7 \times 10^{-4} . \tag{6.3}$$

In later measurements, H. Paik and K. D. Osborn found that the SiN_x I used had $\tan(\delta_x) \approx 7\times10^{-4}$ in the low power limit [43]. Thus the T_1 I found in device DS6 was consistent with loss in the as-grown SiN_x films. Later, H. Paik and K. D. Osborn found that the loss could be greatly reduced by growing SiN_x so that it was Si-H rich, providing a clear path for making further improvement in T_1 [43].

Note that if some of the relaxation is caused by dissipation in the leads or the junction's AlO_x dielectric, then Eq. 6.3 is an upper bound on the loss tangent of the SiN_x. From Eq. 6.2, using $C_J \approx 0.1$ pF, $C_x \approx 0.5$ pF, $\tan(\delta_1) = 1.6 \times 10^{-3}$ and $R_{eff} = 8$ GΩ, I find $T_1 \approx 88$ ns. This is still short because of the effect from the junction's dielectric.

6.1.6 Rabi Oscillations, Ramsey Fringe and Decoherence

In device DS6, I measured Rabi oscillations by applying resonant microwave pulses of controlled duration. In Fig. 6.8(b), 6.776 GHz microwave power was turned on at t = 0 and left on. The state of the system was then interrogated at time t by sending a short current pulse on the microwave line and checking whether the device switched to the voltage state. I repeated this process 2000 times for each amplitude of the current pulse and used the resulting switching curves at each time t to extract the probability P_1 to be in the excited state at time t (see Chapter 8).

In Fig. 6.8 (b), clear oscillations are seen out to about 100 ns. By fitting the curve to an exponentially decaying oscillation, I found a Rabi decay time $T' \approx 42$ ns. To avoid decoherence from a discrete TLS defect I found at 6.7 GHz (see Fig. 6.5 and 6.7), these Rabi oscillations were taken at 6.776 GHz, far from the TLS resonance. This best Rabi decay time of 42 ns was about twice as long as found in the group's best previous device DS3 [42].

The time constant T' for the decay of the Rabi oscillations, the energy relaxation time T_1, and coherence time T_2 are related by [50, 96]

$$\frac{1}{T'} = \frac{1}{2T_1} + \frac{1}{2T_2}. \tag{6.4}$$

Using this relationship and $T_1 \approx 32$ ns, I can estimate that $T_2 \approx 61$ ns $\approx 2T_1$ in device DS6. Since $T_2 \approx T_1$, this means that decoherence is dominated by relaxation and the dephasing time T_ϕ is much greater than T_1.

T_2 and T_1 and T_ϕ are related by [97, 98]

$$\frac{1}{T_2} = \frac{1}{2T_1} + \frac{1}{T_\phi}. \tag{6.5}$$

Thus $1/T_\phi = 1/T_2 - 1/T_1 \approx 1/(1\ \mu\text{s})$.

I also tried doing Ramsey measurements in device DS6 (see Fig. 6.9). It was difficult to obtain good data, probably because of the anomalous switching behavior and because the coherence time for the device was so short. Figure 6.9 shows an example of where there is some detuning ($\approx$ 100 MHz) and $f_{01} = 6.974$ GHz. The plot shows a few

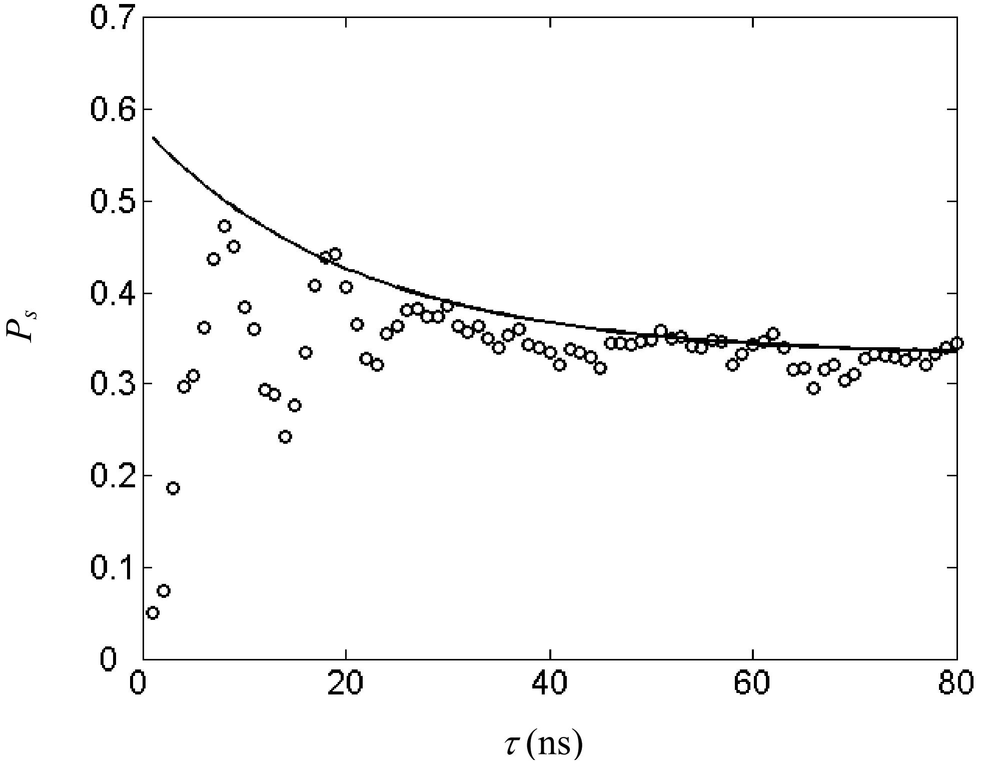

Figure 6.9: Open circles show Ramsey fringe measurement from device DS6, *i.e.* the probability of switching versus time between two π/2 pulses. Solid curve shows fit to exponential decay with time constant $T_2^* \approx 21$ ns. The oscillations show that the microwaves for the π-pulses were detuned by about 100 MHz from the resonance frequency of 6.974 GHz.

periods of an oscillation (Ramsey fringes). I can roughly estimate the decay time $T_2^* \approx 20$ ns by fitting the curve. This time is similar to $T_2^* \approx 16$ ns obtained from the FWHM of the spectrum, as one would expect. Both are shorter than $T_2 \approx 61$ ns and this suggests that there is low frequency noise present that is causing inhomogeneous broadening.

Table 6.1 summarizes the results obtained from device DS6 (see section 6.9).

6.2 Device DS8

The overall design of device DS8 is basically the same as that of device DS6. The main differences are that DS8 has a smaller (2 μm^2) qubit junction with a smaller critical current (77 nA) and the (Si-H rich) SiN_x layer for the shunting capacitor C_x had much lower loss (see Chapter 5). In device DS8, I mainly used the current pulse readout technique.

6.2.1 Current-Flux (I-Φ) Characteristics

Figure 6.10 shows an I_b vs. Φ_a characteristic for device DS8. By fitting this data, I obtained $I_{01} = 77$ nA, $I_{02} = 1.365$ μA, $L_1 = 1.5$ nH, $L_2 = 60$ pH and $M_\phi = 1.53$ pH.

In DS8, $I_{01} = 77$ nA was much smaller than $I_{01} = 0.5$ μA in device DS6 and it produced no overlap region in the flux states, *i.e.* there was only one stable flux state at any given bias point. The usual trajectory I obtained for the measurements followed the dotted line in Fig. 6.10. In this case, I used a fixed flux offset and ramped the current up to a specific level. This sets f_{01}. I then did a pulse readout measurement to find the switching probability curves which I then used to find P_s.

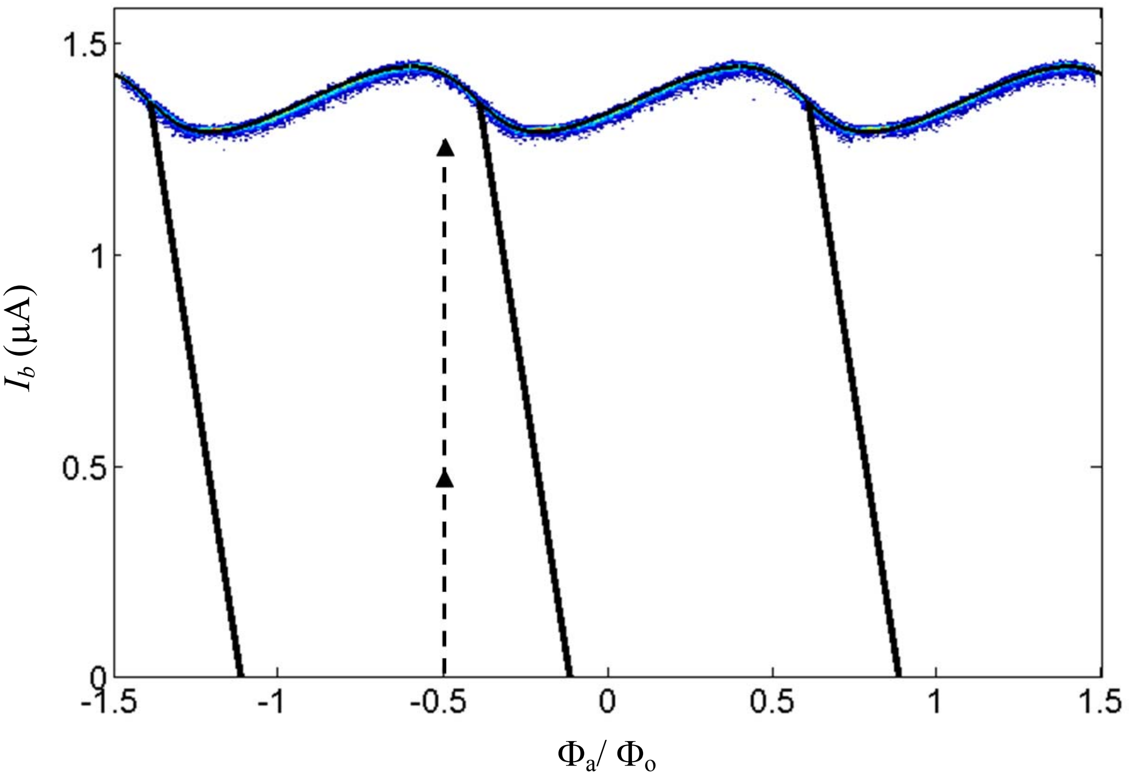

Figure 6.10: I-Φ curve for device DS8 and bias trajectory. If the trajectory goes over the blue line and the junction will switch to the voltage state. The color points are data and the solid lines are fit.

6.2.2 Switching Curves

Figure 6.11 shows some examples of switching curves in device DS8, measured during a Rabi oscillation [95]. The open triangles were taken while -90 dBm of microwave power was applied at 3.520 GHz and the open circles were taken with a microwave turned off. These two curves are virtually identical and correspond to the switching curves when the qubit is in the ground state. I measured these two switching curves to check whether -90 dBm was low enough to be considered as no power. The stars were taken when the qubit was placed into a saturated state by applying a long microwave pulse and the diamonds were taken after the qubit state was excited by a π/2-pulse. Notice that these two curves are similar but not the same. For a conventional s-curve, the π/2 and saturation curve should be identical. Also, neither of these curves shows a clear plateau at $P_s = 0.5$, as would be expected for conventional switching curves [42, 99-101]. These features are examples of anomalous switching behavior.

The open squares in Fig. 6.11 were taken after the qubit was excited by a π-pulse. Interestingly, the π-pulse curve (squares) and the π/2-pulse curve (diamonds) look like horizontally translated versions of the s-curve for 0 (circles). Furthermore the π/2 curve (diamonds) does not look like one would expect because it is not the weighted sum of the π-pulse curve and the 0-state curve.

The anomalous curves I obtained from device DS8 turned out to be an interesting phenomenon that was similar to some anomalies I had observed in DS6. I will discuss the phenomena in detail in Chapter 7 and describe how I was able to extract the probability P_1 of being in the excited state. In this chapter, I need to clearly distinguish between P_s

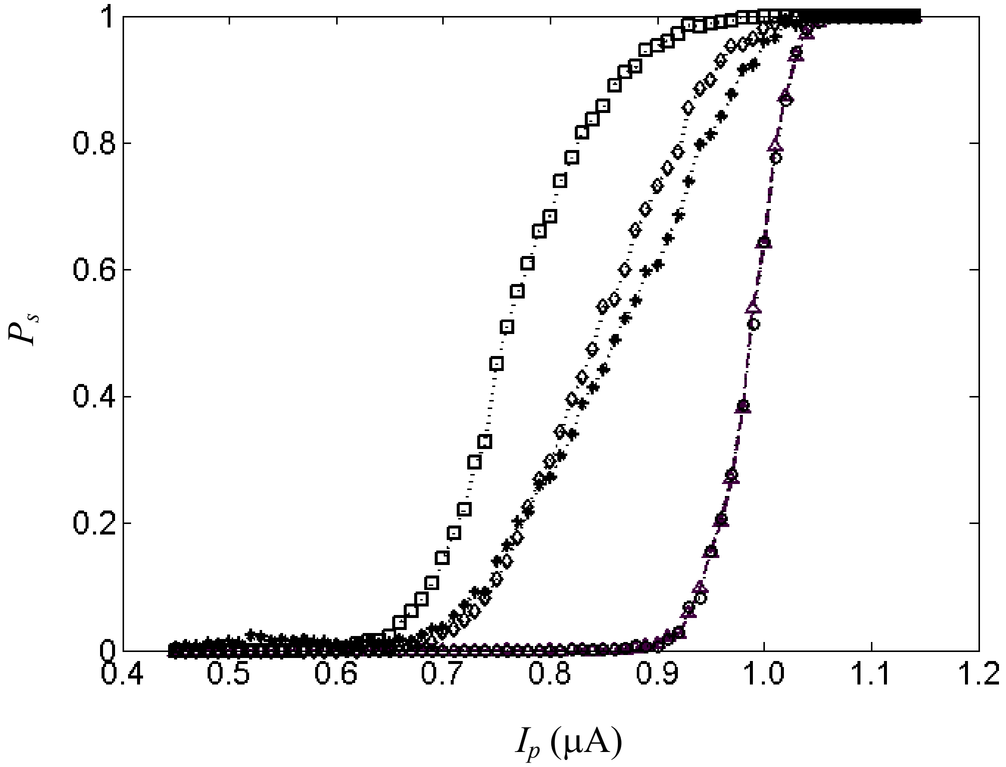

Figure 6.11: Switching probability P_s versus amplitude of current pulse I_p for device DS8. The open triangles were taken with a microwave output power of -90 dBm and the open circles were taken with a no applied microwave power; the two curves are virtually identical. The stars were taken when the qubit was in the saturated state and the diamonds were taken after the qubit was excited by a π/2-pulse. The open squares were taken after the qubit was excited by a π-pulse. The π/2 and saturation curve show no sign of a plateau at $P_s = 0.5$ and thus are anomalous.

(the switching probability) and P_1 (the probability to be in the excited state), and defer the discussion of P_1 extraction from P_s to Chapter 7.

6.2.3 Transition Frequency Spectrum

Figure 6.12 shows spectroscopic data I obtained from device DS8. The accessible qubit resonance frequencies (3-4 GHz) of device DS8 were lower than the resonance frequencies (6-7 GHz) of device DS6 because of the smaller critical currents in DS8. Although this frequency was about half of what I wanted, I note that for f_{01} = 3 GHz, $hf_{01}/k_B \approx$ 150 mK which is still much higher than 20 mK [45]. Figure 6.12 also shows that the small area qubit junction had one splitting over a frequency range of about 1 GHz.

In order to measure this spectrum, I fixed the bias flux and I swept the bias current to vary the resonance frequency. The microwave pulse was turned on for a long enough time to put the qubit into the saturated state. I then used the current pulse technique to measure the switching probability. [33, 36, 91]. It took more than a day to obtain the spectrum over the 1 GHz frequency range because thousands of repetitions of the pulse measurement were required to obtain good statistics at each point sampled.

A careful look at the spectrum in Fig. 6.12 reveals that the width of the resonance peak varied depending on the bias point. Figure 6.13 shows a plot of the spectroscopic coherence times T_2^* (from the FWHM of the peak using Eq. 6.1 versus the 0-to-1 transition frequency. There are a couple of small peaks in the plot and a large peak at 3.78 GHz. The large peak occurs in the region of the avoided crossing and suggests that the TLS has a relatively long life (of the order of 100 ns). I obtained the longest Rabi

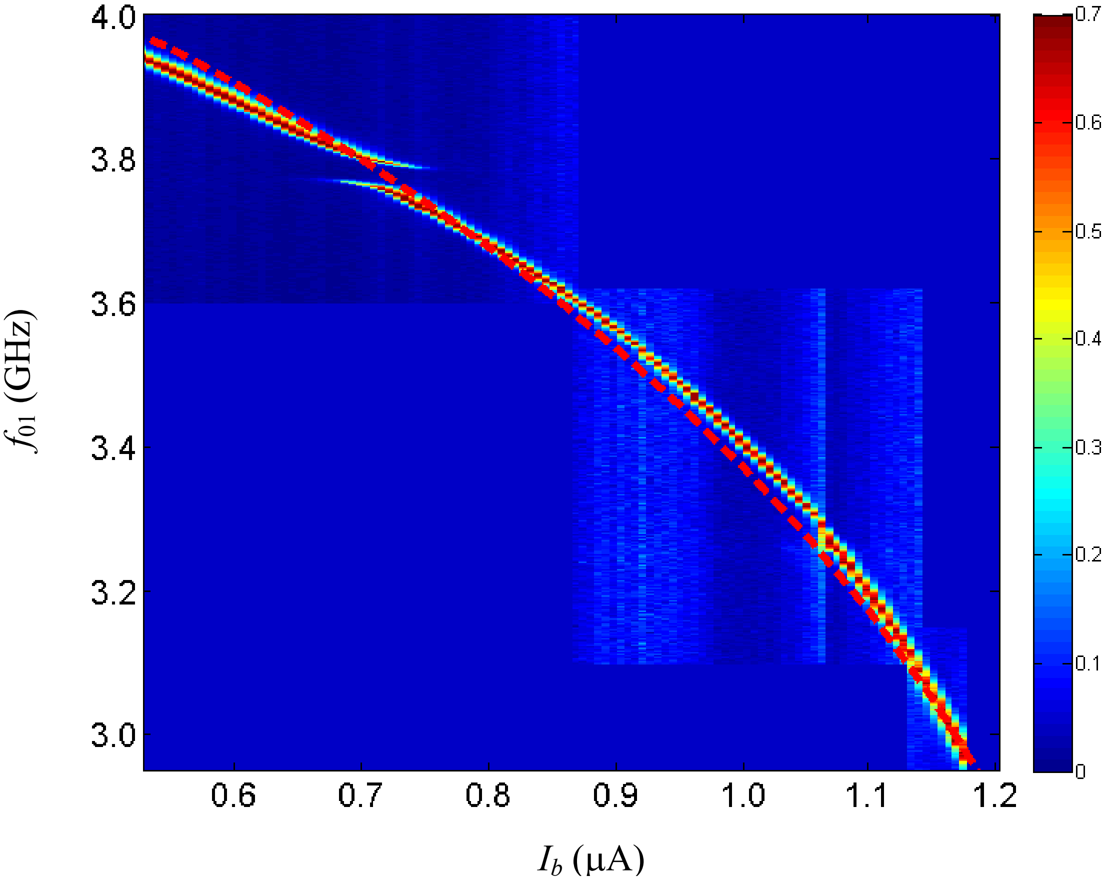

Figure 6.12: 0-to-1 transition frequency versus bias current of device DS8 measured at 20 mK and $\Phi_a = -0.38\ \Phi_o$ using the current pulse readout technique. The spectrum shows one clear avoided level crossing at 3.78 GHz and one possible splitting near 3.29 GHz. Blue represents no switching probability and red represents 50 % switching probability. A dashed red curve is fit using normal modes approximation as discussed in Chapter 2.

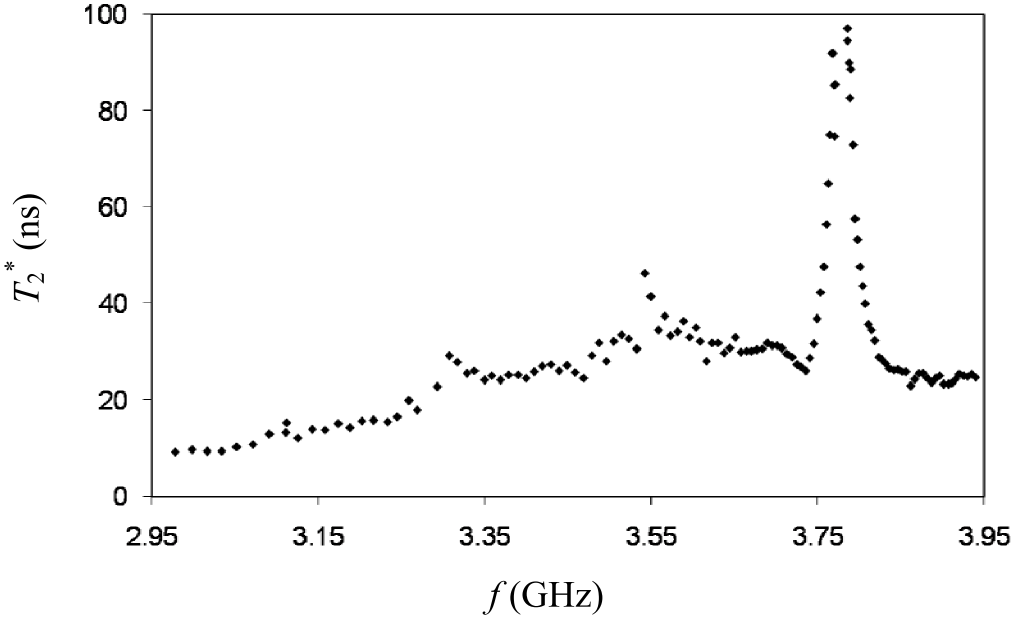

Figure 6.13: Spectroscopic coherence time T_2^* versus the resonance frequency f measured from the spectrum by sweeping the bias current. Because of an avoided level crossing around 3.78 GHz, there were two peaks that peaks showed narrower widths and gave a longer T_2^*. Except for that area, the spectroscopic coherence time T_2^* was largest near 3.55 GHz, close to the bias point where I obtained the best Rabi and relaxation data.

decay time near a resonance frequency of 3.52 GHz, which is close to the frequency of 3.55 GHz where there is a small peak in the plot of T_2^*.

There is something else about Fig. 6.13 that is worth noting. Overall, the spectroscopic coherence time T_2^* depends fairly systematically and smoothly on the bias point. In the middle frequency range, T_2^* seems to have larger values compared to at lower or higher frequencies. This suggests that T_2^* is being influenced by coupling of the qubit to the rest of the circuit rather than by TLS's [102].

6.2.4 Splitting Characterization

Martinis *et. al.* has argued that TLS defects in the junction dielectric are a major source of decoherence [103]. At Maryland, T. A. Palomaki found several avoided level crossings in the spectra of his devices and investigated the coupling between the qubit and the TLS's [77]. When the qubit resonance frequency matches the resonance frequency of the TLS, an avoided level crossing is produced in the spectrum. Martinis's group at NIST, Boulder, first showed that the coherence times of a phase qubit improved when the number of TLS's was reduced by making the junction smaller [43, 104].

Figure 6.13 shows one clear avoided crossing at 3.78 GHz. The splitting size is about 38 MHz. For these spectra, I used a relatively small frequency step of 2 MHz, so I could have resolved splittings that were much smaller than the one I found, if they were there. Of course, it is possible there were splittings smaller than 2 MHz, which I could not resolve.

Figure 6.14 shows line-cuts through the resonance peaks near the avoided level crossing. The solid curves are a χ^2 fit to Lorentzian peaks. The fits are okay, but some

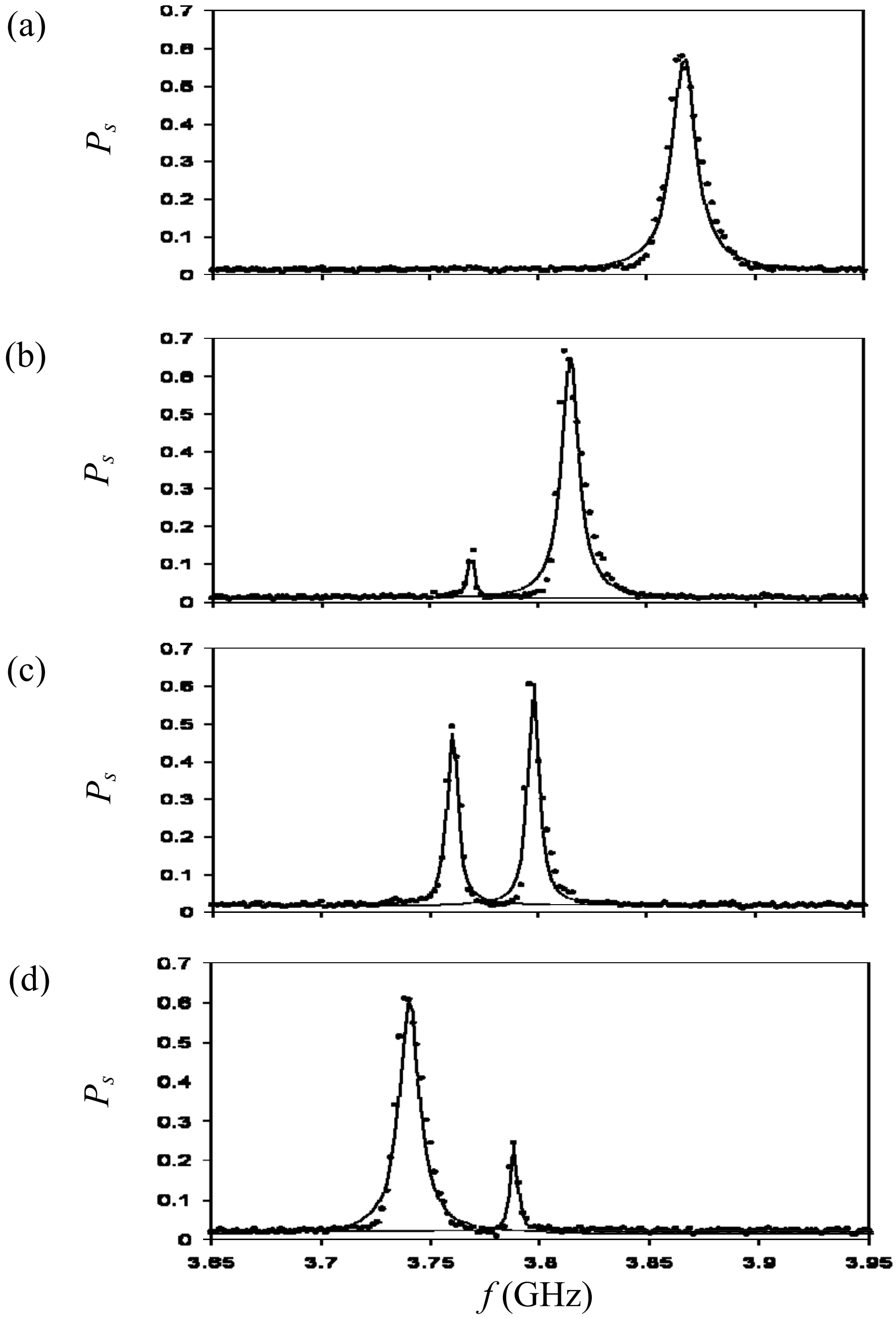

Figure 6.14: Points show measured resonance peaks in P_s versus f near an avoided crossing in device DS8 for $I_b = 0.615$ μA, (b) $I_b = 0.680$ μA, (c) $I_b = 0.709$ μA and (d) $I_b = 0.739$ μA and $\Phi_a = -0.38\ \Phi_o$. Curves are χ^2 fit to one or two Lorentzian peaks. The FWHM of the peaks in traces a-d are (0 MHz, 13 MHz), (3.5 MHz, 9MHz), (5.6 MHz, 6 MHz) and (11 MHz, 3.5 MHz).

clear deviations are present. The FWHM varies from 3.5 MHz to 13 MHz, corresponding to spectroscopic times of 100 ns to 25 ns.

6.2.5 Relaxation Rate

I measured the relaxation rate in device DS8 over a wide bias range. However, due to the anomalous behavior of the switching curves (see Chapter 7), I did not understand how to interpret the data until long after it was acquired. In fact, when I took data, I still did not know how the anomalous switching curves could be interpreted. After a couple of months, we began to have some ideas about what was happening and developed a tentative model as described in detail in Chapter 7.

Figure 6.15 (a) shows data from a relaxation time measurement obtained from the device at 3.520 GHz. The relaxation time of $T_1 \approx 280$ ns was by far the longest our group had found up to this point. This T_1 was about 10 times those T. A. Palomaki found in DS3 and also about almost 10 times longer than I found in DS6 [42]. Although T_1 was shorter than what I aimed for, 1 μs, it was a big improvement. I note that in general, I tried to avoid operating near an avoided crossing because it might affect the qubit performance. I note that at other biases, the relaxation rate was not this long. Figure 6.15 (b) shows a more typical relaxation curve measured at 3.694 GHz. Here $T_1 \approx 120$ ns.

As I discussed in sections 3.6 and 6.1.5, using $C_J \approx 0.05$ pF, $C_x \approx 0.83$ pF, $\tan(\delta_1) \approx 1.6 \times 10^{-3}$, $\tan(\delta_x) \approx 3 \times 10^{-5}$ and $R_{eff} \approx 0.34$ MΩ in device DS8, I find $T_1 \approx 300$ ns from Eq. 6.2 (see Table 3.1). In this case, the junction dielectric becomes a dominant source and the relaxation time closely matches $T_1 \approx 280$ ns that I obtained from the measurement. Relaxation in device DS8 still seems to be dominated by the junction dielectric.

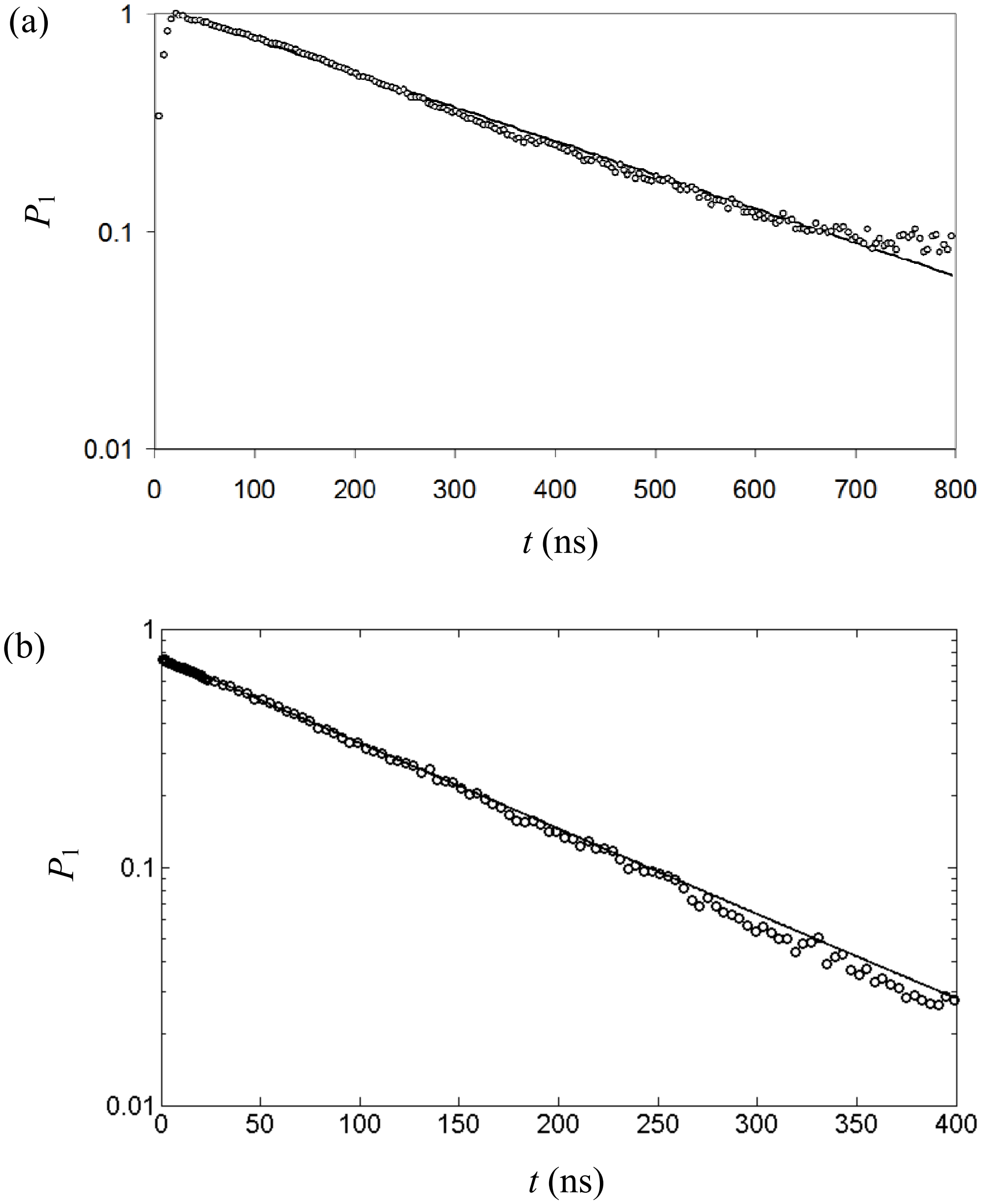

Figure 6.15: (a) The best relaxation curve obtained in device DS8 has $T_1 \approx 280$ ns measured at 3.520 GHz. (b) A typical relaxation curve in device DS8 with $T_1 \approx 120$ ns measured at 3.694 GHz. Points show probability P_1 versus time following application of a π-pulse. The points were extracted from the χ^2 fit to the full switching curves measured at each time, as discussed in Chapter 7. Straight lines are fit to an exponential decay.

6.2.6 Rabi Oscillations, Ramsey Fringe and Decoherence

I made many measurements of Rabi oscillations in device DS8 at various bias points. As discussed in the previous section, and in Chapter 7, I needed to measure complete switching curves to figure out what P_1 was at any time during the oscillations. Figure 6.16 (a) shows the best Rabi oscillation data I measured. For this data, the frequency was 3.520 GHz. This best case showed a Rabi decay time $T' \approx 120$ ns. This was 3-4 times longer than I found in device DS6. Depending on the bias point, the Rabi decay time also changed. Using the best $T_1 \approx 280$ ns and $T' \approx 120$ ns [see Fig. 6.15 (a) and 6.16 (a)] I obtained, $T_2 \approx 76$ ns, which is 25 % larger than that for device DS6. I also note that at other biases, the Rabi oscillations were not this long lived. Figure 6.16 (b) shows a more typical Rabi oscillation measured at 3. 420 GHz. Here $T' \approx 90$ ns.

I also did switching curve measurements of the Ramsey fringes. It was not easy to fit the switching curves to extract P_1 for the Ramsey fringe measurement, so instead Fig. 6.17 shows Ramsey measurement data for the switching probability P_s measured at one current pulse amplitude. Fig. 6.17 shows Ramsey fringes I obtained for a detuning of -10 MHz and a detuning of -90 MHz. Fitting gave a decay time $T_2^* \approx 43$ which is close to the best T_2^* I obtained from spectroscopy (see Fig. 6.13).

6.2.7 State Tomography

The relatively long coherence time in device DS8 allowed me to do state tomography measurements for the first time in our group. Tomography measurements

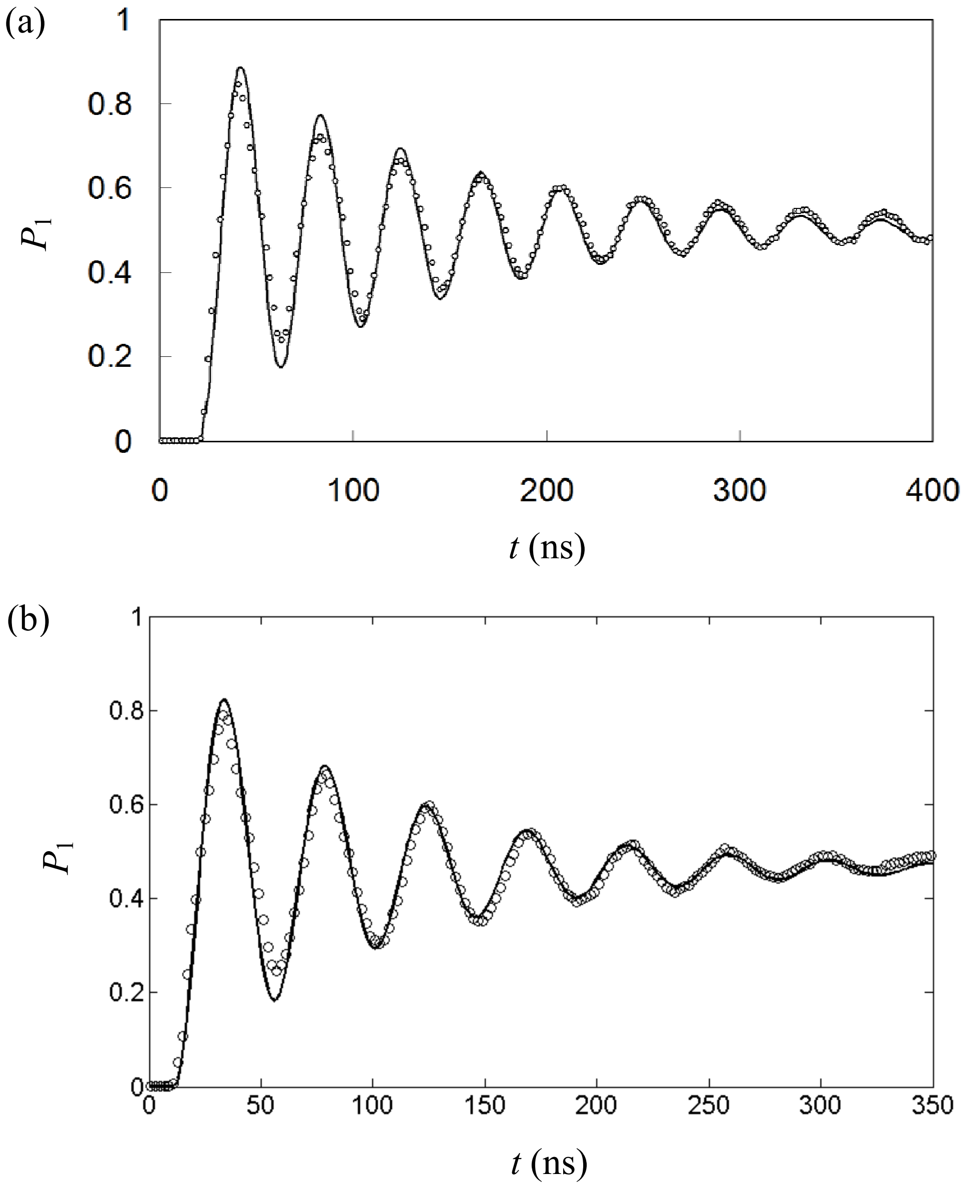

Figure 6.16: (a) Best Rabi oscillation curve is device DS8 plotted as P_1 versus time. Fit into decaying sine wave with $T' \approx 120$ ns which is 3 times longer than DS6. The device was measured at 3.520 GHz. (b) A typical Rabi curve with $T' \approx 90$ ns measured at 3.420 GHz. In both cases, the points were obtained by fitting the switching curves of Rabi oscillation measurement. Each data point was also extracted from the χ^2 fit of one full switching curve measured at each time.

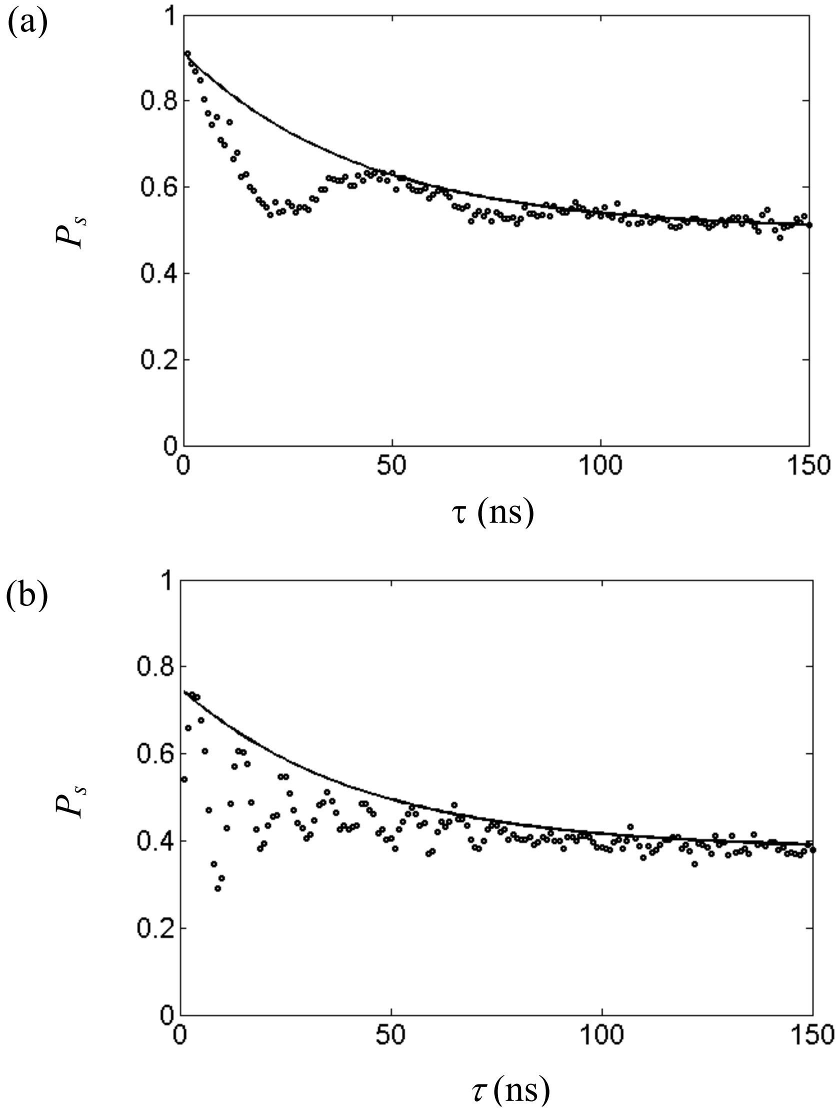

Figure 6.17: (a) Ramsey fringe curve P_s (switching probability versus time) measured at one current pulse amplitude in device DS8. The frequency of the measurement pulse was detuned -10 MHz from the resonance frequency of 3.543 GHz. (b) Ramsey fringes for detuning of -90 MHz. For both cases, the decay time $T_2^* \approx 43$ ns.

can be used to check every point would take too long that a qubit has really been prepared in the intended state [104, 105]. In a tomography measurement, the qubit is first prepared in the desired state, the state is then rotated to many possible points on the Bloch sphere and then measured. Two separate microwave pulses are required, the first to initialize the state of the qubit, and the second to rotate the state. For the second microwave pulse, the qubit state is rotated to any location on the Bloch sphere by varying the amplitude and phase. The amplitude and phase of the pulse were set using an IQ mixer (see Chapter 5). The phase ϕ was set by the voltage difference on I and Q ports in the mixer according to

$$\phi = \tan^{-1}\frac{V_I}{V_Q} \tag{6.5}$$

where V_I and V_Q mean the dc voltage amplitude applied to the I port and Q port of the IQ mixer.

Figures 6.18, 6.19 and 6.20 show my results from tomography measurement on device DS8 as well as simulations. In Fig. 6.18, the tomography was done for the qubit prepared in the ground state. In Fig. 6.19, the qubit was prepared in the $\left(|0\rangle + |1\rangle\right)/\sqrt{2}$ superposition state. Fig. 6.20 was obtained when the qubit was prepared in the $|1\rangle$ state. Examination of the figures shows good agreement for the ground state $|0\rangle$. The superposition state $\left(|0\rangle + |1\rangle\right)/\sqrt{2}$ of Fig. 6.19 mainly differ by a rotation of about 45° counterclockwise. Finally the tomography of the $|1\rangle$ (Fig. 6.20) is more consistent with a detuning of -105 MHz during the preparation and a 3π/4 rotation for the preparation state (not fully rotated for the $|1\rangle$).

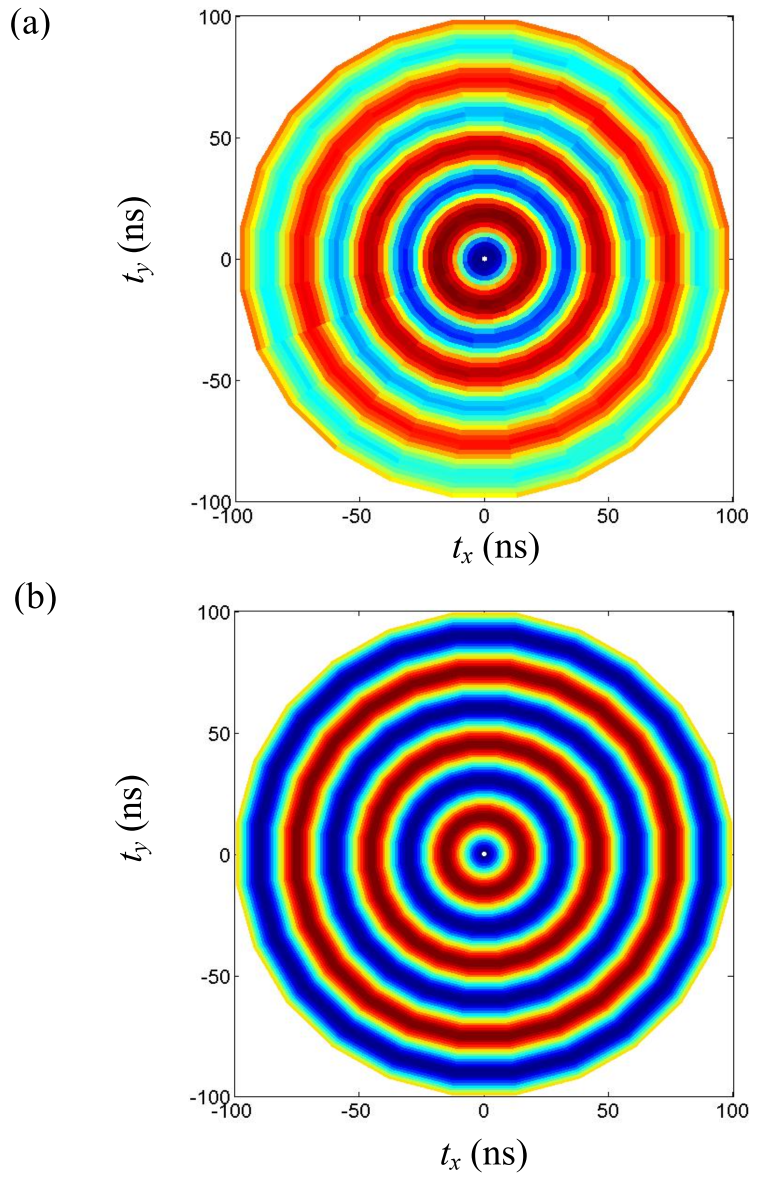

Figure 6.18: (a) Radial state tomography of device DS8 for the $\left|0\right\rangle$ state for I_b = 1.04 μA, Φ_a = -0.215 Φ_o, f_{01} = 3.519 GHz and $P_{\mu\omega}$ = 16 dBm (source power). (b) Simulation. Except for dephasing, the simulation matches the data.

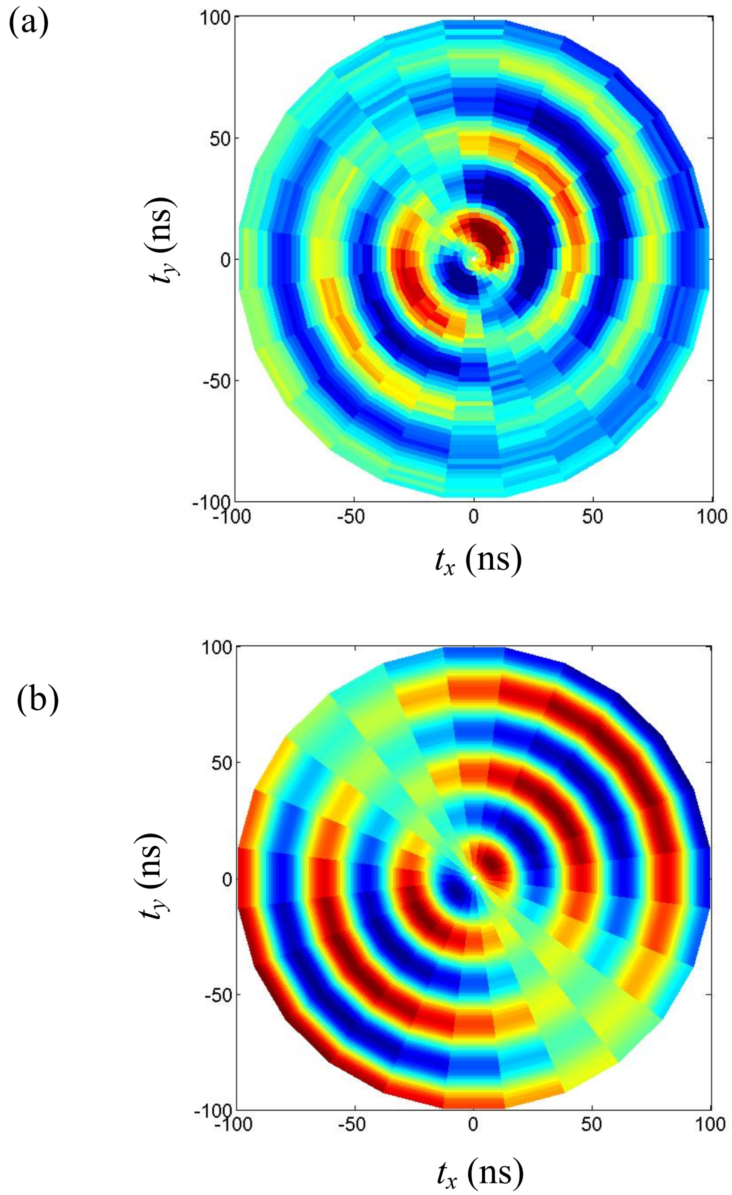

Figure 6.19: (a) Radial state tomography of device DS8 for the $\left(|0\rangle+|1\rangle\right)/\sqrt{2}$ state for I_b = 1.04 μA, Φ_a = -0.226 Φ_o , f_{01} =3.520 GHz and $P_{\mu\omega}$ = 16 dBm (source power). (b) Simulation with 45° rotation counterclockwise. Except for 45° overall rotation, the data and simulation match qualitatively.

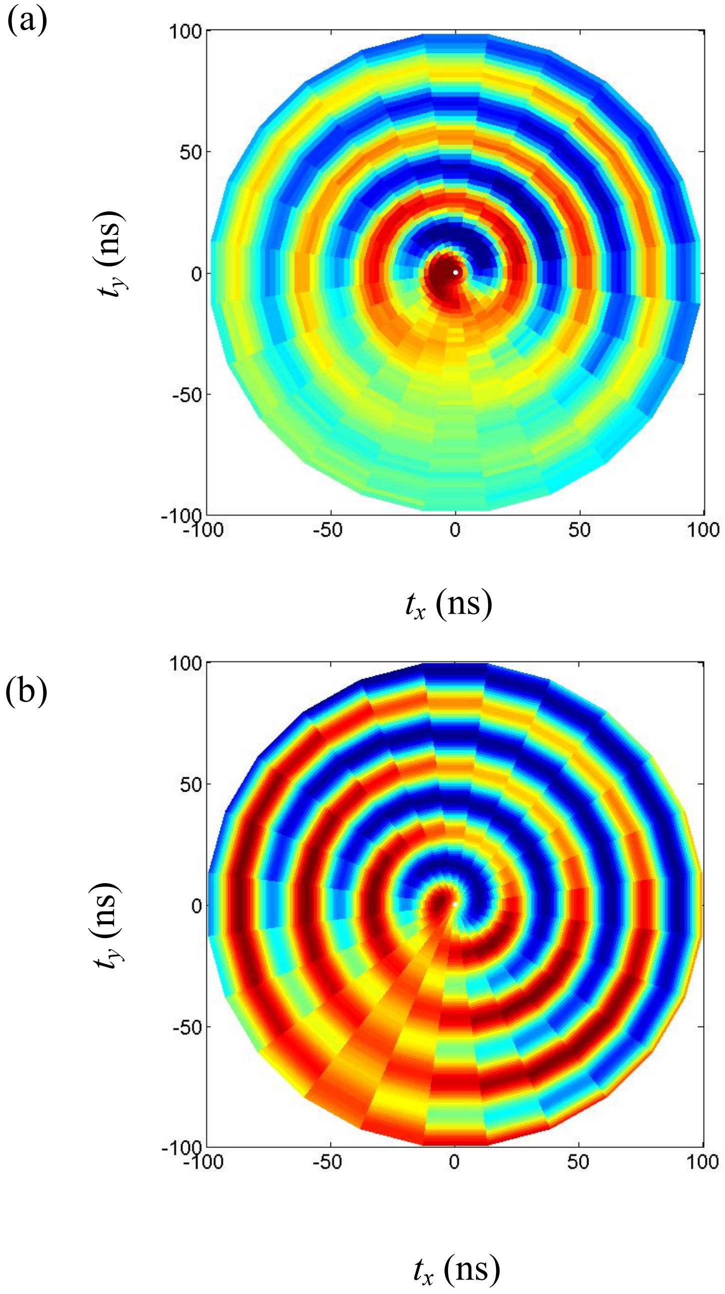

Figure 6.20: Radial state tomography of device DS8 for the $|1\rangle$ state for I_b = 1.04 μA, Φ_a = -0. 215 Φ_o , f_{01} = 3.519 GHz and $P_{\mu\omega}$ = 16 dBm (source power). Color corresponds to probability of switching. The data shows a spiraling pattern indicating detuning. (b) Simulation shows effect of -105 MHz detuning and a 3π/4 rotation for the preparation state.

The plots were obtained by measuring Rabi oscillations for 12 different phases. If you make a cut through the plots along a single line at angle ϕ, it produces one Rabi oscillation data set taken with fixed V_I and V_Q. The measured tomography pattern definitely changes depending on the initial state of the qubit and the state can be identified by comparing the data to simulations. I was not able to get a really good $|1\rangle$ state tomography. As in Fig. 6.20, they always appeared to be detuned.

6.3 Comparison of DS6, DS8 and DS3

I fabricated many devices, but only succeeded in measuring devices DS6 and DS8. I succeeded in achieving longer coherence times but not as long as my goal of 1 μs. In Table 6.1, I summarized the key parameters and times for devices DS6, DS8 and DS3 [42]. The main differences between DS6 and DS8 are the critical currents of the junctions, the area of the junctions and the SiN_x used for the dielectric layer in the shunting capacitor C_x.

First, DS6 and DS8 had fewer splittings than device DS3. In a 1 GHz frequency range, DS6 and DS8 had only one clear splitting. In contrast, DS3 had 8 splittings in a 1.2 GHz range. Thus, by reducing the area of the junction, many TLS defects were removed. However, device DS6 did not improve as much as I had hoped. Discrete TLS's were apparently not the main source of decoherence in our phase qubits. I obtained a longer relaxation time and a longer coherence time from DS8 by using a low-loss dielectric in the shunting capacitor. The Si-H rich SiN_x for device DS8 had $\tan(\delta) \approx 3\times10^{-5}$, which was less than $\tan(\delta) \approx 7\times10^{-4}$ of N-H rich SiN_x for device DS6. The relaxation time T_1 I found in DS8 suggested that the dielectric loss of the shunting capacitor was likely still a major source of relaxation. However, it was not the dominant factor for decoherence since T_2 and T_ϕ were about 80 ns. As summarized in Table 6.1, the relaxation time T_1 of device DS8 is about 10 times that of device DS3 and the Rabi decay time T' of device DS8 is about 4 times that of device DS3. These numbers show that device DS8 was a much better qubit than our previous devices. Although it did not reach our goal of $T_1 \approx 1$

Table 6.1: Parameters obtained for devices DS3 [42], DS6 and DS8. T_2 is obtained from $1/T' = 1/2T_1 + 1/2T_2$ and T_ϕ is obtained from $1/T_2 = 1/2T_1 + 1/T_\phi$.

Device	DS8	DS6	DS3
substrate	Al_2O_3	Al_2O_3	Al_2O_3
add C_x	Si-H rich SiN_x	N-H rich SiN_x	-
C_x (pF)	0.83	0.98	-
C_J (pF)	0.05	0.1	0.4
I_{01} (μA)	0.08	0.50	1.22
I_{02} (μA)	1.36	2.46	8.63
$f_{01,J1}$ (GHz)	3-4	6-7	10-11
$f_{01,J2}$ (GHz)	13-14	12-13	10-11
A_{J1} (μm^2)	2	4	15
T_1 (ns)	280	32	28
T'(ns)	120	42	27
T_2 (ns)	76	61	26
T_ϕ (ns)	88	1301	42

μs, analysis of the contribution to the loss from C_x and C_J gave $T_1 \approx 300$ ns, which was in good agreement with the data.

6.4 Summary

In this chapter, I discussed the results from SQUID phase qubits DS6 and DS8. For these device, I showed clear frequency dependent variations in T_2^* and the relaxation time T_1 and coherence time T_2 of the device was clearly superior to our previous devices; the best relaxation time ($T_1 \approx$ 280 ns) I found in device DS8 was an order of magnitude longer than in the group's earlier devices and T_1 was approaching the best times of about 500 ns obtained by other groups using phase qubits [106, 107]. The improvement mainly came by using a small junction and a shunting capacitor with a small loss tangent.

Chapter 7

Understanding the Anomalous Switching Curves

7.1 Introduction

In this chapter, I discuss my observations of anomalous switching curves (s-curves) in device DS8 and examine the underlying physics that causes the effect. Before examining anomalous switching curves, however, it is helpful to first review how I measured s-curves, discuss what one would expect ordinary s-curves to look like, and then identify what needs to be measured to be able to tell if s-curves are anomalous.

To clearly identify anomalous switching, I needed to measure three different switching curves: the s-curve for the ground state $\left|0\right\rangle$, the s-curve for the excited state $\left|1\right\rangle$ and the s-curve for the superposition state $\left(\left|0\right\rangle+\left|1\right\rangle\right)/\sqrt{2}$. I used the experimental set-up described in section 5.3.2 for doing this.

To measure the switching curve for the ground state $\left|0\right\rangle$, the qubit was first prepared in the ground state by waiting long enough for the device to relax to the ground state and not applying any microwaves. As described in Chapter 5, I then applied a brief (2 ns) current pulse of fixed amplitude I_p and recorded whether or not the device switched. I typically repeated this process 2000 times, each time using the same fixed current amplitude, and from this data calculated the probability P_{s0} that the device switched for this specific current amplitude I_p. I then chose the next current amplitude and repeated the entire process to find the switching probability P_{s0} for the new amplitude.

Continuing in this way with successively larger current pulse amplitudes, I mapped out the switching probability P_{s0} as a function of current amplitude I_p for the state $\left|0\right\rangle$. When plotted as a curve of probability P_{s0} versus pulse current amplitude I_p, one finds a characteristic s-shaped curve (see Fig 7.1). As expected, a smaller current pulse amplitude produced a smaller switching probability, and for a large enough pulse amplitude the device switches 100% of the time.

To find the switching curve for the $\left|1\right\rangle$ state, I used the same procedure as for $\left|0\right\rangle$, except that I applied a π-pulse to pump the system into $\left|1\right\rangle$ before applying the measurement current pulse. One expects the resulting switching probability P_{s1} versus the current I_p for the $\left|1\right\rangle$ state to be very similar to P_{s0} and this is generally the case (see Fig. 7.1). The main difference is that for any given current pulse size, the $\left|1\right\rangle$ state has a higher escape probability than the $\left|0\right\rangle$ state because there is a lower escape barrier. The result is that the s-curve for the $\left|1\right\rangle$ state is like the s-curve for $\left|0\right\rangle$ except it has been shifted towards lower pulse current (see Fig. 7.1).

To understand whether or not the switching is anomalous, one needs to also measure the switching curve $P_{\pi/2}$ for the superposition state. To measure this curve, I followed the same procedure as for the ground state, except that I applied a resonant $\pi/2$

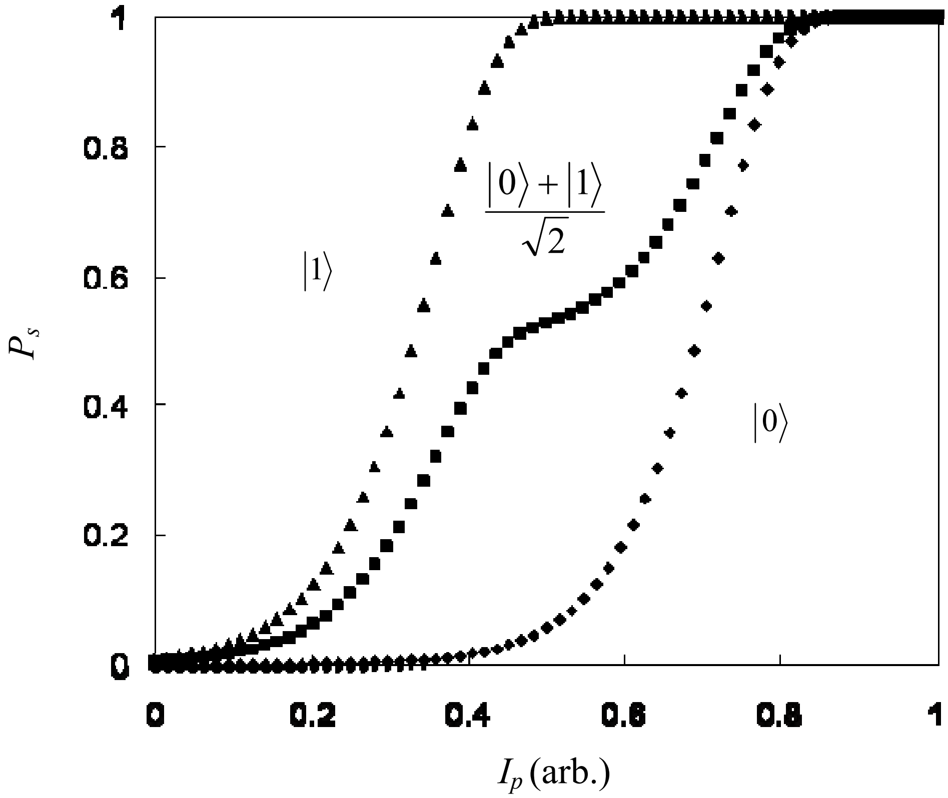

Figure 7.1: Simulation of conventional switching probability s-curves. Plots of switching probability P_{s0}, P_{s1} and $P_{\pi/2}$ versus pulse current amplitude I_p for respectively the ground state $|0\rangle$ (filled diamonds), the excited state $|1\rangle$ (filled triangles) and the superposition state $(|0\rangle+|1\rangle)/\sqrt{2}$ (filled squares). For conventional s-curves $P_{\pi/2} = 0.5\times(P_{s0} + P_{s1})$, *i.e.* it is just the weighted sum of the s-curves for the $|0\rangle$ and $|1\rangle$. Notice also how the s-curve for the superposition state has a clear shoulder near $P_s = 0.5$.

pulse to place the system into the state $\left(|0\rangle+|1\rangle\right)/\sqrt{2}$ before applying a short current pulse. In this superposition state, the probability of finding the system in the ground state is 50% and the probability of finding the system in the excited state is 50%. Thus one would expect that when the system was measured, 50% of the time the state would be projected into the ground state and the device would switch with probability P_{s0}. The remaining 50% of the time the state would be projected into the excited state and would switch with probability P_{s1}. In other words, we expect $P_{\pi/2} = 0.5\times(P_{s0}+P_{s1})$. The filled squares in Fig. 7.2 show a simulation of what one would expect for a conventional $P_{\pi/2}$ switching curve. Notice that the curve does not look much like the s-curves for 0 or 1, but rather it has a well-defined shoulder near $P_s = 0.5$. This is what one expects for a conventional s-curve, and this general behavior is what has been observed previously in many superconducting qubits [42, 99-101].

In contrast to a conventional set of s-curves, Fig. 7.2 shows s-curves that I measured on device DS8. The s-curves for $|0\rangle$ (filled diamonds) and $|1\rangle$ (filled squares) are much as one would expect. They do not appear unusual. On the other hand, the switching curve for the superposition state (filled triangles) does not have a shoulder and is not the weighted sum of the s-curve for the 0 and 1. Instead, the s-curve for the superposition state appears to be like the s-curve for 0, but shifted along the current axis towards lower currents. For comparison, the solid curve shows what would be expected for the superposition state if the switching curves were conventional, i.e. the solid curve shows $0.5\times P_{s0}+0.5\times P_{s1}$ where P_{s0} and P_{s1} are the measured switching curves for $|0\rangle$ and $|1\rangle$. Clearly the data differs qualitatively and quantitatively from what would be expected

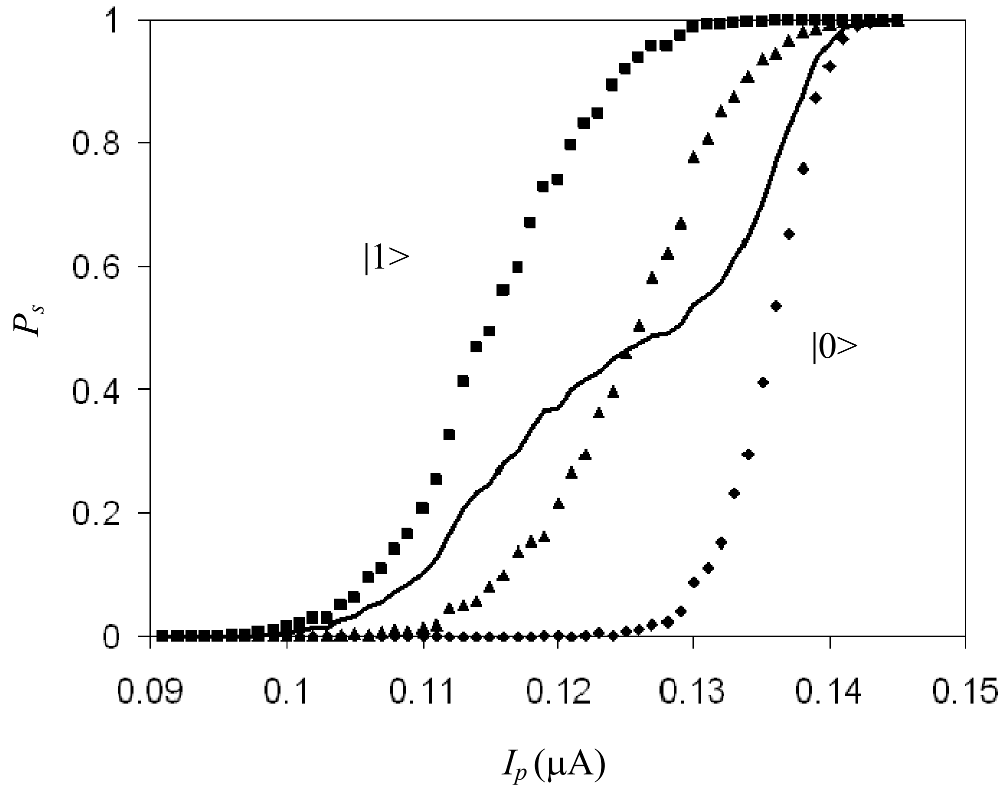

Figure 7.2: Switching probability P_s versus current pulse amplitude I_p for device DS8. The switching curve for the ground state $|0\rangle$ (filled diamond) and the excited state $|1\rangle$ (filled triangle) are shown in the plot as Fig. 7.1. The switching curve for the superposition state (filled square) is also presented in the plot, but it is not the weighted sum of two other curves and it seems to be shifted from the right to the left. For comparison, the solid curve is a weighted sum of two other curves.

for a conventional s-curve for the superposition state. I can conclude that this set of switching curves is anomalous.

One might think that perhaps the problem is that the superposition state was not prepared in an ideal superposition state. However, the measured s-curve for this “middle” state cannot be obtained from any constant weighted combination of the curve for P_{s0} and P_{s1}. Furthermore, measurements of s-curves at other points on the Rabi sphere show similar behavior, *i.e.* the measured s-curves show no shoulder and cannot be written as a weighted sum of P_{s0} and P_{s1}. Thus I can conclude that it is not a state preparation problem, but something unusual in the measurement itself.

7.2 Strong Coupling and the Born-Oppenheimer Approximation

7.2.1 Coupling Regime

In order to understand what is producing anomalous switching curves in device DS8, we need to consider again the Hamiltonian of the dc SQUID phase qubit.

In general, we can write the Hamiltonian for the dc SQUID phase qubit as $H = H_1 + H_2 + H_{12}$, where H_1 is the Hamiltonian of the qubit junction, H_2 is the Hamiltonian of the isolation junction and H_{12} describes the coupling between the two junctions. The coupling is due to the fact they are both in the same SQUID loop. K. Mitra [55] examined this Hamiltonian in detail in a regime where the two junctions were weakly coupled. Weak coupling means that the qubit can be treated as an independent junction to a good approximation. The weak coupling-regime corresponds to $I_{01}L >> \Phi_o$, where I_{01} is the critical current of the qubit junction and L is the loop inductance. This weak-coupling condition is equivalent to saying that the loop inductance L must be much larger than the

Josephson inductance of the qubit junction L_J.

A key point at this stage is to recognize that device DS8 is not in this weak-coupling regime. For device DS8, I estimate that $I_{01}L \approx 0.1\ \Phi_o$ which is far from the weak coupling regime. In this case, it will not be a good approximation to treat the qubit junction as an independent Josephson junction and we will need to re-examine the SQUID Hamiltonian for the case where $I_{01}L << \Phi_o$.

I note that the limit $I_{01}L << \Phi_o$ also effectively occurs in the quantronium qubit. Quantronium consists of a Cooper pair box (CPB) that is coupled to a large area Josephson junction that is used for state readout. The coupling between the CPB and large area junction is achieved by placing them in the same loop, much as the two junctions of the dc SQUID phase qubit are coupled together by the loop. In analyzing the behavior of quantronium, A. Cottet argued that the Born-Oppenheimer approximation was valid [108] and this proved to be useful for understanding the behavior of the device. This raises the question of whether the same approximation can be used in a dc SQUID phase qubit operating outside of the weak-coupling regime.

To understand why the Born-Oppenheimer approximation can be made in device DS8, I note that approximation is usually encountered in discussions of molecules or solids [109]. The idea is that a molecule is composed of nuclei and electrons that interact strongly with each other because they are charged. Since the nuclei are much heavier than the electrons, they tend to move more slowly and the energy scale associated with exciting motion of the nuclei will be much lower than that associated with exciting the electrons. The Born-Oppenheimer approximation involves assuming that the behavior of the electrons can be understood by treating the nuclei as if they were fixed. That is, in the

Born-Oppenheimer treatment of a molecule, one places nuclei at fixed locations and solve the resulting Schrödinger equation for the electrons. One can do this for many different nuclei positions and map out the resulting effective potential energy of the nuclei as a function of their position. The next step in the Born-Oppenheimer Approximation is to solve the effective Hamiltonian for the nuclei using the effective potential. The key to the validity of the approximation is that the electrons respond much more quickly than the nuclei.

We can now see why the Born-Oppenheimer approximation may be applicable in a dc SQUID phase qubit. In device DS8, the two junctions are coupled together by the loop inductance, but they have quite different resonance frequencies. I typically operated the qubit junction with a frequency in the 3-4 GHz range while the estimated plasma frequency of the isolation junction was about 14 GHz (see Table 6.1). This difference in frequency happened because the qubit junction had a much smaller critical current than the isolation junction and the qubit junction was also shunted by the added SiN_x capacitor (which is analogous to adding mass). Thus, the dynamics governing the detection junction phase γ_2 are relatively fast compared to the dynamics governing the qubit junction phase γ_1. Although the difference in the frequencies (a factor of 5) is not as extreme as for nuclei and electrons in a molecule (a factor of 100), it is plausible that the Born-Oppenheimer approximation will be a reasonable approximation.

7.2.2 Hamiltonian of the dc SQUID Phase Qubit

To quantify the coupling between the junctions, we need to examine the SQUID Hamiltonian. K. Mitra wrote the Hamiltonian for the dc SQUID phase qubit as [55]

$$H = \frac{{p_1}^2}{2m_1} + \frac{{p_2}^2}{2m_2} + U(\gamma_1 , \gamma_2) \tag{7.1}$$

where

$$\begin{aligned} U(\gamma_1 , \gamma_2) = & - I_{01} \frac{\Phi_0}{2\pi} \cos(\gamma_1) - I_{02} \frac{\Phi_0}{2\pi} \cos(\gamma_2) - \left(I \frac{\Phi_0}{2\pi} \frac{L_2}{L} \right) \gamma_1 - \left(I \frac{\Phi_0}{2\pi} \frac{L_1}{L} \right) \gamma_2 + \\ & + \frac{1}{2L} \left(\frac{\Phi_0}{2\pi} \right)^2 \left(\gamma_1 - \gamma_2 - 2\pi \frac{\Phi_a}{\Phi_0} \right)^2 \end{aligned} \tag{7.2}$$

Here m_1 and m_2 are the effective mass (see Eq. 2.9), p_1 and p_2 are the canonical momentum of the qubit junction and the detection junction, γ_1 and γ_2 are the phase differences across the junctions, I is the bias current, I_{01} and I_{02} are the critical currents of the two junctions, L_1 is the inductance of the arm of the SQUID that has the qubit junction, L_2 is the inductance of the arm of the SQUID that has the detection junction, $L= L_1+L_2$ and Φ_a is the flux applied to the SQUID loop.

The SQUID Hamiltonian can be divided into three parts,

$$H = H_1(\gamma_1, p_1) + H_2(\gamma_2, \gamma_2) + H_{12}(\gamma_1 , \gamma_2) \tag{7.3}$$

where the Hamiltonian H_1 of the qubit junction is

$$H_1(\gamma_1, p_1) = \frac{p_1^2}{2m_1} - \mathrm{I}_{o1} \frac{\Phi_o}{2\pi} \cos(\gamma_1) - \mathrm{I} \frac{\Phi_o}{2\pi} \frac{L_2}{L} \gamma_1 + \frac{1}{2L} \left(\frac{\Phi_o}{2\pi} \right)^2 \left(\gamma_1 - 2\pi \frac{\Phi_a}{\Phi_o} \right)^2 , \tag{7.4}$$

the Hamiltonian H_2 of the detection junction is

$$H_2(\gamma_2, p_2) = \frac{p_2^2}{2m_2} - \mathrm{I}_{o2} \frac{\Phi_o}{2\pi} \cos(\gamma_2) - \mathrm{I} \frac{\Phi_o}{2\pi} \frac{L_1}{L} \gamma_2 + \frac{1}{2L} \left(\frac{\Phi_o}{2\pi} \right)^2 \left(\gamma_2^2 + 4\pi \frac{\Phi_a}{\Phi_o} \gamma_2 \right) \tag{7.5}$$

and the coupling Hamiltonian H_{12} is

$$H_{12}(\gamma_1, \gamma_2) = -\frac{1}{L} \left(\frac{\Phi_o}{2\pi} \right)^2 \gamma_1 \gamma_2 \, . \tag{7.6}$$

With a minor rearrangement, the detection junction Hamiltonian H_2 can also be written in the form:

$$H_2(\gamma_2, p_2) = \frac{p_2^2}{2m_2} - \mathrm{I}_{o2}\frac{\Phi_o}{2\pi}\cos(\gamma_2) + \frac{\Phi_o}{2\pi L}(\Phi_a - \mathrm{I}\,L_1)\gamma_2 + \frac{1}{2L}\left(\frac{\Phi_o}{2\pi}\right)^2 \gamma_2^2 . \qquad (7.7)$$

Equation 7.7 will be convenient to use when we apply the Born-Oppenheimer approximation because the first order term in γ_2 has been separated from second order terms.

7.2.3 Device Parameters outside the Weak Coupling Regime

Before considering the coupling regime that device DS8 operated in, note that in a conventional SQUID phase qubit, the critical current I_{01} of the qubit junction is typically a few μA and this is comparable to the critical current of the detection junction I_{02}. With a loop inductance $L \approx L_1 \approx 1$ nH, one finds $L_1 I_{01} \approx \Phi_o$. This implies that the critical current is large enough that the SQUID loop can trap enough circulating current to produce more than one metastable flux state of the loop. In the rf SQUID phase qubit [103], the extra flux state is used to detect the state of the qubit (the excited state can tunnel from one flux state to the other).

We can see the importance of the condition $L_1 I_{01} \approx \Phi_o$ by considering Eq. 7.4 for the Hamiltonian H_1 for the qubit junction. The last term is

$$+\frac{1}{2L}\left(\frac{\Phi_o}{2\pi}\right)^2\left(\gamma_1 - 2\pi\frac{\Phi_a}{\Phi_o}\right)^2 . \qquad (7.8)$$

This is a quadratic potential with an energy scale of order $\Phi_o^2/8\pi^2 L$. This term represents inductive energy stored in the loop inductance and in Eq. 7.4 it adds to the washboard potential of the junction which has a scale of order $E_{J1} = I_{01}\Phi_o/2\pi$. For $E_{J1} >> \Phi_o^2/8\pi^2L$, one finds a tilted washboard potential with many local minima and a minor contribution from the quadratic inductive term. The local minima correspond to different amounts of circulating current in the loop. As we will see, this is the weak coupling limit. The weak coupling limit $E_{J1} >> \Phi_o^2/8\pi^2L$ can also be written as

$$2LI_{01}/\Phi_o >> 1/2\pi \tag{7.9}$$

or

$$I_{01}L >> \Phi_o/4\pi \qquad \text{(weak coupling regime)} \tag{7.10}$$

In contrast, for $E_{J1} << \Phi_o^2/8\pi^2$, one finds that the washboard potential makes only a minor contribution to the potential term in Eq. 7.4. In this limit the potential changes from being a washboard potential to a distorted quadratic potential. As shown in Fig. 7.3(a), the potential along the γ_1 direction looks very different from a washboard potential. In the γ_1 direction, U has an overall quadratic shape (with some small ripples), a single minimum, and no tunneling barrier to a set of running states (states with $V > 0$). In contrast, in the γ_2 direction, U is just the usual 1-D tilted washboard potential, as one would expect for a current biased junction. If the coupling between γ_1 and γ_2 could be ignored, this implies that the qubit junction does not have a barrier to tunnel through (or states to tunnel to) and would not be able to switch to the voltage state. On the other hand, the detection junction can still switch to the voltage state by tunneling through its potential barrier. In this case, an excited state of the qubit junction cannot itself tunnel, but rather it can only affect the tunneling rate of the detection junction. This is quite a different process than in a conventional phase qubit, where the excited state of the qubit

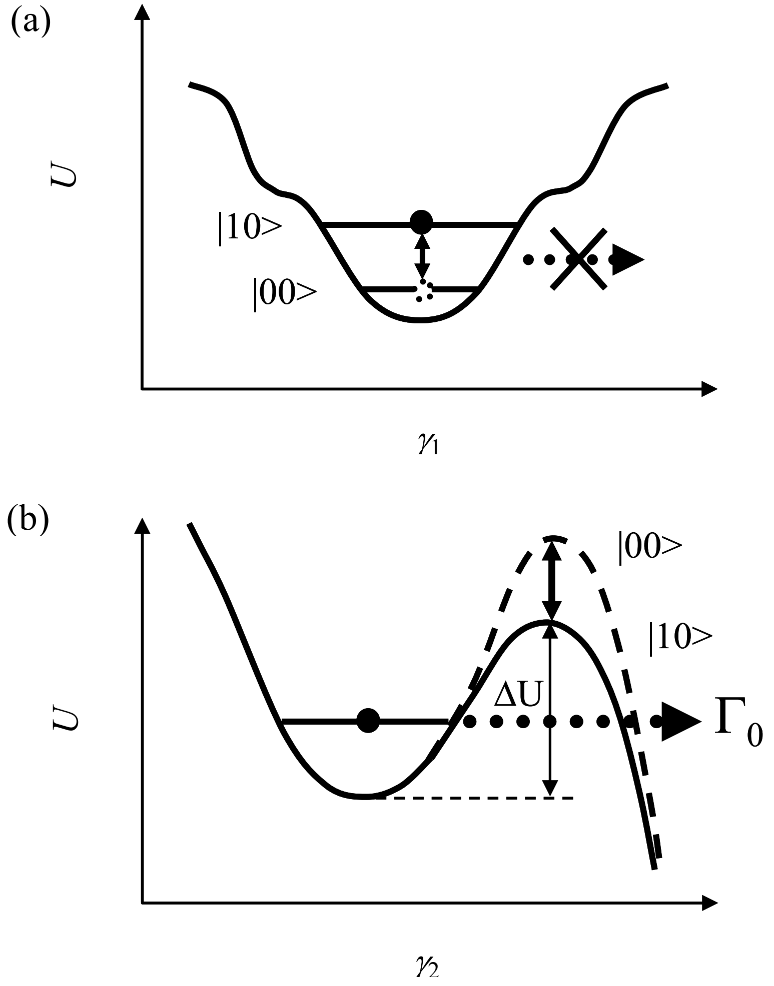

Figure 7.3: (a) Schematic picture of the potential energy U of the qubit junction versus the qubit junction phase difference γ_1 when $I_{01}L << \Phi_o/4\pi$. The potential is a distorted parabola, with a single minimum, and no tunneling barrier to running states. (b) Schematic picture of the potential energy U of the detection junction versus γ_2 when $I_{02}L >> \Phi_o/4\pi$. The potential is the familiar tilted washboard potential. The barrier height ΔU is modulated by current in the loop, which will be affected by the state of the qubit.

junction causes direct increase in the rate of tunneling of the qubit junction.

Note also from Eq. 7.6 that the coupling Hamiltonian H_{12} is of order $\Phi_o^2/4\pi^2 L$ while the qubit potential term in H_1 is of order $E_{J1} = I_{01}\Phi_o/2\pi$. Thus the ratio of the coupling term to the junction potential energy is of order $\Phi_o/2\pi L I_{01}$. For the coupling between the two junctions to be weak, we thus require that this ratio be small, *i.e.*

$$\Phi_o/2\pi L I_{01} << 1 \tag{7.11}$$

or

$$L I_{01} >> \Phi_o/2\pi \qquad \text{(weak coupling regime)} \tag{7.12}$$

Equation 7.12 is practically the same condition found in Eq. 7.10 that distinguishes whether the SQUID has multiple trapped flux states. For a typical SQUID phase qubit, we argued above that $L I_{01} \approx \Phi_o$, so that Eq. 7.12 and 7.10 are reasonably well-satisfied. Thus the coupling in a conventional phase qubit will be relatively small (less than 1) although clearly far from negligible. I note that K. Mitra has examined this situation much more thoroughly and found that for typical phase qubit parameters the junction coordinate can indeed be well-approximated as an ideal independent phase qubit [55].

We now consider the regime that device DS8 operated in. Device DS8 had $I_{01} \approx$ 80 nA and $I_{02} \approx 1.37\ \mu$A. The small value of I_{01} produced a Josephson inductance $L_{J1} \geq 3$ nH that was greater than the loop inductance ($L \approx 1$ nH), even when the device was unbiased. Furthermore, one finds $L_1 I_{01} \approx 0.06\ \Phi_o$. In this limit, the interaction term H_{12} is larger than the qubit junction potential term and the qubit potential in H_1 is more closely approximated as a distorted parabola than a tilted washboard potential. Therefore, in device DS8, we cannot treat the qubit junction as an independent particle moving in a washboard potential and we will need to be careful in treating the coupling to the isolation junction.

7.2.4 Working through the Born-Oppenheimer Approximation

With this background, we can now try applying the Born-Oppenheimer approximation to the Hamiltonian of a dc SQUID phase qubit. Because the resonance frequency of the qubit junction in device DS8 (3.5 GHz) is much less than the plasma frequency of the isolation junction (about 14 GHz), I will assume without further justification that the dynamics of γ_2 of the detection junction are much faster than the dynamics of γ_1 of the qubit junction. With this assumption, the Born-Oppenheimer approximation [109] says that the wavefunction of the system can be written as

$$\Psi(\gamma_1,\gamma_2) = \chi(\gamma_1,\gamma_2)\phi(\gamma_1). \tag{7.13}$$

The next step is using the Born-Oppenheimer approximation to solve Schrödinger's Equation,

$$H(\gamma_1,\gamma_2)\Psi(\gamma_1,\gamma_2) = E\Psi(\gamma_1,\gamma_2). \tag{7.14}$$

Using Eq. 7.13 this becomes

$$H(\gamma_1,\gamma_2)\chi(\gamma_1,\gamma_2)\phi(\gamma_1) = E\chi(\gamma_1,\gamma_2)\phi(\gamma_1). \tag{7.15}$$

In our case

$$H = H_1(\gamma_1, p_1) + H_2(\gamma_2,\gamma_2) + H_{12}(\gamma_1\,,\gamma_2\,) \tag{7.16}$$

where as noted previously, the Hamiltonian H_1 of the qubit junction is

$$H_1(\gamma_1, p_1) = \frac{p_1^2}{2m_1} - \mathrm{I}_{\mathrm{o}1}\frac{\Phi_o}{2\pi}\cos(\gamma_1) - \mathrm{I}\frac{\Phi_o}{2\pi}\frac{L_2}{L}\gamma_1 + \frac{1}{2L}\left(\frac{\Phi_o}{2\pi}\right)^2\left(\gamma_1 - 2\pi\frac{\Phi_a}{\Phi_o}\right)^2, \tag{7.17}$$

the Hamiltonian H_2 of the detection junction is

$$H_2(\gamma_2,p_2)=\frac{p_2^2}{2m_2}-\mathrm{I}_{o2}\frac{\Phi_o}{2\pi}\cos(\gamma_2)-\mathrm{I}\frac{\Phi_o}{2\pi}\frac{L_1}{L}\gamma_2+\frac{1}{2L}\left(\frac{\Phi_o}{2\pi}\right)^2\left(\gamma_2^2+4\pi\frac{\Phi_a}{\Phi_o}\gamma_2\right) \quad (7.18)$$

and the coupling Hamiltonian H_{12} is

$$H_{12}(\gamma_1,\gamma_2)=-\frac{1}{L}\left(\frac{\Phi_o}{2\pi}\right)^2\gamma_1\gamma_2 . \quad (7.19)$$

To find $\chi(\gamma_1,\gamma_2)$, I now assume that γ_1 changes so slowly that it can be taken as a fixed parameter. In other words, we assume that the kinetic energy term for γ_1 can be ignored in Eq. 7.17. Since we take γ_1 as being fixed at this stage, H_1 will introduce a fixed term that depends on our choice of γ_1 but will not influence the dynamics of γ_2. Similarly since γ_1 is taken as constant, the factor $\phi(\gamma_1)$ in Eq. 7.15 can be cancelled from both sides. Thus we can ignore H_1 and $\phi(\gamma_1)$ for now and Eq. 7.15 reduces to an effective Schrödinger equation for the detection junction

$$H_2'\chi(\gamma_1,\gamma_2)=[H_2(\gamma_2,p_2)+H_{12}(\gamma_1,\gamma_2)]\chi(\gamma_1,\gamma_2)=E_2(\gamma_1)\,\chi(\gamma_1,\gamma_2). \quad (7.20)$$

Here I note that the eigenvalue of the equation $E_2(\gamma_1)$ will depend on γ_1 since H_{12} depends on both γ_1 and γ_2. We will see that $E_2(\gamma_1)$ acts as an effective potential energy for the qubit junction due to coupling to the isolation junction.

Substituting for H_2 and H_{12}, I can write H_2' explicitly as

$$H_2'=\frac{p_2^2}{2m_2}-\mathrm{I}_{o2}\frac{\Phi_o}{2\pi}\cos(\gamma_2)+\frac{\Phi_o}{2\pi L}(\Phi_a-\mathrm{I}\,L_1)\gamma_2+\frac{1}{2L}\left(\frac{\Phi_o}{2\pi}\right)^2\gamma_2^2-\frac{1}{L}\left(\frac{\Phi_o}{2\pi}\right)^2\gamma_1\gamma_2 . \quad (7.21)$$

By rearranging slightly, H_2' can be written as

$$H_2' = \frac{p_2^2}{2m_2} - \mathrm{I}_{o2}\frac{\Phi_o}{2\pi}\cos(\gamma_2) + \frac{1}{2L}\left(\frac{\Phi_o}{2\pi}\right)^2\left[\gamma_2 + \frac{2\pi}{\Phi_o}\left(-\frac{\Phi_o}{2\pi}\gamma_1 + \Phi_a - \mathrm{I}\,L_1\right)\right]^2$$
$$- \frac{1}{2L}\left(\frac{\Phi_o}{2\pi}\right)^2\left[\frac{2\pi\,\Phi_a - 2\pi\,\mathrm{I}\,L_1}{\Phi_o} - \gamma_1\right]^2. \qquad (7.22)$$

Since γ_1 is taken as constant, the last term yields a constant offset. I can also define an effective applied flux:

$$\Phi_{eff} = \Phi_a - \mathrm{I}\,L_1 - \frac{\Phi_o}{2\pi}\gamma_1 \qquad (7.23)$$

and then write the Hamiltonian H_2' in a familiar form:

$$H_2' = \frac{p_2^2}{2m_2} - \mathrm{I}_{o2}\frac{\Phi_o}{2\pi}\cos(\gamma_2) + \frac{1}{2L}\left(\frac{\Phi_o}{2\pi}\right)^2\left[\gamma_2 + \frac{2\pi\,\Phi_{eff}}{\Phi_o}\right]^2 + \alpha \qquad (7.24)$$

where

$$\alpha = -\frac{1}{2L}\left(\frac{\Phi_o}{2\pi}\right)^2\left[\frac{2\pi\Phi_a - 2\pi\,\mathrm{I}\,L_1}{\Phi_o} - \gamma_1\right]^2 \qquad (7.25)$$

just depends on γ_1. Equation 7.24 is just the Hamiltonian of an rf SQUID, and we can find the energy $E_2(\gamma_1)$ and $\chi(\gamma_1,\gamma_2)$ by solving Eq 7.21 in the usual way. Of course we will need to do this for many values of γ_1 corresponding to different values of effective flux.

Once we have found $E_2(\gamma_1)$ and $\chi(\gamma_1,\gamma_2)$, we can proceed to find $\phi(\gamma_1)$. To see how to do this, consider Eq. 7.15 again. We can write

$$\left(H_1(\gamma_1,p_1) + H_2(\gamma_2,\gamma_2) + H_{12}(\gamma_1,\gamma_2)\right)\chi(\gamma_1,\gamma_2)\phi(\gamma_1) = E\chi(\gamma_1,\gamma_2)\phi(\gamma_1) \qquad (7.26)$$

We also now have that

$$\begin{aligned}(H_1 + H_2 + H_{12})\chi(\gamma_1,\gamma_2)\phi(\gamma_1) &= (H_1 + H_2')\chi(\gamma_1,\gamma_2)\phi(\gamma_1) \\ &= H_1(p_1,\gamma_1)\chi(\gamma_1,\gamma_2)\phi(\gamma_1) + E_2(\gamma_1)\chi(\gamma_1,\gamma_2)\phi(\gamma_1)\end{aligned} \qquad (7.27)$$

And thus we can write an effective Hamiltonian for the qubit junction

$$H_1(p_1,\gamma_1)\chi(\gamma_1,\gamma_2)\phi(\gamma_1)+E_2(\gamma_1)\chi(\gamma_1,\gamma_2)\phi(\gamma_1)=E\chi(\gamma_1,\gamma_2)\phi(\gamma_1) \tag{7.28}$$

Finally, we assume that $\chi(\gamma_1,\gamma_2)$ does not vary rapidly with γ_1, and that therefore we can neglect any action of H_1 on $\chi(\gamma_1,\gamma_2)$ and treat it instead as a constant. Eq. 7.28 can then be simplified to

$$H_1(p_1,\gamma_1)\phi(\gamma_1)+E_2(\gamma_1)\phi(\gamma_1)=E\,\phi(\gamma_1) \tag{7.29}$$

This is just an effective 1-D Hamiltonian for the qubit junction and we can find the energy eigenvalues E and the wavefunction $\phi(\gamma_1)$ in the usual way, at least in principle. This completes the application of the Born-Oppenheimer approximation to the dc SQUID phase qubit.

7.2.5 Dependence of the Barrier Height on the Qubit State

From the above analysis, we can now understand how a change in state of the qubit junction can lead to an effective tilt of the tunneling barrier of the isolation junction. Consider again the factor Φ^I_{eff} introduced above in our discussion of the effective Hamiltonian H_2' of the detection junction. I defined the effective flux as

$$\Phi_{eff}=\Phi_a-\mathrm{I}\,L_1-\frac{\Phi_o}{2\pi}\gamma_1\;. \tag{7.30}$$

Notice that Φ_{eff} contains the phase γ_1 of the qubit junction and that this phase enters into the potential in much the same way as, and in linear combination with, the applied flux and the bias current.

I thus conclude that a change in the phase of the qubit junction γ_1 will behave much like an effective change in the current I applied to the device. Since applying current will cause the tunnel barrier of the isolation junction to change, the implication is that different γ_1 will likewise produce different tunneling rates. We can extract this tilting term in the detection junction Hamiltonian H_2' and it is just

$$H_{tilt}^{I} = -\left[\gamma_1 \frac{1}{L}\left(\frac{\Phi_o}{2\pi}\right)\right]\frac{\Phi_o}{2\pi}\gamma_2 . \tag{7.31}$$

Examination of this expression reveals the effect of a change in γ_1 is to produce an effective current change in the detection junction given by

$$\delta I_2^{eff} = \gamma_1 \frac{1}{L}\left(\frac{\Phi_o}{2\pi}\right). \tag{7.32}$$

Let us now suppose that the detection junction is in the ground state. The approximate rate at which the detection junction will tunnel to the voltage state is then given by

$$\Gamma \approx f_P \exp(-7.2\frac{\Delta U}{\hbar\omega_P}) \tag{7.33}$$

where $f_p = \omega_p/2\pi$ is the plasma frequency of the detection junction and ΔU is the potential barrier height of the detection junction [see Fig. 7.3(b)]. In general, the detection junction is biased with an average current I_2 and this will set the barrier height ΔU. The barrier height can then be perturbed by a small amount due to an applied current pulse I_p or because of an effective current change δI_2^{eff} due to changes in γ_1. For a small current change δI_2 in the detection junction, one can show that Eq. 7.33 gives an exponential change in the tunneling rate, which we can write as

$$\Gamma \approx \Gamma_0 \exp(A\ \delta I_2) = \Gamma_0 \exp(A\ (I_p + \delta I_2^{eff})) = \Gamma_0 \exp\left(A\ I_p + \gamma_1 \frac{A}{L}\left(\frac{\Phi_0}{2\pi}\right)\right). \tag{7.34}$$

Here Γ_0 is the tunneling rate for δI_2=0 and the factor A is a logarithmic slope of the escape rate with current which depends only weakly on the bias. The implication of Eq. 7.34 is that the tunneling rate will depend on the phase of the qubit junction.

7.2.6 Superposition State

I now consider the situation when the qubit state is in a superposition of $|0\rangle$ and $|1\rangle$ and the detection junction is in the ground state. The time-dependent state of the entire system can be expressed as

$$|\Psi(t)>=\alpha\,|00>+\beta\exp\big(i(\omega_{01}t+\phi)\big)|10> \tag{7.35}$$

Here the first index in the ket is for the state of the qubit junction *J1* and the second index is for the state of the detection junction *J2*, ω_{01} is the 0-to-1 transition frequency of the qubit at the bias point, ϕ is the initial phase factor of the superposition state and α and β can be taken as positive real numbers that satisfy $\alpha^2+\beta^2 = 1$.

We now treat the effective perturbation current in the isolation junction as a quantum operator. The expectation value of δI_2 at time t is then

$$\begin{aligned}<\Psi\,|\,\delta I_2\,|\,\Psi>=\alpha^2<00\,|\,\delta I_2\,|\,00>+\beta^2<10\,|\,\delta I_2\,|\,10>\\ +2\,|\,\alpha\,||\,\beta\,|\cos(\phi+\omega t)<00\,|\,\delta I_2\,|\,10>.\end{aligned} \tag{7.36}$$

This can be written as

$$<\Psi\,|\,\delta I_2\,|\,\Psi>=\alpha^2 I_{00}+\beta^2 I_{11}+2\,|\,\alpha\,||\,\beta\,|\cos(\phi+\omega t)I_{01} \tag{7.37}$$

where I_{00} = <00|δI_2|00> is the expectation value of δI_2 when the qubit junction and isolation junction are in the ground state, I_{11} = <10|δI_2|10> is the expectation value of δI_2 when the qubit junction is in the excited state and the isolation junction is in the ground state and I_{01} = <00|δI_2|10> is an interference term.

From Eqs. 7.34 and 7.37, I can then obtain an expression for the tunneling rate at time t

$$\Gamma \approx \Gamma_0 \exp[A(\alpha^2 I_{00} + \beta^2 I_{11} + 2|\alpha||\beta|\cos(\omega_{01} t + \phi) I_{01})]. \qquad (7.38)$$

In going from Eq. 7.34 to Eq. 7.38, I had to assume that I could replace δI_2 by the expectation value $<\Psi|\delta I_2|\Psi>$. This is a key assumption and it would take a much more thorough examination of the situation to understand whether in fact it is justifiable. This theoretical issue is not simple, and since this is an experimental thesis, I will instead take this as a model assumption, and examine the consequences.

From Eq. 7.38 we now see that the tunneling rate of the detection junction depends on the state of the qubit junction and it depends on time. The exponent corresponds to a superposition of current flow in the |00> and |01> states as well as an interference term. This time varying current perturbs the tunnel barrier and causes a rapid variation in its escape rate. In practice the device is ordinarily pulsed for only a brief time τ, and either tunnels or does not during this time. Given the tunneling rate as a function of time, the probability P_s that the system switches to the voltage state between time $t = 0$ and $t = \tau$ is

$$P_s = 1 - \exp\left(-\int_0^\tau \Gamma(t) dt \right). \qquad (7.39)$$

Given Eq. 7.38, we can write

$$P_s = 1 - \exp\left(-\int_0^\tau \Gamma_0 \exp[A(\alpha^2 I_{00} + \beta^2 I_{11} + 2|\alpha||\beta|\cos(\omega_{01} t + \phi) I_{01}] dt \right). \qquad (7.40)$$

This expression for P_s can be simplified somewhat to obtain

$$P_s = 1-\exp\left(-\Gamma_0 \exp[A(\alpha^2 I_{00} + \beta^2 I_{11})] * \int_0^\tau \exp[2A|\alpha||\beta| I_{01} \cos(\omega_{01} t + \phi)] dt \right). \quad (7.41)$$

Note in Eq. 7.41 that the $\cos(\omega_{01}t+\phi)$ term is in the exponent and it will tend not to be averaged away during the integration unless $2A|\alpha||\beta|I_{01} << 1$. Notice also that if I_{01} vanishes, then this difficulty goes away, and one obtains simply

$$P_s = 1-\exp\left(-\Gamma_c \exp[A(\alpha^2 I_{00} + \beta^2 I_{11})]\right). \quad (7.42)$$

Unfortunately, there is no reason to expect that I_{01} vanishes or $2A|\alpha||\beta|I_{01} << 1$ in general, so we will need to use Eq. 7.41. In the general expression (Eq. 7.41), there does not appear to be an analytical solution to the remaining integration and one must generally resort to approximations or numerical calculation of the integral.

The case of interest experimentally corresponds to a relatively long duration measurement pulse, *i.e.* $\omega_{01}\tau >> 1$. In this case, it is easy to see that the result becomes insensitive to the phase and that the exponential acts like a rectifier on the cosine term, *i.e.* each positive swing of the $\cos(\omega t)$ produces an exponentially larger contribution than a negative swing, and the more swings there are the larger the integral is. In this limit, the integral will grow linearly with the time, and we can define an effective time τ_{eff} for the pulse by writing

$$\int_0^\tau \exp[2A|\alpha||\beta| I_{01} \cos(\omega_{01} t + \phi)] dt = \tau_{eff} \exp\left(2A|\alpha||\beta| I_{01}\right). \quad (7.43)$$

One then obtains

$$P_s = 1-\exp\left[-\Gamma_c \tau_{eff} \exp\left\{ A\left(\alpha^2 I_{00} + \beta^2 I_{11} + 2|\alpha||\beta||I_{01}|\right)\right\}\right]. \quad (7.44)$$

Further analysis shows that the factors $\Gamma_0 \tau_{eff}$ and A can be absorbed into dimensionless effective current terms $\hat{I}_{00}$, $\hat{I}_{11}$ and $\hat{I}_{01}$. For example, I can define $\hat{I}_{00}=\{A\ln(\Gamma_o\tau_{eff})\}I_{00}$. We can then write simply

$$P_s(I_p)\approx 1-\exp(-\exp(\alpha^2\hat{I}_{00}+\beta^2\hat{I}_{11}+2|\alpha||\beta|\hat{I}_{01})). \qquad (7.45)$$

Here I write P_s as a function of I_p because the effective current terms $\hat{I}_{00}$, $\hat{I}_{11}$ and $\hat{I}_{01}$ will in general be functions of the current pulse amplitude I_p applied to the device. P_s will also depend on the pulse duration τ and the bias point. In principle, we should be able to obtain these effective current terms from analysis of the system Hamiltonian. In practice, I extracted these parameters from the data, as described in the next section, and tested whether the switching curves obeyed Eq. 7.45 for different state amplitudes α and β.

A key point is that Eq. 7.45 produces switching curves which are anomalous for superposition states. Suppose for example that the system is prepared in a superposition state with $\alpha=\beta=1/\sqrt{2}$. In this case, Eq. 7.45 yields a switching curve of the form:

$$P_{s,\pi/2}(I_p)\approx 1-\exp(-\exp(\hat{I}_{00}/2+\hat{I}_{11}/2+\hat{I}_{01})) \qquad (7.46)$$

This expression is not equal to the weighted sum of the switching curve for 0 and 1. Thus

$$0.5\times P_{s,0}(I_p)+0.5\times P_{s,1}(I_p)\approx 1-\frac{1}{2}\exp(-\exp(\hat{I}_{00}))-\frac{1}{2}\exp(-\exp(\hat{I}_{11}))\neq P_{s,\pi/2}(I_p). (7.47)$$

Thus the curves predicted by Eq. 7.45 are anomalous.

7.3 Analysis of Switching Curves

7.3.1 Analysis Procedure

Equation 7.45 for P_s can now be compared to measured switching data. The idea is that I can vary α and β by examining states at different times during a Rabi Oscillation and check whether the resulting switching curves obey Eq. 7.45. Since the theory I presented above did not give an explicit form for $\hat{I}_{00}$ and $\hat{I}_{11}$ and $\hat{I}_{01}$, I will need to find them from the experiment. Once these are found (from the switching curves for three different states) the switching curves for all other states should be predictable from Eq. 7.45.

To proceed, I first find $\hat{I}_{00}$ and $\hat{I}_{11}$ as a function of I_p from the measured switching curves for the |00> and |10> state, respectively. To find $\hat{I}_{00}$, I prepare the qubit in the ground state (I always have the detection junction in the ground state before applying a measurement pulse) and measure the experimental probability of switching P_{s0} versus I_p. In this case $\alpha = 1$, $\beta = 0$, and Eq. 7.45 gives

$$P_{s,0}(I_p) \approx 1 - \exp(-\exp(\hat{I}_{00})) \qquad (7.48)$$

and I can then find $\hat{I}_{00}$ as a function of the current pulse amplitude by plugging my measured values for $P_s(I_p)$ into

$$\hat{I}_{00}(I_p) = \ln\{-\ln(1 - P_{s0}(I_p))\}. \qquad (7.49)$$

Figure 7.4 shows an example of a plot of $\hat{I}_{00}$ that I extracted from measurements on device DS8.

To find $\hat{I}_{11}$, I prepared the qubit in the excited state by applying a π-pulse and

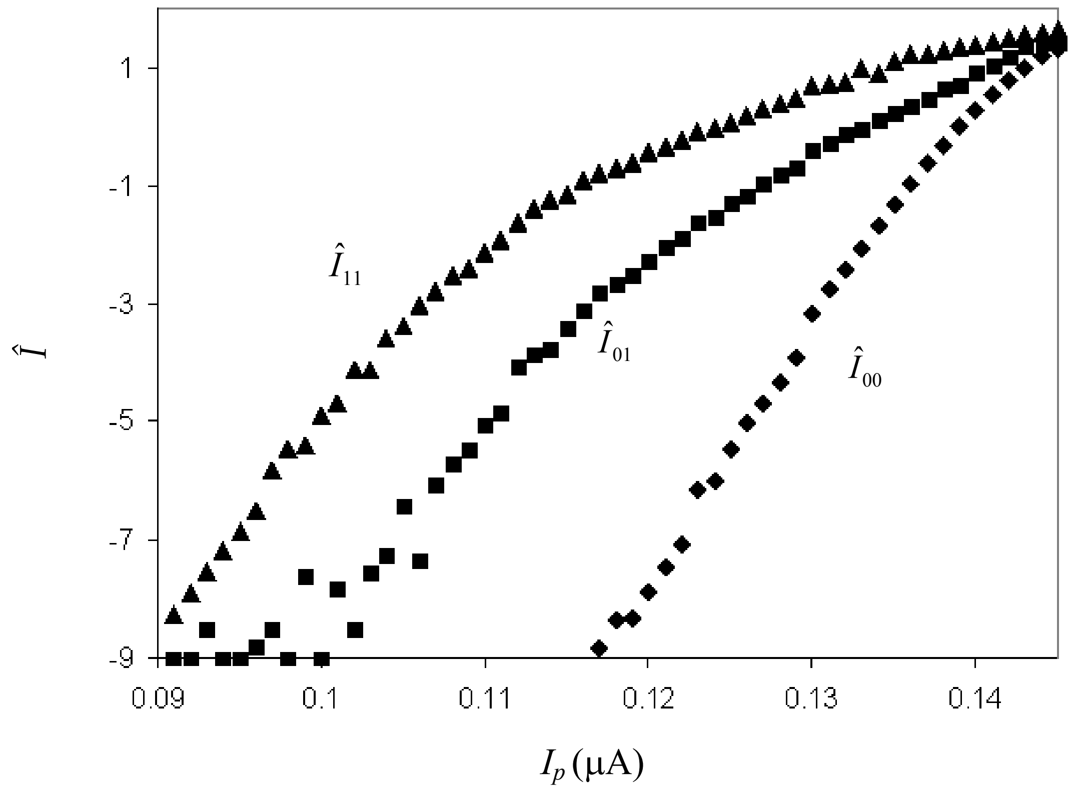

Figure 7.4: Extracted effective current functions $\hat{I}_{11}$ (filled triangles), $\hat{I}_{01}$ (filled squares) and $\hat{I}_{00}$ (filled diamonds) from the measured switching curves. The Î curves were obtained from the relation $\hat{I}(I_p) = \ln\{-\ln(1 - P_s(I_p))\}$. For this data, the device DS8 was biased at $I_b = 0.916$ μA, $f_{01} = 3.520$ GHz, and $\Phi_a = -0.38\ \Phi_o$.

measured the experimental probability of switching P_{s1} versus I_p. In this case, $\alpha = 0$, $\beta = 1$, and Eq. 7.45 gives

$$P_{s1}(I_p) \approx 1 - \exp(-\exp(\hat{I}_{11})) \tag{7.50}$$

and thus I can find $\hat{I}_{11}$ as a function of the current pulse amplitude by plugging my measured values of P_{s1} into

$$\hat{I}_{11}(I_p) = \ln\{-\ln(1 - P_{S1}(I_p))\}. \tag{7.51}$$

Figure 7.4 also shows a plot of $\hat{I}_{11}$ that I extracted from measurements on device DS8.

Once $\hat{I}_{00}$ and $\hat{I}_{11}$ are known as a function of I_p, I then found $\hat{I}_{01}$ by applying Eq. 7.45 to the switching curve for a superposition state. In principle any superposition state will do, and for simplicity I used the superposition state $\left(|0\rangle + |1\rangle\right)/\sqrt{2}$ which I prepared using a π/2 pulse. In this case, $\alpha = \beta = 1/\sqrt{2}$, and Eq. 7.45 gives

$$P_{s,\pi/2}(I_p) \approx 1 - \exp(-\exp(\hat{I}_{00}/2 + \hat{I}_{11}/2 + \hat{I}_{01})) \tag{7.52}$$

and I can then find $\hat{I}_{01}$ as a function of the current pulse amplitude by plugging my measured values for $P_{s,\pi/2}$ into

$$\hat{I}_{01}(I_p) = \ln\{-\ln(1 - P_{s,\pi/2}(I_p))\} - \frac{\hat{I}_{00}(I_p)}{2} - \frac{\hat{I}_{11}(I_p)}{2}. \tag{7.53}$$

Figure 7.4 shows a plot of $\hat{I}_{01}$ that I extracted from measurements on devices DS8. I note that I_{01} is relatively featureless and relatively small compared to $\hat{I}_{01}$ and $\hat{I}_{11}$. Although the $\hat{I}_{01}$ term was not doing much, it was not negligible, and the agreement between the measured switching curves and the model was much poorer without this term.

With $\hat{I}_{00}$, $\hat{I}_{11}$ and $\hat{I}_{01}$ determined, I can then test the validity of Eq. 7.45. To do this, I measured switching curves at different times during a Rabi oscillation. Ignoring decoherence, the measured s-curve at any specific time during a Rabi oscillation should correspond to a specific α and β. I used χ^2 minimization to find the α and β that gave the best fit between the model and the data, and used the extracted β to find an estimate for $P_1 = \beta^2$ for the state. Because $\hat{I}_{00}$, $\hat{I}_{11}$ and $\hat{I}_{01}$ are themselves somewhat uncertain (since they came from the data), it is necessary to take this uncertainty into account in the minimization procedure. The interference term $\hat{I}_{01}$ was particularly difficult to determine accurately and has a large uncertainty.

I can write χ^2 explicitly as

$$\chi^2 = \sum_{n=1}^{N} \frac{\left(P_s^{data}(I_{p,n}) - P_s^{theory}(I_{p,n}, \beta)\right)^2}{\left(\sigma_{ps,n}^{data}\right)^2 + \left(\sigma_{ps,n}^{theory}\right)^2} \quad . \tag{7.54}$$

One then needs to find the value of β that minimizes χ^2. Here N is the total number of currents at which the switching curve was measured, $I_{p,n}$ is the *n-th* measurement pulse current, $P_s^{data}(I_{p,n})$ is the measured switching probability at current pulse $I_{p,n}$, $P_s^{theory}(I_{p,n}, \beta)$ is the theoretical value from Eq. 7.45 for the switching probability given the amplitude β to be in the excited state (I also use $\alpha = \sqrt{1-\beta^2}$), $\sigma_{ps,n}^{data}$ is the statistical uncertainty in the *n-th* measured probability, and $\sigma_{ps,n}^{theory}$ is the statistical uncertainty in the *n-th* theoretical probability (taking into account that this theory was found in part from some measured data).

7.3.2 Comparing the Model to Measured Switching curves

Figure 7.4 shows switching curves I measured in device DS8 for qubit state $|0\rangle$ (filled diamonds), $|1\rangle$ (filled triangles) and the superposition state of $|0\rangle$ and $|1\rangle$ (filled squares) created by applying a $\pi/2$ pulse. For these measurements, the qubit was biased with $\Phi_a = -0.38\ \Phi_o$, $I_b = 0.916\ \mu A$, and was at 20 mK. To prepare the $|1\rangle$ state, I applied resonant microwaves at frequency $f = 3.520$ GHz at a power of 16 dBm (source power) for 11 ns. To prepare the superposition state, I applied resonant microwaves at frequency $f = 3.520$ GHz at a power of 16 dBm (source power) for 23 ns.

First note in Fig. 7.4 that the measured switching curve for the superposition state (filled squares) shows no sign of a shoulder at $P_s = 0.5$. As I noted previously, this indicates that the curve is anomalous and that the measurement is not projecting the state to $|0\rangle$ or $|1\rangle$. In particular, the measured curve for the superposition state (filled squares) looks quantitatively and qualitatively quite different from the weighted sum of the $|0\rangle$ and $|1\rangle$ switching curves. Instead, the measured switching curve for the superposition state looks like it is shifted to lower current compare to the switching curve for the ground state. This is qualitatively what one would expect if the state of the qubit was altering the current in the detection junction, as is the basis for the simple model.

The three black solid curves in Fig. 7.5 show the result of fitting the model to the data at intermediate times in a Rabi oscillation using the χ^2-minimization procedure described above (with the excited state amplitude β as the only adjustable parameter). In Fig. 7.5, the individual switching curves were measured at 2 ns increments from time t = 23 ns (state 0) when the microwaves were turned on, to time t = 43 ns when the π-pulse

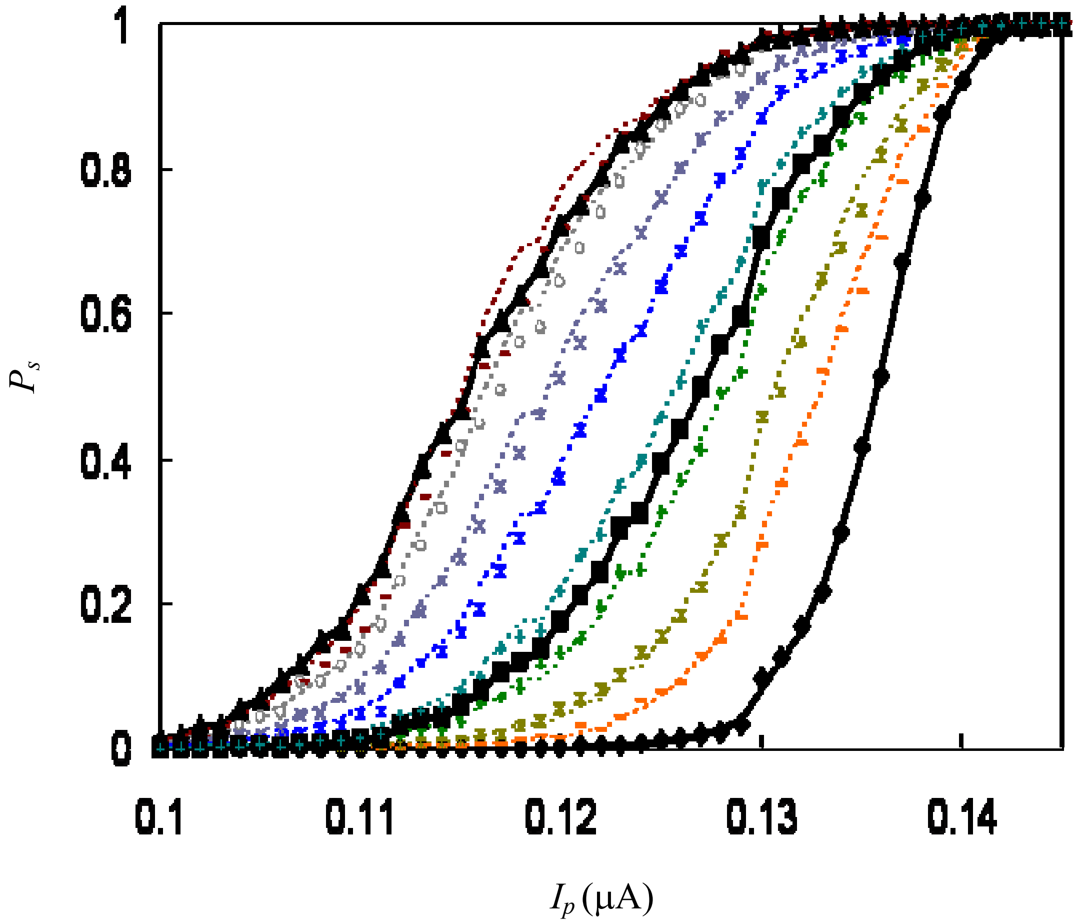

Figure 7.5: Measured s-curves for state $|1\rangle$ (filled triangles), 50% superposition state $(|0\rangle + |1\rangle)/\sqrt{2}$ (filled squares), and ground state $|0\rangle$ (filled diamonds). Additional points (data) and dotted curves [fits from Eq. 7.25] are for s-curves at intermediate times during a Rabi oscillation when resonant microwaves were applied to the qubit at 3.52 GHz. The times were t = 0 ns, 6 ns, 8 ns, 10 ns, 11 ns, 12 ns, 14 ns, 16 ns, 18 ns, 20 ns and 24 ns.

was complete (state 1). As is shown, I find good agreement between the measured s-curves (colored symbols) and the resulting fits (dotted curves) and I can conclude that this simple model is doing a reasonable job of capturing the behavior of the anomalous switching curves.

7.4 Switching Curves during a Rabi oscillation

Figures 7.6(a) shows a false color plot of a full set of switching curves I obtained in device DS8 during a Rabi oscillation and Fig. 7.7 shows a relaxation curve. In these figures, I am plotting the time along the x-axis, the pulse current along the y-axis, and the switching probability is represented as a color. Here red means a switching probability of 1 and blue means 0. Thus, at large pulse currents the color is red (100% switching) while at low pulse currents the color is blue (no switching). The data was taken in increments of 2 ns along the x-axis and 1 nA along the y-axis. A subset of this same data is shown as s-curves in Fig. 7.5. For the Rabi measurements, the qubit was biased with $\Phi_a = -0.38\ \Phi_o$, $I_b = 0.916\ \mu A$, and as usual the device was at 20 mK. I applied resonant microwaves at a frequency 3.520 GHz and a power of 16 dBm (source power). For the relaxation measurements, I applied resonant microwaves at frequency 3.520 GHz and a power of 16 dBm (source power) for 800 ns.

In Fig. 7.6(b), (c), (d) and (e), I also show individual switching curves at 3 ns, 31 ns, 41 ns and 351 ns. As discussed in the previous sections, the switching curves shift up and down along the current axis. As time increases, this back and forth shifting washes out and the switching broadens into a flat band.

As discussed above, from the data in Fig. 7.6, I extracted $P_1 = \beta^2$ as a function of

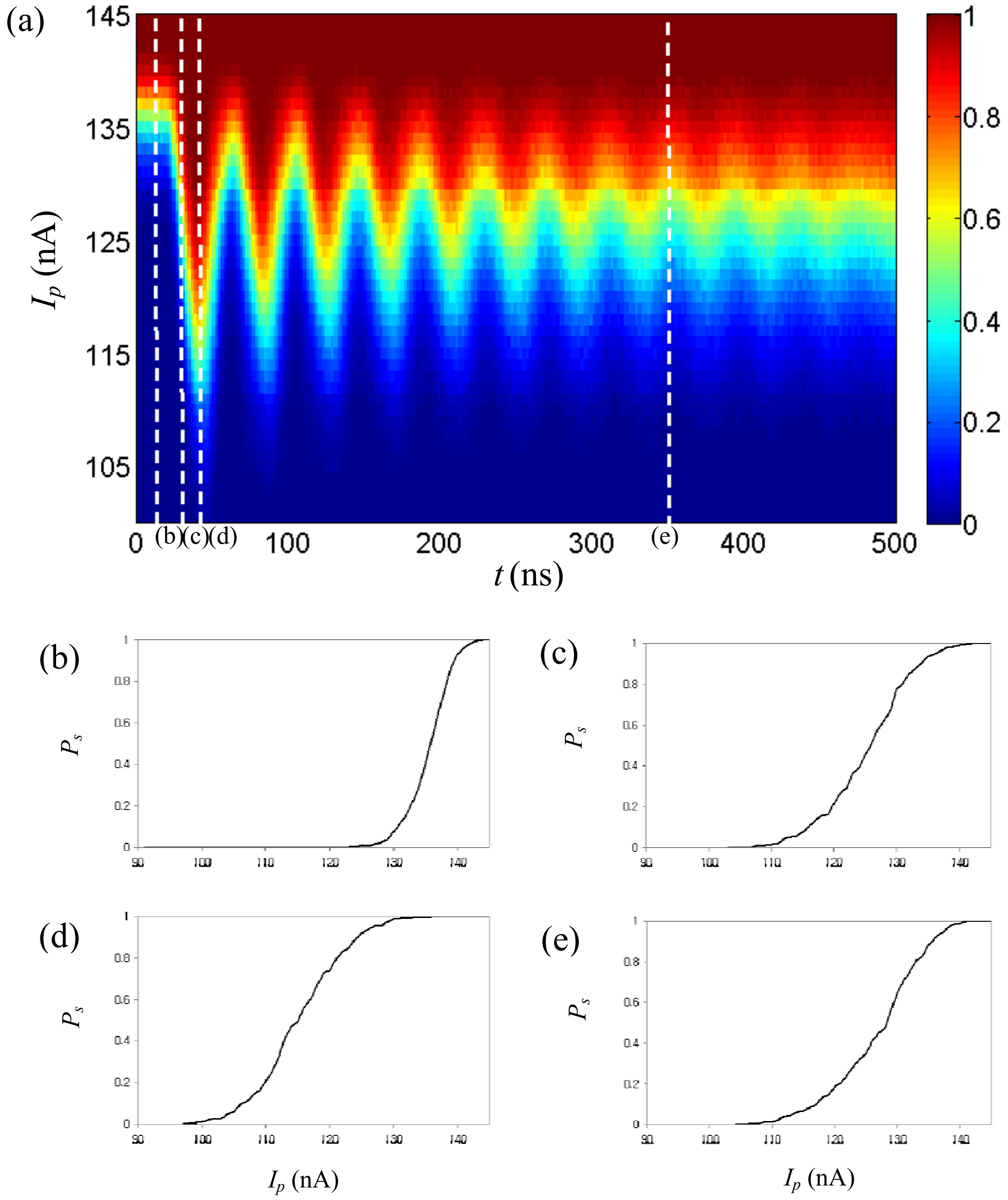

Figure 7.6: (a) Measured switching curve data for a Rabi oscillation measurement at 3.520 GHz. Red indicates 100% switching probability and blue represents 0 switching probability. Line cuts through the data in (a) at times of (b) 3 ns, (c) 31 ns, (d) 41 ns and (e) 351 ns.

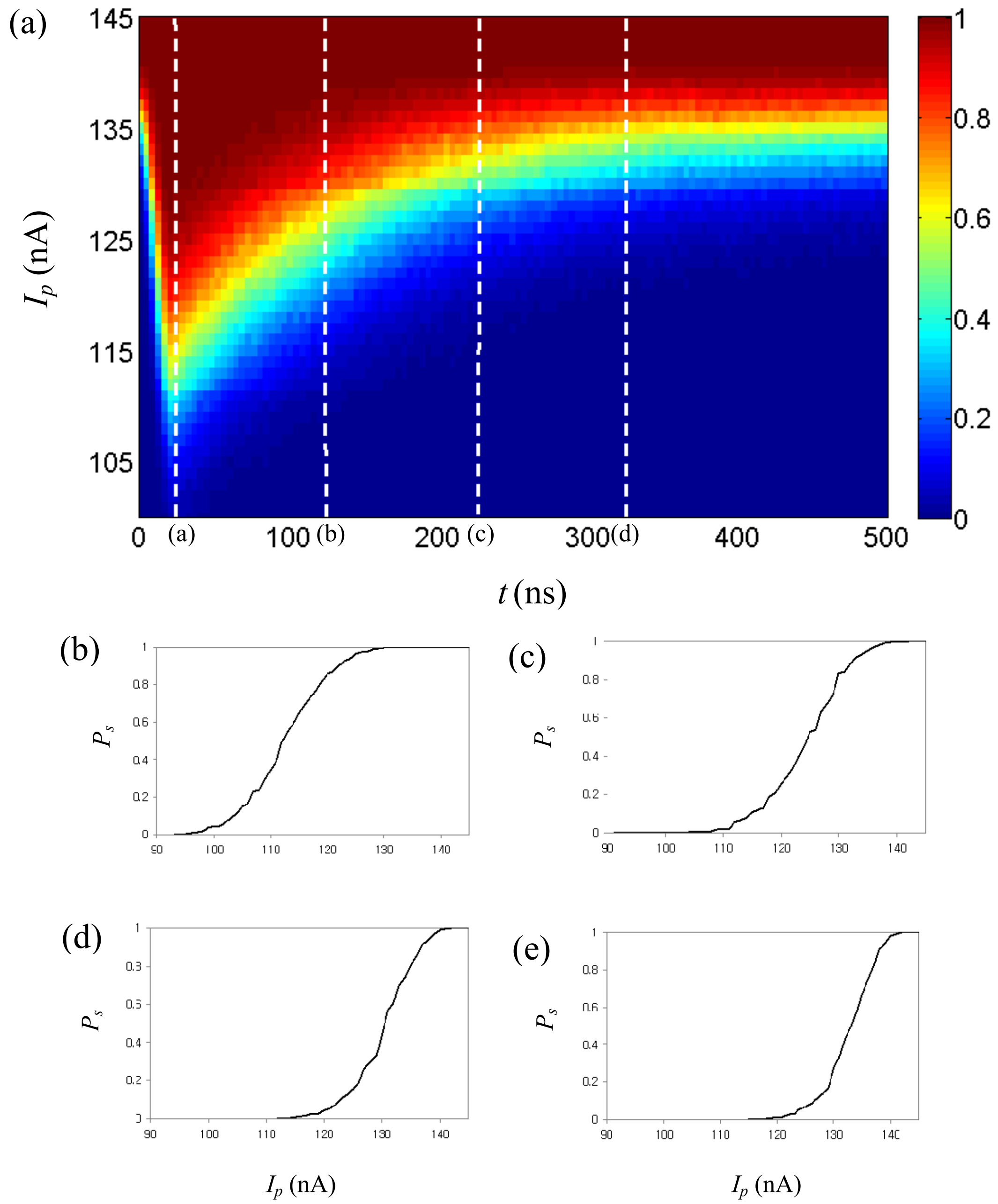

Figure 7.7: (a) False color plot of switching probability versus pulse current and time for a relaxation measurement at 3.520 GHz in device DS8. Red indicates 100% switching probability and blue represents 0 switching probability. Line cuts through the data in (a) at times (b) 21 ns, (c) 121 ns, (d) 221 ns and (e) 321 ns are displayed.

time during the Rabi oscillation. Figure 7.8(a) shows the resulting plot of P_1 versus time. It is a reasonable looking curve for a Rabi oscillation, and one finds a decay time of $T' \approx$ 120 ns. This is the same result I presented in Fig. 6.16(a) in Chapter 6.

Figure 7.9(a) shows another set of switching curves for a Rabi oscillation at a different bias point. For this measurement the flux bias was $\Phi_a = -0.38\ \Phi_o$, the current bias was $I_b = 0.978\ \mu A$, the qubit resonance frequency was 3.420 GHz and I used a microwave power of 16 dBm (source power). The plot shows similar switching curves and I extracted a Rabi decay time of $T' \approx 90$ ns which is shorter than the time measured at 3.520 GHz, as shown in Fig. 7.8(a).

Figure 7.10 shows additional measurements of switching curves taken during a Rabi oscillation in device DS8. One of the switching curves was measured with a microwave power of -48 dBm and the other one was measured with a power of -51 dBm. The powers listed are those at the microwave source. A 3 dB difference is about 2 times difference in power and Ω_{01} changed from 35.7 MHz to 27.4 MHz. Since the Rabi frequency scales with the device amplitude, rather than the device power, one would expect the Rabi frequency to increase by $\sqrt{2} = 1.4$. The observed increase is a factor of 1.3 which is in rough agreement.

7.5 Relaxation

Figure 7.7 (a) shows a false color plot of a full set of switching curves that I obtained during a relaxation measurement after a π-pulse excitation in device DS8. The color index is the same as Fig. 7.6 (a). Figures 7.7(b), (c), (d) and (e), show individual switching curves at 21 ns, 121 ns, 221 ns and 321 ns respectively. The switching curve

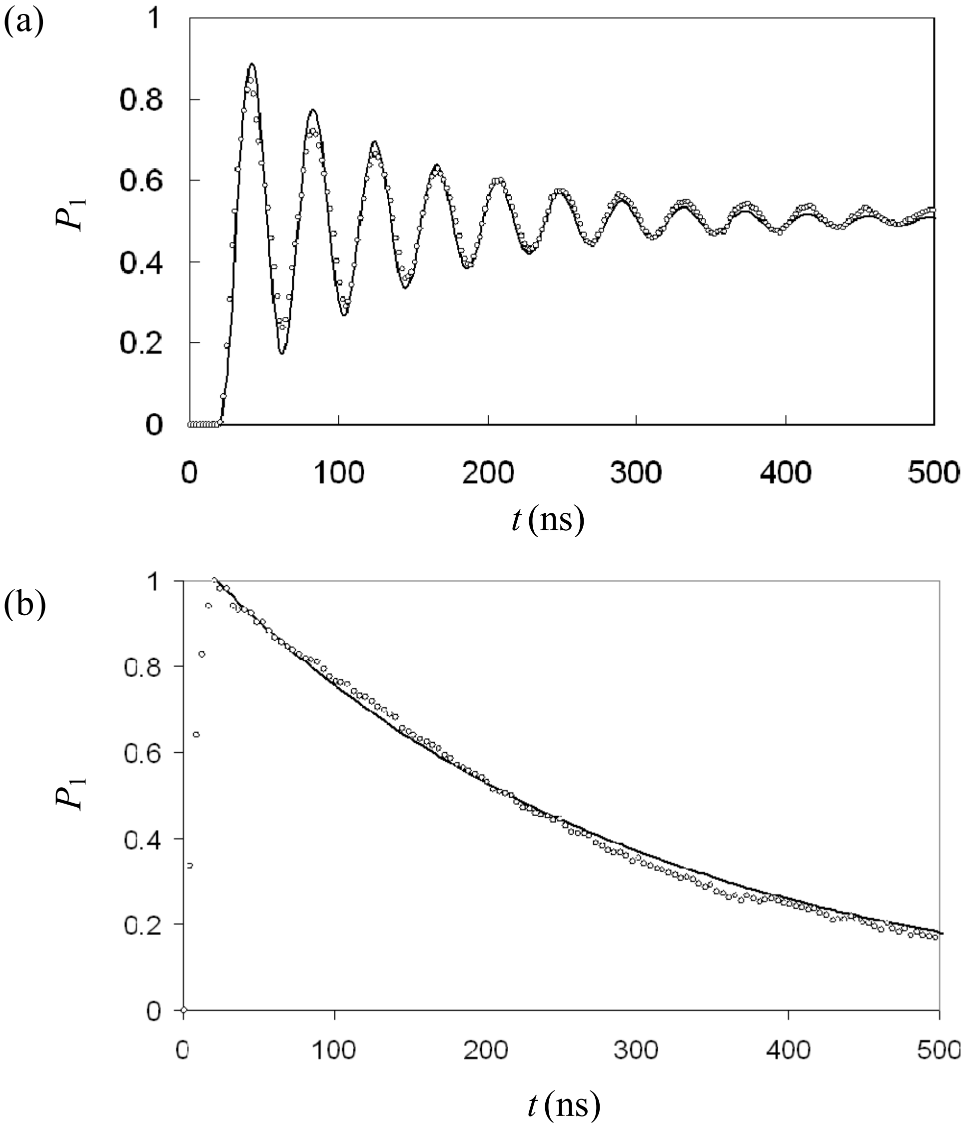

Figure 7.8: Measurements on device DS8 at f = 3.520 GHz. (a) Open circles show extracted probability P_1 to be in the excited state versus time during a Rabi oscillation. Solid curve shows fit to Rabi oscillation with decay time $T' \approx$ 120 ns. (b) Open circles show probability P_1 to be in the excited state versus time and solid curve shows fit to relaxation with $T_1 \approx$ 280 ns.

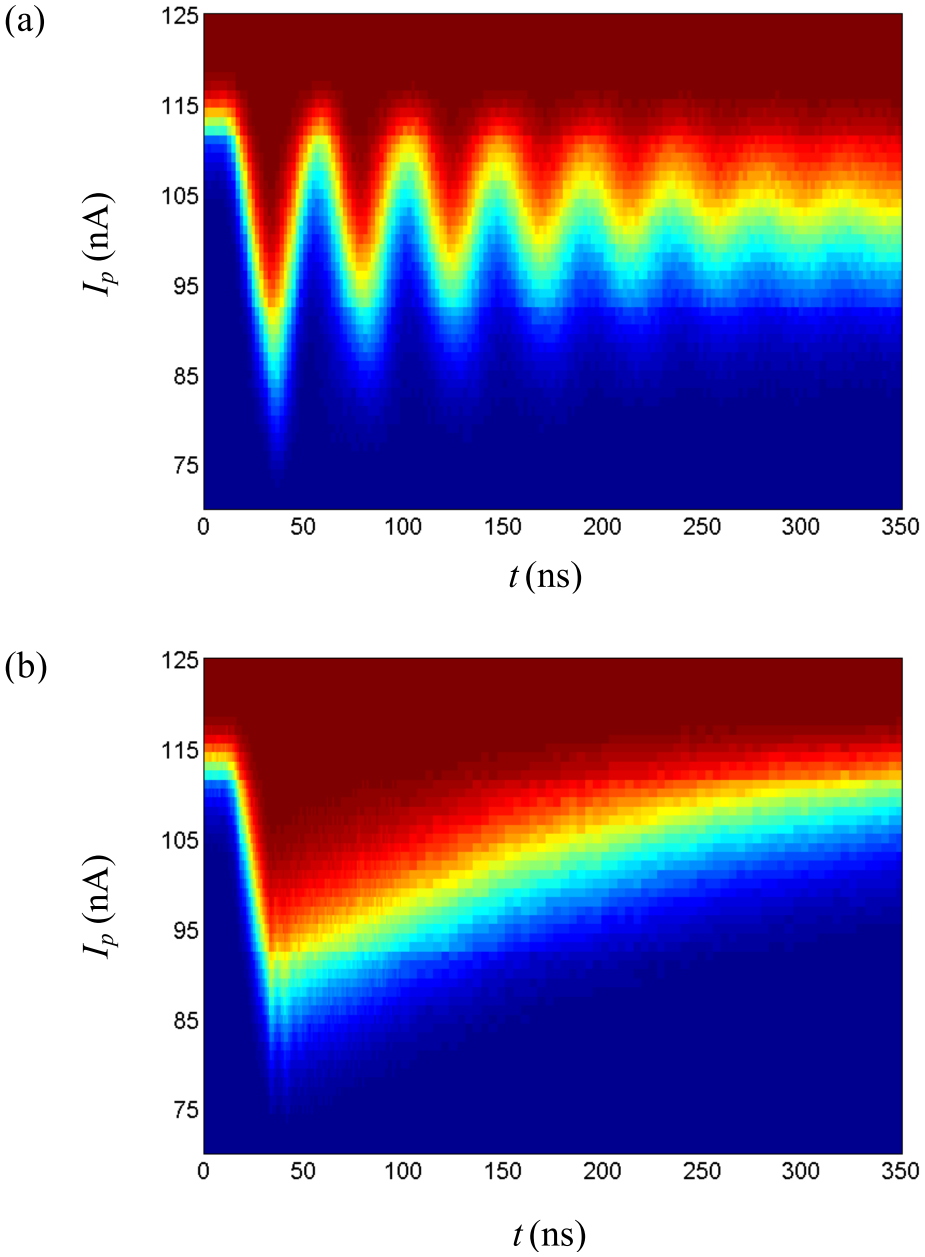

Figure 7.9: Measurements on device DS8 at $f = 3.420$ GHz. False color plot of switching probability versus time for (a) a Rabi oscillation measurement (Rabi decay time $T' \approx 90$ ns) and (b) a relaxation measurement (relaxation time $T_1 \approx 250$ ns). Red indicates 100% switching probability and blue represents 0 switching probability.

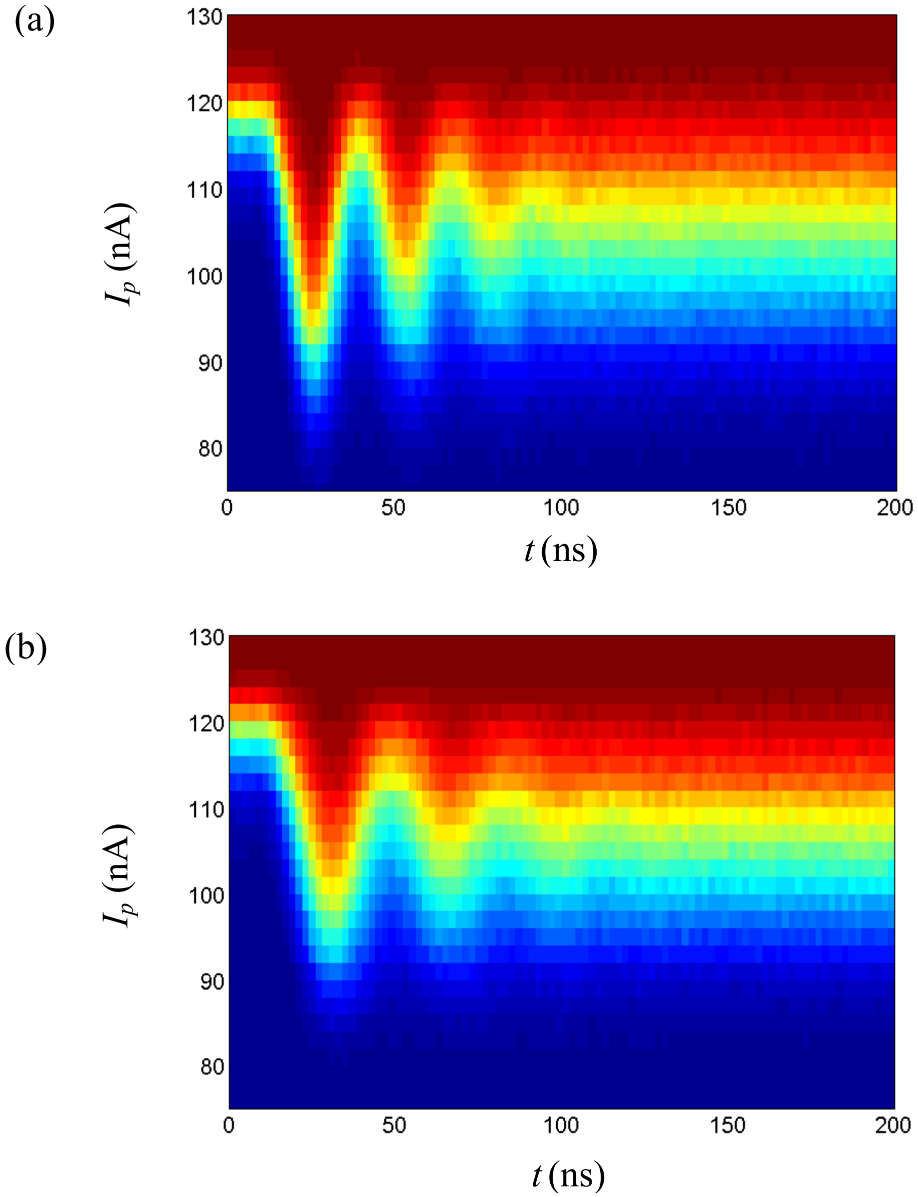

Figure 7.10: False color plot of measured switching curves for a Rabi oscillation measurement at 3.694 GHz in device DS8 with microwave source power of (a) -48 dBm and (b) -51dBm. The Rabi frequencies Ω_{01} are (a) 35.7 MHz at -48 dB and (b) 27.4 MHz at -51 dB. As expected the Rabi frequency changes depending on the microwave power. Red indicates 100% switching probability and blue represents 0 switching probability.

shifts in one direction after the π-pulse excitation and the shape of the switching curve does not change much. In this case, the qubit switching curve at long times appears to be different from and broader than the switching curve at $t = 0$. This suggests that the qubit has not fully relaxed to the ground state, even at 350 ns.

In Fig. 7.8(b), results are shown for P_1 versus time during a π-pulse followed by relaxation, obtained from analysis of the switching curves shown in Fig. 7.8(a). A clean exponential relaxation is seen with a single time constant $T_1 \approx 280$ ns. This relaxation time is close to the value of 300 ns that was expected based on Eq. 7.25 and about a factor of 9 longer than I found in device DS6 [95].

Finally, in Fig. 7.9(b), I show another set of switching curve data for relaxation at a flux bias $\Phi_a = -0.38\ \Phi_o$, the current bias was $I_b = 0.978$ μA and a resonance frequency of 3.420 GHz. The plot shows a relaxation time of $T_1 \approx 250$ ns which is somewhat shorter than I found in the data measured at 3.520 GHz shown in Fig. 7.7(a).

7.6 Unusual Implications for State Measurement

A pure quantum state can be represented as a point on the Bloch sphere with well-defined angles θ and ϕ. As I discussed above, I obtained the amplitude β to be in the excited state by fitting the switching curves data to a model given by Eq. 7.45. This fitting procedure assumed that the system is always in a pure quantum state, or at least that the state has not de-cohered over a range of θ. This will be a poorer and poorer approximation as the state of the system suffers decoherence, and in fact, the fits to Eq. 7.45 are not good at long times.

Assuming that the above analysis is correct, and this is still an open question, it can be extended to include the effects of decoherence. In particular, additional information about the distribution of θ can be extracted from the switching curves.

To see qualitatively how this works, I assume that the system is not in a pure state but has an incoherent distribution of θ and ϕ. In this case, the switching curve is given by

$$P_s(I_p) = 1 - \int_0^{2\pi} d\phi \int_0^{\pi} P_s(\theta) P_1(\theta,\phi) \sin(\theta) d\theta \tag{7.54}$$

where the switching curve in a pure state is defined as

$$P_s(\theta) = P_{\alpha\beta}(I_p) \tag{7.55}$$

with $\alpha = \cos(\theta/2)$ and $\beta = \sin(\theta/2)$. Since switching curves are not dependent on ϕ, $P_1(\theta, \phi)$ can be integrated over ϕ and we can define a distribution over just θ as

$$P_1(\theta) = \int_0^{2\pi} P_1(\theta,\phi) \sin(\theta) d\phi\,. \tag{7.56}$$

Using Eq. 7.56, Eq. 7.54 can be written as

$$P_s(I_p) = 1 - \int_0^{\pi} P_{\alpha\beta}(I_p) P_1(\theta) d\theta\,. \tag{7.57}$$

Next, notice that if one takes a derivative of the switching curve with respect to the pulse current that one finds

$$\frac{\partial P_s(I_p)}{\partial I_p} = \int_0^{\pi} \frac{\partial P_{\alpha\beta}(I_p)}{\partial I_p} P_1(\theta) d\theta\,. \tag{7.58}$$

The derivative of the switching curves will be sharply peaked at the value of the current I_p where the s-curve has its largest slope. From the general behavior of the anomalous switching curves, if the system is in a pure state (specifically at a well-defined θ), this will give a fairly sharp and well-defined peak. I can define $I_s(\theta)$ to be the current at which the sharpest increase happens in the switching curve when the state has angle θ on the Bloch sphere. Treating this sharp peak as a δ-function:

$$\frac{\partial P_{\alpha\beta}(\theta)}{\partial I_p} \approx \delta\big(I_p - I_s(\theta)\big). \tag{7.59}$$

Eq. 7.58 can then be re-written as

$$\frac{\partial P_s(I_p)}{\partial I_p} \cong \int_0^{\pi} \delta\big(I_p - I_s(\theta)\big) P_1(\theta) d\theta = P_1(\theta(I_p)) \frac{d\theta}{dI_p} \tag{7.60}$$

Thus, the probability distribution in θ can be written as

$$P_1(\theta(I_p)) \approx \frac{dI_p}{d\theta} \frac{\partial P_s(I_p)}{\partial I_p}. \tag{7.61}$$

In practice, the function $\theta(I_p)$ can be obtained from measurements of a Rabi oscillation. Equation 7.61 then says that the distribution of the state on the Bloch sphere can be obtained approximately from the current derivative of the switching curve.

Figure 7.11 shows false color plots of dP_s/dI_p that I obtained by differentiating the switching curve data shown in Figs. 7.7 and 7.8. Note for example in Fig. 7.11(a) how for the first few cycles of the Rabi oscillation that dP_s/dI_p has a fairly sharp peak, and this peak moves continuously in time. For large times, dP_s/dI_p is spread out. The implication from Eq. 7.35 is that $P(\theta)$ is relatively sharply peaked on the Bloch sphere initially, but that as time goes on it becomes more and more spread out. Figure 7.11 (b) shows something similar happening during a relaxation measurement. I note that this extraction of information from the anomalous switching curves is somewhat analogous to doing state tomography and that plots of dP_s/dI_p, such as these shown in Fig. 7.11 directly shows both decoherence and relaxation.

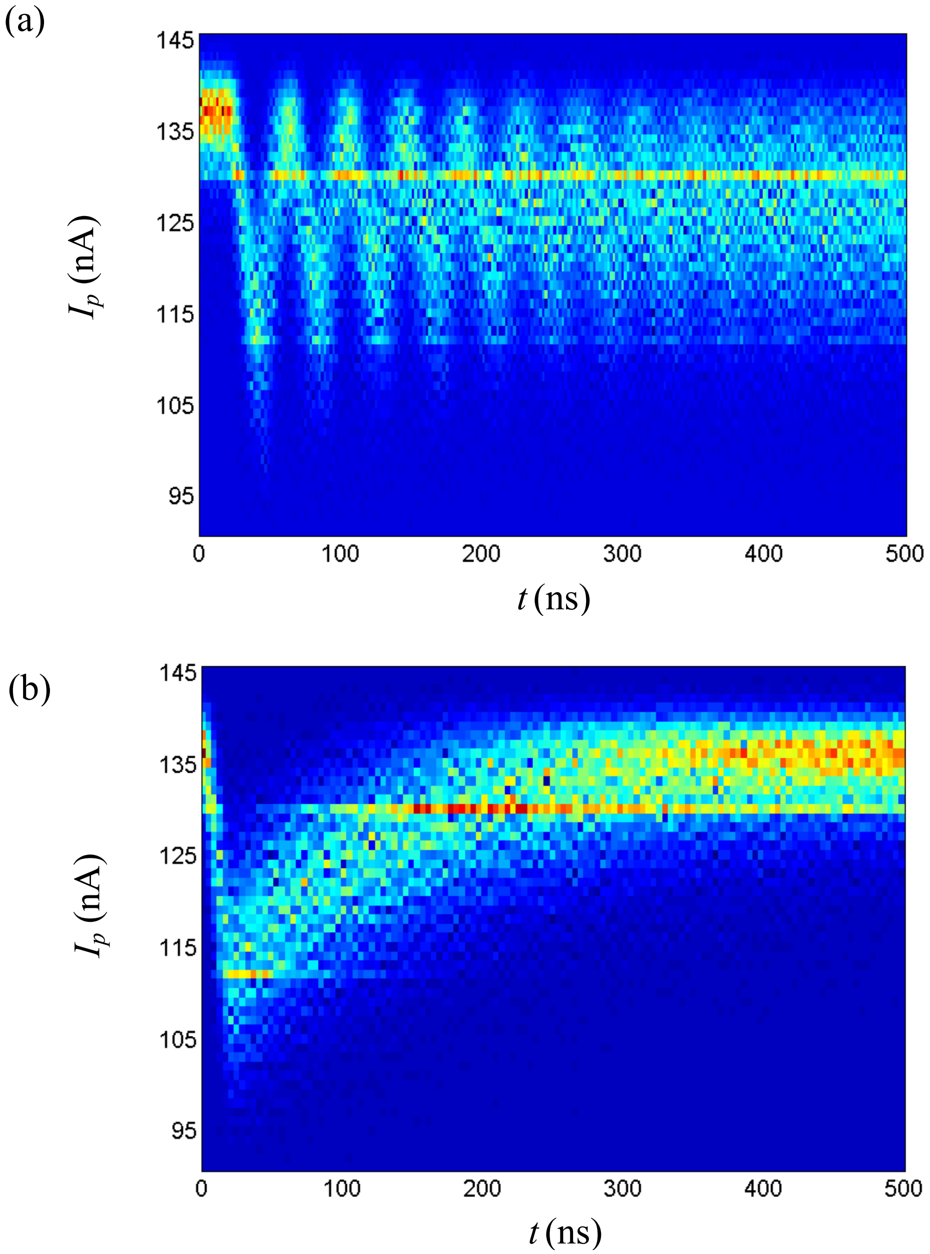

Figure 7.11: (a) False color plot of $\mathrm{d}P_s/\mathrm{d}I_p$ as a function of the pulse current I_p and time t for Rabi switching curves shown in Fig. 7.6(a). Blue corresponds to $\mathrm{d}P_s/\mathrm{d}I_p = 0$ and yellow to a large value for $\mathrm{d}P_s/\mathrm{d}I_p$. For the first few oscillations, $\mathrm{d}P_s/\mathrm{d}I_p$ has a sharp peak that moves continuously. For large times, $\mathrm{d}P_s/\mathrm{d}I_p$ is spread out. (b) False color plot of $\mathrm{d}P_s/\mathrm{d}I_p$ as a function of the pulse current I_p and time t for the relaxation switching curve data shown in Fig. 7.7(a). $\mathrm{d}P_s/\mathrm{d}I_p$ is spread out once relaxation starts at about 20 ns.

7.7 Summary

In this chapter, I discussed my observation and analysis of anomalous switching curves in dc SQUID phase qubit device DS8. Examination of the SQUID Hamiltonian in the limit where my device operates shows that the qubit junction cannot be treated as an independent junction and that it cannot tunnel (on its own) to the voltage state unless the detection junction switches to the voltage state. I discussed how the Born-Oppenheimer approximation can be applied to the SQUID Hamiltonian and how this leads to a simplified model of anomalous switching. Using this model, I was able to fit the data qualitatively and extract $P_1(t)$ during Rabi oscillation and relaxation measurements.

Chapter 8

Conclusions

In this thesis, I reported my research on dc SQUID phase qubits. My work focused on improving the relaxation time, but I also found some surprising behavior in the switching curves. In this chapter, I summarize my main findings and make suggestions for future work to resolve some of the remaining issues.

8.1 Design and Characterization of a dc SQUID Phase Qubit

The basic design of my Al/AlO$_x$/Al phase qubits was motivated by previous work by our group and the Martinis group [29]. The approach I used was to combine an LC isolation network and an LJ isolation network to better isolate a phase qubit from dissipation and current noise from the bias leads. I also attached a low-loss shunting capacitor to the qubit junction to reduce the impact of dielectric loss in the tunnel junction. Furthermore I reduced the size of the qubit junction to reduce the number of TLS defects.

For device DS6, I used a relatively lossy (N-H rich) SiN$_x$ layer as an insulating layer to make the capacitors that shunted the junction. The relaxation time T_1 and Rabi decay time T' in device DS6 were a bit longer than in our groups earlier devices but much shorter than I had expected. In particular, if the relaxation from the current bias lines was the main source of dissipation, then the device should have had a much longer coherence time and relaxation time. The device showed a transition spectrum which contained one visible splitting in frequency range of about 0.8 GHz, consistent with the junction area of 4 $(\mu\text{m})^2$. I found a best relaxation time of $T_1 \approx 32$ ns, a best Rabi decay time of $T' \approx 42$ ns, a maximum estimated spectroscopic coherence time of $T_2^* \approx 16$ ns and a coherence time of $T_2 \approx 61$ ns. The Rabi decay time T' was twice as long as that of the previous device DS3 which T.A. Palomaki measured. However, it was only after my measurement that it was realized that the SiN_x I used had a relatively high dielectric loss [$\tan(\delta) \approx 7\times10^{-4}$] in the shunting capacitor and this produced the relatively short T_1 and T_2 (see Table 6.1 for a summary of key result on DS6 and DS8).

In device DS8, I made a smaller ($\approx 2\ \mu\text{m}^2$) qubit junction and used a low-loss (Si-H rich) SiN_x layer for the capacitors [43]. I also designed the inductors for the LC isolation to be more symmetrically to reduce flux noise coupling in to the large filter inductors. The transition spectrum showed one visible splitting in about a 1 GHz frequency range, which was reasonable given the junction area. I found a best relaxation time of $T_1 \approx 280$ ns, a maximum Rabi decay time of $T' \approx 120$ ns, a maximum spectroscopic coherence time of $T_2^* \approx 46$ ns (excluding the splitting area) and a maximum estimated coherence time of $T_2 \approx 76$ ns. The device performed much better than any previous devices in our group. Due to the longer coherence time, I was able to obtain reasonable state tomography. I also tried state tomography on $|0\rangle$ and found results $|1\rangle$ and $(|0\rangle + |1\rangle)/\sqrt{2}$ consistent with detuning from the resonance.

Comparing the two devices DS6 and DS8, DS8 had longer T', T_1 and T_2 than DS6. The likely reason is that there was less dielectric loss in the Si-H rich SiN_x I used in device DS8 than in the N-H rich SiN_x of device DS6. T_1 was not as long as desired (> 1 μs), but as-built device had somewhat different parameters than the design and the resulting T_1 was quite consistent with loss in the SiN_x capacitor [43].

In both devices, I definitely reduced the number of TLS's by making a smaller area qubit junction. However, discrete TLS's did not seem to be a major source of decoherence in either device.

Both DS6 and DS8 operated in an unconventional parameter regime. Device DS6 showed some anomalous results, but the significance of these anomalies was not apparent to me when I measured this device. Device DS8 showed clearly anomalous switching curves. We developed an ad-hoc model to explain this anomalous behavior; the qubit junction is prevented from tunneling while state detection can only happen if the isolation junction tunnels.

8.2. Anomalous Switching Curves

Perhaps, the most interesting result from my research is the observation of anomalous switching curves in device DS8. Subsequently A. J. Przybysz and R. Budoyo observed anomalous s-curves in a second device. In a conventional s–curve, the π/2-superposition state shows a shoulder in the middle of the curve. In general, a conventional s-curve is the weighted sum of the s-curves for $\left|0\right\rangle$ and $\left|1\right\rangle$ because the measurement is projective to the state $\left|0\right\rangle$ or $\left|1\right\rangle$. In device DS8, the s-curves were, however, shifted along the current pulse amplitude, without showing any plateau, when the qubit was in the superposition state. To explain this situation, I used a model in which the two junctions are coupled, although the interaction between them is still weak in some sense (the Born-Oppenheimer approximation). By using the model, I found an approximate relation between the state of the qubit, the current through the detection junction *J2*, and the switching probability P_s. The equation described anomalous switching curves and emphasized the importance of perturbation to the current in the detection junction. Depending on the state of the qubit, the potential barrier height of the detection junction is modulated and it changes the detection junction escape rate.

This situation happened in my device DS8 because it was in a different parameter regime; the qubit junction had a Josephson inductance that was large compared to the loop inductance. This situation was reproduced by A. J. Przybysz in the next device PB9 [110] and this verified that the anomalous switching phenomena were repeatable.

8.3. Future Work

Although the maximum relaxation time T_1 in device DS8 was consistent with dielectric loss in the shunting capacitor, this does not mean that it necessarily was the actual dominant mechanism or that no other mechanism contributed. Thus the exact sources for relaxation in my device are an open question. A key test would be to build another device with a lower dielectric loss and see if T_1 showed further improvement. With this in mind, A. J. Przybysz built device PB9 using an interdigitated capacitor on sapphire. Such a structure should have much lower loss [111]. They found T_1 to be similar to what I found, but were able to show that this loss was due to strong coupling between the microwave line and the qubit; this is now believed to be the main source of decoherence in device PB9. The implication is that reducing the coupling to the microwave line should improve the relaxation time significantly. Of course, this will require another device, which is currently being designed by R. Budoyo.

The second puzzle that clearly needs more work is the issue of the anomalous switching curves. One of the key issues was whether other devices show the phenomena. This has been answered by A. J. Przybysz and R. Budoyo who found that device PB9 also showed clearly anomalous switching curves. Another key issue is the parameter range necessary to see the effect. This is still an open question. Clearly, more work is needed on a careful and thorough theoretical analysis of the system to settle the underlying cause of the phenomena. In this thesis, I argued for a model based on current redistribution. But the argument is not rigorous and it could be wrong. A thorough theoretical analysis is clearly work for the future.

Finally, actually achieving $T_1 > 1$ μs in a phase qubit remains an unsolved experimental challenge. However, based on my research and that of other groups, this now appears to be completely feasible.

Bibliography

[1] R. P. Feynman, “Simulating Physics with Computers,” International Journal of Theoretical Physics **21** (6-7), 467 (1982).

[2] R. L. Rivest, A. Shamir, and L. Adleman, “Method for Obtaining Digital Signatures and Public-key Cryptosystems,” Communications of the ACM **21**(2), 120 (1978).

[3] P. W. Shor, “Polynomial-time algorithms for prime factorization and discrete logarithms on a quantum computer,” SIAM Journal on Computing **26**(5), 1484 (1997).

[4] M. A. Nielsen, and I. L. Chuang, Quantum Computation and Quantum Information (Cambridge University Press, 2000).

[5] J. S. Bell, “The Paradox of Einstein, Podolsky and Rosen – Action at a Distance in Quantum-Mechanics,” Speculations in Science and Technology **10**(4), 269 (1987).

[6] D. Deutsch, “Quantum-Theory, the Church-Turing Principle and the Universal Quantum Computer,” Proceedings of the Royal Society of London Series a-Mathematical Physical and Engineering Sciences **400**(1818), 97 (1985).

[7] D. Deutsch, and R. Jozsa, “Rapid Solution of Problems by Quantu Computation,” Proceedings of the Royal Society of London Series a-Mathematical Physical and Engineering Sciences **439**(1907), 553 (1992).

[8] L. K. Grover, “Quantum mechanics helps in searching for a needle in a haystack,” Phys. Rev. Lett. **79**(2), 325 (1997).

[9] D. P. DiVencenzo, "Topics in Quantum Computers," (1996).

[10] M. Nakahara, and T. Ohmi, Quantum Computing, From Linear Algebra to Physical Realizations (CRC Press, 2008).

[11] L. M. K. Vandersypen, M. Steffen, G. Breyta, C. S. Yannoni, M. H. Sherwood, and I. L. Chuang, “Experimental realization of Shor's quantum factoring algorithm using nuclear magnetic resonance,” Nature **414**(6866), 883 (2001).

[12] S. L. Braunstein, C. M. Caves, R. Jozsa, N. Linden, S. Popescu, and R. Schack, “Separability of Very Noisy Mixed States and Implications for NMR Quantum Computing,” Phys. Rev. Lett. **83**(5), 1054 (1999).

[13] N. A. Gershenfeld, and I. L. Chuang, “Bulk spin-resonance quantum computation,” Science **275**(5298), 350 (1997).

[14] D. G. Cory, A. F. Fahmy, and T. F. Havel, “Ensemble quantum computing by NMR spectroscopy,” Proceedings of the National Academy of Sciences of the United States of America **94**(5), 1634, (1997).

[15] R. Hanson, L. P. Kouwenhoven, J. R. Petta, S. Tarucha, L. M. K. Vandersypen, “Spins in few-electron quantum dots,” Rev. Mod. Phys. **79**(4), 1217 (2007).

[16] L. P. Kouwenhoven, D. G. Austing, and S. Tarucha, “Few-electron quantum dots,” Rep. Prog. Phys. **64**, 701–736 (2001).

[17] T. Fujisawa, D. G. Austing, Y. Tokura, Y. Hirayama, and S. Tarucha, “Allowed and forbidden transitions in artificial hydrogen and helium atoms,” Nature **419**(6904), 278 (2002).

[18] T. Hayashi, T. Fujisawa, H. D. Cheong, Y. H. Jeong, and Y. Hirayama, “Coherent manipulation of electronic states in a double quantum dot,” Phys. Rev. Lett. **91**(22), 226804 (2003).

[19] I. H. Deutsch, G. K. Brennen, and P.S. Jessen, “Quantum computing with neutral atoms in an optical lattice,” Fortschritte der Physik 48, 925 (2000).

[20] R. Blatt, and D. Wineland, “Entangled states of trapped atomic ions,” Nature **453**(7198), 1008 (2008).

[21] H. Haffner, “Scalable multiparticle entanglement of trapped ions,” Nature **438**(7068), 643 (2005).

[22] M. Devoret, J. Martinis, and J. Clarke, “Measurement of Macroscopic Quantum Tunneling out of the Zero-Voltage State of a Current-Biased Josephson Junction,” Phys. Rev. Lett. **55**(18), 1908 (1985).

[23] Y. Nakamura, Y. A. Pashkin, and J. S. Tsai, “Coherent control of macroscopic quantum states in a single-Cooper-pair box,” Nature **398(**6730), 786 (1999).

[24] J. H. Plantenberg, P. de Groot, C. Harmans, and J. E. Mooij, “Demonstration of controlled-NOT quantum gates on a pair of superconducting quantum bits,” Nature **447**(7146), 836 (2007).

[25] E. Lucero, M. Hofheinz, M. Ansmann, R. C. Bialczak, N. Katz, M. Neeley, A. D. O’Connell, H. Wang, A. N. Cleland, and J. M. Martinis, “High-fidelity gates in a single Josephson qubit,” Phys. Rev. Lett. **100**(24), 247001 (2008).

[26] D. Vion, A. Aassime, A. Cottet, P. Joyez, H. Pothier, C. Urbina, D. Esteve, and M. H. Devoret, "Manipulating the quantum state of an electrical circuit," Science **296**(5569), 886 (2002).

[27] J. Koch, T. Yu, J. Gambetta, A. A. Houck, D. I. Schuster, J. Majer, A. Blais, M. H. Devoret, S. M. Girvin, and R. J. Schoelkopf, "Charge-insensitive qubit design derived from the Cooper pair box," Phys. Rev. A **76**(4), 042319 (2007).

[28] R. Ramos, M. Gubrud, A. Berkley, J. R. Anderson, C. J. Lobb, and F. C. Wellstood, "Design for effective thermalization of junctions for quantum coherence," IEEE Trans. Appl. Supercond. **11(**1), 998 (2001).

[29] J. M. Martinis, S. Nam, J. Aumentado, and C. Urbina, "Rabi oscillations in a large Josephson-junction qubit," Phys. Rev. Lett., **89**(11), 117901 (2002).

[30] J. M. Martinis, M. H. Devoret, and J. Clarke, "Experimental tests for the quantum behavior of a macroscopic degree of freedom: The phase difference across a Josephson junction," Phys. Rev. B **35**(10), 4682 (1987).

[31] J. M. Martinis, Macroscopic Quantum Tunneling and Energy-Level Quantization in the Zero Voltage State of the Current-Biased Josephson Junction, Ph. D. thesis, University of California (1985).

[32] A. O. Caldeira and A. J. Leffett, "Influence of Dissipation on Quantum Tunneling in Macroscopic Systems," Phys. Rev. Lett. **46**(4), 211 (1981).

[33] T. A. Palomaki, S. Dutta, R. M. Lewis, H. Paik, K. Mitra, B. K. Cooper, A. J. Przybysz, A. J. Dragt, J. R. Anderson, C. J. Lobb, and F. C. Wellstood, "Pulse current measurements and Rabi oscillations in a dc SQUID phase qubit," IEEE Trans. Appl. Supercond. **17**(2), 162 (2007).

[34] H. Paik, B. K. Cooper, S. K. Dutta, R. M. Lewis, R. C. Ramos, T. A. Palomaki, A. J. Przybysz, A. J. Dragt, J. R. Anderson, C. J. Lobb, and F. C. Wellstood, "Measurements of decoherence in three dc SQUID phase qubits," IEEE Trans. Appl. Supercond. **17(**2), 120 (2007).

[35] H. Kwon, A. J. Przybysz, T. A. Palomaki, R. M. Lewis, B. S. Palmer, H. Paik, S. K. Dutta, B. K. Cooper, J. R. Anderson, C. J. Lobb, and F. C. Wellstood, "Dc SQUID Phase Qubit With an LC Filter," IEEE Trans. Appl. Supercond. **19**(3), 957 (2009).

[36] K. B. Cooper, M. Steffen, R. McDermott, R. W. Simmonds, S. Oh, D. A. Hite, D. P. Pappas, and J. M. Martinis, "Observation of quantum oscillations between a Josephson phase qubit and a microscopic resonator using fast readout," Phys. Rev. Lett. **93**(18), 180401 (2004).

[37] O. Buisson, F. Balestro, J. P. Pekola, F. W. Hekking, “One-shot quantum measurement using a hysteretic dc SQUID,” Phys. Rev. Lett. **90**(23), 230304 (2003).

[38] M. Ansmann, H. Wang, R. C. Bialczak, M. Hofheinz, E. Lucero, M. Neeley, A. D. O’Connell, D. Sank, M. Weides, J. Wenner, A. N. Cleland, and J. M. Martinis, “Violation of Bell's inequality in Josephson phase qubits,” Nature **461**(7263), 504 (2009).

[39] A. Berkley, H. Xu, M. Gubrud, R. C. Ramos, J. R. Anderson, C. J. Lobb, and F. C. Wellstood, “Characterization of an LC-isolated Josephson junction qubit,” IEEE Trans. Appl. Supercond. **11**(2), 952 (2003).

[40] A. Berkley, H. Xu, R. Ramos, M. A. Gubrud, F. W. Strauch, P. R. Johnson, J. R. Anderson, A. J. Dragt, C. J. Lobb, and F. C. Wellstood, “Entangled macroscopic quantum states in two superconducting qubits,” Science **300**(5625), 1548 (2003).

[41] S. Dutta, H. Xu, A. Berkley, R. C. Ramos, M. A. Gubrud, J. R. Anderson, C. J. Lobb, F. C. Wellstood, “Determination of relaxation time of a Josephson junction qubit,” Phys. Rev. B **70**(14), 140502 (2004).

[42] T. A. Palomaki, dc SQUID phase qubit, Ph.D. thesis, University of Maryland (2008).

[43] H. Paik, and K. D. Osborn, “Reducing quantum-regime dielectric loss of silicon nitride for superconducting quantum circuits,” Appl. Phys. Lett. **96**(7), 072505 (2010).

[44] B. D. Joesphson, “Possible new effects in superconductive tunneling,” Phys. Lett. **1**(7), 251 (1962).

[45] M. Tinkham, Introduction to Superconductivity, 2nd ed. (Dover Publications, Mineola, New York , 1996).

[46] F. W. Strauch, Theory of Superconducting Phase Qubits, Ph. D. thesis, University of Maryland, College Park (2004).

[47] A. J. Berkley, A Josephson Junction Qubit, Ph.D. thesis, University of Maryland, College Park (2003).

[48] T. A. Fulton and L. N. Dunkleberger, “Lifetime of the zero-voltage state in Josephson tunnel junctions,” Phys. Rev. B **9**(11), 4760 (1974).

[49] M. Bűttiker, E. P. Harris, and R. Landauer, “Thermal activation in extremely underdamped Josephson-junction circuits,” Phys. Rev. B **28**(3), 1268 (1983).

[50] H. Xu, Quantum Computing with Josephson Junction Circuits, Ph.D. thesis, University of Maryland, College Park (2004).

[51] S. K. Dutta, Characterization of Josephson Devices for Use in Quantum Computation, Ph.D. thesis, University of Maryland (2006).

[52] H. Paik, Coherence in dc SQUID Phase Qubits, Ph.D. thesis, University of Maryland (2007).

[53] C. D. Tesche, Noise and Optimization of the dc SQUID, Ph.D. Thesis, University of California (1978).

[54] A. Barone and G. Paterno, Physics and Applications of the Josephson Effect (Wiley, New York, 1982).

[55] K. Mitra, F. W. Strauch, C. J. Lobb, J. R. Anderson, F. C. Wellstood, and Eite Tiesinga, "Quantum behavior of the dc SQUID phase qubit," Phys. Rev. B **77**(21), 214512 (2008).

[56] T. A. Palomaki, S. K. Dutta, H. Paik, H. Xu, J. Matthews, R. M. Lewis, R. C. Ramos, K. Mitra, P. R. Johnson, F. W. Strauch, A. J. Dragt, C. J. Lobb, J. R. Anderson and F. C. Wellstood, "Initializing the flux state of multiwell inductively isolated Josephson junction qubits," Phys. Rev. B **73**(1), 014520 (2006).

[57] B. K. Cooper, (unpublished).

[58] F. Bloch, "Nuclear Induction," Phys. Rev. **70** (7 and 8), 460 (1946).

[59] J. M. Martinis, S. Nam, J. Aumentado, K. M. Lang, C. Urbina, "Decoherence of a superconducting qubit due to bias noise," Phys. Rev. B **67**(1), 094510 (2003).

[60] H. Nyquist, "Thermal Agitation of Electric Charge in Conductors," Phys. Rev. **32**, 110 (1928).

[61] J. B. Johnson, "Thermal Agitation of Electricity in Conductors," Phys. Rev. **32**, 97 (1928).

[62] M. H. Devoret, in Fluctuations Quantiques (Elsevier, Science, 1997).

[63] L. Allen and J. H. Eberly, Optical Resonance and Two-Level Atoms (Dover Publications, 1987).

[64] A. Abragam, The Principles of Nuclear Magnetism (Oxford, London, 1961).

[65] M. Herald and J. Marion, Classical Electromagnetic Radiation, 3rd ed. (Saunders College Publishing, Fort Worth, 1995).

[66] D. Griffiths, Introduction to Quantum Mechanics, 2nd ed. (Benjamin Cummings, 2004).

[67] J. Clarke and A. I. Braqingki, The SQUID Handbook: Fundamentals and Technology of SQUIDs and SQUID Systems, 1st ed. (Wiley-VCH, 2004).

[68] F. C. Wellstood, Excess Noise in the dc SQUID; 4.2K to 20mK, Ph.D. thesis, University of California, Berkeley (1988).

[69] F. C. Wellstood, C. Urbina, and J. Clarke, "Low-frequency Noise in dc Superconducting Quantum Interference Devices Below 1-K," App. Phys. Lett. **50**(12), 772, (1987).

[70] R. C. Bialczak, R. McDermott, M. Ansmann, H. Hofheinz, N. Katx, E. Lucero, M. Neeley, A. D. O'Connell, H. Wang, A. N. Cleland, and J. M. Martinis, "1/f Flux Noise in Josephson Phase Qubits," Phys. Rev. Lett. **99**(18), 187006 (2007).

[71] D.J. Van Harlingen, T. L. Robertson, B. L. T. Plourde, P. A. Reichardt, T. A. Crane, and John Clarke, "Decoherence in Josephson-junction qubits due to critical-current fluctuations," Phys. Rev. B **70**(6), 064517 (2004).

[72] A. B. Zorin, F.-J. Ahlers, J. Niemeyer, T. Weimann, H. Wolf, V. A. Krupenin, and S. V. Lotkhov, "Background charge noise in metallic single-electron tunneling devices," Phys. Rev. B, **53**(20), 13682 (1996).

[73] M. Kenyon, C. J. Lobb, and F. C. Wellstood, J. Appl. Phys. **88**, 6536 (2000).

[74] D. I. Shuster, Circuit Quantum Electrodynamics, Ph.D. thesis, Yale University, (2007).

[75] R. M. Lewis, B. K. Cooper, , S. K. Dutta, H. Paik, T. A. Palomaki, H. Kwon, A. J. Przybysz, J. R. Anderson, C. J. Lobb and F. C. Wellstood, "Flux Noise in the dc SQUID Phase Qubit Measured by Microwave Reflectometry," manuscript under preparation.

[76] R. H. Koch, D. P. DiVincenzo and J. Clarke, "Model for 1/f Flux Noise in SQUIDs and qubits," Phys. Rev. Lett. **98**(26), 267003 (2007).

[77] T. A. Palomaki, S. K. Dutta, R. M. Lewis, A. J. Przybysz, H. Paik, B. K. Cooper, H. Kwon, J. R. Anderson, C. J. Lobb and F. C. Wellstood, "Multilevel spectroscopy of two-level systems coupled to a dc SQUID phase qubit," Phys. Rev. B **81**(14), 144503 (2010).

[78] J. M. Martinis, K. B. Cooper, R. McDermott, M. Steffen, M. Ansmann, K. D. Osborn, K. Cicak, S. Oh, D. P. Pappas, R.W. Simmonds, and C. C. Yu,

"Decoherence in Josephson Qubits from Dielectric Loss," Phys. Rev. Lett. **95**(21), 210503 (2005).

[79] P. K. Day, H. G. LeDuc, B. A. Mazin, A. Vayonakis, and J. Zmuidzinas, "A broadband superconducting detector suitable for use in large arrays," Nature **425**(6960), 817 (2003).

[80] A. J. Berkley, A. J. Berkley, H. Xu, M. A. Gubrud, R. C. Ramos, J. R. Anderson, C. J. Lobb, and F. C. Wellstood, "Characterization of an LC-isolated Josephson Junction Qubit," IEEE Trans. Appl. Supercond. **13**(2), 952 (2003).

[81] S. S. Mohan, Simple Accurate Expressions for Planar Spiral Inductances, IEEE J. Solid-State Circuits, **34**(10), 1419 (1999).

[82] IC Editor, Inc., ICED is now a freeware. http://www.iceditors.com.

[83] Berkeley Microlab, University of California, CA. http://microlab.berkeley.edu.

[84] SUSS MicroTec, Schlei heimer Str. 90, D 85748 Garching, Germany. http://www.suss.com.

[85] T. A. Fulton and G. J. Dolan, "Observation of Single-electron Charging Effects in Small Tunnel Junctions," Phys. Rev. Lett. **59**(1), 109 (1987).

[86] R. V. Scheer, Ultra-thin Tunnel Barrier Control of Al/Al_2O_3/Al (Superconducting) Tunnel Junctions, Final Report (1998).

[87] MicroChem Corp., 1254 Chestnut Street, Newton, MA 02464. http://www.microchem.com.

[88] THERMOCOAX SAS, BP 26, 61438 FLERS CEDEX, France http://www.thermocoax.com.

[89] A. B. Zorin, "The thermocoax cable as the microwave frequency filter for single electron circuits," Rev. Sci. Instrum. **66**(8), 4296 (1995).

[90] K. Bladh, D. Gunnarsson, E. HÄurfeld, S. Devi, C. Kristoffersson, B. Smalander, S. Pehrson, T. Claeson, P. Delsing, and M. Taslakov, "Comparison of cryogenic filters for use in single electronics experiments," Rev. Sci. Instrum. **74**(3), 1323 (2003).

[91] J. Claudon, F. Balestro, F. W. J. Hekking, and O. Buisson, "Coherent Oscillations in a Superconducting Multilevel Quantum System," Phys. Rev. Lett. **93**(18), 187003 (2004).

[92] N. Katz, M. Ansmann, Radoslaw C. Bialczak, Erik Lucero, R. Mcdermott, Matthew Neeley, Matthias Steffen, E. M. Weig, A. N. Cleland, John M. Martinis, A. N. Korotkov, "Coherent State Evolution in a Superconducting Qubit from Partial-Collapse Measurement," Science **312**(5779), 1498 (2006).

[93] R. F. Voss and R. A. Webb, "Macroscopic Quantum Tunneling in 1-μm Nb Josephson Junctions," Phys. Rev. Lett. **47**(4), 265 (1981).

[94] P. Bertet, I. Chiorescu, K. Semba, C. J. P. M. Harmans, and J. E. Mooij, "Detection of a persistent-current qubit by resonant activation," Phys. Rev. B. **70**(10), 100501, Sep. (2004).

[95] H. Kwon, A. J. Przybysz, B. K. Cooper, H. Paik, K. D. Osborn, B. S. Palmer, R. Budoyo, J. R. Anderson, C. J. Lobb and F. C. Wellstood, "Anomalous switching curves in a dc SQUID phase qubit," accepted in IEEE Trans. Appl. Supercond. (2010).

[96] R. A. Smith, "Excitation of transitions between atomic or molecular energy levels by monochromatic laser radiation," Proc. R. Soc. Lond. A **362**(1708), 1 (1978).

[97] G. Burkard, R. H. Koch, and D. P. DiVincenzo, "Multilevel quantum description of decoherence in superconducting qubits," Phys. Rev. B **69**(6), 064503 (2004).

[98] G. Ithier, E. Collin, P. Joyez, P. J. Meeson, D. Vion, D. Esteve, F. Chiarello, A. Shnirman, Y. Makhlin, J. Schriefl, and G. Schoen, "Decoherence in a superconducting quantum bit circuit," Phys. Rev. B **72**(13), 134519 (2005).

[99] T. Picot, A. Lupascu, S. Saito, C. K. P. M. Harmans and J. E. Mooij, "Role of relaxation in the quantum measurement of a superconducting qubit using a nonlinear oscillator," Phys. Rev. B, **78**(13), 132508 (2008).

[100] A. Lupascu, E. F. C. Driessen, L. Roschier, C. J. P. M. Harmans and J. E. Mooij, "High-Contrast Dispersive Readout of a Superconducting Flux Qubit Using a Nonlinear Resonator," Phys. Rev. Lett. **96**(12), 127003 (2006).

[101] C. T. Rigetti, Quantum Gates for Superconducting Qubits, Ph.D. thesis, Yale University, (2009).

[102] A. J. Przybysz, H. Kwon, R. Budoyo, B. K. Cooper, E. Crowe, A. J. Dragt, J. R. Anderson, C. J. Lobb and F. C. Wellstood, "Operation of a Phase Qubit that is Insensitive to Dephasing from Critical Current Fluctuations," manuscript under preparation.

[103] R. W. Simmonds, K. M. Lang, D. A. Hite, S. Nam, D. P. Pappas, J. M. Martinis, “Decoherence in Josephson Phase Qubits from Junction Resonators,” Phys. Rev. Lett. **93**(7), 077003 (2004).

[104] M. Steffen, M. Ansmann, R. McDermott, N. Katz, R. C. Bialczak, E. Lucero, M. Neeley, E. M.Weig, A. N. Cleland, and J. M. Martinis, “State Tomography of Capacitively Shunted Phase Qubits with High Fidelity,” Phys. Rev. Lett. **97**(5), 050502 (2006).

[105] M. Steffen, M. Ansmann, R. C. Bialczak, N. Katz, E. Lucero, R. McDermott, M. Neeley, E. M. Weig, A. N. Cleland, and J. M. Martinis, “Measurement of the Entanglement of Two Superconducting Qubits via State Tomography,” Science **313**(5792), 1423 (2006).

[106] E. Hoskinson, F. Lecocq, N. Didier, A. Fay, F. W. J. Hekking, W. Guichard, and O. Buisson, “Quantum dynamics in a camelback potential of a dc SQUID,” Phys. Rev. Lett. **102**(9), 097004 (2009).

[107] M. Ansmann, Benchmarking the Superconducting Josephson Phase Qubit - The Violation of Bell's Inequality, Ph.D. thesis, University of California, Santa Barbara (2009).

[108] A. Cottet, Implentation of a Quantum Bit in a Superconducting Circuit, Ph.D. thesis, University of Paris VI (2009).

[109] Max Born, J. Robert Oppenheimer, “Zur Quantentheorie der Molekeln (On the quantum theory of molecules),” Annalen der Physik **84**, 457 (1927).

[110] A. J. Przybysz, H. Kwon, R. Budoyo, B. K. Cooper, E. Crowe, A. J. Dragt, J. R. Anderson, C. J. Lobb and F. C. Wellstood, “Identifying sources of decoherence in a dc SQUID phase qubit with a sub-μm junction and interdigitated capacitor,” submitted to IEEE Trans. Appl. Supercond. (2010).

[111] K. Cicak, M. S. Allman, J. A. Strong, K. D. Osborn and R. W. Simmonds , “Vacuum-Gap Capacitors for Low-Loss Superconducting Resonant Circuits,” IEEE Trans. Appl. Supercond. **19**(3), 948 (2009).

[112] E. L. Hahn, “Spin Echoes,” Phys. Rev. **80**(4), 580 (1950).

[113] F. Yoshihara, K. Harrabi, A. O. Niskanen, Y. Nakamura, and J. S. Tsai, “Decoherence of Flux Qubits due to 1/f Flux Noise,” Phys. Rev. Lett. **97**(16), 167001 (2006).